Equilibrium Point Control of a Programmable Mechanical Compliant Manipulator

by

Damien Clapa

B.Sc. University of Alberta

A THESIS SUBMITTED IN PARTIAL FULFILMENT OF

THE REQUIREMENTS FOR THE DEGREE OF

MASTER OF APPLIED SCIENCE

in

THE FACULTY OF GRADUATE STUDIES

(Department of Mechanical Engineering)

We accept this thesis as conforming

to the required standard

THE UNIVERSITY OF BRITISH COLUMBIA

August 2004

Library Authorization

Damien Clapa
Name of Author *(please print)*

27/08/2004
Date (dd/mm/yyyy)

Title of Thesis: Equilibrium Point Control of a Programmable Mechanical Compliant Manipulator

Degree: M.A.Sc. Mechanical Engineering Year: 2004

Department of Mechanical Engineering
The University of British Columbia
Vancouver, BC Canada

Abstract

This thesis presents the design and experimental application of the Equilibrium Point Hypothesis as a controller model for a programmable mechanical compliant manipulator. A planar manipulator was designed and constructed with two joints, each powered by a pair of antagonistic McKibben actuators (air muscles). Programmable mechanical compliant manipulators provide increased intrinsic safety and the ability to implement a controller based on the EP Hypothesis becomes possible. The EP Hypothesis presents a model describing how human arm motions may be controlled. A previously developed geometrically derived force model for air muscles was modified leading to the formulation of a linearizing and decoupling compensator. This compensator, in conjunction with a proportional, integral controller operating on air supplied to the muscles, provided stable control of the stiffness and EP of each joint of the manipulator. A benefit of this combined EP and stiffness control is that a single control strategy can be used both to control the manipulator position in free-space and to provide interaction control for contact tasks.

A series of experiments were performed to demonstrate the controller behaviour in free space, in transition from free space to contact, and in contact with the environment. The free space experiments were done mainly to characterize the controller behaviour. The transition task involves moving in free space to contacting a surface at different velocities and contact angles. The contact task is a wiping motion along a surface with a prescribed normal force. The effect on introducing an unexpected "bump" along the surface was examined, as were velocity effects.

The stable behavior during transition from free-space to contact is a notable result. Because the manipulator follows an equilibrium-point trajectory with a programmed stiffness, no additional compensation is required when contacting objects in the workspace. Additionally the precise location of the object is not important as the mechanical compliance of the manipulator compensates for small contact position errors.

The results of the surface wiping tasks showed that it is possible to generate a wiping EP and stiffness trajectory that results in the predicted normal force while wiping a surface. Additionally, the mechanical compliance of the manipulator allows for stable response to unpredicted disturbances such as the presence of a significant bump on the smooth surface.

Table of Contents

Abstract ii
Table of Contents iii
List of Tables v
List of Figures vi
Nomenclature x
Acknowledgements xiii
Chapter 1 Introduction 1
1.1 Case for assistive robots and personal care 1
1.2 What will the robots need to be capable of? 3
1.3 Air Muscles 4
1.4 EP control 4
1.4.1 Background 5
1.5 EP Control and PMC Actuators 6
1.5.1 Interaction Tasks 8
1.6 Scope and Objective 8
1.7 Outline of Thesis 9
Chapter 2 Air Muscle Design 10
2.1 Introduction 10
2.2 System Overview 10
2.3 Air Muscle Properties 12
2.3.1 Observed Limitations 13
2.3.2 Geometric Models of Air Muscles 13
2.3.3 The empirical Modification to above model 15
2.4 Symmetric sizing method 17
2.5 Summary 25
Chapter 3 Electro-mechanical design and control of a PMC robot 26
3.1 Introduction 26
3.2 Manipulator 26
3.3 Valves 31
3.3.1 Sizing Valve Orifices 32
3.3.2 Selecting Constant Frequency for operation 35
3.4 Instrumentation, Drivers and DAQ 36
3.5 Controller 36
3.6 Summary 40
Chapter 4 Experimental Methods 42
4.1 Introduction 42
4.2 Free-Space Testing 44
4.2.1 Description of the test 44
4.2.2 Experimental measurements 45
4.3 Transition Testing 45
4.3.1 Description of the test 45

4.3.2 Experimental measurements....46
4.4 Contact Testing....47
4.4.1 Description of the test....47
4.4.2 Experimental measurements....50
4.5 Summary....50
Chapter 5 Results and Discussion....51
5.1 Introduction....51
5.2 Free-space task results....52
5.3 Transition Results....57
5.4 Contact Results....62
5.4.1 Velocity, Stiffness and EP Results....69
5.4.2 Repeatability Results....72
5.5 Summary....72
Chapter 6 Conclusions & Recommendations....74
6.1 General recommendations....75
6.2 Specific Recommendations for this Experimental Work....76
Bibliography....78
Appendix A Air Muscle Equations....81
A.1 Air Muscle Equations for the Appendix....81
Appendix B Muscle Construction....83
Appendix C Matlab Optimization Files....88
C.1 Optimize_Mount_Length.m....88
C.2 solverbn.m....89
C.3 Stiffness1.m....91
C.4 minimizethis.m....92
Appendix D Manipulator Bill of Materials....93
Appendix E Detailed Machining Drawings....97
Appendix F Assembly Instructions....123
Appendix G Sensors and Calibrations....126
G.1 Experimental Equipment Specifications....126
G.1.1 Solenoid Valves....128
G.1.2 Sensotec Pressure Transducers....129
G.1.3 AutoTran Pressure Transducers....130
G.1.4 Force Transducer....131
G.1.5 Length Encoders....132
G.2 Calibration of Equipment....133
G.2.1 Calibration of Sensotec Pressure Transducers....133
G.2.2 Calibration of Auto Tran Pressure Transducers....135
G.2.3 Calibration of Precision Transducers Force Transducer....136
G.2.4 Calibration of US Digital Length Encoders....137
Appendix H....138
H.1 Free-Space Tests....138
H.2 Contact Tests....138
H.3 Transition Tests....139
Appendix I Summary of Transition Tests....140
Appendix J Summary of Contact Tests....149

List of Tables

Table 3.1 – Design Requirements 28
Table 4.1 – Summary of Testing 43
Table 4.2 – List of transition test numbers 46
Table 4.3 – List of all contact test numbers 49
Table 5.1 – Summary of Mean Absolute Error for the transition testing 61
Table 5.2 – Summary of Errors without the bump present 68
Table 5.3 – Summary of Errors with the bump present 69
Table B.1 – Air Muscle Supplies 83
Table D.1 – BOM-1 94
Table D.2 – BOM-2 95
Table D.3 – BOM-3 96

List of Figures

Figure 1.1 – Rotary Joints Powered by Opposed Pairs of Air Muscle Actuators 7
Figure 2.1 – Overview of manipulator concept appropriate for demonstrating EP control 11
Figure 2.2 – Additional components required for powering the air muscle 11
Figure 2.3 – Rendering of a section of air muscle (from Shadow Robot Company) 12
Figure 2.4 – Force versus length relationship for an air muscle 12
Figure 2.5 – Air Muscle Actuator 13
Figure 2.6 – Manipulator configuration for muscle calibration 15
Figure 2.7 – Measured force and calculated force for an air muscle 16
Figure 2.8 – Absolute error in force between calculation and measured 17
Figure 2.9 – Simple rotary joint powered by a pair of air muscles 18
Figure 2.10 – Force versus length at different pressures 19
Figure 2.11 – Useful range for a single muscle 19
Figure 2.12 – Working range of each muscle 20
Figure 2.13 – Configuration where maximum and minimum stiffness most constrained 21
Figure 2.14 – Maximum torque Constraint 21
Figure 2.15 – Stiffness versus pressure at a constant length 23
Figure 2.16 – Small stiffness constraint 23
Figure 2.17 – Highest stiffness constraint 24
Figure 3.1 – Manipulator with muscles 27
Figure 3.2 – Finalized manipulator design 29
Figure 3.3 – Close-up of back of manipulator 29
Figure 3.4 – Plot of the range of motion of the manipulator 30
Figure 3.5 – Torques for 20N force normal to the wiped surface 31
Figure 3.6 – Partially disassembled Matrix valve with orifice plate 33
Figure 3.7 – Inlet orifice sized to allow no more than 1N discreet force steps for smallest possible inflation 34
Figure 3.8 – Final inlet and outlet orifice sizes with inflation and deflation times roughly matched 35
Figure 3.9 – Schematic of planar robot controller 37
Figure 4.1 – X and Y axis origin location 43

Figure 4.2 – Diagram of the range of motion during the free space task 44
Figure 4.3 – Diagram of transition task 46
Figure 4.4 – Diagram of contact test 47
Figure 4.5 – Diagram of EP adjustments 48
Figure 4.6 – Contact test with a smooth wall 49
Figure 4.7 – Contact task with a bump present 50
Figure 5.1 – Commanded position vs. time for free-space tests (thick lines are desired and thin lines are measured) 52
Figure 5.2 – Error in x_{EP} versus x for free-space tests 53
Figure 5.3 – Error in x_a vs. x 54
Figure 5.4 – Error in k_y versus x 55
Figure 5.5 – Mean Absolute Error of k_y versus v_x 56
Figure 5.6 – Mean absolute error x_{EP} versus v_x 56
Figure 5.7 – Transition test #1 y_a and y_{EPd} with and without the wall versus path 57
Figure 5.8 – Transition test #1 y_{EPa} and y_{EPd} with and without the wall versus path 58
Figure 5.9 – Transition test #1 k_{ya} and k_{yd} with and without the wall versus path 59
Figure 5.10 – Transition test #9 k_{ya} and k_{yd} with and without the wall versus trajectory 60
Figure 5.11 – Transition test #1 actual and predicted force with and without the wall versus trajectory 61
Figure 5.12 – Test #10 without bump (y versus x) 63
Figure 5.13 – Test #10 with bump y versus x 64
Figure 5.14 – Test #10 without bump k_y versus x 65
Figure 5.15 – Test#10 with bump k_y versus x 65
Figure 5.16 – Test#10 force versus x without bump 66
Figure 5.17 – Test#10 force versus x with bump 67
Figure 5.18 – Summary of y_{EP} error 70
Figure 5.19 – Summary of k_y error 71
Figure 5.20 – Summary of force error 72
Figure B.1 – Tools and supplies to make air muscles 84
Figure B.2 – Soldering the brass inserts 84
Figure B.3 – Putting inserts into the plastic and surgical tubing 85
Figure B.4 – Plastic and surgical tubing connected and plugged with brass inserts 85
Figure B.5 – End loop of the air muscle 86

Figure B.6 – Exploded view 86
Figure B.7 – Clamping down an O-Clamp 87
Figure B.8 – Completed air muscle mounted to the arm 87
Figure E.1 – Drawing 1 98
Figure E.2 – End Effector 99
Figure E.3 – Link 2 and sprocket 100
Figure E.4 – Pulley 1 and big gear 101
Figure E.5 – Pulley 2 and big gear 102
Figure E.6 – Link drive assembly 103
Figure E.7 – Encoder and gear 104
Figure E.8 – Box 105
Figure E.9 – Adaptor 1 106
Figure E.10 – Adaptor 2 107
Figure E.11 – Adaptor 3 108
Figure E.12 – Link 2 109
Figure E.13 – Timing belt sprocket 2 110
Figure E.14 – Shaft 2 111
Figure E.15 – Pulley 1 112
Figure E.16 – Big gear 113
Figure E.17 – Timing belt sprocket 1 114
Figure E.18 – Pulley 2 115
Figure E.19 – Shaft 1 116
Figure E.20 – Link 1 117
Figure E.21 – Fitting 118
Figure E.22 – Small gear 119
Figure E.23 – Top 120
Figure E.24 – Side 121
Figure E.25 – Base 122
Figure I.1 – Transition test #1 140
Figure I.2 – Transition test #2 141
Figure I.3 – Transition test #3 142
Figure I.4 – Transition test #4 143
Figure I.5 – Transition test #5 144

Figure I.6 – Transition test #6 145
Figure I.7 – Transition test #7 146
Figure I.8 – Transition test #8 147
Figure I.9 – Transition test #9 148
Figure J.1 – Contact test #1 150
Figure J.2 – Contact test #2 151
Figure J.3 – Contact test #3 152
Figure J.4 – Contact test #4 153
Figure J.5 – Contact test #5 154
Figure J.6 – Contact test #6 155
Figure J.7 – Contact test #7 156
Figure J.8 – Contact test #8 157
Figure J.9 – Contact test #9 158
Figure J.10 – Contact test #10 159
Figure J.11 – Contact test #11 160
Figure J.12 – Contact test #12 161
Figure J.13 – Contact test #13 162
Figure J.14 – Contact test #14 163
Figure J.15 – Contact test #15 164
Figure J.16 – Contact test #16 165
Figure J.17 – Contact test #17 166
Figure J.18 – Contact test #18 167
Figure J.19 – Contact test #19 168
Figure J.20 – Contact test #20 169
Figure J.21 – Contact test #21 170
Figure J.22 – Contact test #22 171
Figure J.23 – Contact test #23 172

Nomenclature

A_e	Area of orifice
dl_i	Inner surface displacement
ds_i	Area vector
J	Jacobian of manipulator
K_c	Carestian end point stiffness matrix
K_j	Joint space stiffness matrix
L	Length of an air muscle
L_{mount}	Mounting length of an air muscle
L_{max}	Longest length of muscle at end of range
L_{min}	Shortest length of muscle at end of range
L_{zero}	Length at which muscle delivers no axial force
P	Absolute pressure inside air muscle
P_{atm}	Atmospheric Pressure (1 bar at sea level)
P_g	Gauge pressure inside air muscle
P_{max}	Maximum allowable muscle gauge pressure
P_{min}	Minimum allowable muscle gauge pressure
R	Gas constant
T	Temperature of air inside muscle
S_i	Inner surface displacement
V	Volume inside of muscle
X	Cartesian end point trajectory
X_a	Actual Cartesian location of the end point

X_{EP}	Cartesian end point equilibrium trajectory
c	A term introduced to account for constant force offset in air muscle
b	Braid length of an air muscle
dV	Volume Change
f	Muscle axial force
f_{max}	Maxium available muscle force
k_i	Stiffness of joint i
k_m	Stiffness of a single muscle
k_{max}	Maximum available joint stiffness
k_{min}	Minimum available joint stiffness
k_x	X-axis end point stiffness
k_{xy}	Cartesian cross stiffness term
k_y	Y-axis end point stiffness
m	Mass of air inside air muscle
n	Number of turns in braid of an air muscle
p^*	Critical back pressure
p_o	Stagnation pressure
r	Pulley radius
v_x	X-axis velocity of end point
x_a	Actual X-axis position of the end point
x_{EP}	X-axis endpoint equilibrium position
x_{EPa}	Actual X-axis endpoint equilibrium position
x_{EPd}	Desired X-axis endpoint equilibrium position

y_a	Actual Y-axis position of the end point
y_{EP}	Y-axis endpoint equilibrium position
y_{Epa}	Actual Y-axis endpoint equilibrium position
y_{Epd}	Desired Y-axis endpoint equilibrium position
κ	Muscle Stiffness
τ	Joint torque
τ_{max}	Maxium available joint torque
θ	Joint angle
θ_a	Actual joint angle
θ_d	Desired joint angle
θ_{EP}	Equilibrium joint angle
θ_{max}	Maxium angular range of motion
ADL	Activities of daily living
EP	Equilibrium Position
MAE	Mean average error
PPC	Programmable passive compliance
PMC	Programmable mechanical compliance
PWM	Pulse Width Modulation
RMSE	Root mean squared error

Acknowledgements

I would like to thank Leanne first and foremost for her unending support and encouragement through this long journey.

I would like to thank my supervisors, Dr. Elizabeth Croft and Dr. Antony Hodgson, for their guidance and assistance. I would also like to thank the many fellow graduate and undergraduate students at UBC who have helped in so many ways.

The assistance of the faculty and staff of the Mechanical Engineering Department was greatly appreciated. I would also like to acknowledge the financial support of the Natural Sciences and Engineering Research Council of Canada.

Chapter 1
Introduction

1.1 Case for assistive robots and personal care

In the coming decades, there will be increased demand for nontraditional technologies, such as robotics, for the care of an increasingly dependent elderly population. This increased demand will be driven by a number of factors, including the changing demographics in North America and Europe. While the number of people who can expect to live to advanced age is increasing quickly, the fraction of them who will be disabled will quite likely be no different than it was 25 years ago [1]. The increasing number of disabled elderly people will likely outpace any growth in either formal or informal care sources, and will require affordable technologies to assist in tasks of daily living to avoid institutionalization. Affordable in-home robotics is potentially one part of the solution.

Elderly people who are experiencing progressive disability are in a precarious situation, particularly if they are living on low or fixed incomes. As a group, they are likely to face enormous difficulties for three reasons [2]: (i) people have longer life expectancies today than ever before, (ii) disability rates for people over 65 are three times that of those between 35 and 65, and (iii) extended families are shrinking. At present, formal (paid) care is generally insufficient to keep most elderly disabled in their homes. Only those individuals with access to

informal care, usually from family members, are able to live at home [3]. Studies have also shown that the frequency that family members, especially children, tend to visit is inversely proportional to the level of disability [4].

Although modern medicine and improved living conditions have been successful in extending peoples life expectancy, the disability rate of the elderly has not decreased in 20 years [1]. More than 40% of those over the age of 65 are disabled, with the majority reporting disabilities including predominantly either mobility or agility limitations. Based on this fact, there is reason for concern, as the percentage of people over the age of 65 will increase dramatically in the next 30 years [5].

Common sense suggests, and studies [6] have shown, that elderly people would prefer to live in their own homes rather than in an institution. Interestingly, while cognitive disability is an indicator for institutionalization, physical disability is not. Even so, the majority of elderly requiring care suffer from functional disabilities [3]. The best predictor of institutionalization is socio-economic [7].

The five tasks that make it increasingly difficult to live at home with disabilities are: bathing, toilet, transfer, eating and dressing [8]. Collectively these tasks are referred to as the Activities of Daily Living (ADL). The larger the number of these tasks a person requires assistance with, the more difficult it is to continue independent living. There are many diseases and disorders common to the elderly that contribute to the loss of agility and dexterity. Arthritis is the single most reported dexterity related disease of the elderly, affecting 2/3 of those over the age of 65 [9]. Tremor is a symptom of a number of diseases common among elderly people. Something as simple as fastening the buttons of a favorite shirt may be enough to keep someone in their home and away from social interaction. The need for aid with the five ADL's leads to a feeling of helplessness and loss of independence and places strain on those who provide informal care [3]. A robotic aid that can assist with the 5 ADL's would be enormously helpful to those requiring aid presently.

In summary, changing demographics demand a cost effective way of helping functionally disabled people perform simple daily tasks. The ability to perform these tasks without human aid will allow an increasing number of people to live in their own homes with dignity. The work in this thesis is part of an ongoing, worldwide, interest in robotic devices as home assistants. A

future-developed robotic aid that could physically assist with the five key tasks discussed above would reduce the formal or informal care taking burden.

1.2 What will the robots need to be capable of?

Future robotic aids assisting disabled elderly people in their homes will need to safely interact with humans [10,11]. The five key tasks of daily living mentioned above all share one important element: they all require physical interaction with the disabled person.

A means by which the designer of an assistive robot can be certain the device will be safe is of great importance. Furthermore, such an assistive robot should emulate human manipulation characteristics. Human muscles are extraordinary actuators. People can vary the force and stiffness of most of their joints independently. One class of actuators, namely, the Programmable Passive Compliant (PPC) actuator, has been identified by other robot designers as being promising for this type of activity [12] in terms of safety and stiffness variability. The goal of this work will be to investigate the potential of this class of actuators for the design and control of safe interactive robots.

In this work we will use the term Programmable Mechanical Compliant Actuator or PMC actuator. A PMC actuator is one which is mechanically compliant but whose compliance is variable. This differs from feedback-generated compliance in that the compliance at any instant is a mechanical property of the system, independent of sensors, feedback or control. For interaction with humans, mechanical compliance is intrinsically safer [13].

Electrically- and hydraulically-powered robots are not normally designed to be compliant. Although there are techniques such as impedance control which can make such robots appear to the user as if they were light and compliant, such techniques are limited by the torque range of the actuators and the bandwidth of the controller system [14]. If the robot becomes un-powered, it will revert to a heavy, stiff state. Thus, relying on control alone to introduce compliance is not an intrinsically safe approach [12,13]. Furthermore, such actuators are generally expensive and therefore unsuited for our intended application.

A PMC actuated robot will embody the physical elements most suitable for safe human interactions. One of the reasons why humans are good at interacting with an unstructured environment is that our muscles are effectively PMC actuators. There are many tasks where

precision is secondary to compliance, for example, shaving. This design approach is hypothesized to reduce the computational load when interacting in unstructured tasks [13]. In this work, a PMC actuated robot is designed and a strategy for control of this robot for a human-interaction type task is developed.

1.3 Air Muscles

Of the various PMC actuators that have been developed, one of the most interesting and most developed are air muscle actuators. Air muscles are simple and inexpensive. They have existed under various names, including: McKibben Muscles, Air Muscles and Rubbertuators, since their initial development in the 1950's [15]. Most past work has focused on using air muscles as a low cost and lightweight replacement for traditional robotic actuators in high precision positioning tasks. However, while the intrinsic compliance of these actuators makes them unsuited to such tasks, these very properties make them ideal for use in an assistive robotic device.

The first proposed use for air muscles in the 1960's was in an orthotic device [15]. Since then at least two companies have attempted to commercialize the actuator. First Bridgestone and later Festo. Neither commercial version has seen significant market penetration. The actuators are nonlinear and have not proven suitable for the types of tasks most researchers have proposed.

When implemented in an opposed pair, the resulting joint exhibits similar characteristics to human joints such as the elbow or knee. The compliance is variable and independent of position, and the response to perturbations is also similar to human joint-muscle systems. In this work it is proposed that a neuromotor-science based control model would be appropriate for application to an air muscle actuated robot operating in a human environment, specifically in the context of safe interaction with humans.

1.4 EP control

Much of the existing literature on intrinsically compliant actuators is related to the problem of accurate position control of a robot powered by such actuators [16, 17]. However, there is a broad class of tasks where high positional accuracy is secondary to dependable programmable compliance. Many day-to-day tasks carried out by humans do not require fine position control,

and the inherent compliance of a person's limbs enables appropriate interaction forces to be generated during execution of such tasks [18].

Neuromotor scientists have proposed numerous control schemes to explain how animals control their muscles. One method has been useful in describing a wide range of human motor tasks. Equilibrium Point Control was first proposed in the 1960's by Feldman [19] and can serve as a possible model for a controller for air muscles. EPC is a promising approach for controlling PMC assistive robots.

1.4.1 Background

Numerous experiments have been conducted to test the EPC model [18-21]. There is still controversy regarding how appropriate this model is for understanding actual motor control processes. The controversy is largely irrelevant to our interests. The fact that a large number of tests have shown that this model fits experimental data well suggests that if this control method is used with PMC actuators, humanlike movement should result.

EP control suggests that the brain develops a virtual trajectory for a limb to follow based on what it knows about the environment at the time of the formulation of the trajectory [18]. This virtual trajectory is a set of equilibrium joint positions and stiffnesses. These are two independent trajectories. Because of compliance, the limb will not exactly follow the virtual trajectories but instead will follow one that is governed by interactions between the limb and the environment.

Although inertial effects and contact disturbances can cause limbs to deviate from the equilibrium trajectory, the spring-like properties of the peripheral neuromuscular system produce appropriate corrective forces in response to these deviations. With practice, the brain can learn to compensate for the inertial, frictional and contact loads experienced in a particular task and can construct feed-forward EP and compliance trajectories suitable for carrying out very complex motions in space. If the details of the achieved trajectory are important, the subject can compute an inverse model to predict the outcome.

One important aspect of compliant control is that for most joints the stiffness can also be chosen. This helps to ensure that the trajectory followed is as planned based on what is known about the environment and possible interactions. When walking, a very compliant posture is maintained by most of the body's joints. When we inadvertently trip over something our body is often able

to find a new stable posture even before we have a chance to respond. Centrally, we can vary the stiffness of the virtual trajectory as needed for our task. Hitting a tennis ball certainly requires a very stiff forearm, while shaving our face does not.

In human arms, controlling the level of coactivation of the muscles and altering reflex gains can vary the stiffness of the elbow joint. From one starting point, a new EP and joint stiffness can be chosen substantially independently. Neuromotor researchers have demonstrated that arm movement has a significant feed-forward component that can be represented as an open loop equilibrium point (EP) trajectory followed by the joints when executing motion tasks [20, 21].

A robot controller based on the EP approach is promising both because of the benefits of the intrinsic safety of this approach and because data collected from observation of humans can serve quite directly as control input to a biomimetic manipulator. This independence of joint stiffness and EP is utilized in the design and control of the experimental manipulator developed in this work.

1.5 EP Control and PMC Actuators

Several experimental robots have been constructed utilizing McKibben (air muscle) actuators [16, 17, 22-24]. These actuators behave in many respects similarly to human muscles [33]. By constructing robot joints powered by antagonistic pairs of McKibben air muscles, they, like human joints, exhibit adjustable compliance throughout their range of motion [16, 23]. Figure 1.1 shows a joint constructed with opposed pairs of air muscles.

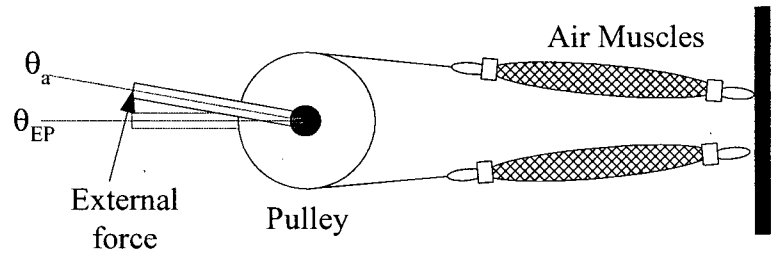

Figure 1.1 – Rotary Joints Powered by Opposed Pairs of Air Muscle Actuators

Colbrunn [26] developed a method to independently vary the stiffness and position of a rotary joint powered by air muscles. In a joint as shown above when the forces in both muscles of an opposed pair remain balanced, the joint will not move, but its stiffness will increase. Imbalances in the forces of the two muscles in an opposed pair will cause a change in the equilibrium angle of the joint (θ_{EP}), the angle where the joint will move to if no external joint torque is present. Colbrunn exploited the properties of air muscles to develop a walking robot that remained passive throughout most of its range of motion to conserve air pressure in the tank powering his robot.

Colbrunn demonstrated that it is possible to decouple the control of stiffness and desired angular position for a single joint powered by two opposed McKibben air muscle actuators. The decoupling compensator assumes that the joint stiffness and angular position can be decoupled with a pair of constant gains over the complete workspace of the joint. This simple approximation allowed for acceptable results for the purpose for which the muscles were used. The actual input to the muscles was pressure, which was measured and controlled directly. Stiffness and angular position were calculated.

Colbrunn successfully demonstrated independent control of both joint angle and joint stiffness with a set of very simple control laws. Joint angle is directly measured by a rotary encoder and the force in each muscle is measured with a force transducer. Colbrunn reported good success with this method. His measure of success was to have the majority of the motion of the leg happen in the passive phase. That is, he set the equilibrium position and allowed the compliance of the actuators to move the leg into the next position.

Tonietti and Bicchi [13, 22] demonstrated an alternative solution for the decoupling of joint stiffness and θ_d. Their model assumes that the inverse model of stiffness and position to

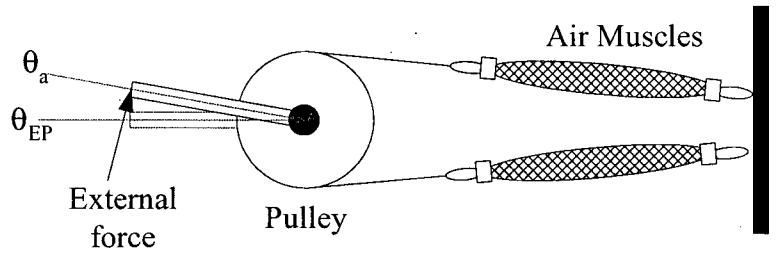

Figure 1.1 – Rotary Joints Powered by Opposed Pairs of Air Muscle Actuators

Colbrunn [26] developed a method to independently vary the stiffness and position of a rotary joint powered by air muscles. In a joint as shown above when the forces in both muscles of an opposed pair remain balanced, the joint will not move, but its stiffness will increase. Imbalances in the forces of the two muscles in an opposed pair will cause a change in the equilibrium angle of the joint (θ_{EP}), the angle where the joint will move to if no external joint torque is present. Colbrunn exploited the properties of air muscles to develop a walking robot that remained passive throughout most of its range of motion to conserve air pressure in the tank powering his robot.

Colbrunn demonstrated that it is possible to decouple the control of stiffness and desired angular position for a single joint powered by two opposed McKibben air muscle actuators. The decoupling compensator assumes that the joint stiffness and angular position can be decoupled with a pair of constant gains over the complete workspace of the joint. This simple approximation allowed for acceptable results for the purpose for which the muscles were used. The actual input to the muscles was pressure, which was measured and controlled directly. Stiffness and angular position were calculated.

Colbrunn successfully demonstrated independent control of both joint angle and joint stiffness with a set of very simple control laws. Joint angle is directly measured by a rotary encoder and the force in each muscle is measured with a force transducer. Colbrunn reported good success with this method. His measure of success was to have the majority of the motion of the leg happen in the passive phase. That is, he set the equilibrium position and allowed the compliance of the actuators to move the leg into the next position.

Tonietti and Bicchi [13, 22] demonstrated an alternative solution for the decoupling of joint stiffness and θ_d. Their model assumes that the inverse model of stiffness and position to

pressures can be found. This method is not appropriate for an error-based controller as it can lead to instability between the muscles. In this work, it is proposed to instead find the map between the differential change in stiffness and position to differential change in mass of air in each muscle over the full operating range. This approach is expected to allow stable, compliant control of multiple PMC actuators. This benefit derives from the fact that the mass of air in a muscle is independent of the length of the muscle.

1.5.1 Interaction Tasks

ADL tasks required for assistive living include free space, transition and contact tasks. In this work we will investigate all three tasks as part of experimental testing of the design and control strategies proposed. In particular, the transition from free space motion to contact is a type of task that poses many difficulties for traditional robotic manipulators. For rigid robots, complex techniques for switching between multiple control strategies [27,28] are used to overcome this difficult type of transition. A wiping task is representative of many ADL tasks and requires free-space, transition and contact motion. Thus in the experimental work of this thesis, a wiping task is used as the exemplar motion.

Other researchers have explored the possibility of using mechanically compliant actuators to create robots that are intrinsically compliant [22- 25]. A manipulator that can use a single control strategy to perform free-space motion, contact interaction, and transition interaction tasks would potentially be very desirable for use in human environments.

1.6 Scope and Objective

The objective of the work described here is to demonstrate that a programmable mechanical compliant manipulator can be controlled with a simple control strategy based on EP control.

The PMC actuators chosen to use in this demonstration are air muscles. Muscles were designed and built in the lab for this project. An empirical model was developed to allow for the calculation of muscle force from pressure and length. Because no documented method could be found, an algorithm for sizing a pair of muscles and pulley radius for a joint like the one shown in Figure 1.1 was developed.

A manipulator was designed and constructed to perform three tests identified as appropriate for testing the hypothesis. This manipulator has two air muscle actuated links. Valves and other electro-mechanical components were purchased, modified or built to allow for a PC to control the manipulator. An EP inspired controller was developed and implemented to allow for the desired testing. Three sets of experiments, covering free-space, transition and contact tasks were performed and analyzed.

The original contributions of this work are: (i) a method was developed to facilitate the design of rotary air muscle driven joints including proper muscle selection, (ii) a decoupling compensator was developed to map error in joint stiffness and joint EP to error in the mass of air in each muscle, (iii) an EP inspired control algorithm was developed, implemented and tested on the robot.

1.7 Outline of Thesis

Chapter 1, Introduction - This chapter discusses the motivation for this work, presents air muscles, EP Hypothesis and the notion of programmable mechanical compliance (PMC) and provides a discussion of work that has been done by others in the area of controlling McKibben air muscles.

Chapter 2, Air Muscle Design – This chapter describes the design of the air muscles used in this work. The empirical force model used will be described as well as the symmetric joint sizing method.

Chapter 3, Electro-Mechanical Design and Control of a PMW Robot – This chapter details the design of the manipulator, valve selection and development of the EP controller.

Chapter 4, Experimental Methods – A description of the three experiments conducted to evaluate the capabilities of the manipulator and controller. The three tests are a free-space motion test, a transition from free-space to contact task and a contact task.

Chapter 5, Results and Discussion - A presentation and discussion of the results of the three tests described in Chapter 4.

Chapter 6, Conclusions and Recommendations.

Chapter 2
Air Muscle Design

2.1 Introduction

Air muscles have unique properties that can be exploited to construct a simple, low cost, PMC robotic device. In this chapter, these properties are investigated with a view to reducing the instrumentation necessary for such a device. As well, in the second part of this chapter, the optimization of air-muscle properties for a specific robotic design is discussed.

2.2 System Overview

Air muscles, a manipulator and supporting hardware were all required before it would be possible to demonstrate an EP inspired controller of a PMC manipulator. The system envisioned for demonstrating the three experimental tasks chosen is diagramed in Figure 2.1 below. The central disk pictured at the base of the manipulator is actually two concentric pulleys stacked vertically. The first pulley is directly attached to link 1 and the second pulley drives link 2 through a toothed belt. The calibrations can be found to translate the output of the potentiometer shown in the figure to give both the current link angles and the muscles lengths.

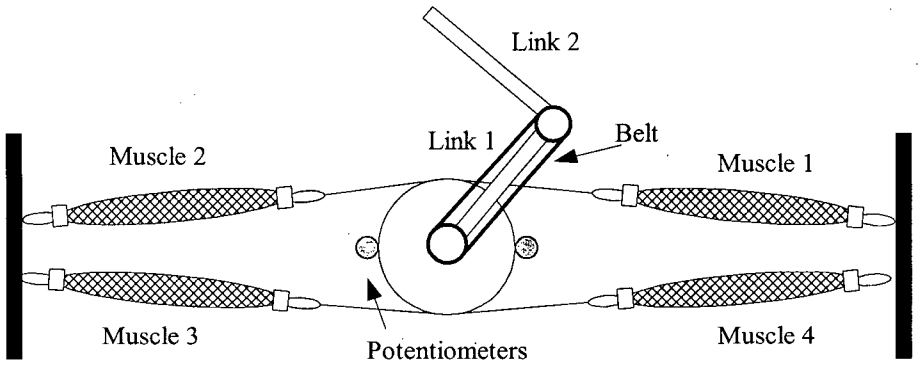

Figure 2.1 – Overview of manipulator concept appropriate for demonstrating EP control

In addition to the manipulator and muscles, a valve and pressure transducer for each muscle are required. The overall system design for the hardware shown in Figure 2.1 and Figure 2.2 is discussed in Chapter 3.

The above-diagramed system has the properties required such that each joint stiffness (k_1 and k_2) as well as equilibrium angles for each link (θ_{EP1} and θ_{EP2}) can each be independently controlled. The relationships between these parameters are discussed in the remainder of this chapter and in Chapter 3.

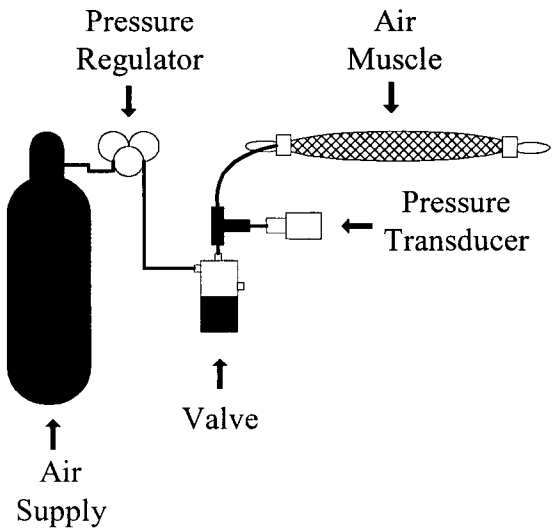

Figure 2.2 – Additional components required for powering the air muscle

2.3 Air Muscle Properties

McKibben muscles principally consist of a nylon braid encasing a latex rubber tube. The nylon braiding can be purchased from electrical supply stores and the rubber tubing was standard surgical natural latex tubing available from medical supply stores. The construction method is described in Appendix A[29].

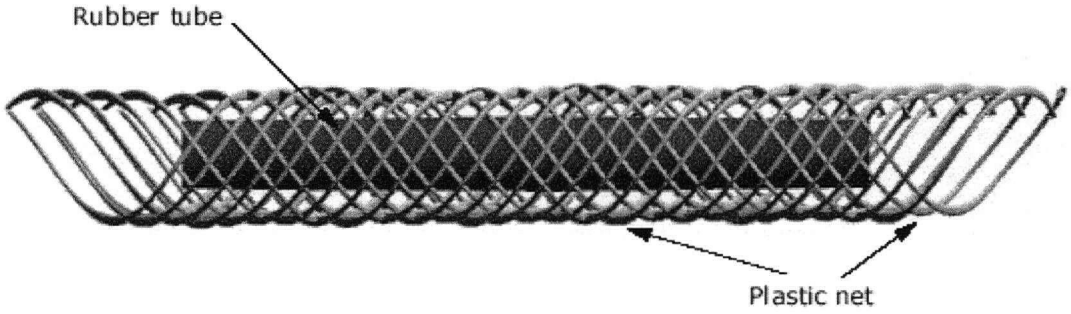

Figure 2.3 – Rendering of a section of air muscle (from Shadow Robot Company)

According to the Shadow Robot Company, a 6mm diameter air muscle has the "strength, speed and fine stroke of a finger muscle in a human hand" and "an Air Muscle 30mm in diameter is capable of lifting more than 70 Kg at a pressure of only four bar"[29]. The air muscle exerts its maximum force at maximum extension. As extension decreases, the force that it exerts decreases at a decreasing rate. This means that small changes in force can be achieved by using a larger muscle at an extension below its maximum. The sketch graph below shows the relationship between force and extension for a constant pressure.

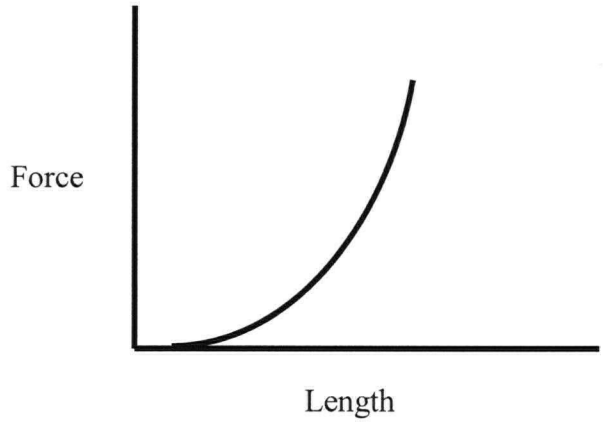

Figure 2.4 – Force versus length relationship for an air muscle

The air muscle takes advantage of the geometry of its outer shell to generate a contracting force when inflated. The muscle has two main components: an outer shell and an inner bladder. The outer shell is typically made of nylon and the inner bladder of latex or synthetic rubber. One of the air muscles used for this work is shown in Figure 2.5 below. The bladder is required to contain the gas used to power the actuator. The nylon braid converts the pressure in the actuator to tension in the braid, which exerts force in the axial direction.

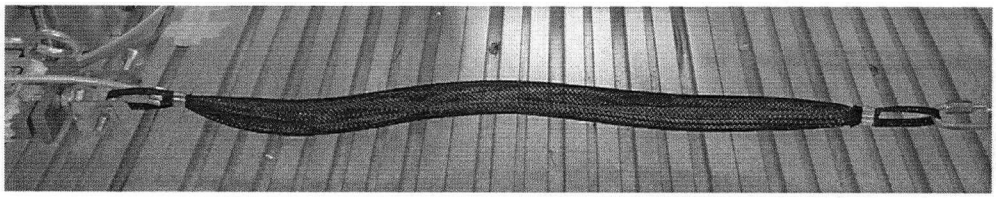

Figure 2.5 – Air Muscle Actuator

The theoretical rest length of an air muscle is equal to the length at which its volume is maximized. In reality, due to end effects the rest length of an unloaded actuator is not quite at the point of maximum volume.

For the purposes of this work, it is desirable to reduce the amount of instrumentation required. One way to accomplish this is to avoid the use of force transducers for each muscle. Instead, the pressure and length of each air muscle is used to calculate the force and stiffness of each muscle. The empirical equation that is fit to each muscle is presented in the following sections.

2.3.1 Observed Limitations

There is a maximum and minimum force achievable for the air muscles. The maximum force and pressure are physical design limitations particular to the way the muscles are constructed. The minimum pressure is required to keep the bladder inflated and the minimum force is required to avoid large hysteresis. These mechanical limits are: maximum pressure of 7 bar, minimum pressure of 1 bar and a maximum force of 100 N.

2.3.2 Geometric Models of Air Muscles

Various groups have modeled air muscles in different ways. A geometric model suggested by Chou and Hannaford [31] is the principal model used in this research. The geometric model of

the air muscle originally appears in Chou but was modified by Colbrun [26] to a more useful form. His formulation is outlined below.

Neglecting the frictional losses, the work done on the system will equal the work extracted from system.

$$dW_{in} = \int_{Surface} (P - P_{atm}) dl_i \cdot ds_i = (P - P_{atm}) \int_{Surface} dl_i \cdot ds_i = P_g dV \tag{2.1}$$

Where:

P=Absolute internal gas pressure

P_{atm}=Atmospheric pressure

P_g=Gage pressure

S_i=Inner surface displacement

ds_i=Area vector

dl_i=Inner surface displacement

dV=Volume Change

Chou shows that this ultimately yields Equation 2.2 below. The rest of the formulation can be found in Appendix B. The force generated by a muscle is a function of two geometric properties, b and n, and the internal pressure (P_g) and the length (L) of the muscle. The constant b is equal to the length of the nylon strands in the braid if they were pulled straight. The constant n is equal to the number of turns in the helix that makes up the braid.

$$f = \frac{P_g b^2 (3\frac{L^2}{b^2} - 1)}{4\pi n^2} \tag{2.2}$$

In theory the muscle should have maximum force at its most extreme length (where the maximum possible length is equal to b) and generate no force at the position where the maximum volume is achieved, which can be shown to be when:

$$3L^2/b^2 = 1 \tag{2.3}$$

as derived from Equation 2.2.

2.3.3 The empirical Modification to above model

The geometric force model for McKibben actuators was used to solve for force in each muscle as a function of pressure and current length as shown by [30]. This theoretical model was found to be unsatisfactory for this purpose. An offset (c) was subtracted to account for end-effects. This near constant offset has been reported by others [26]. Rather than trying to measure the geometric properties b and n, instead the terms b,n,c were empirically fit to data collected for each actuator throughout the pressure, length and force ranges of interest. A least squares fit was used to solve for the values.

$$f = \frac{P_g b^2}{4\pi n^2}\left[\frac{3L^2}{b^2} - 1\right] - c \tag{2.4}$$

The air muscles chosen for this work had the following physical characteristics: ½ inch nylon braid, ¼ inch latex tubing, b = 480mm, and n = 6.8 turns. The calibrated values are approximately in agreement with the geometric values. The values for one of the muscle calibrations were: b=501mm, n=5.6782 and c=28.1193. An example plot of a single muscle calibration is shown below in Figure 2.7. The absolute force error over the range of motion for the wiping task is shown in Figure 2.8. This plot was generated from data collected from the completed manipulator with the stiffness controller, described in Chapter 3, implemented. To calibrate all of the muscles each joint was in turn cycled through the full required range of motion for the experiments (θ_{EP} minimum θ_{EP} maximum) with three constant joint stiffnesses (k_i) of 15Nm/rad, 22.5Nm/rad and 30Nm/rad. Figure 2.6 below shows the setup used to calibrate the muscles.

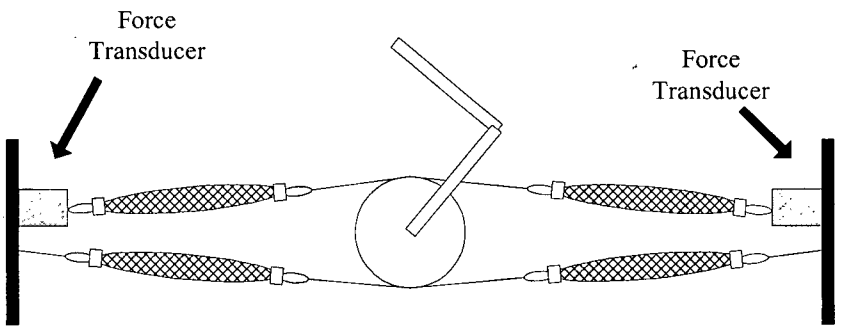

Figure 2.6 – Manipulator configuration for muscle calibration

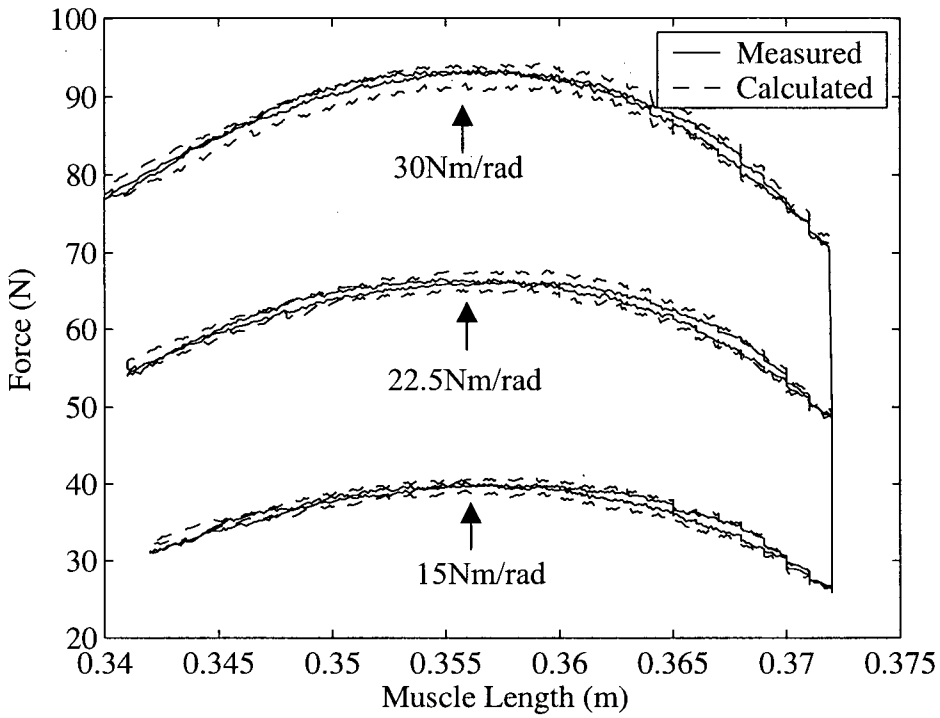

Figure 2.7 – Measured force and calculated force for an air muscle

The error in the calculated force exhibits hysteresis as shown in Figure 2.8. The error does not increase linearly with the magnitude of the force. The absolute error is generally less than 2N throughout the entire muscle operating range of lengths and force. This level of error is considered sufficient for our application. Using calculated force in place of force transducers in our system results in only small errors in force.

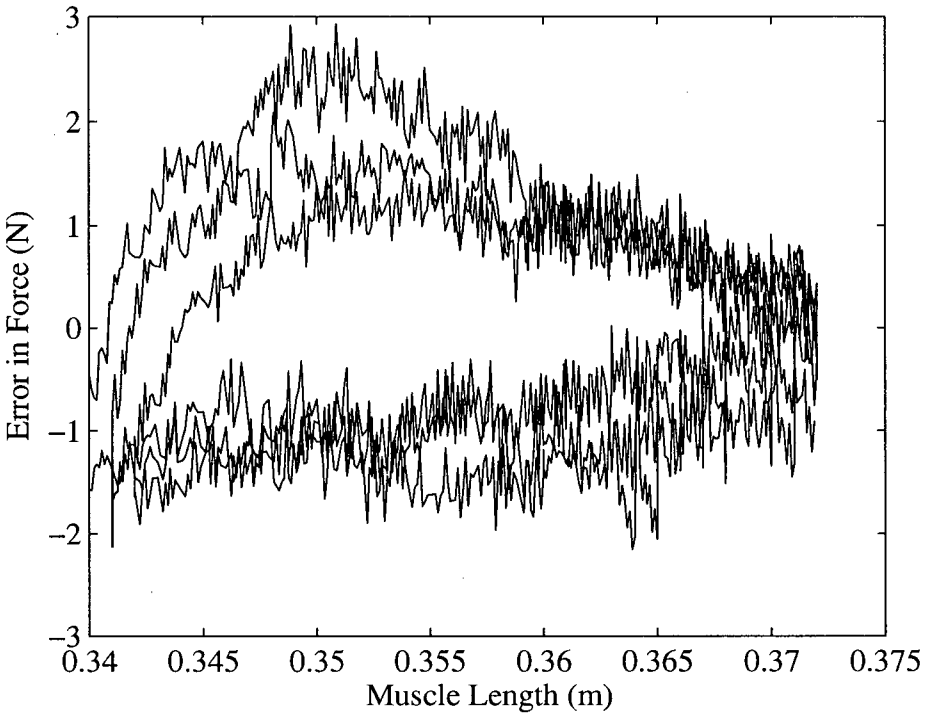

Figure 2.8 – Absolute error in force between calculation and measured

2.4 Symmetric sizing method

Although quite a few people have built manipulators from air muscle actuators, there is no published description of how one might select the most appropriate muscles for a given task. As this research is primarily intended to show the benefits of using PMC joints to perform interaction tasks a method for properly choosing joint parameters to satisfy constraints derived from a desired task was developed.

Given a joint such as the one shown in Figure 2.9 below, the parameters L_{mount}, r, b and n can be chosen to yield different available ranges of k and θ_{EP} as well as joint torque (τ). Because of the properties of the actuator, the true range of available k and τ will vary with the actual angle of the joint (θ_a). The goal of the method described below is to ensure between the desired limits of θ_{EP} the joint will possess the ability to achieve a prescribed range of k and τ.

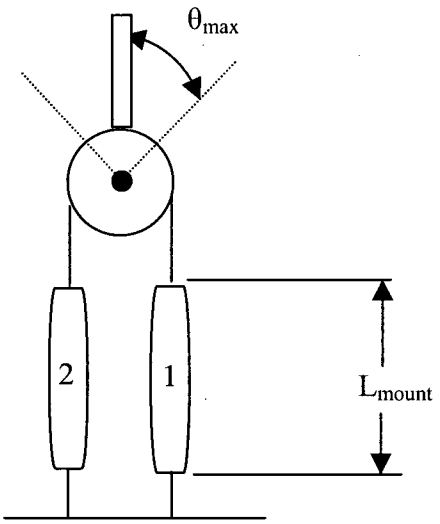

Figure 2.9 – Simple rotary joint powered by a pair of air muscles

For the hypothetical joint task a required maximum joint torque is known and is defined as τ_{max}. Also, for simplicity, it is assumed the range of motion is symmetric and known and defined as $\pm\ \theta_{max}$ as shown in the above figure. In addition the maximum and minimum joint stiffnesses are symmetric and defined as k_{max} and k_{min}

There are also several constraints that are relevant: maximum axial force in muscle is a constant across all muscle sizes and defined as f_{max}. After building several muscles and exposing them to sufficient axial force to initiate failure, this was found to be primarily a limitation on the end fitting. The nylon braiding and tubing can shear if exposed to excess clamping force. This presented a limit to how much axial force the end fittings could take before coming apart. For different designs this may change but the premise that some maximum force is achievable still holds although the limiting factor may change. The maximum inflation pressure is assumed to be constant across all muscle sizes and is defined as P_{max}. The minimum inflation pressure is a constant across all muscle sizes and defined as P_{min}. Also, the ratio of n/b is bounded above and below based on available braid sizes. Although commercially available nylon braid is only available in discreet steps of n/b, any size between could be custom built in theory. Practically choosing the closest n/b will suffice.

It is helpful to see what the force output of an air muscle is versus length for a given pressure.

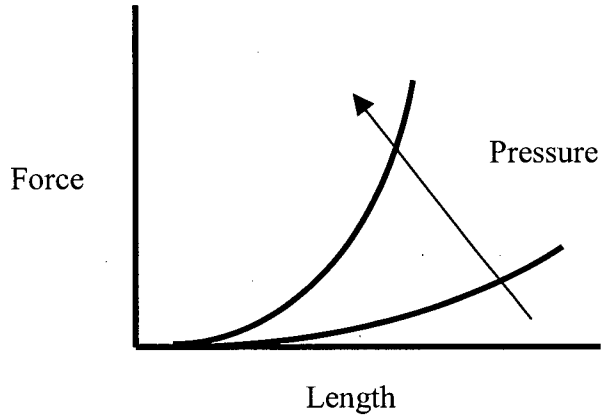

Figure 2.10 – Force versus length at different pressures

Additional assumptions for this method include the following. The mounting length of both muscles is equal when θ is equal to zero; for example, $L_{mount1}=L_{mount2}$. The working range of the manipulator is defined by the application and is symmetric about $\theta=0$. The working range is equal to $\pm\ \theta$. Muscle length can never exceed b as this is the length of a single strand of the braid. Muscle length can never be less than the length where volume is maximum and axial force is zero defined as L_{zero}.

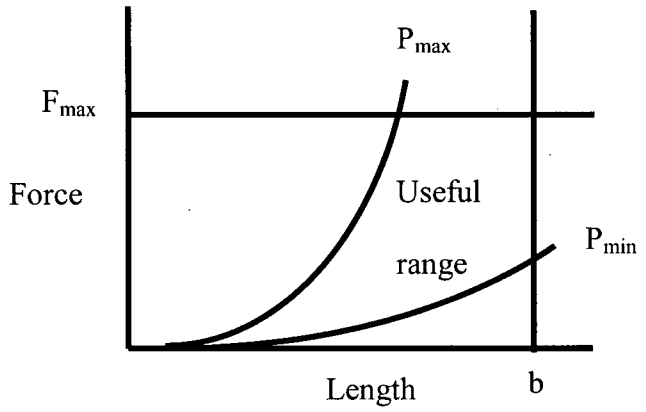

Figure 2.11 – Useful range for a single muscle

The mounting length of the muscle must fall within this region and the working region for the muscle is defined as shown below in Figure 2.12. The width of the working region is equal to $\theta_{max}r$ to allow for the range of motion defined by θ_{max}.

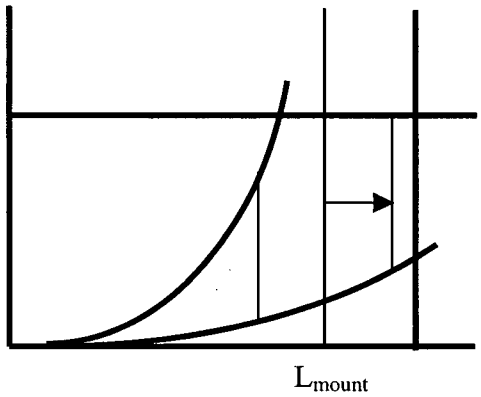

Figure 2.12 – Working range of each muscle

Now the maximum and minimum working lengths of each muscle can be defined:

$$L_{\max} = L_{mount} + \Delta\theta r \tag{2.5}$$

$$L_{\min} = L_{mount} - \Delta\theta r \tag{2.6}$$

Two constraints must hold at this point:

$$L_{\max} \leq b \tag{2.7}$$

$$L_{\min} \leq L_{zero} \tag{2.8}$$

Examining the torque constraint, one can note that it is most difficult to satisfy this when the joint is configured as shown in Figure 2.13.

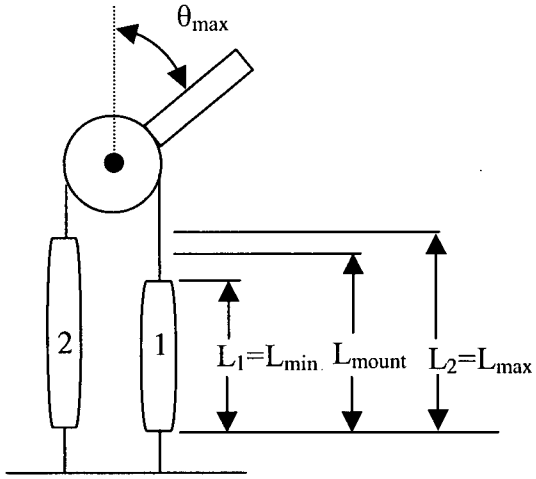

Figure 2.13 – Configuration where maximum and minimum stiffness most constrained

In this configuration muscle 1 is at length L_{min} and muscle 2 is at length L_{max}. Superimposing both muscles onto one force length plot as shown in Figure 2.14 below is helpful to visualize the impact of the torque constraint. Muscle 1 is at point A and muscle 2 at point B.

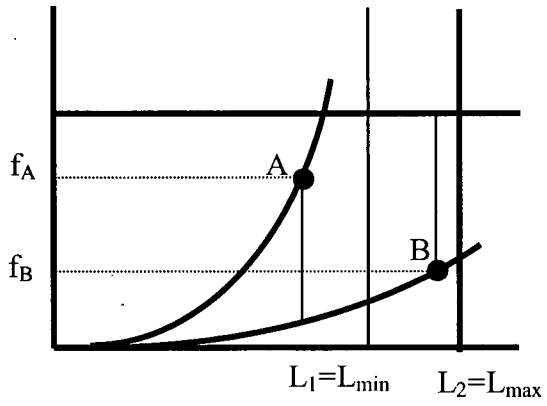

Figure 2.14 – Maximum torque Constraint

In this configuration the maximum torque that can be generated is defined by:

$$\tau_{max\_act} = (f_A - f_B)r \tag{2.9}$$

Where f_A is equal to either

$$f_A = f(L_{\min}, P_{\max}) \text{ if} \tag{2.10}$$

$$f(L_{\min}, P_{\max}) \le f_{\max} \text{ or} \tag{2.11}$$

$$f_A = f_{\max} \tag{2.12}$$

and

$$f_B = f(L_{\max}, P_{\min}). \tag{2.13}$$

τ_{max} must satisfy the constraint:

$$\tau_{\max\_act} \ge \tau_{\max}. \tag{2.14}$$

To investigate the joint stiffness constraints, the stiffness relations of the air muscles are established.

Rearranging the Equation 2.2, yields:

$$f = P_g 3AL^2 - BP_g \tag{2.15}$$

where, $A = \frac{1}{4\pi n^2}$, and $B = \frac{b^2}{4\pi n^2}$.

Each muscle volume[30] is calculated as:

$$V = BL - AL^3. \tag{2.16}$$

Thus, the change in volume with respect to length is

$$\phi = \frac{\partial V}{\partial L} = B - 3AL^2 \tag{2.17}$$

Using equations 2.15-17 yields the solution of muscle stiffness, κ, as the change in force with respect to length where mass is held constant as,

$$\kappa = \left.\frac{\partial f}{\partial L}\right|_{m=const} = mR\frac{T}{V^2}\phi^2 + P_g 6LA \tag{2.18}$$

where, gauge pressure is related to air mass and volume by,

$$P_g = \frac{mRT}{V} - P_{atm}. \tag{2.19}$$

This equation shows that for a given length, the stiffness varies linearly with pressure.

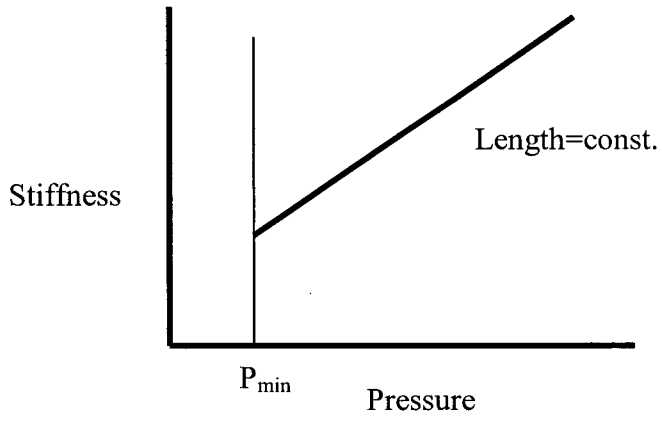

Figure 2.15 – Stiffness versus pressure at a constant length

The most difficult configuration to generate a small joint stiffness occurs when attempting to generate a large clockwise torque in the configuration shown in Figure 2.13 above. Figure 2.16 below shows the points on the force length plot for each muscle to achieve minimum joint stiffness, $k_{min.}$ Muscle 1 is at point C and Muscle 2 at point B.

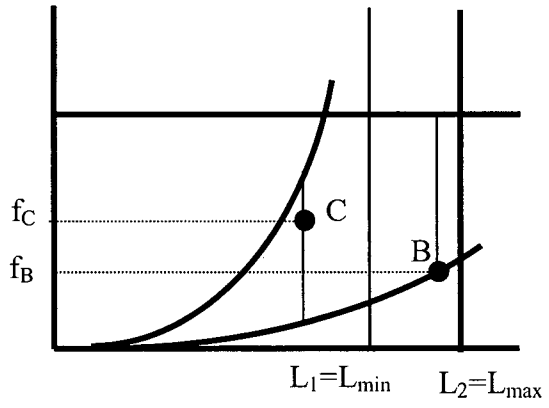

Figure 2.16 – Small stiffness constraint

To obtain the lowest possible stiffness at this configuration while applying the largest required torque, both muscles would need to generate the least force possible to apply the maximum torque.

$$f_C = f_B + \frac{\tau_{\max}}{r} \tag{2.20}$$

$$k_{\min\_act} = r^2(\kappa_c + \kappa_B) \tag{2.21}$$

$$k_{\min\_act} \leq k_{\min} \tag{2.22}$$

The most difficult configuration to generate a large joint stiffness occurs when attempting to generate a large counter-clockwise torque in the configuration shown in Figure 2.13 above.

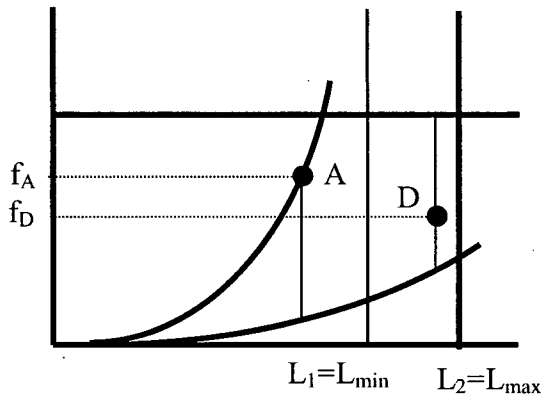

Figure 2.17 – Highest stiffness constraint

To obtain the highest possible stiffness at this configuration while applying the largest required counter-clockwise torque, both muscles would need to generate the most force possible to apply the maximum force. This is shown in Figure 2.17 above.

$$f_D = f_A - \frac{\tau_{\max}}{r} \tag{2.23}$$

$$k_{\max\_act} = r^2(\kappa_A + \kappa_D) \tag{2.24}$$

$$k_{\max\_act} \geq k_{\max} \tag{2.25}$$

This above method for sizing air-muscles was programmed into Matlab. The function 'fmincon', which is an optimization routine that accepts nonlinear constraints, was used to minimize the mounting length subject to the above nonlinear constraints given in Equations 2.5 to 2.25. The MatLab files can be found in Appendix C. For the case where k_{max}=30Nm/rad,

k_{min}=15Nm/rad, τ_{max}=3.1Nm and θ_{max}= π/16 the following values were found: b=514mm, n=5.74, r=90mm and L_{mount}=393mm.

Unfortunately, there was no material available with an n/b ratio as suggested by the optimization. Muscles with b=480mm, n=6.8 and L_{mount}=360mm are predicted by the same equations used in the optimization to yield a joint with: k_{min}=18.0, k_{max}=32.8 Nm/rad and τ_{max} = 6.15N when used with a r=90mm pulley over the same θ_{max}. In reality, the working stiffness range was slightly greater than this prediction and was in fact satisfactory for the experiments.

2.5 Summary

It was shown that using a simple empirical model of the air muscle force relationship to length and pressure, an accurate force calculation can be made. All four muscles used in testing were calibrated using the method outlined in Section 2.3. The errors in using a calculated force rather than measured force are small (typically less than 2N).

Additionally, a method for solving optimal air muscle parameters for desired PMC joint characteristics was discussed. The relevant constraints that are important when performing this optimization were presented along with a description of the logic behind their importance. Matlab code was developed to allow for choosing muscle parameters to yield minimum mounting length of air muscle in a PMC to minimize the space of the device.

Chapter 3
Electro-mechanical design and control of a PMC robot

3.1 Introduction

In this chapter, the design of an air muscle actuated two-link planar manipulator is discussed[1]. An air source and suitable valves to inflate and deflate the muscles were required along with a suite of electronics including sensors, valve drivers and the DAQ and computer to implement the EP-controller in an experimental setup. Additionally, the controller development is detailed. This chapter will describe the above requirements and the chosen solutions leading to the complete electro-mechanical system.

3.2 Manipulator

A two link planar manipulator was chosen as the platform for testing for several reasons. The two-link manipulator is sufficient to allow for control of the stiffness of the endpoint in the

[1] This work was done with the assistance of two undergraduate students as part of their fourth year project

direction of the surface to be wiped. For the proposed simple wiping task, the 2-degree of freedom manipulator met the necessary requirements for a test platform. Figure 3.1 below shows the final system installed in the Industrial Automation Laboratory at UBC.

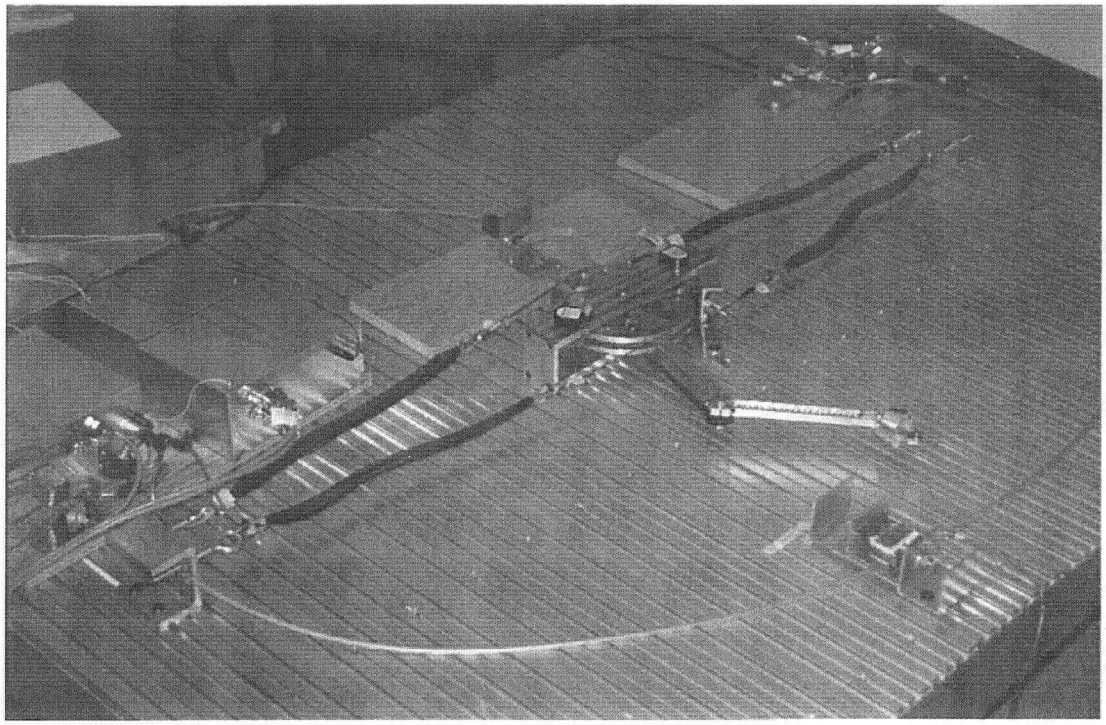

Figure 3.1 – Manipulator with muscles

Table 3.1 lists the specifications and constraints for the design of the manipulator.

Table 3.1 – Design Requirements

Dimensions	
Link length	227mm
Pulley diameter	≅180 mm
Forces	
Maximum Y-axis force	~20 N
Maximum force on a pulley	~200 N
Configuration	- Angle of the second joint independent of the first - Design must include two encoders - Easy to install on the lab table - The motion must be in the horizontal plan
Material	All custom parts in aluminum or steel

The sizing of the manipulator and the choice of appropriate air muscles were inherently linked. The final sizes chosen were eventually derived from a few simple constraints imposed at the beginning of the design process. The manipulator was sized based on the desired workspace and forces. The finalized planar manipulator design is shown in Figure 3.2. The bill of materials for the assembled manipulator can be found in Appendix D.

As shown in Figure 3.3, the two links are driven from the base of the manipulator. The distal joint is driven from the base through a timing belt and pair of sprockets. This allows the air muscles to be longer than the links and also reduces link mass and complexity of the manipulator. Each joint has a pulley mounted at the base and a pair of antagonistic PMC actuators.

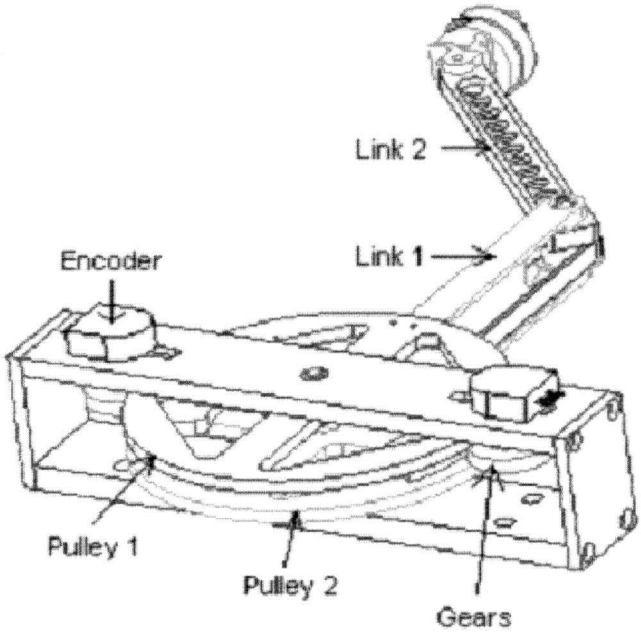

Figure 3.2 – Finalized manipulator design

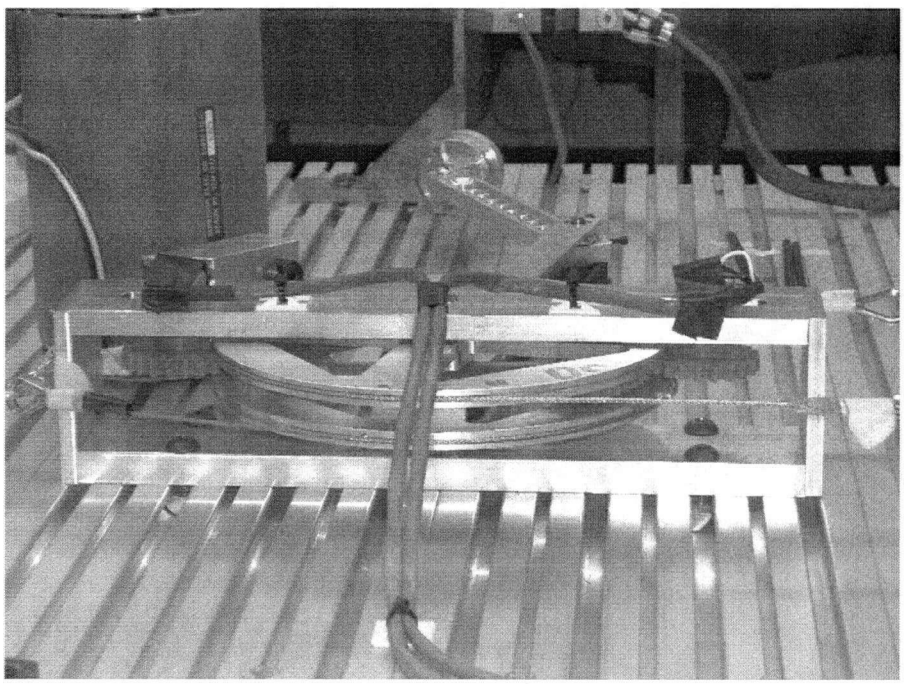

Figure 3.3 – Close-up of back of manipulator

All components were designed in Pro/Engineer. The production drawings are in Appendix E and the assembly procedure is in Appendix F. Figure 3.4 shows a sweep of postures of the manipulator wiping the surface at the prescribed distance of 0.4m.

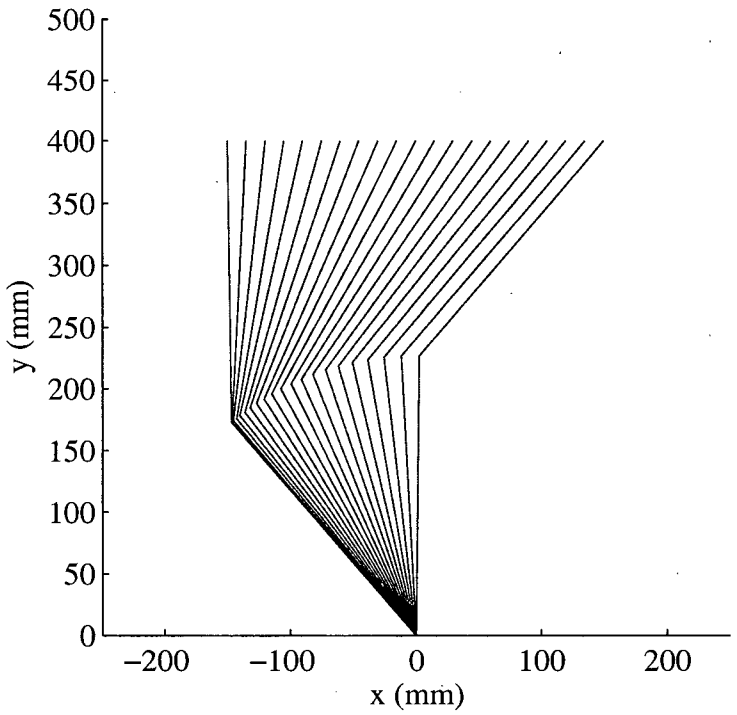

Figure 3.4 – Plot of the range of motion of the manipulator

The expected torques at each joint are shown in Figure 3.5 for an end point force of 20N in the Y-axis direction.

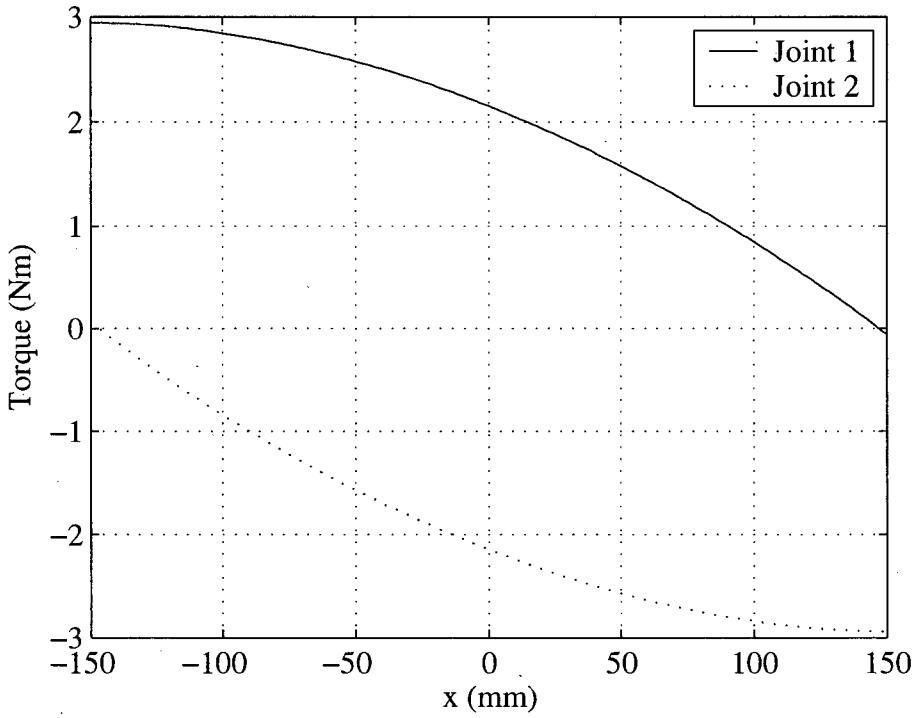

Figure 3.5 – Torques for 20N force normal to the wiped surface

Encoders mounted on the joints were used for all early development work. For the final experiments the encoders were replaced with single turn potentiometers configured to vary between 0-5 Volts each turn, to integrate with the final (Labview) control platform.

3.3 Valves

There are a number of ways that the state of the PMC's can be varied. The two basic methods are pressure control and mass flow control. There are several valve choices that could be considered: proportional pressure control valves, proportional mass flow control valves, and solenoid valves.

Mass flow control is the preferred method for operating air muscles. Because of their low cost and controllability, solenoid valves were chosen. Unfortunately, solenoid valves only offer one steady state mass flow (on/off). However, advances in solenoid valves have led to very fast solenoid opening times. Therefore, a PWM strategy can be used to vary the average mass flow rate through the valve. As will be discussed in Section 3.5, a control strategy that varies mass

flow rate to cause the joints to follow *EP* and *K* trajectories will be developed. The output of this controller is a duty cycle to the valves.

Matrix valves[34] were selected based on price and speed. They produce a 3 position, 3 way solenoid with opening time around 2ms. This allows for a single valve per PMC. Each valve has 3 ports and 3 positions, meaning they can be open to supply, open to vent or closed.

In the manipulator setup, the four Matrix solenoid valves operated on the PWM signal. They have a maximum frequency of 200 Hz and the minimum time to open of 2 ms. They have three different positions to allow for: an inlet from an air supply to the actuator, an outlet from the actuator to the atmosphere and a closed position where no air is exchanged. For further specifications refer to Appendix B.

The following sub-section discusses the sizing of orifice plates for both the inlet and outlet of the valves for effective PWM control of the valves. As well, the selection of the operating frequency is described.

3.3.1 Sizing Valve Orifices

When dealing with a large pressure drop from the supply to muscle, compressible flow must be considered. This introduces choked flow through the orifice that graduates into subsonic flow as the back pressure increases past the critical values. These relations are useful in sizing the orifice and theoretical mapping of the mass flow rate. The pressure drop over the orifice governs whether the flow is choked. The critical back pressure to stagnant pressure ratio is:

$$\frac{p^*}{p_o} = 0.5283 \tag{3.1}$$

This ratio value is specific for air. Here, p* is the critical back pressure at which the flow becomes sonic. The stagnation pressure , p_o, is the pressure of the air with no velocity. For any back pressure lower than the critical pressure, the flow through the orifice is choked. Under these conditions, the mass flow rate is independent of the back pressure.

$$\dot{m}_{\max} = \frac{0.6847 p_o A_e}{(RT_o)^{1/2}} \tag{3.2}$$

It is assumed that the supply air is at room temperature and is stagnant. A_e is the area of the orifice and R is the gas constant. When the back pressure has increased such that the flow is subsonic, the calculations are more complex. At subsonic conditions, the back pressure is equal to the pressure in the orifice. Now the mass flow rate is dependent on the back pressure as illustrated in the equation below,

$$\frac{\dot{m}}{A_e}\frac{\sqrt{RT_o}}{p_o} = \sqrt{7\left(\frac{p}{p_o}\right)^{2/1.4}\left[1-\left(\frac{p}{p_o}\right)^{0.4/1.4}\right]} \tag{3.3}$$

For deflation of the muscles, the same theory applies where it is assumed that the air in the muscle is stagnant and and the back pressure is atmospheric pressure. Instead of having a changing back pressure, the supply pressure is changing.

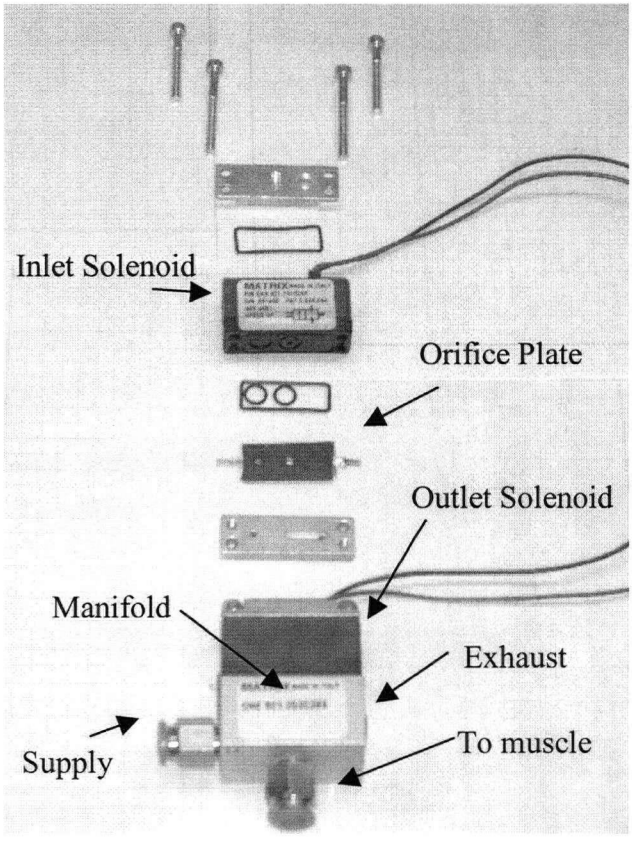

Figure 3.6 – Partially disassembled Matrix valve with orifice plate

The Matrix valves were not able to deliver exactly the performance required without modification. An orifice plate was added to both the inlet and outlet side of the valves to lower

the maximum flow rate through the valve. The testing method for selecting the orifice is described in the Appendix E. The results of these tests show that the best inflation orifice hole diameter is 0.508mm while the best deflation orifice hole diameter is 0.787mm.

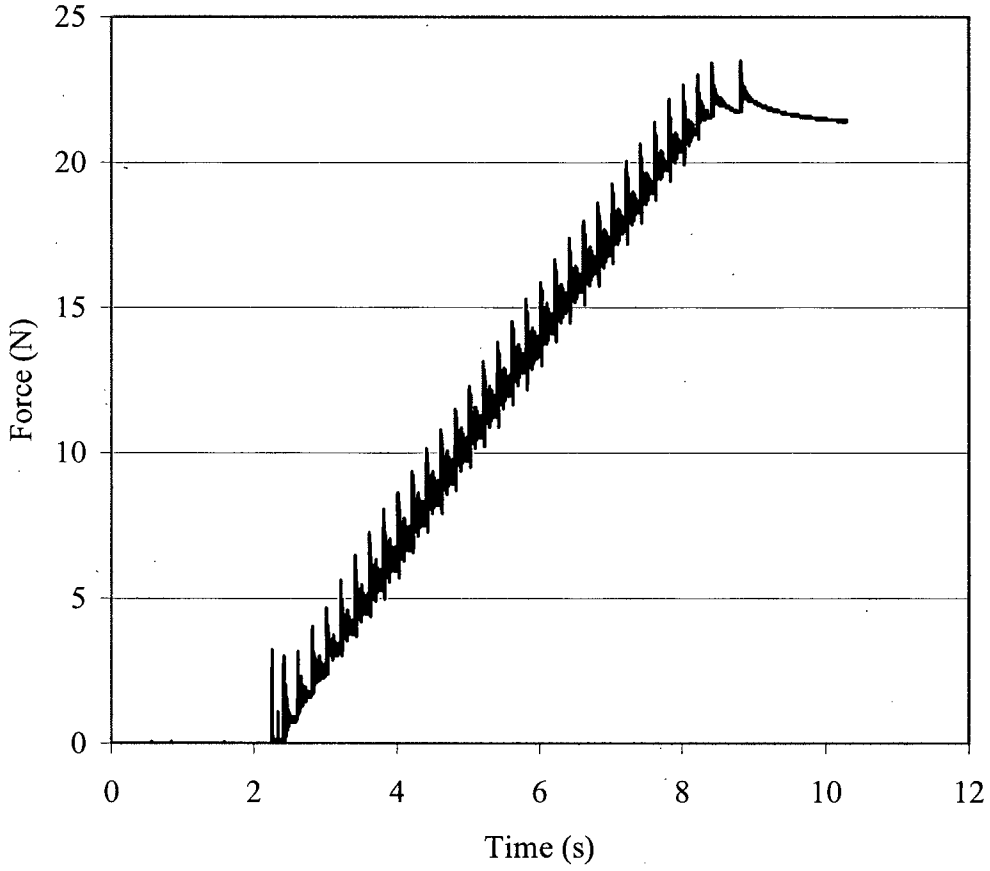

Figure 3.7 – Inlet orifice sized to allow no more than 1N discreet force steps for smallest possible inflation

With the chosen inlet orifice size it is shown in the above figure that the maximum change in normal force to the surface is 1 N per injection of gas into the muscle. The graph in Figure 3.7 was generated from data with the manipulator in the orientation where the force normal to the surface is most sensitive to actuator changes. The force steps show small ringing due to the manipulator joints being underdamped.

The outlet was also tested to ensure that the flow in and out of the actuator was roughly balanced. The fill and deflate time are 1.8s and 1.75s respectively. This balance is considered

satisfactory, given in-house machining capabilities, and precision machining of the orifices was not considered necessary.

Figure 3.8 shows a plot of the inflation and deflation pressure versus time of a muscle with the modified valves installed.

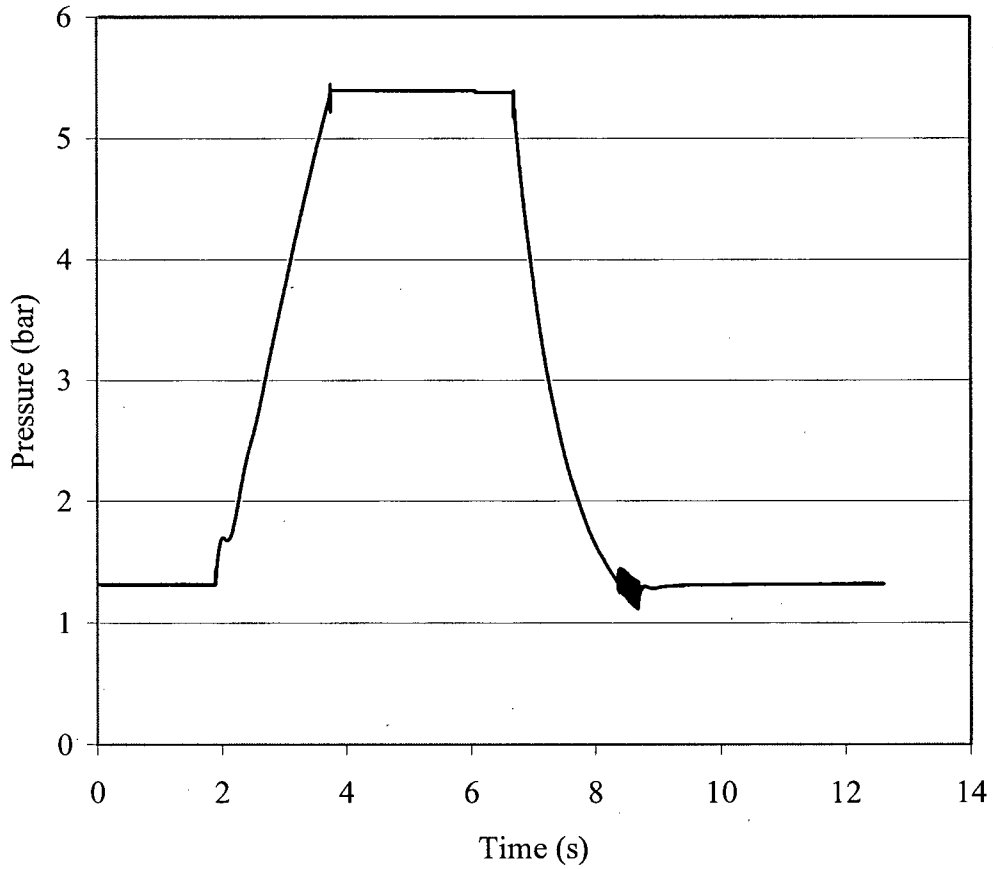

Figure 3.8 – Final inlet and outlet orifice sizes with inflation and deflation times roughly matched

3.3.2 Selecting Constant Frequency for operation

It was desired to have the air flow into the muscles appear as close to infinitely variable as possible. However, this results in a trade off between frequency and range of useful duty cycles available. The valves had a minimum time to open of approximately 2 ms. The controller is designed in such a way that any commanded duty cycle that results in an open command of less

than 2 ms is held for 2 ms regardless. This is the minimum command time for this valve. A frequency of 500 Hz would result in two flows being allowable, either closed or open for the minimum pulse. In reality the valves have a maximum recommended operating frequency of 200 Hz. Instead at least a 10:1 turndown ratio for the valve was selected. The quantity of gas released with a 3ms pulse is roughly 10 times less than the full open value. The operating frequency was set at 30 Hz to give a 10:1 ratio between maximum and minimum continuous flow. The flow is variable in very small increments between these limits. The counter/timer chip driving the PWM signal is capable of 0.4 microsecond steps.

3.4 Instrumentation, Drivers and DAQ

ORTS[31], a UBC developed real-time operating system, was used to run all early testing. National Instruments hardware and Labview software was used instead for the final experiments due to the added flexibility of that package and the wealth of examples and support available.

All of the sensors were calibrated for their expected operating range before proceeding from this point. The sensor information and calibrations are listed in Appendix D. The values from the calibrations were entered into National Instruments Measurement Explorer for use in all Labview code used in this research. The sensors were recalibrated as required throughout the experiments.

3.5 Controller

Using the force model given in Equation 2.4, a controller was developed to allow for the simultaneous control of both joint stiffness and equilibrium position of each joint in the robot.

The controller used for the manipulator is shown in Figure 3.8. In the experiments that follow, the Cartesian space trajectories are pre-computed and converted to joint space trajectories before motion begins. The controller operates at 30 Hz and each control decision is based on digitally filtered data collected at 300 Hz.

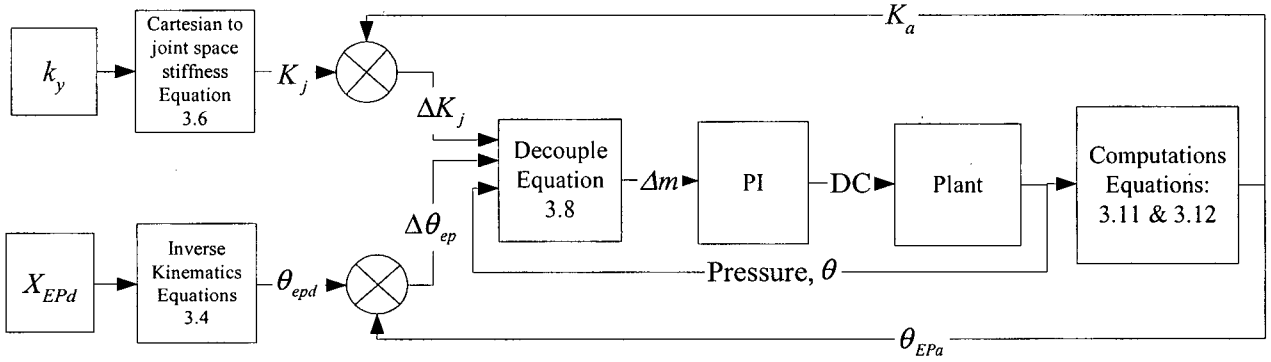

Figure 3.9 – Schematic of planar robot controller

The desired Cartesian equilibrium trajectory, $X_{EPd,}$ is first converted to a joint space trajectory using the inverse kinematics of the manipulator[35].

$$\theta_2' = \tan^{-1}(\pm\sqrt{1-D^2}) \tag{3.4a}$$

Where D is given by

$$D = \cos\theta_2' = \frac{x^2 + y^2 - a_1^{\,2} - a_2^2}{2a_1a_2}. \tag{3.4b}$$

Where a_i is the link length. Yielding:

$$\theta_1 = \tan^{-1}(y/x) - \tan^{-1}\left(\frac{a_2\sin\theta_2'}{a_1 + a_2\cos\theta_2'}\right) \tag{3.4c}$$

and

$$\theta_2 = \theta_1 + \theta_2'. \tag{3.4d}$$

Next, the stiffness is transformed from Cartesian to joint space. The Cartesian stiffness matrix, K_c is defined as

$$K_c = \begin{bmatrix} k_x & k_{xy} \\ k_{yx} & k_y \end{bmatrix} \tag{3.5}$$

Cartesian stiffness and position equilibrium point trajectories are generated and converted to joint space with inverse kinematics. k_y is prescribed and k_x is solved to satisfy k_1=k_2. This

constraint minimizes the amount of gas used over the prescribed task. $k_{xy}=k_{yx}$ is solved such that the cross terms in the joint space stiffness matrix are zero, reflecting the physical nature of the system.

$$K = \begin{bmatrix} k_1 & 0 \\ 0 & k_2 \end{bmatrix} = J^T K_c J \text{ [32]} \tag{3.6}$$

Where the manipulator Jacobian, J, is:

$$J = \begin{bmatrix} -a_1 \sin(\theta_1) & -a_2 \sin(\theta_2) \\ a_1 \cos(\theta_1) & a_2 \cos(\theta_2) \end{bmatrix} \tag{3.7}$$

The singular positions of the Jacobian are outside the task workspace. As shown in Figure 3.9, the errors in stiffness, K, and equilibrium position, θ_{ep}, along with the most recent observation of the angular position and pressures is fed into a decoupling block. The decoupler uses the partial derivatives of stiffness and theta with respect to mass to transform from stiffness and EP to error in mass for each muscle.

$$\begin{bmatrix} \Delta m_1 \\ \Delta m_2 \end{bmatrix} = \begin{bmatrix} \frac{\partial k}{\partial m_1} & \frac{\partial k}{\partial m_2} \\ \frac{\partial \theta_{eq}}{\partial m_1} & \frac{\partial \theta_{eq}}{\partial m_2} \end{bmatrix}^{-1} \cdot \begin{bmatrix} \Delta k \\ \Delta \theta_{EP} \end{bmatrix} \tag{3.8}$$

In order to obtain these derivatives, one can note that torque in each joint is given by:

$$\tau = k(\theta - \theta_{EP}), \tag{3.9}$$

and can also be represented by,

$$\tau = r(f_1 - f_2) \tag{3.10}$$

The joint stiffness is:

$$k = r^2(\kappa_1 - \kappa_2), \tag{3.11}$$

Solving Equation 3.9 for θ_{EP} and substituting from Equations 3.10 and 3.11 yields,

$$\theta_{EP} = \theta - \frac{(f_1 - f_2)}{r\ (\kappa_1 + \kappa_2)}. \tag{3.12}$$

The partial derivatives required for the decoupler are then:

$$\frac{\partial k}{\partial m_1} = r^2\left(\frac{\partial \kappa_1}{\partial m_1}\right), \tag{3.13}$$

$$\frac{\partial k}{\partial m_2} = r^2\left(\frac{\partial \kappa_2}{\partial m_2}\right), \tag{3.14}$$

$$\frac{\partial \theta_{EP}}{\partial m_1} = \frac{\dfrac{\partial f_1}{\partial m_1}}{r(\kappa_1 + \kappa_2)} - \frac{(f_1 - f_2)}{r(\kappa_1 + \kappa_2)^2}\frac{\partial \kappa_1}{\partial m_1}, \tag{3.15}$$

$$\frac{\partial \theta_{EP}}{\partial m_2} = \frac{-\dfrac{\partial f_2}{\partial m_2}}{r(\kappa_1 + \kappa_2)} - \frac{(f_1 - f_2)}{r(\kappa_1 + \kappa_2)^2}\frac{\partial \kappa_2}{\partial m_2}. \tag{3.16}$$

Equation (2.4) yields:

$$f = P_g 3AL^2 - BP_g - c. \tag{3.17}$$

The equation derived for joint stiffness, κ in Section 2.4 is still valid even with the constant c in the above equation.

$$\kappa = \frac{\partial f}{\partial L_{|m=const}} = mR\frac{T}{V^2}\phi^2 + P_g 6LA. \tag{3.18}$$

For each muscle the change in muscle stiffness with respect to mass is

$$\frac{\partial \kappa}{\partial m} = RT\frac{3A^2L^4 + B^2}{L^2\left(-B + AL^2\right)^2}, \tag{3.19}$$

and the change in force with respect to mass is

$$\frac{\partial f}{\partial m} = -RT\frac{\left(-B + 3AL^2\right)}{L\left(-B + AL^2\right)}. \tag{3.20}$$

The muscle mass errors for each muscle then enter the PID block and a resulting duty cycle input to the valves is generated. The PI controller was tuned using a Ziegler-Nichols technique on the actual hardware. The manipulator was given constant stiffness trajectory for each joint of 15Nm/rad and a step input for desired joint equilibrium position, θ_{EPd}. The integral term was set to zero and the proportional gain was increased until continuous oscillations were observed. The gains were then solved according to the Ziegler-Nichols method. The gains were set to P=0.25 and I=0.05.

The duty cycle (DC) in the valve controller is then updated and the airflow in and out of the valves varies accordingly. A positive output from the PI controller demands in airflow into the valves and a negative output from the PI controller demands exhaust of air from the actuator. Sensors measure the angular positions and muscle pressures.

The sensor data is fed back to the decoupler and forward into the calculation block. The calculation block solves the current actual stiffness of each joint and the current actual EP of each joint using Equations 3.11 and 3.12.

3.6 Summary

In this section the steps required to ready all electrical and mechanical hardware for our experiments was presented.

A manipulator was designed and built to satisfy some general design constraints introduced to ensure the final manipulator would be appropriate for desired testing. The manipulator designed was a planar 2 link robot powered by two pairs of antagonistically mounted air muscles.

Solenoid valves were chosen to control air flow to the air muscles. The valves were chosen for their speed and suitability for use with PWM control. Orifice plates were sized and added to the modified valves to reduce the maximum flow rate through the valves. An operating frequency of 30 Hz was chosen to run the PWM controller.

A set of equations to allow for the decoupling of joint stiffness and joint equilibrium angle were developed. This decoupler converts errors in these variables to error values for the quantity of mass of air in each air muscle.

An EP controller was developed and implemented in Labview. A simple PI control loop was used to control the mass of air in and out of the air muscles. The gains were tuned using the Ziegler-Nichols method.

Chapter 4
Experimental Methods

4.1 Introduction

The experimentation described in this chapter was designed to show the strengths and weaknesses of the EP controller, coupled with the air-muscle actuated robot, in free-space, contact and transition tasks. Three sets of experiments were performed, one for each type of task. The experiments are summarized in Table 4.1. The desired trajectory in Cartesian space for X-Y position and stiffness in the Y-direction used for each test was calculated offline. The joint space stiffnesses and equilibrium positions were then calculated and stored in a binary file that was loaded as required for the actual experiments.

Table 4.1 – Summary of Testing

Test Type	Number of Tests	Stiffness	Speeds	Other Variants
Free-Space	10	1200N/m	10 speeds: 15-150 mm/s	None
Contact	46	800N/m 1100N/m 1400N/m	15 mm/s 30 mm/s 75 mm/s	Bump/No Bump y_{EP} = 405,410,415mm (nominal)
Transition	9	1000 N/m	2 mm/s 5 mm/s 10 mm/s	3 approach angles: 30,60,90°

A complete list of all testing performed is provided in Appendix H.

Figure 4.1 below shows the location of the X and Y-axis on the manipulator. All measurements given in this and subsequent chapters are referenced from this origin. The arrows show the positive directions of these two axes.

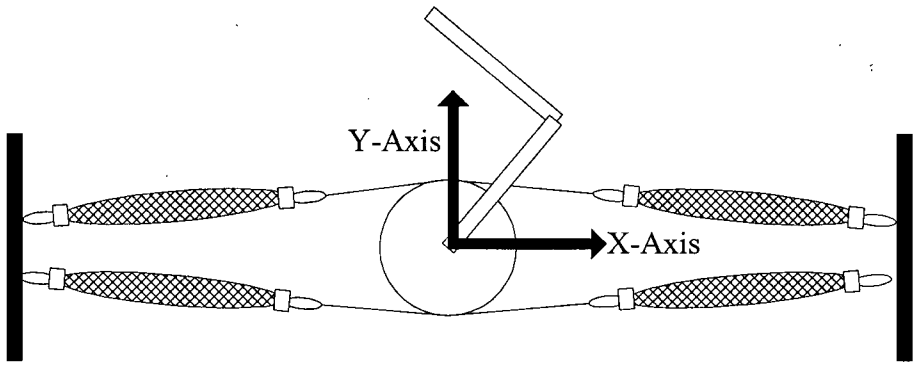

Figure 4.1 – X and Y axis origin location

For each experiment, data acquisition was performed using the same 16-bit DAQ card as used for the controller and streamed to a binary file at 30 Hz. Data was collected from all pressure sensors as well as a force sensor mounted to the wall used in two of the sets of tests. The complete data sets are listed in Appendix H and the analysis of the data is in Chapter 5.

4.2 Free-Space Testing

The free-space tests were performed to evaluate the ability of the controller to follow prescribed non-contact trajectories throughout a range of velocities. The response of the manipulator to increased operating velocity was used to determine the velocities used in subsequent test modes. In this experiment, the equilibrium trajectory of the end effector for a non-contact task is expected to match the actual trajectory with error increasing with velocity due to inertial effects that are unaccounted for in the open loop EP trajectory.

4.2.1 Description of the test

The manipulator was run back and forth along a 150mm, straight-line end point trajectory with a constant Y-axis position of 400mm. The starting X-axis position was at x=75mm and with a turnaround point at x=-75mm. A constant velocity trajectory with instantaneous start/stop and instantaneous change in turnaround velocity was commanded to present a worst-case scenario for each velocity profile. Ten profiles between 15mm/second up to 150mm/ second were tested. Figure 4.2 shows the free-space trajectory. The stiffness along the Y-axis, k_y, was set to 1200 N/m for all velocities.

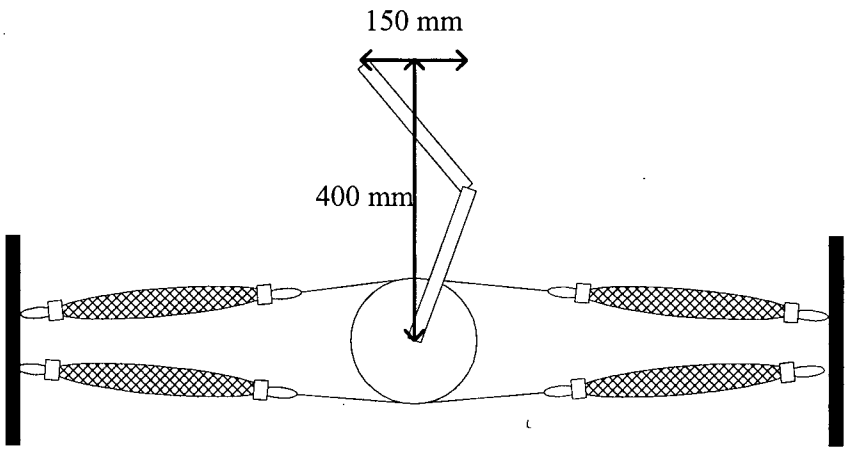

Figure 4.2 – Diagram of the range of motion during the free space task

4.2.2 Experimental measurements

The purpose of this test was to determine the range of useful operating velocities for the manipulator. This range is limited by the size of the muscles and the speed at which the valves can fill them. At some commanded velocity the manipulator will cease to be able to converge to the trajectory that it was ordered to follow. The highest velocity the manipulator can follow and still converge to the desired EP trajectory in the 150mm straight-line motion was established by this test and documented in Section 5.2.

4.3 Transition Testing

The second set of experiments was used to observe the system response when transitioning from free space to contact. The same surface from the contact tests (shown later) was also used for this set of experiments.

When transitioning from free-space motion to contact motion, industrial robots typically require a change in controller. Making this switch requires sensing the moment of contact and stable methods to switch smoothly from one controller to another. EP control should require no switching of controllers. The transition should be smooth due to the compliance of the manipulator and the nature of the control scheme.

4.3.1 Description of the test

A single Y-axis stiffness value of 1000 N/m was chosen for all of the tests; this value is in the middle of the manipulator's available stiffness range in the test configuration. Straight-line path velocities of 2, 5, 10, 20 and 40mm/s were evaluated. These speeds were chosen based on observations of the behavior from the free-space tests. Three different angles of attack into the surface were tested: 30°, 60° and 90°. The wall was placed 400mm away from the origin along the Y-axis. As shown below in Figure 4.3. Each path is 20mm in length for all velocities and angles with 10mm of travel before contacting the wall and 10mm after making contact. The point of contact for all tests was at the point where the X-axis crosses the surface.

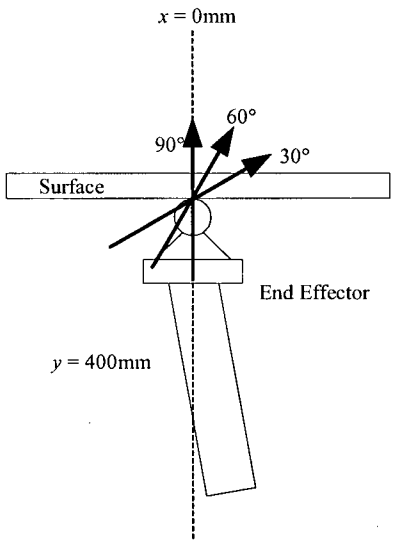

Figure 4.3 – Diagram of transition task

Table 4.2 below is a list of the test numbers for the different combinations of velocity and approach angles investigated in this set of tests.

Table 4.2 – List of transition test numbers

	Velocity		
Angle	2mm/s	5mm/s	10mm/s
30°	1	4	7
60°	2	5	8
90°	3	6	9

4.3.2 Experimental measurements

The behavior during the transition from free-space to contact should be stable and the manipulator should remain controllable. The forces generated should agree within some percentage of the expected forces based on commanded end-point stiffness and EP. The results of this experiment are discussed in Section 5.3.

4.4 Contact Testing

These experiments were designed to evaluate the forces generated normal to a surface while wiping with a prescribed stiffness and equilibrium position. The manipulator end effector was in contact with a surface throughout the task duration. The experiments were performed with and without an unpredicted "bump" disturbance along the surface.

The forces generated due to the contact with the surface should be predictable from the trajectory and the location of the surface. It is expected that the normal force in the surface will be bounded and the behavior of the controller stable and predictable for the contact testing.

4.4.1 Description of the test

The surface was placed 400mm in front of the manipulator. A force transducer was used to record the force normal to the surface.

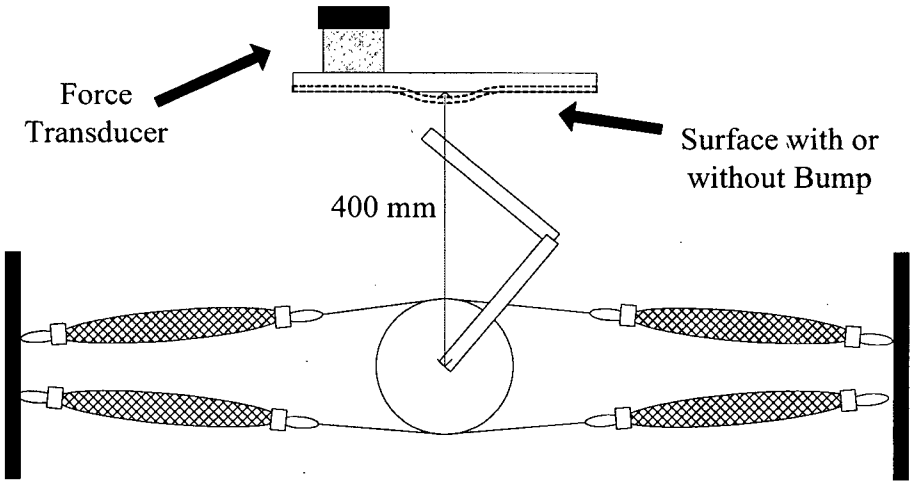

Figure 4.4 – Diagram of contact test

The wiped length had the same position and length as the free space trajectory. All tests followed a left to right motion and back again. There was a 3 second pause after data acquisition began at the beginning and at the turnaround point of the wipe. The tests were performed with three different Y-axis (k_y) stiffness levels: 800N/m, 1100N/m and 1400N/m. The equilibrium path was chosen to maintain a constant force in the absence of a disturbance. The EP path was calculated to compensate for expected deflection in the X-axis and the resulting effect this has on the normal force in the Y-axis. Early tests showed the surface deflected slightly due to its

compliance. This was modeled as a varying contact stiffness across the surface and the EP trajectory (nominally labeled as y_{EP}= 405, 410 and 415 mm) was adjusted accordingly (stiffer on the side where the surface was attached to the force transducer and less stiff moving in the positive x direction). Three velocities were chosen based on results from the free-space tests as listed in Table 4.3.

Figure 4.5 below shows the logic behind the adjustments made to the X_{EP} trajectories to account for both the shift from the contact and from the compliance of the wall. The dashed line indicates the nominal y_{EP}; this is the EP trajectory that would yield the desired force if the wall was infinitely stiff and the principle directions of the Cartesian stiffness matrix of the manipulator were perfectly aligned (normal and perpendicular) to the wall (k_{xy} =0). In fact at the one point in the trajectory, x=0mm, the cross coupling term (k_{xy}) is zero, and then the nominal trajectory yields the desired force with a stiff wall. Points A and C show how the EP trajectory has to be varied to achieve the same force over the surface. At point A, the k_{xy} cross term shifts the end-point farther left and less force is generated than expected. The point A_{EP} represents the direction in which the trajectory must be corrected to counter this effect. The point A'_{EP} goes further to show how the EP trajectory must be adjusted deeper into the surface to achieve the desired force due to the compliance of the wall. Point B and C show the result of this method at the middle and positive end of the trajectory.

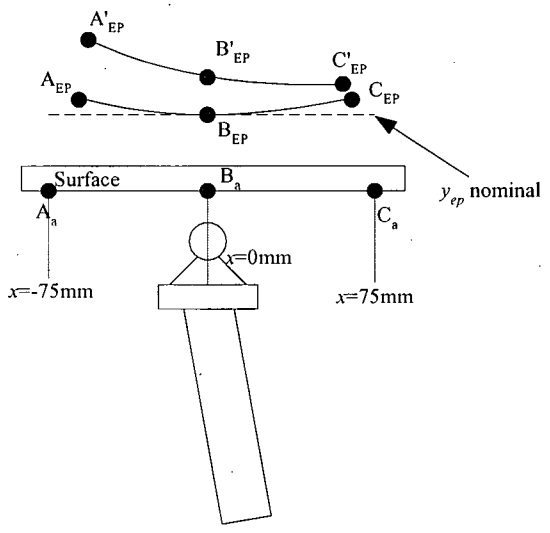

Figure 4.5 – Diagram of EP adjustments

The tests were repeated with a 50mm long, 4mm "bump" present in the center of the wiped path. The results with the bump were also captured. To assess the repeatability of the measurements and testing several points, namely, the 30 mm/s – 410mm y_{EP} points for each stiffness were repeated several times as listed in the second data row of Table 4.3. This table shows the numeric designations of all of the contact tests performed. Figure 4.6 below is a photograph of the manipulator contacting the smooth wiped surface and Figure 4.7 is a photo of the same test with the bump present.

Table 4.3 – List of all contact test numbers

	15 mm/s		30 mm/s			75 mm/s	
y_{EP}	800 N/m	1400 N/m	800 N/m	1100 N/m	1400 N/m	800 N/m	1400 N/m
405 mm	1	3	5	10	15	20	22
410 mm			6,7,8	11,12,13	16,17,18		
415 mm	2	4	9	14	19	21	23

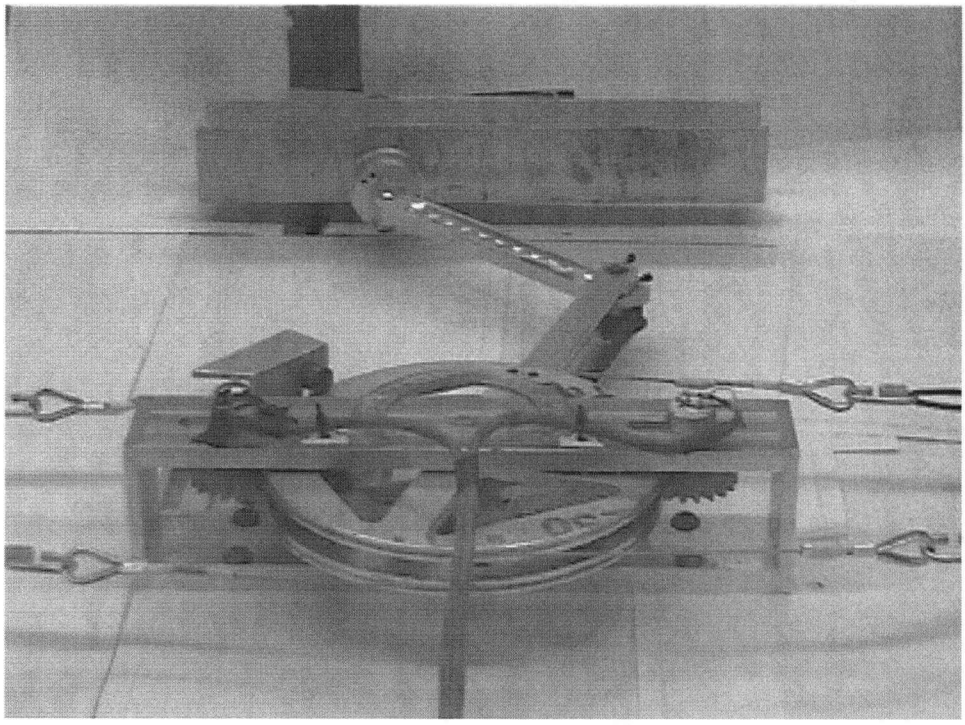

Figure 4.6 – Contact test with a smooth wall

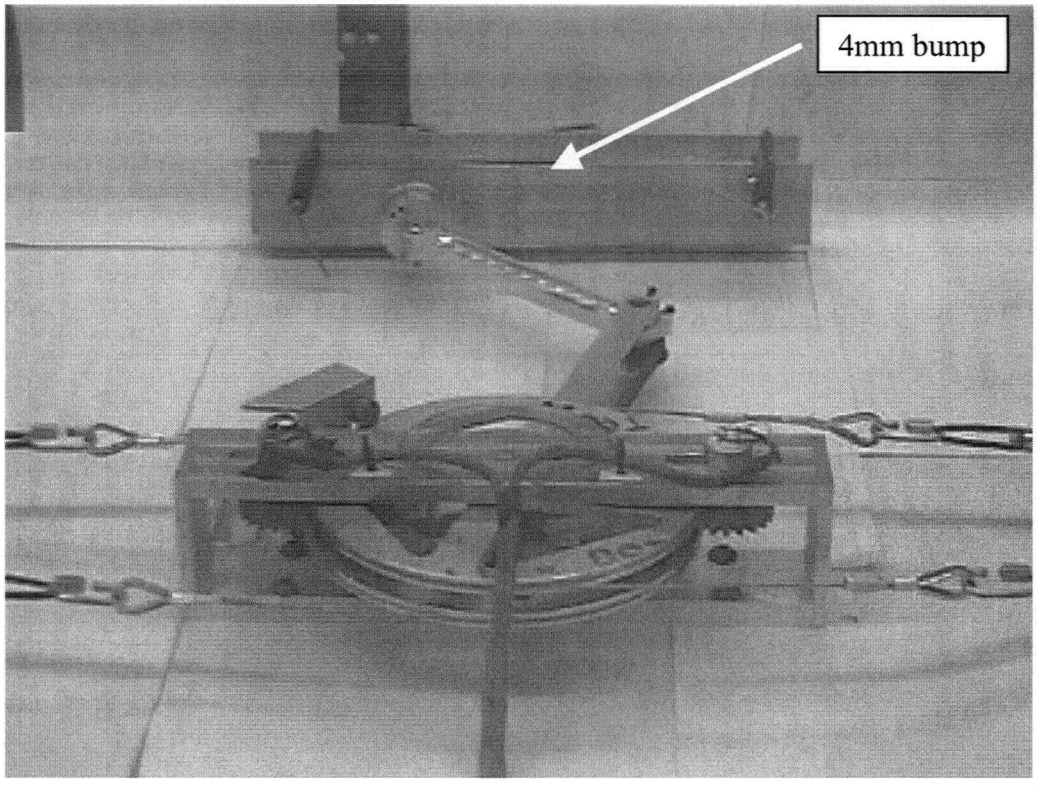

Figure 4.7 – Contact task with a bump present

4.4.2 Experimental measurements

The deviation of the measured forces generated due to contact with the surface from the expected forces based on the commanded end-point stiffness and EP are obtained from this experiment and the results are discussed in Section 5.4.

4.5 Summary

Three sets of tests were devised to test the performance of the manipulator in different tasks. Free-space, contact and transition tests were created to assess the capabilities of the manipulator in each of these three modes of operation. The effect of velocity, stiffness and EP as observed in these experiments are discussed in the following chapter.

Chapter 5
Results and Discussion

5.1 Introduction

The follow sections present the results of the three sets of tests outlined in Sections 4.2-4.4 The key results from each set of tests are presented. Summary data is presented where relevant. The statistic Mean Absolute Error (MAE) is used as a measure of the deviation from the desired value whenever error for a data set is discussed.

$$MAE = \frac{|measured_1 - predicted_1| + |measured_2 - predicted_2| + \ldots + |measured_n - predicted_n|}{n} \quad (5.1)$$

Mean absolute error is the average of the difference between predicted and actual value in all test cases; it is the average prediction error. This statistic is appropriate for data that is not normally distributed as in this case, unlike Root Mean Squared Error (RMSE) which magnifies the effect of outlying data.

5.2 Free-space task results

Figure 5.1 shows the x component of the desired equilibrium point trajectory (x_{EPd}) for different x-direction Cartesian velocities (v_x). The y component (y_{EPd}) is equal to a constant value of 400mm for the entire trajectory. Since there is no surface for the manipulator to interact with, in this test the actual position of the end-point, X_a (where X_a=[x_a y_a]) should be close to the commanded X_{EP} (where X_{EP}=[x_{EP} y_{EP}]) for slow movements and diverge as dynamic effects create joint torques.

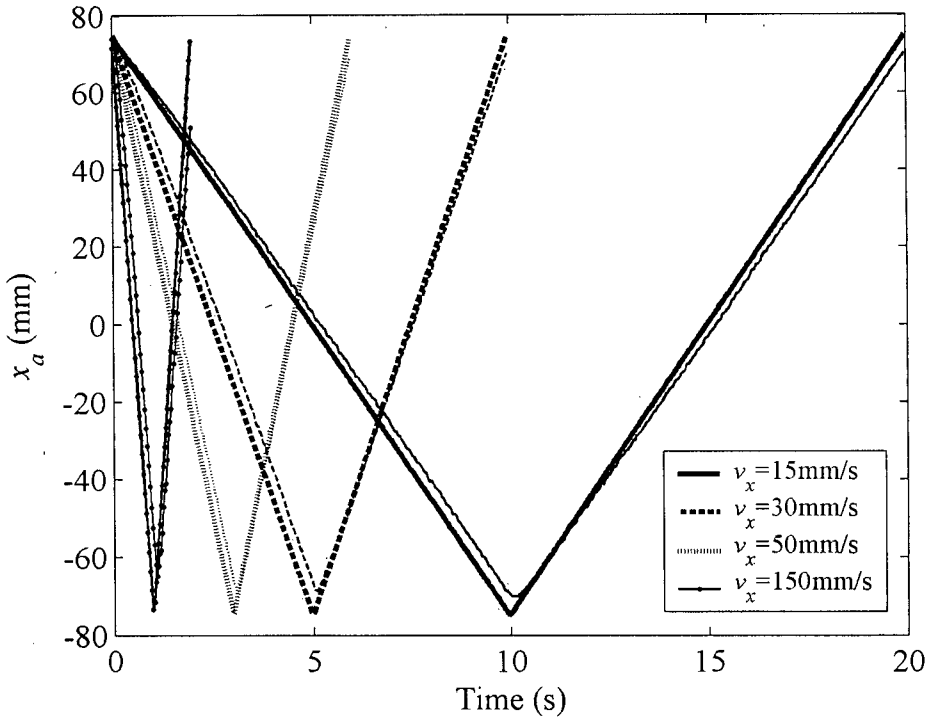

Figure 5.1 – Commanded position vs. time for free-space tests (thick lines are desired and thin lines are measured)

For slower motions it can be observed in Figure 5.2 that the error in X-axis equilibrium position, x_{EP}, is small and increases as the velocity of the manipulator endpoint X-axis velocity ,v_x, increases. The change in commanded trajectory direction requires an instantaneous change in velocity from positive to negative, and would be expected to generate controller error. The start and turn-around points do, in fact, have the largest errors. For v_x = 15mm/s and 30mm/s trajectories, the error converges as the manipulator has time to correct. The v_x=50mm/s case

takes nearly then entire length of the surface to approach zero error. The 150mm/s case does not converge.

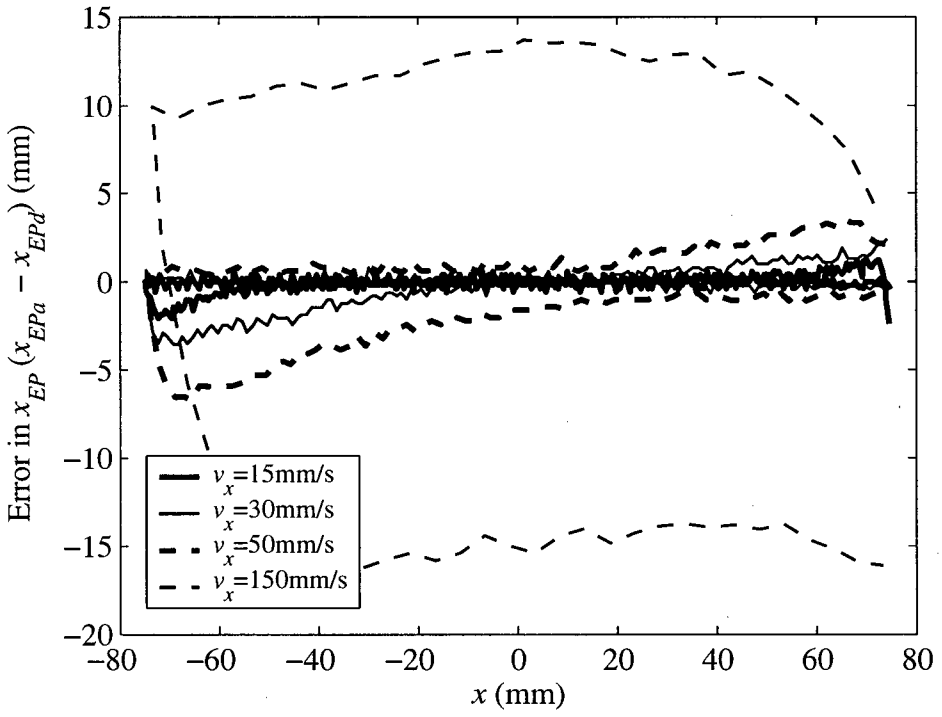

Figure 5.2 – Error in x_{EP} versus x for free-space tests

If there were no (or small) dynamic effects, (i.e. for the low velocity experiments) the X-axis equilibrium position, x_{EP}, and X-axis actual position, x_a, position would be expected to be near coincidental. The error in x in Figure 5.3 shown below, indicates that the results do not follow exactly as predicted. The error in x does increase as the velocity increases but is greater than the x_{EP} error in all cases. There is also a hysteretic effect evident in the figure. Non-zero errors in torque are computed by the system over the motion cycle as the muscles switch from inflation to deflation and the friction force between the muscle braiding and the tubing switches direction. These small errors in computed torques in the controller result in x_{EP} varying from the x_a over the trajectory. Implementation of the controller using force transducers would be expected to remove the hysteresis. However, since the proposed tasks for this robot are not position precision sensitive (stiffness/force behavior is considered primary), once identified, this small hysteresis was not considered problematic.

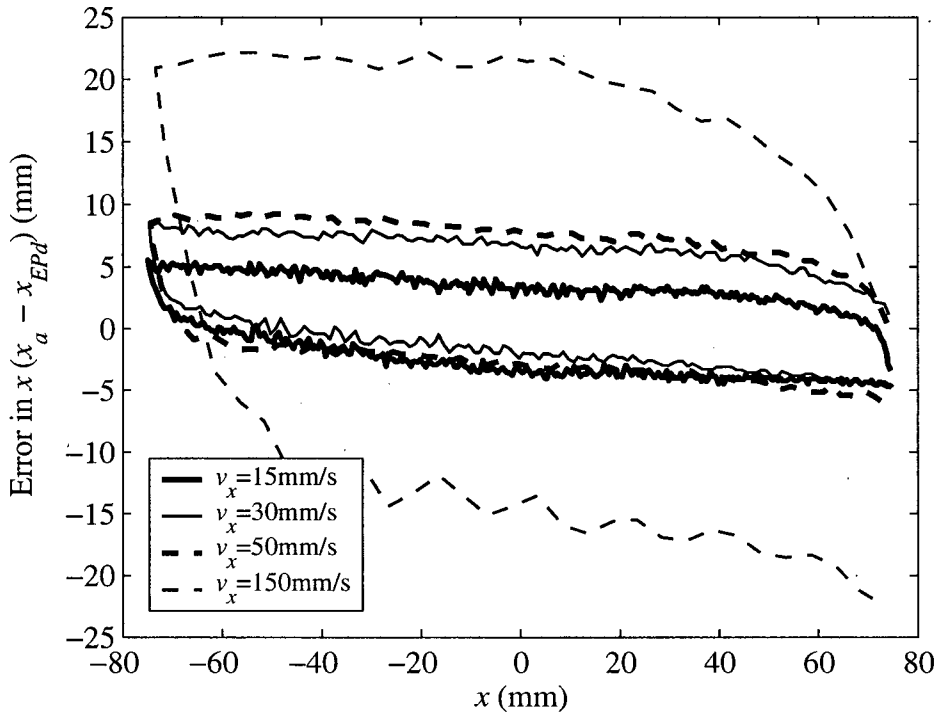

Figure 5.3 – Error in x_a vs. x

The set point for Y-axis stiffness, k_y, in Figure 5.4 below was 1200 N/m throughout the range of the motion. The error in k_y increases as the velocity of the endpoint increases. The trend is similar to the error in X-axis equilibrium position, x_{EP}. Again for the case where X-axis velocity, v_x is 150mm/s, the value for Y-axis end-point stiffness, k_y, does not converge to the set point over the duration of the test.

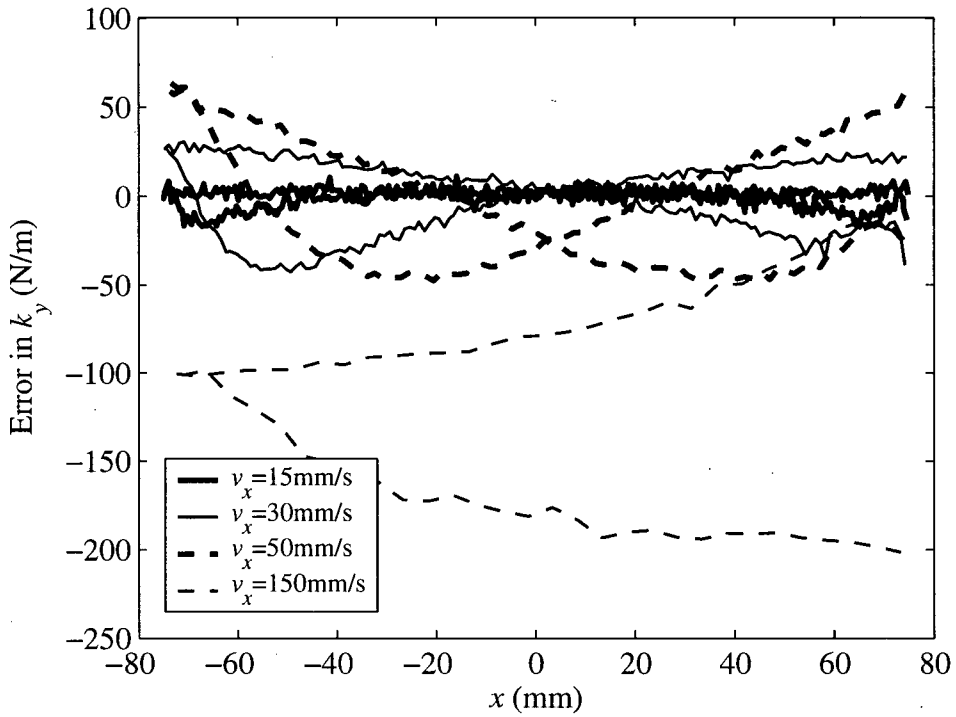

Figure 5.4 – Error in k_y versus x

The summary data presented in Figure 5.5 and Figure 5.6 shows that the error increases as the velocity increases. The speed of the valves is the principal limiting factor at higher speeds. Were the time to open and close the valve faster, the orifice size could be chosen such that the manipulator was faster if this were required. The commanded duty cycle to the valves becomes fully saturated with a commanded path velocity of 150mm/s.

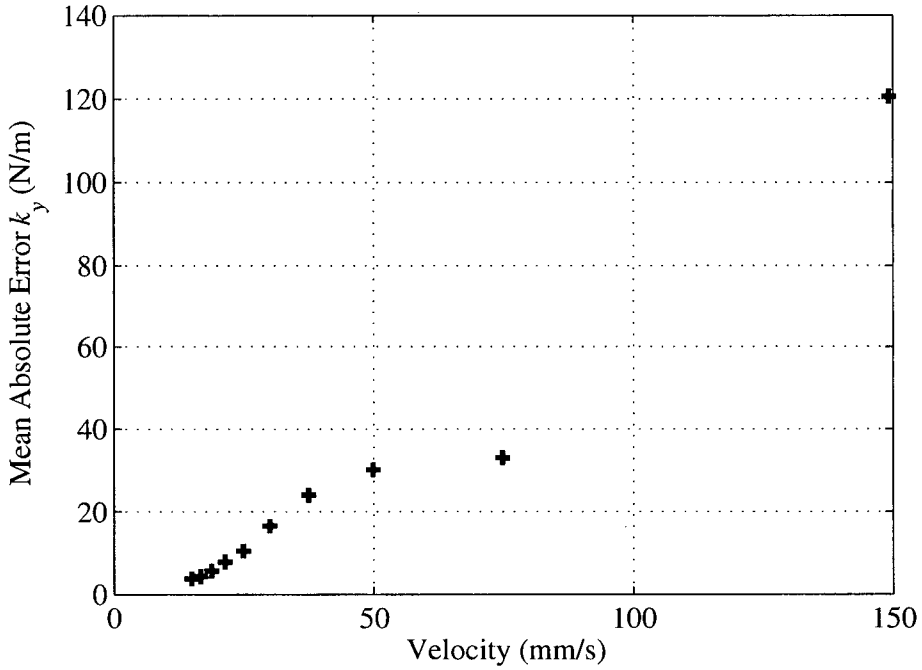

Figure 5.5 – Mean Absolute Error of k_y versus v_x

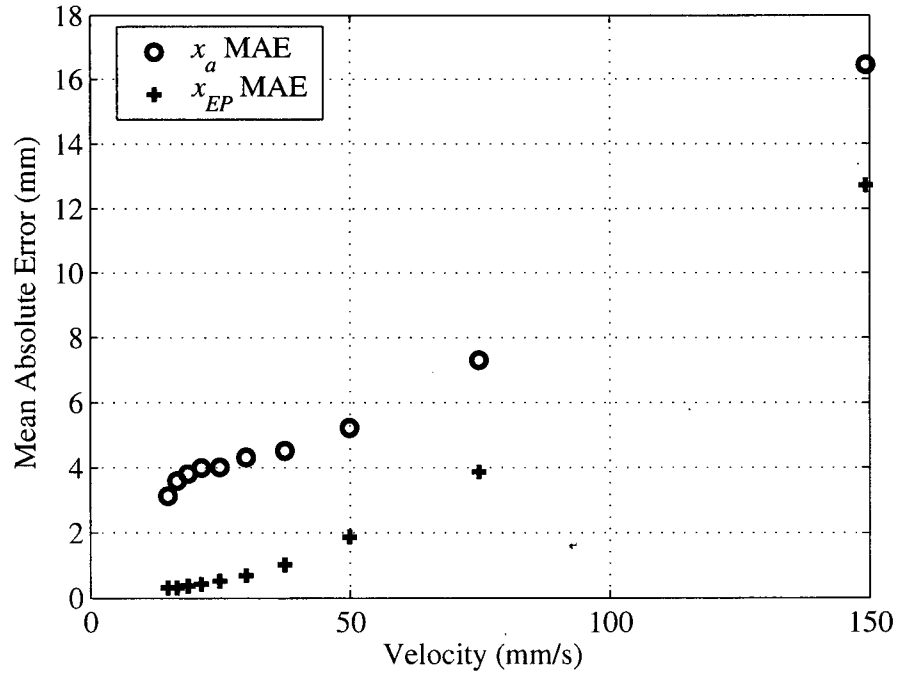

Figure 5.6 – Mean absolute error x_{EP} versus v_x

5.3 Transition Results

The second set of tests demonstrated the transition of the end-effector from free space to contact task. For the range of velocities and angles of approach tested there was little difference in the behavior of the system. All cases behaved as expected. Appendix I contains all test results. In this section only the two most extreme cases are discussed as most of the test results are quite similar. Test #1 was chosen as the case used to present comprehensive example results.

Figure 5.7 shows the result of following a 30° angle of approach trajectory through the center of the workspace. The commanded velocity was 10 mm/s along the path. The k_y stiffness was set to 1000 N/m. Without a wall present the commanded Cartesian end-point trajectory, y_{EP}, and the actual Cartesian end-point y_a (measured) trajectories overlap very well. When the wall was put in place and the manipulator transitions from free-space to contact the results diverge as expected. The 1mm drift into the surface is a result of the non-infinite stiffness of the wall and manipulator.

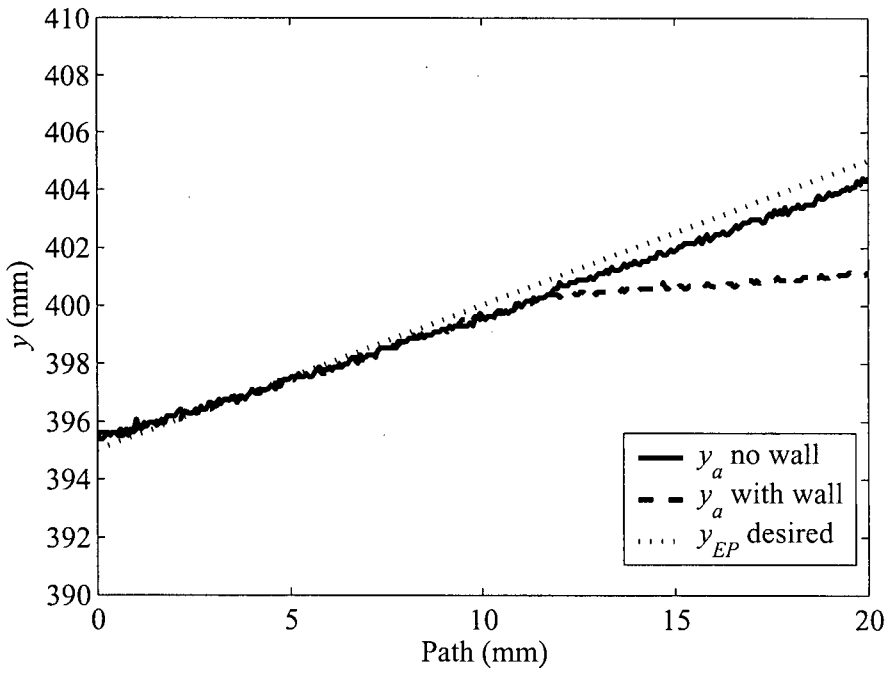

Figure 5.7 – Transition test #1 y_a and y_{EPd} with and without the wall versus path

Figure 5.8 shows the values of Y-axis equilibrium point trajectory, y_{EP}, both with and without the wall, as well as the desired Y-axis equilibrium point trajectory, y_{EPd}. Both agree very well with the desired trajectory. The presence of the wall does not interfere with following the y_{Epd} Y-axis equilibrium point trajectory. The distinction between y_{Epd} and y_a allows the end-point to smoothly transition between free-space and contact with no alteration to the controller. Ultimately, to control the interaction forces, the Y-axis end-point stiffness, k_y, must also be programmed to a desired value.

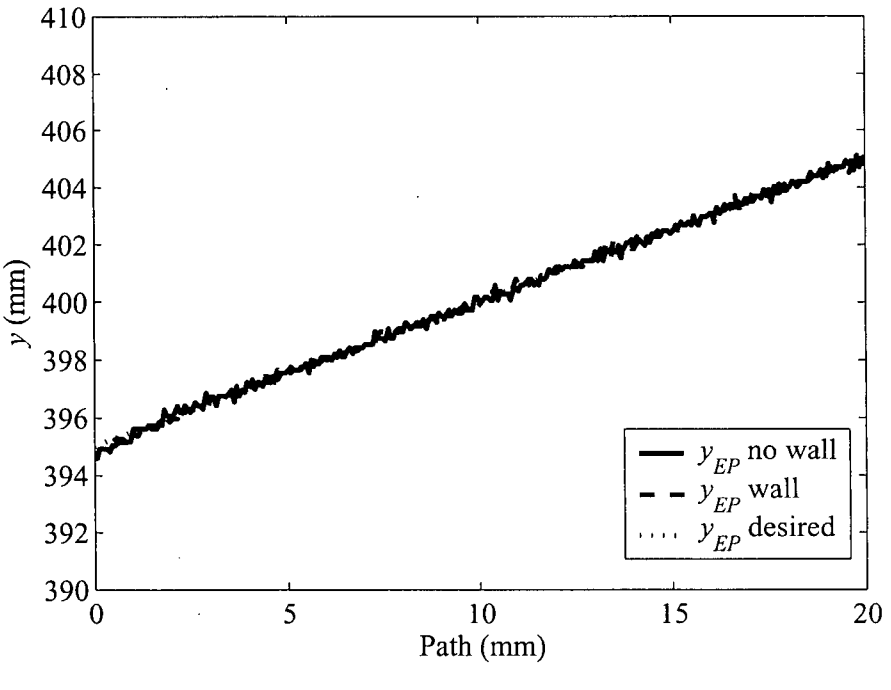

Figure 5.8 – Transition test #1 y_{EPa} and y_{EPd} with and without the wall versus path

The Y-axis end-point stiffness, k_y, behaves somewhat differently than expected. Because the Cartesian end point stiffness, K_c is translated into joint space stiffness, K_j before the task begins, there is no opportunity to adjust for the change in the configuration of the manipulator. The transform from Cartesian to Joint stiffness uses the manipulator Jacobian, which is configuration dependant. The effect of the manipulator not truly being on the EP configuration leads to the Cartesian stiffness at the end point being different than desired. In fact the errors observed in the individual joint stiffnesses, k_1 and k_2 were very small, showing the error in k_y was due to a difference in configuration from planning to execution. For the contact testing experiments

discussed in the following section, this difference was compensated as explained in Section 4.4. Figure 5.9 below shows this resulting shift from interaction with the wall in test #1.

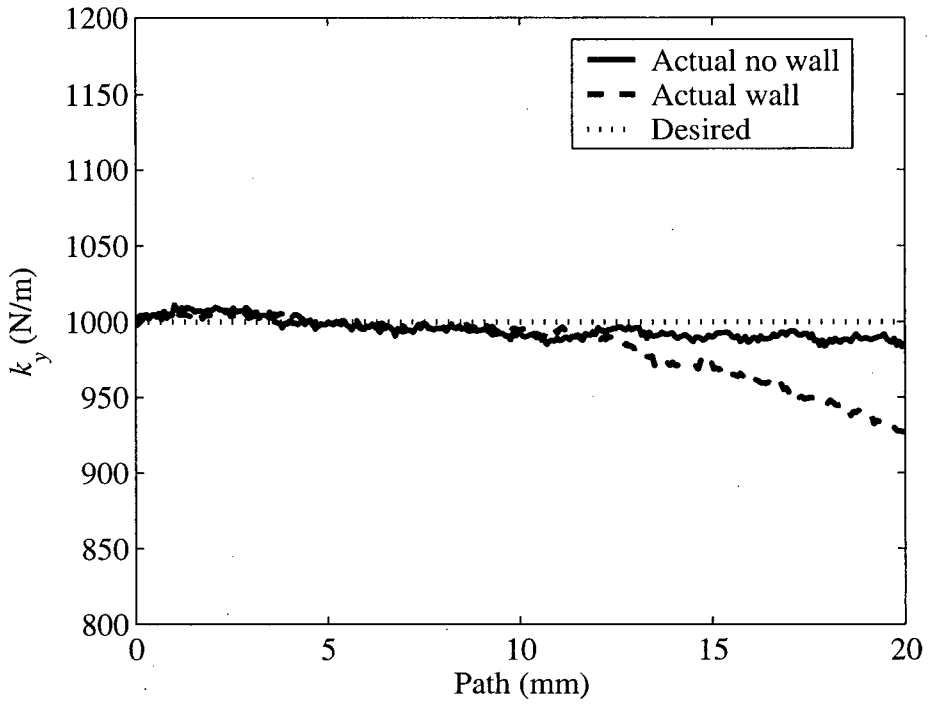

Figure 5.9 – Transition test #1 k_{ya} and k_{yd} with and without the wall versus path

The k_{ya} trajectory varied slightly between tests. It was most different in test #9 (2mm/s, 30°) as shown below in Figure 5.10. The small errors in position coupled with increased velocity created the largest k_y errors.

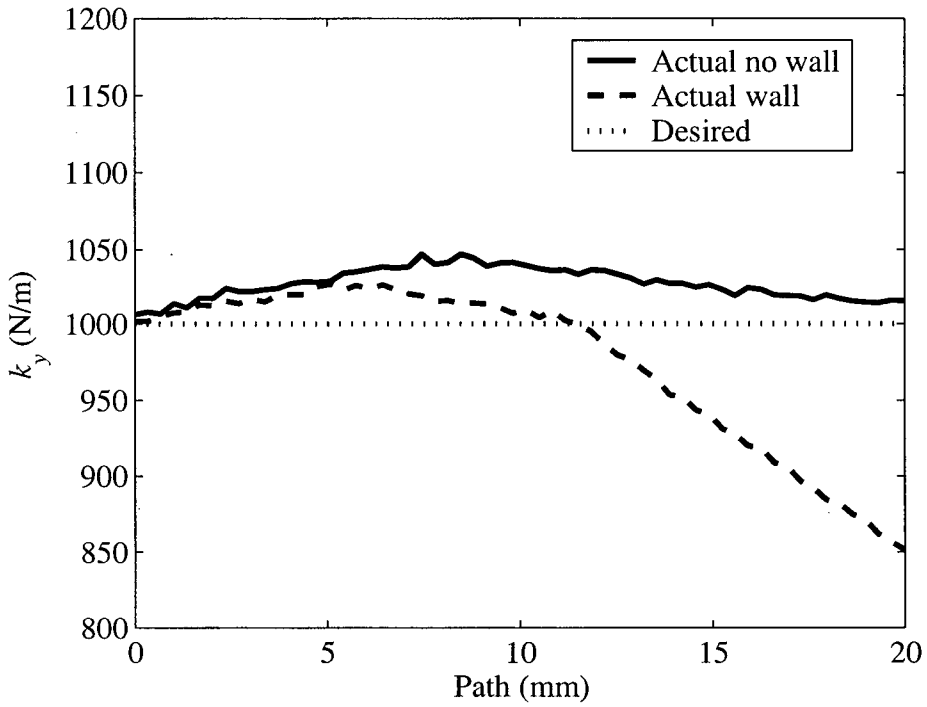

Figure 5.10 – Transition test #9 k_{ya} and k_{yd} with and without the wall versus trajectory

The observed force normal to the wall follows the predicted value within 1N based on the commanded endpoint stiffness and commanded end point position. There is little effect from the X-axis end-point stiffness term, k_x, for these tests because the manipulator is very close to the Y-axis for the entire trajectory. The resulting force into the surface is shown below in Figure 5.11. The expected normal force is 5 N when the manipulator is resting on the surface with an Y-axis equilibrium position 5mm into the surface and Y-axis end-point stiffness of 1000 N/m.

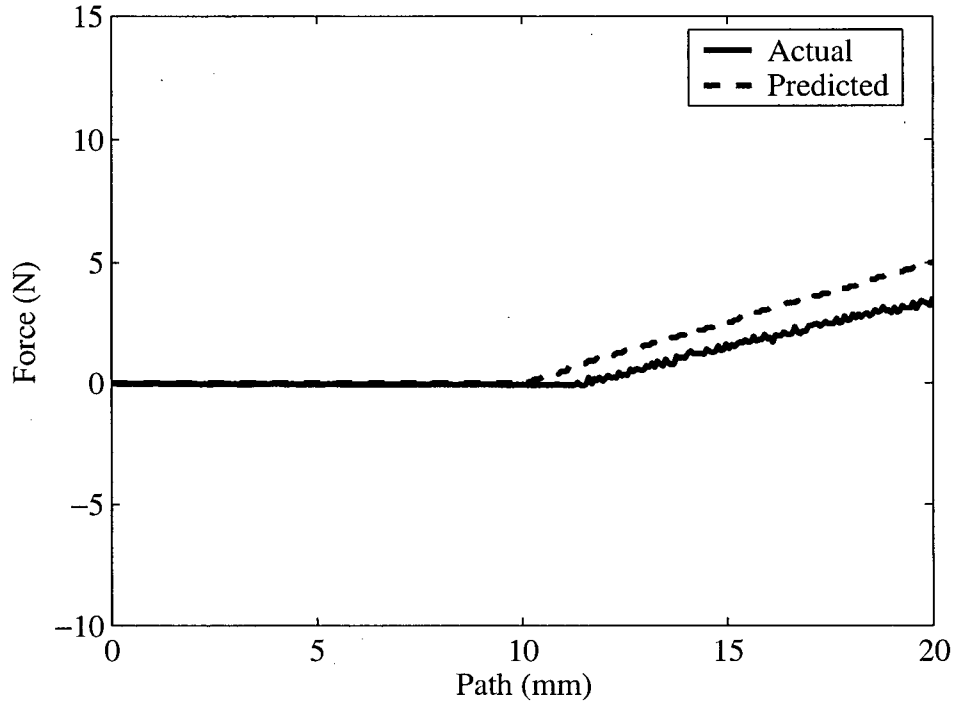

Figure 5.11 – Transition test #1 actual and predicted force with and without the wall versus trajectory

Table 5.1 below shows a complete summary of the Mean Absolute Error for the different variables presented in the above plots for all of the transition tests.

Table 5.1 – Summary of Mean Absolute Error for the transition testing

Test / Error Type	1 v=2 θ=30	2 v=2 θ=60	3 v=2 θ=90	4 v=5 θ=30	5 v=5 θ=60	6 v=5 θ=90	7 v=10 θ=30	8 v=10 θ=60	9 v=10 θ=90
y_{EP} MAE no wall (m)	0.10	0.11	0.15	0.13	4.14	0.18	0.20	0.20	0.35
k_y MAE no wall (N/m)	7.09	9.01	9.70	7.75	17.64	11.48	7.33	12.50	26.90
y_{EP} MAE wall (m)	0.10	0.12	0.13	0.15	0.17	0.15	0.18	0.19	0.20
k_y MAE wall (N/m)	18.60	35.15	41.60	19.77	35.19	41.46	18.17	32.33	52.84
F MAE wall (N)	0.56	0.80	0.93	0.56	0.91	0.95	0.58	0.89	0.94

Testing was performed using three different approach angles. No significant differences in the response of the manipulator were seen for the different approach angles to the wall. The manipulator performed the transition task well for all velocities tested. The highest velocity of

10mm/s did result in larger deviations from the predicted force but these were not considered to be significant in comparison to the predicted force value (i.e. less than <10%).

5.4 Contact Results

The third set of tests executed was a contact task. The manipulator was commanded to wipe a surface with a variety of position EP and stiffness trajectories. The trajectories were generated such that the k_y and the force into the surface should remain equal over the full surface. As discussed in Chapter 4, forces resulting from displacement in X were countered by adjusting the position EP trajectory to compensate. All trajectories were run against a surface mounted to a force transducer. The resulting force into the surface was measured. The tests were run once against the unmodified flat smooth surface and then again with a 4mm smooth bump in the middle of the surface. The test conditions in Table 4.3 are reproduced below for convenience.

Test #10 (v_x =30mm/s, y_{EP} =405mm, k_y =1100N/m) was chosen for example results. Detailed results for all of the 23 test points with and without the bump are presented in Appendix J.

The Y-axis equilibrium position, y_{EP}, is the more important component of the equilibrium position vector, X_{EP}, for ensuring forces due to unexpected position disturbances are as predicted by the EP and stiffness trajectories. Figure 5.12 shows good agreement between the actual and desired Y-axis end-point position, y_{EPa} and y_{EPd}. The value of Y-axis actual position, y_a, is offset as expected, due to the presence of the wall between the manipulator, from the Y-axis equilibrium position, y_{EP}.

Table 4.3 – List of all contact test numbers

	15 mm/s			30 mm/s			75 mm/s		
y_{EP}	800 N/m	1100 N/m	1400 N/m	800 N/m	1100 N/m	1400 N/m	800 N/m	1100 N/m	1400 N/m
405 mm	1		3	5	10	15	20		22
410 mm				6,7,8	11,12,13	16,17,18			
415 mm	2		4	9	14	19	21		23

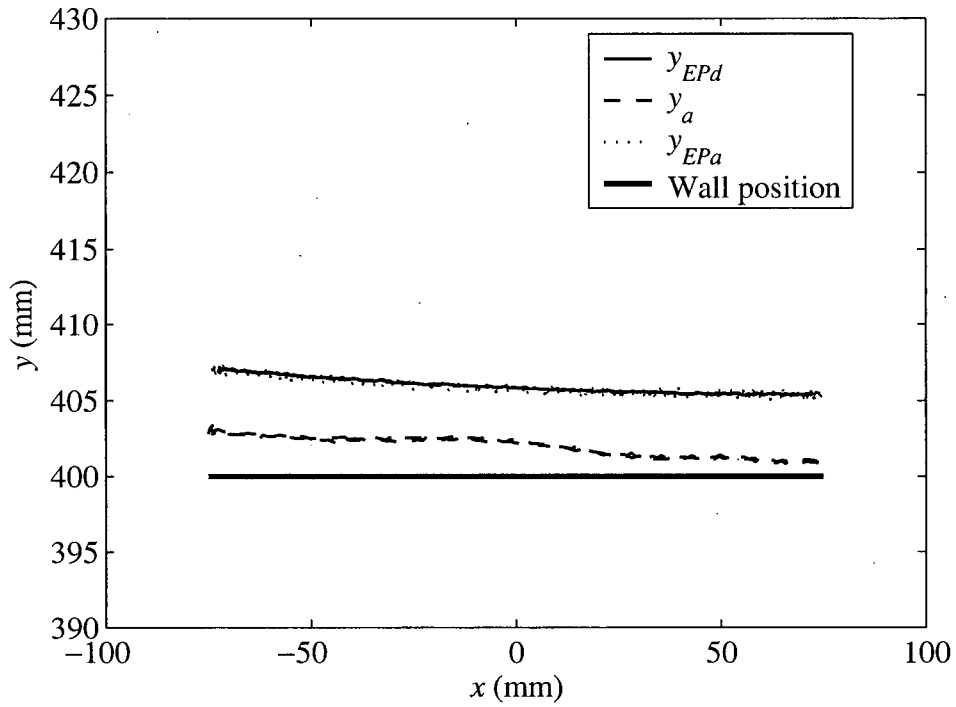

Figure 5.12 – Test #10 without bump (y versus x)

Again adding a bump does not make the task of tracking the Y-axis equilibrium position, y_{EP} particularly more difficult as shown in Figure 5.13, only the Y-axis actual position, y_a, deviates due to the presence of the wall. The 4mm bump is well within the capabilities of the controller's capability for rejection.

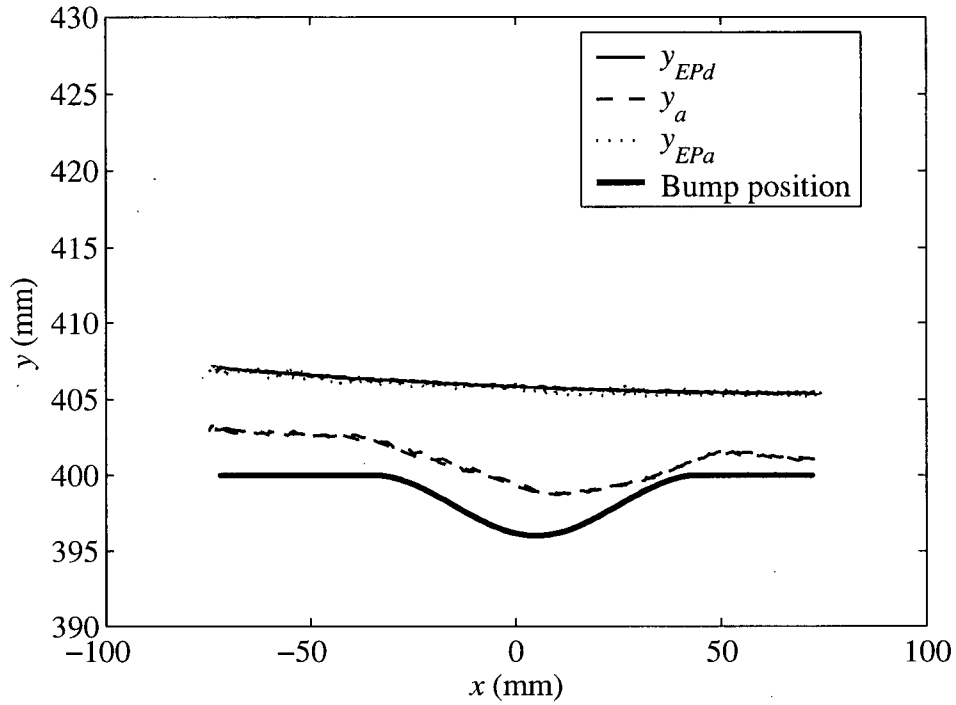

Figure 5.13 – Test #10 with bump y versus x

It is also important that the Y-axis end-point stiffness, k_y, tracks close to the desired value for the forces from the contact to result close to the desired values. Figure 5.14 shows that the k_y values drift around somewhat, but are generally close to the desired value. Figure 5.15 shows that this remains true when the bump is present as well.

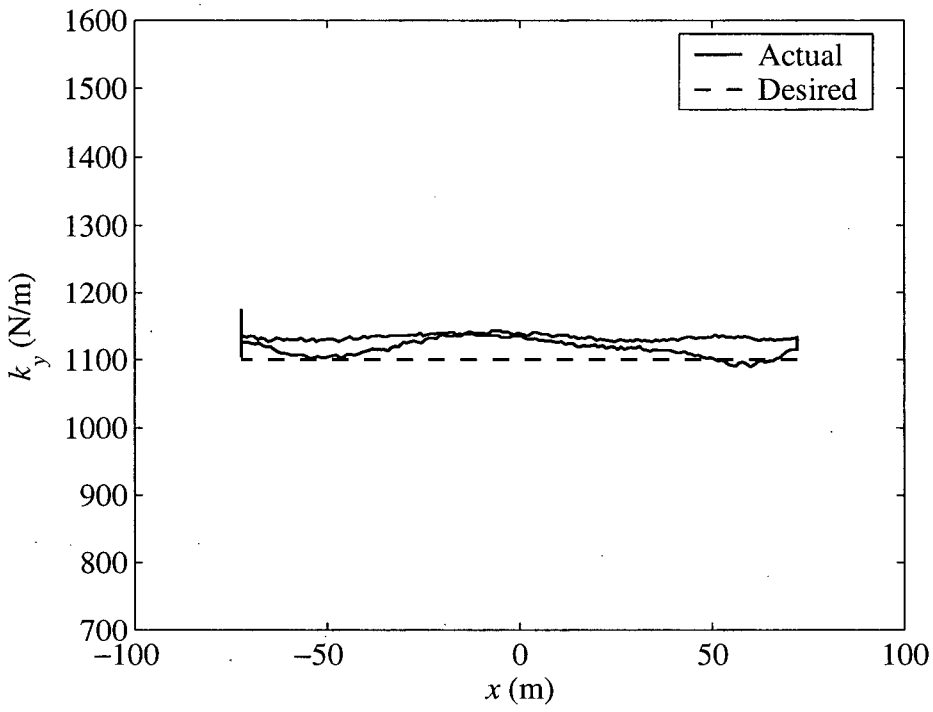

Figure 5.14 – Test #10 without bump k_y versus x

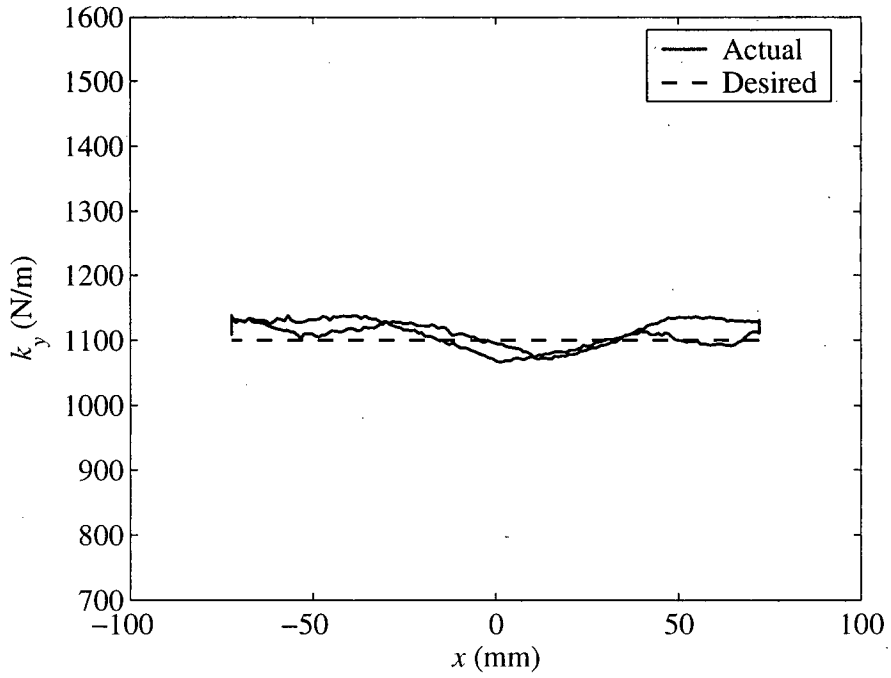

Figure 5.15 – Test#10 with bump k_y versus x

Figure 5.16 and Figure 5.17 show the force response from contact with the wall and without the bump present. These results are again for the case where Y-axis end-point stiffness, k_y, was set to 1100 N/m and Y-axis equilibrium position, y_{EP}, to 405mm, but are representative of the general behavior for all cases tested. The behavior generally followed closely to the predicted response and did not cause instabilities in the system.

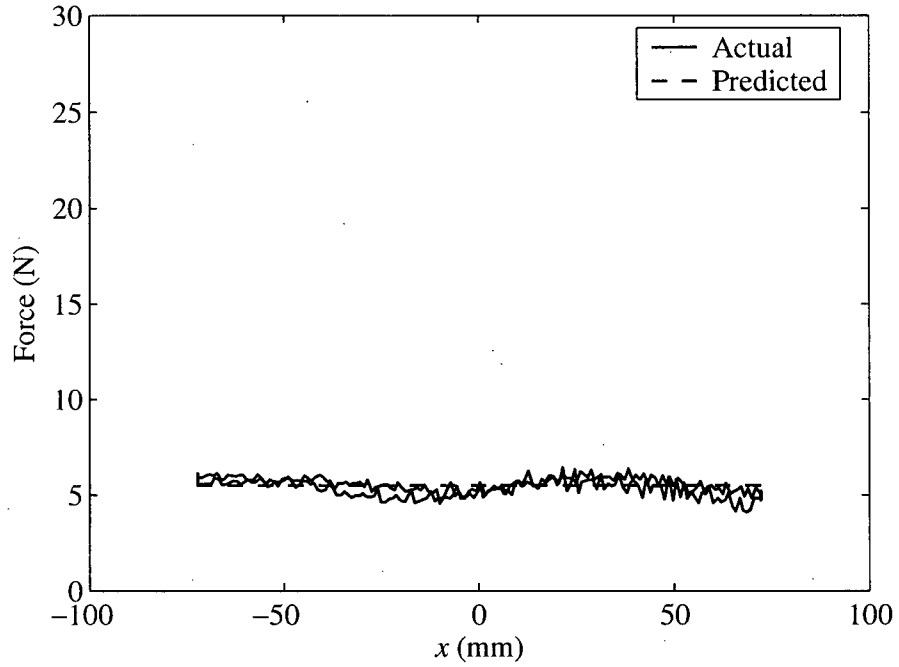

Figure 5.16 – Test#10 force versus x without bump

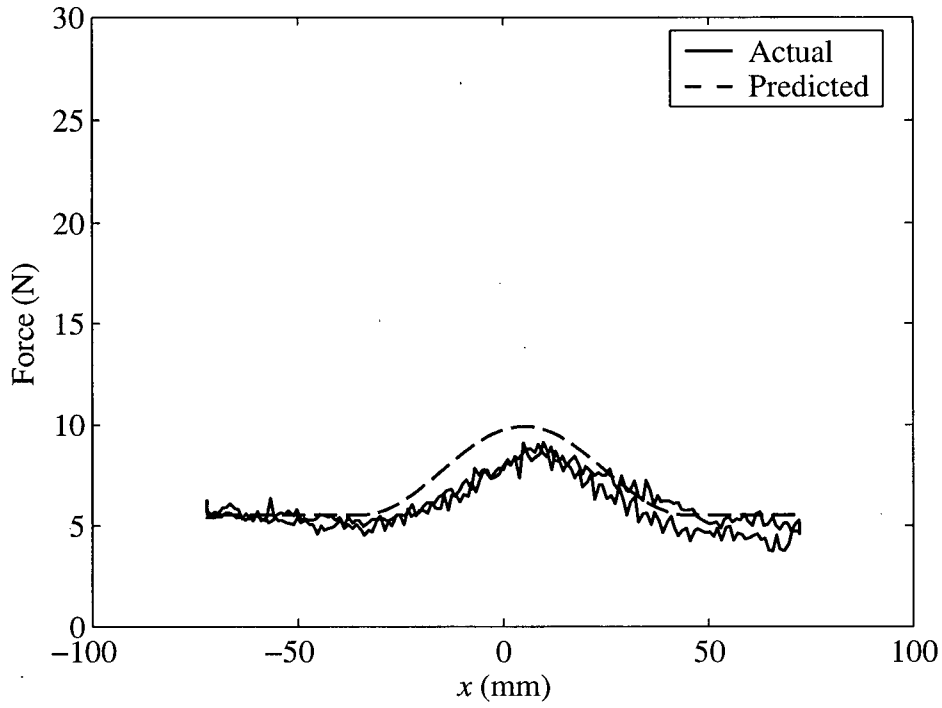

Figure 5.17 – Test#10 force versus x with bump

Table 5.2 and Table 5.3 detail the MAE values for all of the test cases with and without the bump present. The error is given as both the MAE and also the MAE relative the expected value. In the case of Y-axis equilibrium position the error is given relative to the requested depth of contact into the surface.

Table 5.2 – Summary of Errors without the bump present

	y_{EP} MAE		k_y MAE		F MAE	
Test #	(mm)	rel.%	(N/m)	rel. %	(N)	rel.%
1	0.12	2.44%	18.49	2.31%	0.50	12.41%
2	0.14	0.93%	25.21	3.15%	1.72	14.31%
3	0.09	1.85%	97.88	6.99%	1.35	19.34%
4	0.10	0.69%	87.95	6.28%	0.67	3.18%
5	0.14	2.78%	18.41	2.30%	0.59	14.78%
6	0.16	1.63%	17.49	2.19%	0.89	11.14%
7	0.16	1.63%	16.93	2.12%	0.97	12.18%
8	0.17	1.67%	17.40	2.18%	0.97	12.07%
9	0.27	1.78%	22.38	2.80%	1.72	14.36%
10	0.14	2.77%	23.78	2.16%	0.37	6.67%
11	0.17	1.70%	26.91	2.45%	0.77	6.97%
12	0.16	1.57%	27.45	2.50%	0.88	8.04%
13	0.16	1.60%	27.02	2.46%	0.87	7.94%
14	0.21	1.41%	39.44	3.59%	1.46	8.87%
15	0.12	2.46%	35.66	3.24%	0.55	10.09%
16	0.17	1.69%	40.56	2.90%	0.55	3.96%
17	0.16	1.58%	40.72	2.91%	0.68	4.88%
18	0.16	1.64%	41.62	2.97%	0.68	4.86%
19	0.21	1.40%	67.31	4.81%	1.10	5.24%
20	0.25	5.02%	19.70	2.46%	0.64	16.05%
21	0.42	2.79%	25.23	3.15%	1.49	12.42%
22	0.22	4.36%	43.92	3.14%	0.69	9.91%
23	0.39	2.62%	66.18	4.73%	1.15	5.50%

Without the bump present, the errors seen during the contact task are very small. The error in Y-axis equilibrium position, tends to be less than 5% regardless of the speed, depth or stiffness. The relative error in Y-axis stiffness is also generally less than 5%. The error in force is the largest relative to the expected value. This error was seen to be as large as 16.05%. Test case #20 (y_{EP}=405, k_y=800N/m and v_x=75mm/s) generated the largest error in force.

Table 5.3 – Summary of Errors with the bump present

	y_{EP} MAE		k_y MAE		F MAE	
Test #	(mm)	rel.%	(N/m)	rel. %	(N)	rel.%
1	0.16	3.23%	15.75	1.97%	0.50	12.54%
2	0.14	0.95%	19.05	2.38%	1.15	9.62%
3	0.09	1.87%	20.03	1.43%	1.00	14.28%
4	0.09	0.61%	82.52	5.89%	1.52	7.22%
5	0.14	2.89%	15.55	1.94%	0.60	14.91%
6	0.22	2.21%	14.19	1.77%	0.83	10.40%
7	0.18	1.83%	14.40	1.80%	0.81	10.11%
8	0.17	1.70%	14.37	1.80%	0.84	10.55%
9	0.22	1.44%	18.93	2.37%	1.32	11.03%
10	0.13	2.62%	20.11	1.83%	0.60	10.93%
11	0.21	2.07%	23.74	2.16%	0.80	7.28%
12	0.18	1.78%	23.27	2.12%	0.90	8.16%
13	0.17	1.65%	22.81	2.07%	0.91	8.27%
14	0.26	1.71%	36.09	3.28%	1.38	8.35%
15	0.12	2.46%	31.30	2.85%	0.97	17.57%
16	0.17	1.68%	35.15	2.51%	0.93	6.65%
17	0.16	1.56%	35.29	2.52%	1.07	7.68%
18	0.16	1.56%	35.97	2.57%	1.09	7.78%
19	0.21	1.38%	61.69	4.41%	1.45	6.92%
20	0.25	4.96%	20.61	2.58%	0.70	17.58%
21	0.43	2.89%	25.53	3.19%	1.36	11.30%
22	0.22	4.34%	50.98	3.64%	0.97	13.79%
23	0.39	2.60%	63.77	4.56%	1.31	6.23%

The MAE results with the bump present are almost identical to those without. Test case #20 was still the most challenging, showing the largest relative errors. Test case #20 represents the lowest Y-axis end-point stiffness and Y-axis equilibrium position commanded at the highest velocity. The combination of low predicted force and the errors introduced by the high velocity caused the largest observed errors to occur during this test case.

5.4.1 Velocity, Stiffness and EP Results

The following three plots show the effect of changing X-axis velocity (v_x), Y-axis end-point stiffness (k_y) and Y-axis equilibrium position (y_{EP}) had on the tests run without the bump present.

The tests chosen for these plots were four sets of k_y and y_{EP} that were run at each of the three v_x values.

Figure 5.18 is a summary plot of the Y-axis equilibrium position, y_{EP}, MAE for four sets of cases. This plot shows that MAE of y_{EP} increases as the X-axis velocity, v_x, increases. It also increases as the y_{EP} increases. The y_{EP} MAE decreases as the Y-axis end-point stiffness k_y increases for the data shown below.

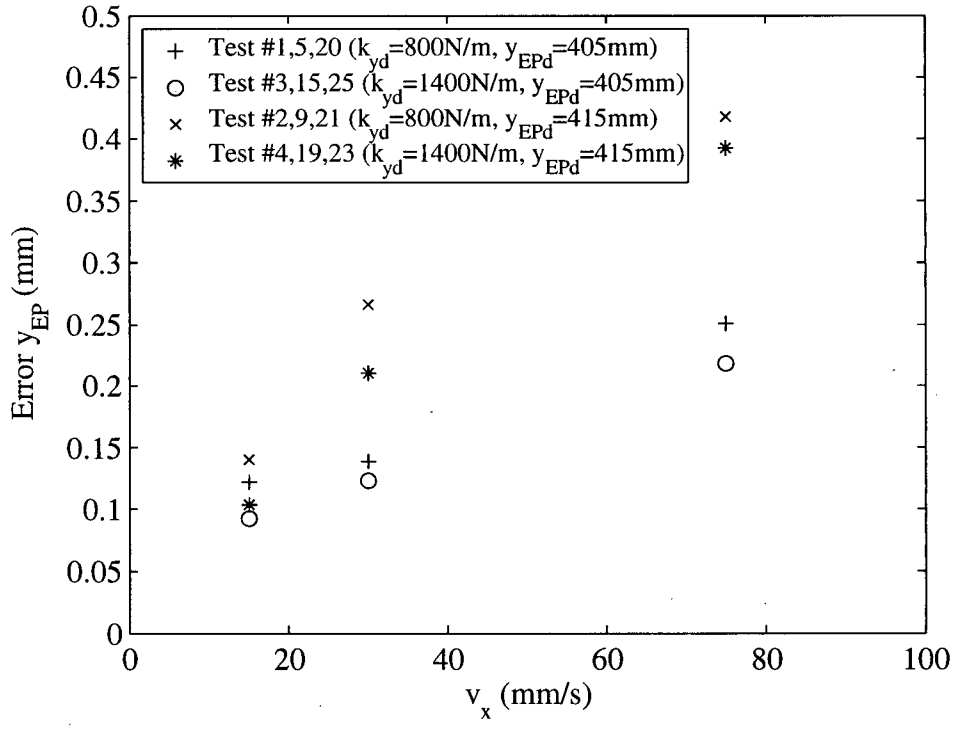

Figure 5.18 – Summary of y_{EP} error

Figure 5.19 is a summary plot of the Y-axis end-point stiffness, k_y, MAE for four sets of cases. This plot shows that MAE of k_y does not appear to be correlated with X-axis velocity, v_x, or Y-axis equilibrium position, y_{EP}, The observed k_y MAE increases as the commanded k_y increases as shown below.

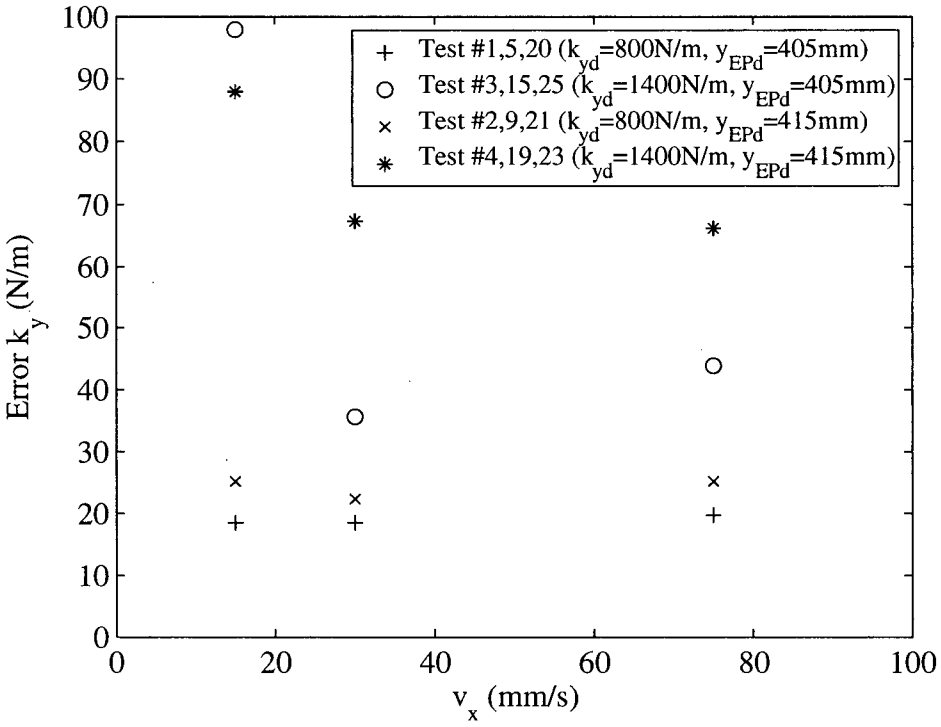

Figure 5.19 – Summary of k_y error

Figure 5.20 is a summary plot of the force MAE for four sets of cases. This plot shows that MAE of force does not appear to be correlated with X-axis velocity, v_x, or Y-axis end-point stiffness, k_y. The Force MAE increases as the Y-axis equilibrium position, y_{EP}, increases for the data shown below.

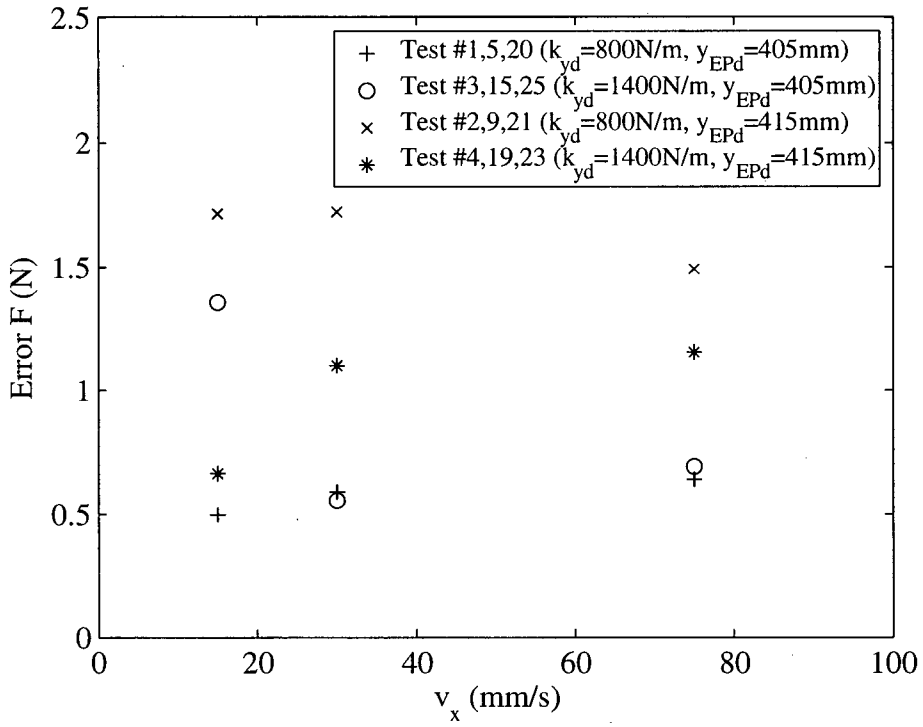

Figure 5.20 – Summary of force error

5.4.2 Repeatability Results

Three test points were repeated three times each. The repeated test data lines up very well. The manipulator delivers near identical behavior on each wipe of the surface when the trajectory is repeated. Detailed results presented in the Appendix and the data from the two above tables supports this assertion. Tests 6,7,8 were a group of three repeated identical trajectories, as were 11,12,13 and 16,17,18. As seen in the above tables, the error for these batches of tests did not vary substantially.

5.5 Summary

The results gathered from these three experiments are very encouraging regarding the usefulness of air muscle actuated PMC manipulators. All three experiments resulted in data in line with expectations.

The free space tests were very useful in determining the appropriate speeds to run the two subsequent tests. While velocities up to 150mm/s were tested it was found to be impractical to

command velocities faster than 75mm/s. Although the end point ceased to follow its commanded trajectory at higher velocities, no system instabilities resulted from executing these trajectories. The valve was simply not able to keep up with the required flow to achieve high velocities. This is due to the sizing of the orifice when the valves were initially calibrated. The orifice sizing, although limiting in terms of velocity, allowed for very smooth motion by keeping the force pulses small.

The transition tests demonstrated the ability of this type of manipulator to transition between free space and contact without either planning for the contact or a change of control strategy. In the case of the tests that were performed in this work, the transition was unplanned. The end point was simply commanded to interfere with the surface. None of the velocities or angles of approach tested caused any instabilities or other unexpected behavior. The forces generated from the unexpected contact with the surface were as expected. The end point stiffness in fact becomes increasingly reduced, as the depth of contact grows larger. This was a result of the particular posture the manipulator was in when making contact and is not a general result.

The contact task demonstrated the capabilities of the controller and manipulator for a wiping task. Force errors remained under 20% from predicted and interestingly did not vary greatly with the presence of an unexpected bump on the surface. The 4mm bump caused the end point to produce greater normal force into the surface, but the actual forces produced matched as well as those without the bump. The larger force is due to the increased deviation from y_{EP} due to the presence of the bmp. It was observed that at higher speeds the error in force normal to the surface increases most appreciably for test cases where the predicted interaction force is low.

Chapter 6
Conclusions & Recommendations

The objectives of this work were to demonstrate the capabilities of a PMC manipulator controlled with an equilibrium point hypothesis inspired controller. Particular interest was taken in the ability of such a device to perform tasks that share characteristics with the activities of daily living. In specific, it was important to demonstrate that a simple PMC manipulator could perform basic free space, transition and contact tasks using a simple and stable controller.

In this thesis a PMC robot with a simple linear PI controller based on the EP hypothesis was presented. A novel method for sizing a PMC joint using air muscles was presented, and an EP controller for the robot was designed and implemented. In a series of experiments it was shown that at low to moderate speeds (given the limitations of the valves of the air muscles) the controller tracks a demanding commanded trajectory, with some hysteresis induced in the computation (rather than direct measurement) of the actuator forces.

The manipulator was designed to be large enough to carry out a wiping task. The muscles for this project were constructed in the lab as suitable muscles were not available for purchase. Solenoid valves were chosen for metering air in and out of the air muscles. Because the behavior of these valves was not well suited to the size of the muscles, orifice plates were designed and fit to each of the valves to reduce the available maximum flow rate in and out of each valve.

The equilibrium point controller was quite simple to program and worked very well. Independent control of joint stiffness and equilibrium position was possible. Close tracking of both of these variables was achievable with simple PI control of the mass flow in and out of each muscle.

The results of the surface wiping tasks showed that it is possible to generate a wiping EP and stiffness trajectory that results in the predicted normal force while wiping the surface. Additionally the mechanical compliance of the manipulator allows for stable response to unpredicted disturbances such as the presence of a significant bump on the smooth surface.

Finally, stable behavior during transition from free-space to contact is a notable result. Because the manipulator follows an equilibrium-point trajectory with a programmed stiffness, no additional compensation is required when contacting objects in the workspace. In addition, knowledge of the precise location of the contact object is not important as the mechanical compliance of the manipulator compensates for small contact position errors.

The particularly low cost of implementation of the technologies used in this work is a promising factor in the development of affordable assistive robotic devices for in home use. The assumption that programmable mechanical compliance adds intrinsic safety to a robot that may interact with people has been supported through the demonstration of transition and contact tasks. This result holds where significant unmodeled disturbances are present, being easily handled by a robot of this type. The biggest trade-off is that it is not possible to generate superhuman stiffnesses with this manipulator were they desired.

The usefulness of this approach is supported by the fact that the EP hypothesis fits a broad range of human motion tasks. The controller demonstrated in this work shows that it is possible to closely control the EP and joint stiffness values of a manipulator. The success of this controller was independently verified by the external force measurement that showed the actual behavior of the manipulator matched the expected behavior.

6.1 General recommendations

With the successful demonstration of a stiffness/EP controller on a planar manipulator now carried out, it is possible for this work to be expanded. There is a wealth of information available from neuromotor control studies regarding the stiffness and EP trajectories that humans

follow when carrying out tasks. Results from the observation of humans can be directly implemented on this system that shares the capability of simultaneously varying EP and stiffness.

A variety of assistive devices using this technology can be imagined. Research can be carried out to help better understand the right characteristics assistive manipulator should possess. Topics for investigation include: (i) the combination of mass, stiffness and size most practical for a reaching manipulator to possess, (ii) methods of user activation, (iii) a practical method for learning from human task examples.

The method detailing the sizing of air muscle parameters could also benefit from further investigation. The method used in this work was only developed to allow for minimization of the mounting length of the air muscles. Relatively simple modifications could allow for other features to be minimized. Of particular interest for mobile applications would be to alter the method to allow for the minimization of the difference in the mass of air in maximum activation versus minimum activation, allowing for increased "fuel efficiency."

6.2 Specific Recommendations for this Experimental Work

The compliance of the surface that was used presented some difficulties and the means by which this compliance was compensated for creates some confusion when interpreting the results. For future testing it would be preferable to use a surface with either uniform stiffness or very high stiffness so that deflections of the wall are negligible. In this case they were neither.

Air muscle models including friction exist. One of these models could be implemented to improve the force prediction capabilities of the model. If an even greater increase in force accuracy is required a transducer on each link could be used. Another approach would be to instrument the end effector with a 3-axis force transducer. This would allow the control loop around end effector force to be closed completely. The added benefit of measuring end point force directly is redundancy and increased safety.

With the current configurations, additional tasks could be attempted. It would be interesting to determine the effect of changing the mass of the endpoint during a motion to simulate picking up an object partway through a motion. Another variant on the tests performed in this work would be to try the wiping task with a higher compliance surface.

Increasing the manipulator to a 3-degree of freedom device would allow for more realistic assistive task demonstrations.

Bibliography

[1] Canada Census Bureau, "How Helathy are Canadians?," Statistics Canada Health Reports, Winter 1999, Vol.11, No.3, pp. 47-61

[2] Sommers, A.R., "Long-Term Care for the Elderly and Disabled – A New Health Priority," *The New England Journal of Medicine*, July 22, 1982, Vol. 307, No.4 pp. 221-226

[3] Jorm, A.F., et al., "The disabled elderly living in the community: care received from family and formal services," *The Medical Journal of Australia*, March 15, 1993, Vol. 158, pp.383-385

[4] Nir, Z., "The Biopsychosocial Adjustment of a Disabled Elderly: A 1- Year Follow-up," *Rehabilitation nursing*, Fan/Feb, 2000, Vol. 25, No. 1, pp. 13-23

[5] Canada Census Bureau, "Health and Activity Limitation Survey, Back-up Tables Provinces and Territories", *1991 Census*, Government of Canada, British Columbia Edition

[6] Kemper, P., "The Use of Formal and Informal Home Care by the Disabled Elderly," *Health Science Research*, October, 1992, Vol. 72, No. 4, pp. 421-451

[7] Ford, A. B., et al., "Impaired and Disabled Elderly in the Community," *American Journal of Public Health, September* 1991, Vol. 81, No. 9 pp. 1207-1209

[8] Boaz, R.F., "Improved Versus Deteriorated, Physical Functioning Among Long-Term Disabled Elderly," *Medical Care*, 1994, Vol.32 No. 6 pp.589-603

[9] Arthritis Society of Canda Website: http://www.arthritis.ca

[10] K. Ikuta and M. Nokata, "Safety Evaluation Method of Design and Control for Human-Care Robots," 2003, *Int. Journal of Robotics Researc*h, vol. 22, pp. 28 1 -297

[11] Y. Yamada, Y. Hirawawa, S. Huang, Y. Umetani and K. Suita, "Human - Robot Contact in the Safeguarding Space," 1997, *IEEE/ASME Trans. On Mechatronic*s, vol. 2, pp. 230-236

[12] Okada, M., Nakamura, Y., Ban, S., 2001, "Design of a Programmable Passive Compliance Shoulder Mechanism", *Proc. Of 2001 IEEE International Conference on Robotics and Automation*, pp.348-353

[13] Bicchi, A., Rizzino, S., Tonietti, G., 2001, "Compliant Design for Intrinsic Safety: General Issues and Preliminary Design", *Intelligent Robots and Systems, 2001. Proceedings. 2001 IEEE/RSJ International Conference on*, Vol. 4, pp. 1864-1869.

[14] Sciavicco, L., Siciliano, B., 1996, *Modeling and Control of Robot Manipulators*, McGraw Hill, New York.

[15] Nickel, V.L., J. Perry, and A.L. Garrett, "Development of useful function in the severely paralyzed hand,", 1963, *Journal of Bone and Joint Surgery*, Vol. 45A, No. 5, pp. 933-952

[16] Tondu, B., Lopez, P., 2000, "McKibben Artificial Muscle Robot Actuators," *IEEE Control Systems Magazine*, pp.15-38

[17] Medrano-Cerda, Gustabo A. Bowler, Colin J. Caldwell, Darwin G., 1995 "Adaptive Position Control of Antagonistic Pneumatic Muscle Actuators", IEEE *International Conference on Intelligent Robots and Systems*, v1, pp. 378-383

[18] Latash, M.L., "Independent Control of Joint Stiffness in the Framework of the Equilibrium-Point Hypothesis," 1992, Biological Cybernetics, Vol.67, pp. 377-384

[19] Feldman, A.G., "Functional Tuning of the Nervous System with Controls of Movement or Maintenance of a Steady Posture: 2. Controllable Parameters of the Muscle," 1966, *Biophysics*, vol. 11, pp. 565-578

[20] Bizzi, E. et al., "Does the Nervous System use Equilibrium-Point Control to Guide Single and Multiple Joint Movements?", 1992, *Behavioral and Brain Sciences*, vol.15, pp. 603-615

[21] Feldman, A., Levin, M., "The Origin and Use of Positional Frame of Reference in Motor Control", 1995, *Behavioral and Brain Sciences*, vol.18, pp. 723-806

[22] Bicchi, A., Rizzino, S., Tonietti, G., 2001, "Adaptive Simultaneous Position and Stiffness Control of a Soft Robot Arm", *Intelligent Robots and Systems, 2001. Proceedings. 2001 IEEE/RSJ International Conference on*, Vol. 4, pp. 1992-1997

[23] Colbrunn, R.W., Nelson, G.M., Quinn, R.D., 2001, "Design and Control of a Robotic Leg with Braided Pneumatic Actuators", *Intelligent Robots and Systems, Proceedings. of IEEE/RSJ International Conference on*, Vol. 2, pp. 992-998

[24] Noritsugu, T., Tanaka, T., "Applications of Rubber Artificial Muscle Manipulator as a Rehabilitation Robot", *IEEE/ASME Transactions on Mechatronics,* Vol. 2, No. 4., pp. 259-267

[25] Tondu, B., Boitier, V. and Lopez, P., 1994 "Naturally Compliant Robot-Arms Actuated By McKibben Artificial Muscles", *Proc. of the 1994 IEEE Int. Conf. On Systems, Man and Cybernetics*, San Antonio, TX, 3:2635-2640

[26] Colbrunn, R.W., 2000, "Design and Control of a Robotic Leg with Braided Pneumatic Actuators," Graduate Thesis, Case Wester Reserve Universtiy

[27] Mills, J.K.; Lokhorst, D.M. , "Stability and Control of Robotic Manipulators During Contact/Noncontact Task Transition," *Robotics and Automation, IEEE Transactions on*, Vol.9, Iss.3, Jun 1993, pp.:335-345

[28] Mills, J.K., David M.L., 1993, "Control of Robotic Manipulators during general task execution: A discontinuous Control Approach," *The International Journal of Robotics Research*, vol.12, No.2, pp.146-163

[29] http://www.shadow.org.uk/index.shtml - Shadow Robot Company Webpage

[30] Chou, C.P. and Hannaford, B., 1996, "Measurement and Modeling of Artificial Muscles", *IEEE Transactions on Robotics and Automation*, Vol. 12, pp. 90-102

[31] http://batman.mech.ubc.ca/~mal/Products.html - ORTS Website

[32] Croft, E.A., "Mech 465 Course Notes," UBC

[33] Klute, G.K., 1999, Czerniecki, J.M., Hannaford, B., "McKibben Artificial Air Muscles: Pneumatic Actuators with Biomechanical Intelligence," *Proc. of IEEE/ASME International Conference on Advanced Intelligent Mechatronics*, pp. 221-226

[34] http:// www.matrix.to.it/ - Matrix Valve Website

[35] Spong, M.W., Vidyasagar, M., 1989 *Robot Dynamics and Control,* Wiley, New York

Appendix A
Air Muscle Equations

A.1 Air Muscle Equations for the Appendix

From Chou

$$dW_{in} = \int_{Surface} (P - P_0) dl_i \cdot ds_i = (P - P_0) \int_{Surface} dl_i \cdot ds_i = P' dV \qquad \text{Equation A.1}$$

Where:

P=Absolute internal gas pressure

Po=Atmospheric pressure

P'=Gage pressure

Si=Inner surface dispacment

Dsi=Area vector

Dli=Inner surface displacement

dV=Volume Change

Where:

$$dW_{out} = -fdL \qquad \text{Equation A.2}$$

and,

$$dW_{out} = dW_{in} \qquad \text{Equation A.3}$$

The force in the muscle can be written as:

$$f = -P' \frac{dV}{dL} \qquad \text{Equation A.4}$$

where the length of the muscle can be represented by

$$L = b \cdot \cos(\theta) \qquad \text{Equation A.5}$$

$$D = \frac{b \cdot \sin(\theta)}{n\pi}$$ Equation A.6

The volume in the muscle is given by:

$$V = \frac{1}{4}\pi D^2 L = \frac{b^3}{4\pi n^2}\sin^2(\theta)\cos(\theta)$$ Equation A.7

$$f = P'\frac{dV}{dL} = P'\frac{dV/d\theta}{dL/d\theta} = \frac{P'b\left(2\cos^2(\theta) - \sin^2(\theta)\right)}{4\pi n^2}$$ Equation A.8

$$f = \frac{P'b^2\left(3\cos^2(\theta) - 1\right)}{4\pi n^2}$$ Equation A.9

$$\cos^2(\theta) = \frac{L^2}{b^2}$$ Equation A.10

Ultimately yielding

$$f = \frac{P'b^2(3\frac{L^2}{b^2} - 1)}{4\pi n^2}$$ Equation A.11

Appendix B
Muscle Construction

Collect all the needed materials for an air muscle and size to correct lengths (see Table 1 and Figure 1 below).

Air Muscle Supplies					
Description	Dimensions	Quantity	Supplier	Product #	Make
Muscle Braiding	1/2" dia	18 1/2" length	Radar Inc. (Seattle)	625300113	N/A
Surgical Tubing	3/16" O.D., 1/32" thick	8" length	Lancaster Medical Supplies	N/A	N/A
Plastic Tubing	4mm O.D., 0.75mm thick	25cm length	Festo	152 584	Festo
Large Brass Insert	1/4" O.D. - 3/16" I.D.	2	Columbia Valve & Fitting	B-405-3	Swagelok
Small Brass Insert	1/4" O.D. - 1/8" I.D.	1	Columbia Valve & Fitting	B-405-2	Swagelok
Aircraft Cable	1/16" dia	2 loops	Steveston Marine & Hardware	N/A	N/A
Aluminum Sleeves	1/16" dia	4	Steveston Marine & Hardware	N/A	N/A
O-Clamps	1/4" nominal dia	3	Acklands & Grainger	FAR HC9-4	Fairview Fittings
Muscle Braiding 2	1/4"dia	2 X 3 3/4" Length	Radar Inc. (Seattle)	624900113	N/A

O.D. - Outer Diameter

I.D. - Inner Diameter

Note: Muscle Braiding 2 was added Aug 13, 2002 because 1/4" braiding was used to make the loops of muscles X1 and X2 instead of Aircraft Cable

Table B.1 – Air Muscle Supplies

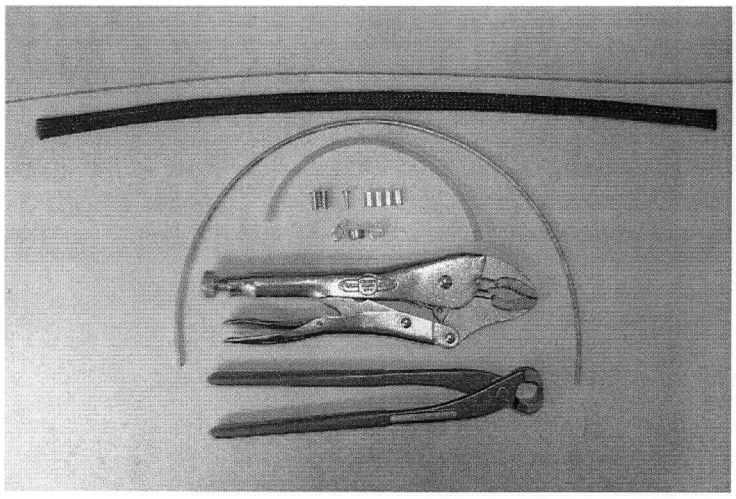

Figure B.1 – Tools and supplies to make air muscles

Solder large and small brass inserts together and plug the other large insert by filling it with solder (see Figure B.2).

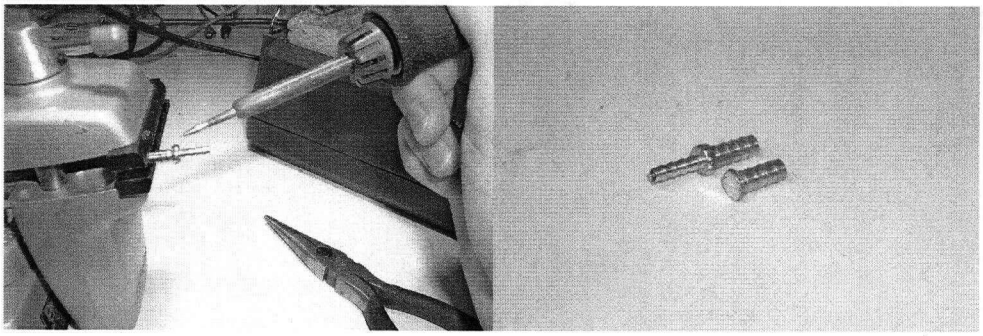

Figure B.2 – Soldering the brass inserts

Push 4mm O.D. plastic tubing over small insert and surgical tubing over the large insert (see Figure B.3).

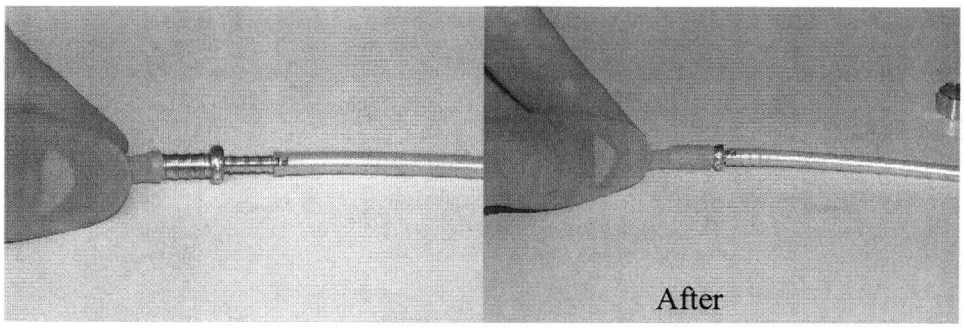

Figure B.3 – Putting inserts into the plastic and surgical tubing

Plug the other end of the surgical tubing with the large solder-filled insert (see Figure 4).

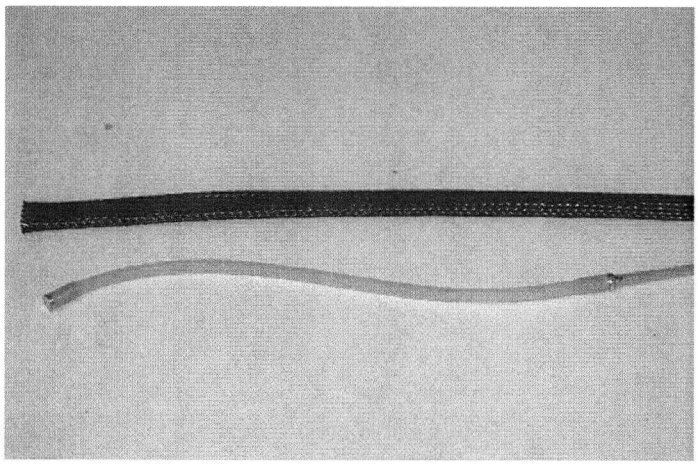

Figure B.4 – Plastic and surgical tubing connected and plugged with brass inserts

Slightly melt both ends of the mesh braiding so they don't fray apart.

Insert the 4mm O.D. plastic tubing into mesh and push it through until it exits the other end.

Now pull the plastic tubing until only the plug at the end of the surgical tubing is showing.

Slide an O-Clamp over the brass plug and also over the braiding.

Pull or push on the plastic tubing until the end of the brass insert is flush with the end of the meshing.

Make a loop with one of the smaller pieces of meshing and slide its 2 ends underneath the O-Clamp. Slide the O-Clamp back over the brass plug snuggly with the two ends of the loop sandwiched between the O-Clamp and the larger braiding (see Figure B.5).

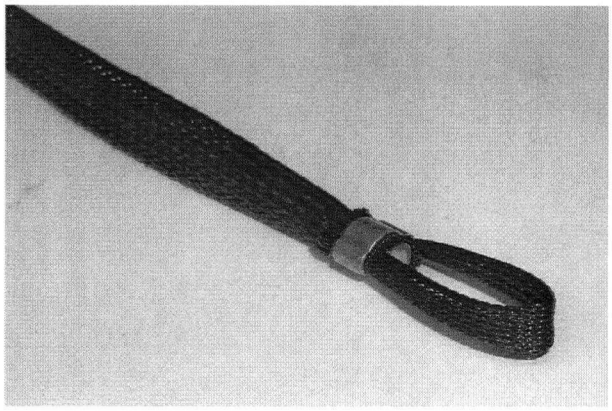

Figure B.5 – End loop of the air muscle

Alternate clamping down either side of the O-Clamp until it's snug and the loop can't be pulled out.

While holding the large mesh braiding pull the plastic tube until the junction of the two tubes comes out.

Now repeat steps 9-12 to the other end of the muscle (see Figure B.6)

Slide another O-Clamp onto the plastic tube and over the braiding and clamp it down just like the others (see Figure B.7).

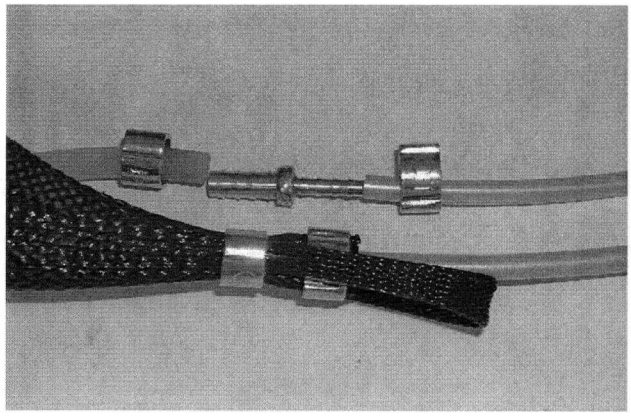

Figure B.6 – Exploded view

Note: Top layout is exploded view of the bottom layout except that the mesh has been removed

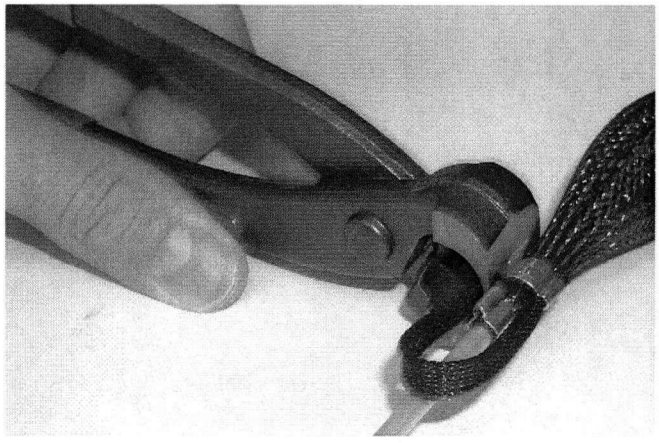

Figure B.7 – Clamping down an O-Clamp

Now that the muscle is finished it can be mounted as part of the arm (see Figure B.8).

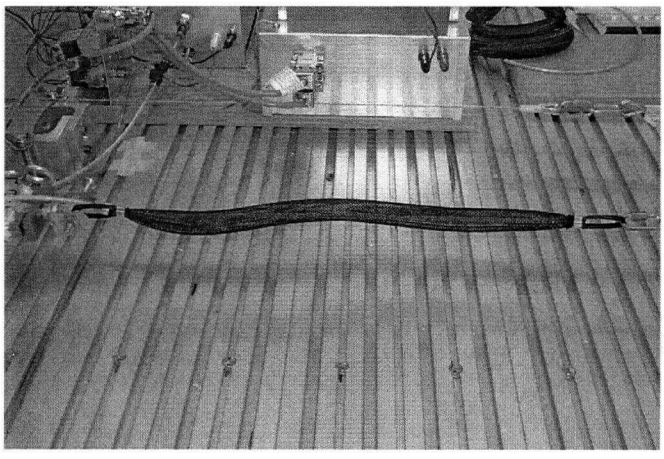

Figure B.8 – Completed air muscle mounted to the arm

Appendix C
Matlab Optimization Files

C.1 Optimize_Mount_Length.m

```
X=fmincon('minimizethis',[6.8 .4 .11 .36],[ ],[ ],[ ],[ ],[5 .4 .02 .32],[6.5 .6 .2 .4],'solverbn')
n=X(1);
b=X(2);
r=X(3);
Lmount=X(4);
%this script solves the following constraints
%The maximum obtainable stiffness is greater then Kstiffmax
%The minimum obtainable stiffness is less then Kstiffmin
%Kstiffmin>0
%The Maximum obtainable torque is greater than TorqueMax
%The working range of the robot is greater than Deltheta
%minimum ratio of n/b>8
%max ratio of n/b<21
%C is a vector that the solver tries to set <=0
%Lmount <

Kstiffmax = 30;
Kstiffmin = 15;
TorqueMax = 3.1;
DelTheta = pi/16;
P(1)=15; %min pressure  is 15 psi
P(2) = 100 ;% max pressure is 100 psi
Fmax=100; %max force is 100N

Lmin=b*cos(54.73561/180*pi);
LPmaxCrossFmax = 1/1050/P(2)*210^(1/2)*(P(2)*(1750*P(2)*b^2+(Fmax+0)*pi*n^2))^(1/2);
LPminCrossFmax = 1/1050/P(1)*210^(1/2)*(P(1)*(1750*P(1)*b^2+(Fmax+0)*pi*n^2))^(1/2);
FPmaxCrossb = P(2)*7000*b^2*(3*b^2/b^2-1)/(4*pi*n^2)-0;
FPminCrossb = P(1)*7000*b^2*(3*b^2/b^2-1)/(4*pi*n^2)-0;
if LPmaxCrossFmax >b
   Lmax=b;
else
   Lmax=LPmaxCrossFmax;
end
if LPminCrossFmax <b
   Lmin1 = LPminCrossFmax;
```

```
   Fmax1=Fmax;
else
   Lmin1 = b;
   Fmax1=FPminCrossb;
end

Lmaxs=[Lmin:.001:Lmax];
Lmins=[Lmin:.001:Lmin1];
Fmaxs=P(2)*7000*b^2.*(3.*Lmaxs.^2./b^2-1)./(4*pi*n^2)-0;
Fmins=P(1)*7000*b^2.*(3.*Lmins.^2./b^2-1)./(4*pi*n^2)-0;
TmaxDes=TorqueMax;
L1=Lmount+r*DelTheta;
L2=Lmount-r*DelTheta;
DeltaF=TmaxDes/r

FA = P(1)*7000*b^2*(3*(L1)^2/b^2-1)/(4*pi*n^2)-0;
FB = P(2)*7000*b^2*(3*(L2)^2/b^2-1)/(4*pi*n^2)-0;

if FB > Fmax
   FB=Fmax
End

FC = FA + DeltaF
FD = FB – DeltaF

KA = stiffness1(n,b,L1,P(1)*7000)
KC = stiffness1(n,b,L2,(FC+0)/(b^2*(3*(L2)^2/b^2-1)/(4*pi*n^2)))
Kmin=r^2*(KA+KC)

KB = stiffness1(n,b,L2,P(2)*7000)
KD = stiffness1(n,b,L1,(FD+0)/(b^2*(3*(L1)^2/b^2-1)/(4*pi*n^2)))
Kmax=r^2*(KB+KD)

MaxTorqueAct = (FB-FA)*r

figure
plot(Lmins,Fmins,'r')
hold
plot(Lmaxs,Fmaxs);
line([ b b],[Fmax1 Fmax]);
line([LPmaxCrossFmax b],[Fmax Fmax]);
line([L1 L1],[FA FC]);
line([L2 L2],[FB FD]);
line([Lmount Lmount],[0 100])
```

C.2 solverbn.m

```
function[C,Ceq]=solverbn(X)

n=X(1);
b=X(2);
r=X(3);
Lmount=X(4);

%this function solves the following constraints
%The maximum obtainable stiffness is greater then Kstiffmax
%The minimum obtainable stiffness is less then Kstiffmin
%Kstiffmin>0
%The Maximum obtainable torque is greater than TorqueMax
%The working range of the robot is greater than Deltheta
%minimum ratio of b/n>.05
%max ratio of b/n<.1
%C is a vector that the solver tries to set <=0
%Lmount < b

Kstiffmax = 30;
Kstiffmin = 15;
TorqueMax = 3.1;
DelTheta = pi/16;

P(1)=20; %min pressure  is 20 psi
P(2) = 100 ;% max pressure is 100 psi
Fmax=100; %max force is 100N

Lmin=b*cos(54.73561/180*pi);


LPmaxCrossFmax = 1/1050/P(2)*210^(1/2)*(P(2)*(1750*P(2)*b^2+(Fmax+0)*pi*n^2))^(1/2);
LPminCrossFmax = 1/1050/P(1)*210^(1/2)*(P(1)*(1750*P(1)*b^2+(Fmax+0)*pi*n^2))^(1/2);

FPmaxCrossb = P(2)*7000*b^2*(3*b^2/b^2-1)/(4*pi*n^2)-0;
FPminCrossb = P(1)*7000*b^2*(3*b^2/b^2-1)/(4*pi*n^2)-0;

if LPmaxCrossFmax >b
   Lmax=b;
else
   Lmax=LPmaxCrossFmax;
end

if LPminCrossFmax <b
   Lmin1 = LPminCrossFmax;
   Fmax1=Fmax;
else
   Lmin1 = b;
```

```
   Fmax1=FPminCrossb;
end

Lmaxs=[Lmin:.001:Lmax];
Lmins=[Lmin:.001:Lmin1];
Fmaxs=P(2)*7000*b^2.*(3.*Lmaxs.^2./b^2-1)./(4*pi*n^2)-0;
Fmins=P(1)*7000*b^2.*(3.*Lmins.^2./b^2-1)./(4*pi*n^2)-0;

TmaxDes=TorqueMax;

L1=Lmount+r*DelTheta;
L2=Lmount-r*DelTheta;
DeltaF=TmaxDes/r

FA = P(1)*7000*b^2*(3*(L1)^2/b^2-1)/(4*pi*n^2)-0;
FB = P(2)*7000*b^2*(3*(L2)^2/b^2-1)/(4*pi*n^2)-0;

if FB > Fmax
   FB=Fmax
end

FC = FA + DeltaF
FD = FB - DeltaF

KA = stiffness1(n,b,L1,P(1)*7000)
KC = stiffness1(n,b,L2,(FC+0)/(b^2*(3*(L2)^2/b^2-1)/(4*pi*n^2)))
Kmin=r^2*(KA+KC)

KB = stiffness1(n,b,L2,P(2)*7000)
KD = stiffness1(n,b,L1,(FD+0)/(b^2*(3*(L1)^2/b^2-1)/(4*pi*n^2)))
Kmax=r^2*(KB+KD)

MaxTorqueAct = (FB-FA)*r

C(1) = Kstiffmax - Kmax;          %ensure the maximum stiffness is possible
C(2) = Kmin - Kstiffmin;          %ensure the minimum stiffness is possible
C(3) = -Kstiffmin                 %ensure the minimum stiffness is positive
C(4) = TorqueMax - MaxTorqueAct;  %ensure the max torque is achievable
C(5) = 0;
C(7) = n/b-21;                    %check the b/n ratio
C(6) = 8 - n/b;                   %check it on the other side
C(8) = DelTheta*r + Lmount -b ;   %check the theta range on the right side

Ceq=[ ]
```

C.3 Stiffness1.m

```
function stiffness1=stiffness1(n,b,L,P)


A=1/(4*pi*n^2);
B=b^2/(4*pi*n^2);
Phi=B-3*A*L^2;
Vol=B*L-A*(L^3);
stiffness1=(P+101000)/Vol*Phi^2+P*6*L*A;
```

C.4 minimizethis.m

```
function valuetomin = objfun(X)

n=X(1);
b=X(2);
r=X(3);
Lmount=X(4);

valuetomin=Lmount;
```

Appendix D
Manipulator Bill of Materials

Table D.1 – BOM-1

Parts Name	Quantity	Material	Attainability	From	Catalogue Info	Cost/unit
Adaptor 1 (Front)	1	Aluminum	Machine	UBC Undergraduate Shop	----------	5.00
Adaptor 2 (Side)	1	Aluminum	Machine	UBC Undergraduate Shop	----------	3.50
Adaptor 3 (Back)	1	Aluminum	Machine	UBC Undergraduate Shop	----------	2.00
Allan Screw (8-32)	8	Steel	Purchase	UBC Mechanical Graduate Shop	----------	0.10
Allan Screw (M8-30)	4	Steel	Purchase	UBC Mechanical Graduate Shop	----------	0.10
Allan Screw (4-40)	8	Steel	Purchase	UBC Mechanical Graduate Shop	----------	0.10
Bearing (Large)	2	400 Series Stainless Steel	Purchase	RotoPrecision Inc. (Distributor) 7342 Winston St. #100 Burnaby, BC V5A 2H1 Tel: (604) 420-1240 Fax: (604) 420-2927 Email: rhonda@rotoprecision.ca http://www.rotoprecision.ca/	Nordex 2002 Catalogue Page 34A ABS-A5-30	4.23
Bearing (Small)	4	400 Series Stainless Steel	Purchase	RotoPrecision Inc.	Nordex Catalogue Page 34A ABS-A5-52	6.23
Dowel Pin (3/32 – 1/2)	4	Stainless Steel	Purchase	RotoPrecision Inc.	Nordex Catalogue Page 19E EPS-A4-11	0.14
Dowel Pin (3/32 – 3/8)	2	Stainless Steel	Purchase	RotoPrecision Inc.	Nordex Catalogue Page 19E EPS-A4-9	0.13
Encoder	2	----------	Purchase	US Digital 11100 NE 34th Circle Vancouver, WA 98682 USA Tel: (360) 260-2468 Fax: (360) 260-2469 Email: sales@usdigital.com www.usdigital.com	ATI Industrial Automation Mechanical Layout: B-3 Drawing #: 9230-05-1074-02	104.71

Table D.2 – BOM-2

Parts Name	Quantity	Material	Attainability	From	Catalogue Info	Cost/unit
Encoder Fitting	2	Aluminum	Machine	UBC Undergraduate Shop	----------	0.50
Encoder Nut	2	Aluminum	Borrow	Industrial Automation Laboratory	----------	----------
Force Transducer	1	----------	Borrow	Damien	----------	----------
Gear (Big)	1	Plastic	Purchase & Machine	Quality Transmission Components 2101 Jericho Turnpike, Box 5416 New Hyde Park, NY 11042-5416 Tel: 516-437-6700 Fax: 516-326-8827 Email: support@qtcgears.com http://www.qtcgears.com	Handbook of Metric Gears Product Guide & Technical Data Catalog Q410 Page 106 Cat #: PSA2-80	171.99
Gear (Small)	2	Plastic	Purchase & Machine	Quality Transmission Components	Handbook ... Catalog Q410 Page 106 Cat #: PS2-20	31.95
Holder – Top	1	Aluminum	Machine	UBC Undergraduate Shop	----------	7.50
Holder – Side	2	Aluminum	Machine	UBC Undergraduate Shop	----------	1.00
Holder – Base	1	Aluminum	Machine	UBC Undergraduate Shop	----------	8.50
Link 1	1	Aluminum	Machine	UBC Undergraduate & Graduate Shop	----------	6.00
Link 2	1	Aluminum	Machine	UBC Undergraduate & Graduate Shop	----------	5.00
Pulley 1	1	Aluminum	Machine	UBC Undergraduate Shop	----------	7.00
Pulley 2	1	Aluminum	Machine	UBC Undergraduate Shop	----------	7.00
Retaining Ring (External)	2	Steel	Purchase	UBC Mechanical Graduate Shop	----------	0.05
Set Screw (4-40)	6	Steel	Borrow	Industrial Automation Laboratory	----------	----------
Set Screw (8-32)	2	Steel	Borrow	Industrial Automation Laboratory	----------	----------
Screw (Countersunk 8/32)	4	Steel	Borrow	Industrial Automation Laboratory	----------	----------
Screw (Flat Head – M3)	6	Steel	Borrow	Industrial Automation Laboratory	----------	----------
Screw (Flat Head – 5/16)	1	Steel	Borrow	Industrial Automation Laboratory	----------	----------
Shaft 1	1	Steel	Machine	UBC Undergraduate Shop	----------	1.00

Table D.3 – BOM-3

Parts Name	Quantity	Material	Attainability	From	Catalogue Info	Cost/unit
Shaft 2	1	Steel	Machine	UBC Undergraduate Shop	----------	0.50
Sprocket 1	1	Plastic	Purchase & Machine	Small Parts Inc. 13980 NW 58th Court P.O. Box 4650 Miami Lakes, FL 33014-0650 Tel: (800) 220-4242 Fax: (800) 423-9009 Email: parts@smallparts.com http://www.smallparts.com	Catalogue 21 Page 395 U-TBPN-16/D	6.59
Sprocket 2	1	Plastic	Purchase & Machine	Small Parts Inc.	Catalogue 21 Page 395 U-TBPN-16/D	6.59
Sprocket Insert	1	Aluminum	Machine	UBC Undergraduate Shop	----------	0.50
Timing Belt	1	Fiberglass reinforced Neoprene	Purchase	Small Parts Inc.	Catalogue 21 Page 396 U-TB6-210	4.20
T-Nuts	4	Aluminum	Borrow	Industrial Automation Laboratory	----------	----------
Washers	2	Aluminum	Borrow	Industrial Automation Laboratory	----------	----------
Wheel	1	Stainless Steel	Borrow	Industrial Automation Laboratory	----------	----------

Appendix E
Detailed Machining Drawings

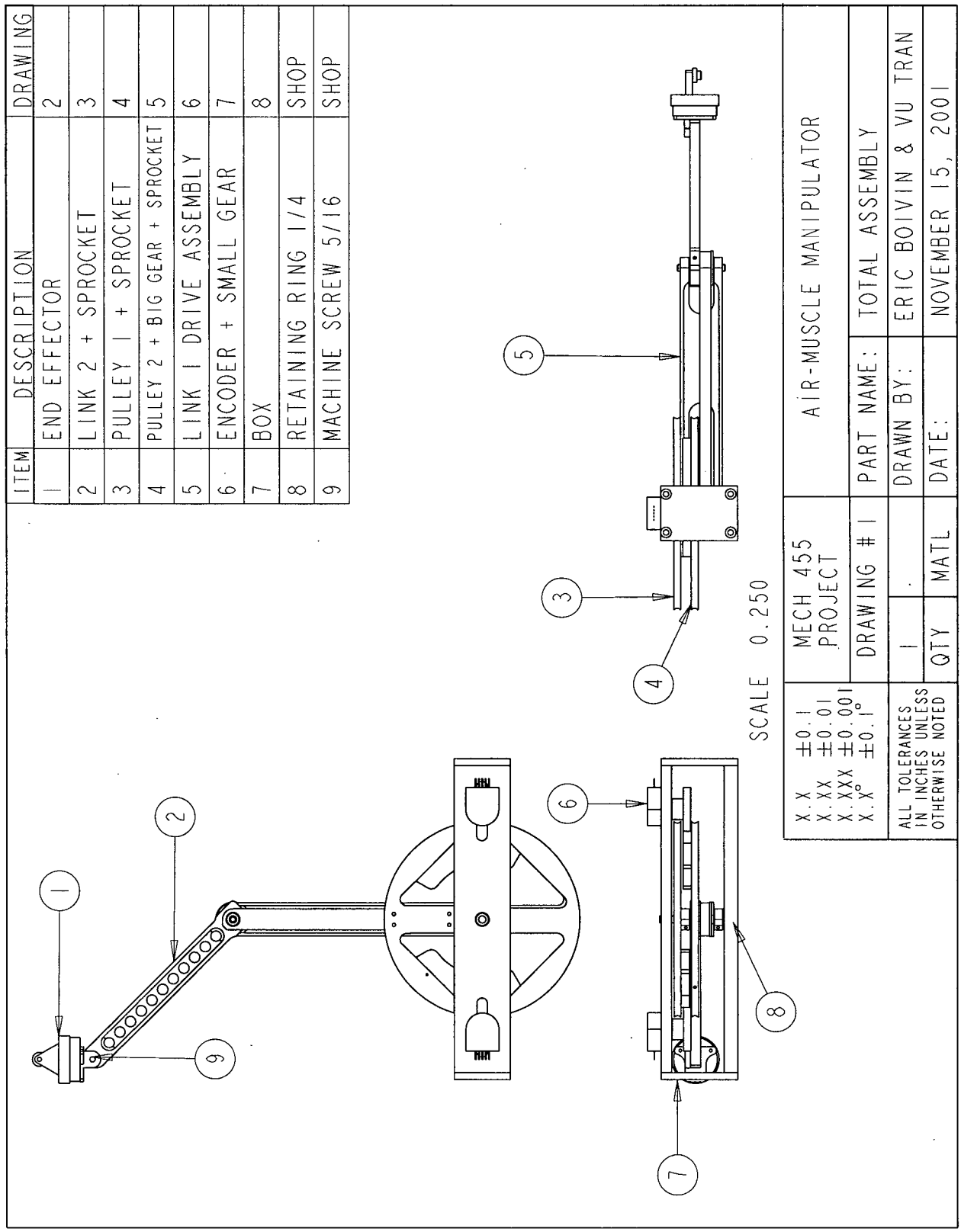

Figure E.1 – Drawing 1

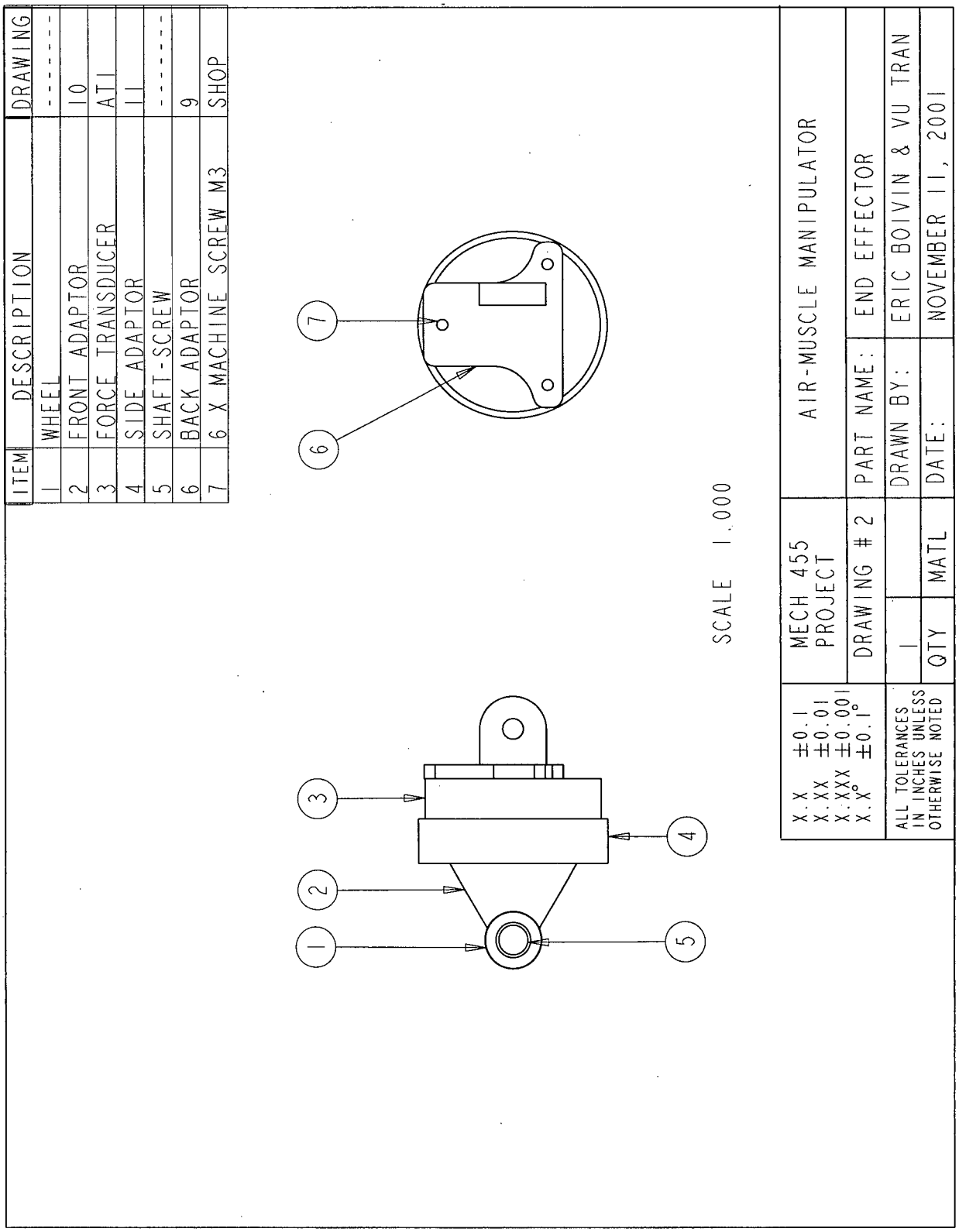

Figure E.2 – End Effector

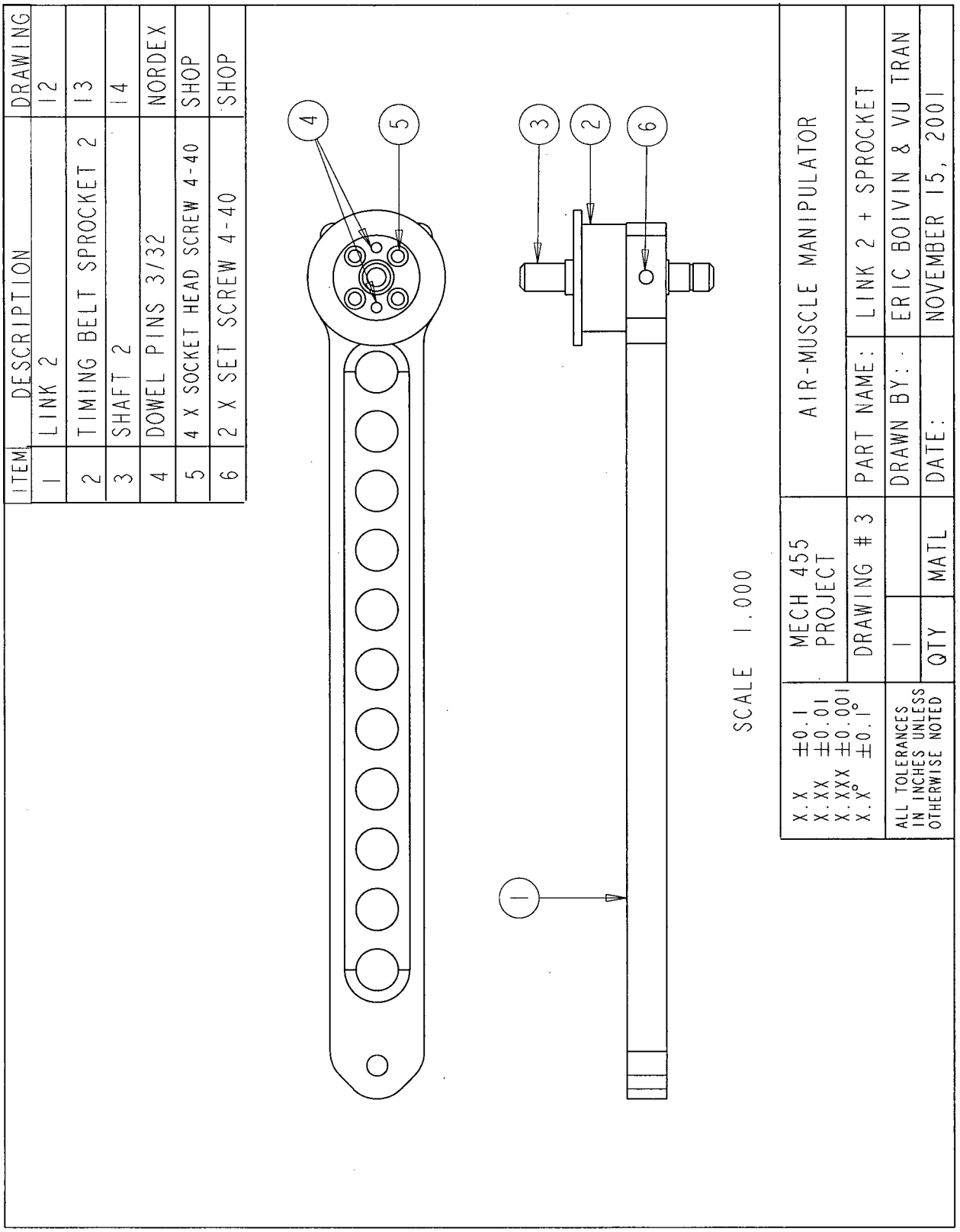

Figure E.3 – Link 2 and sprocket

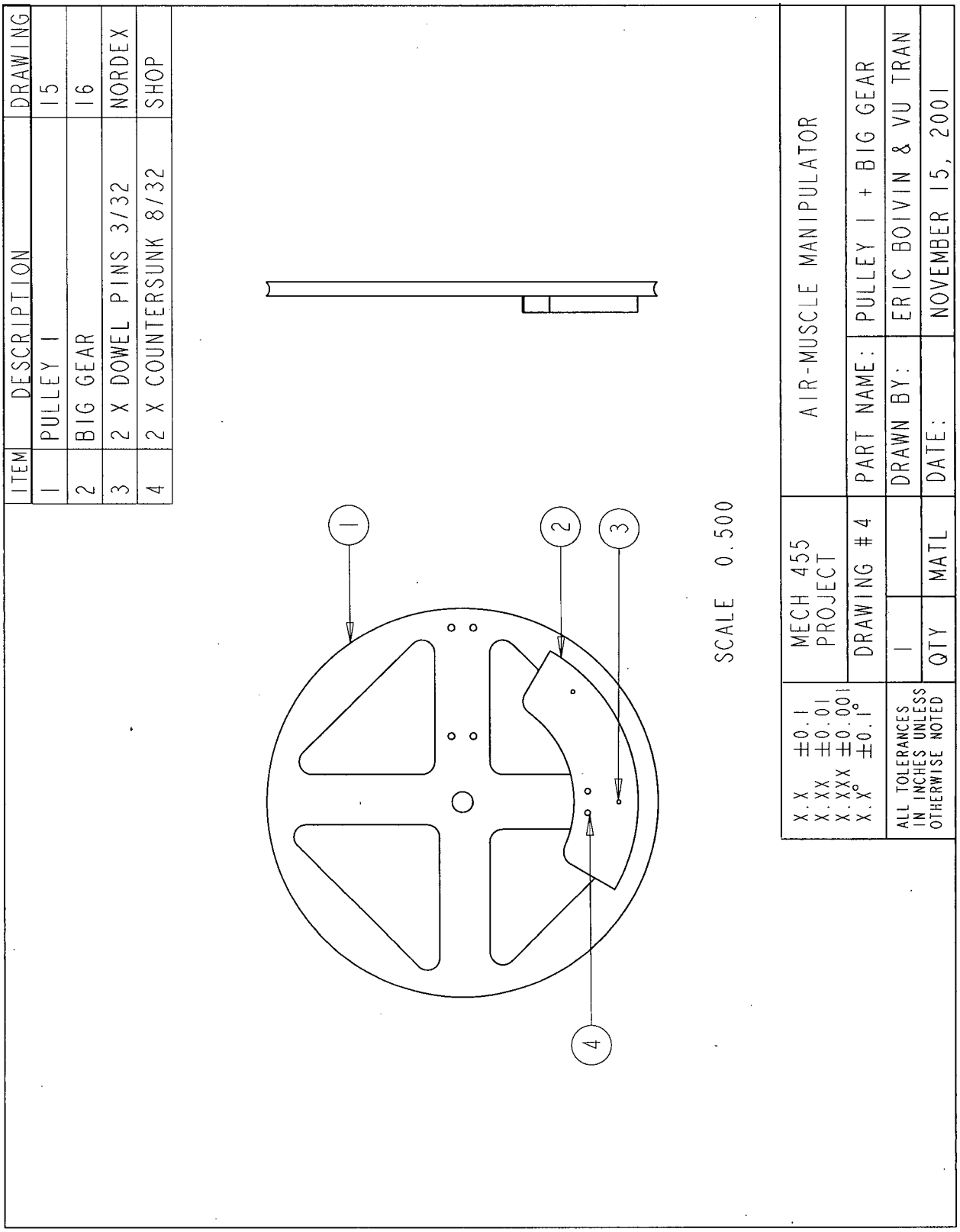

Figure E.4 – Pulley 1 and big gear

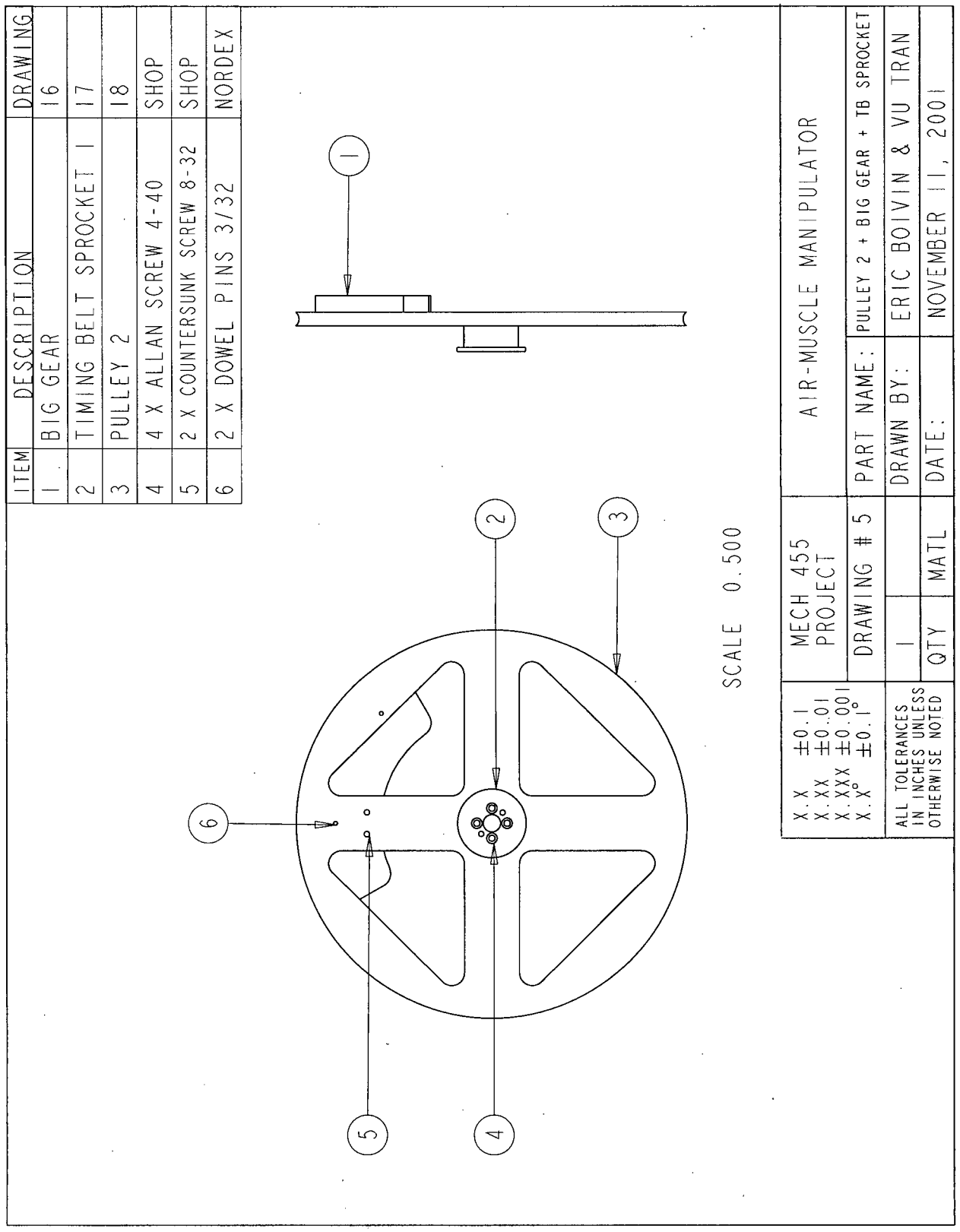

Figure E.5 – Pulley 2 and big gear

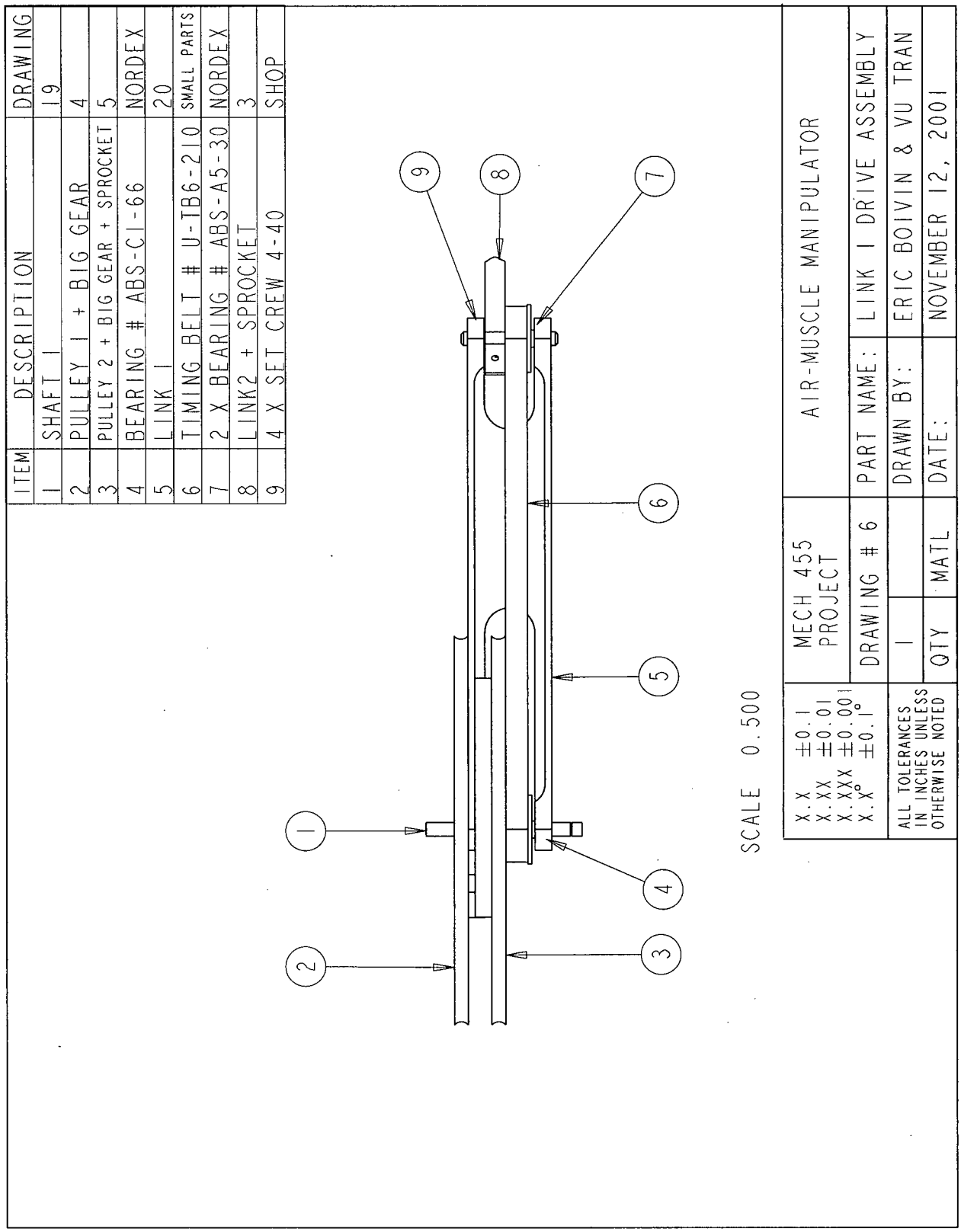

Figure E.6 – Link drive assembly

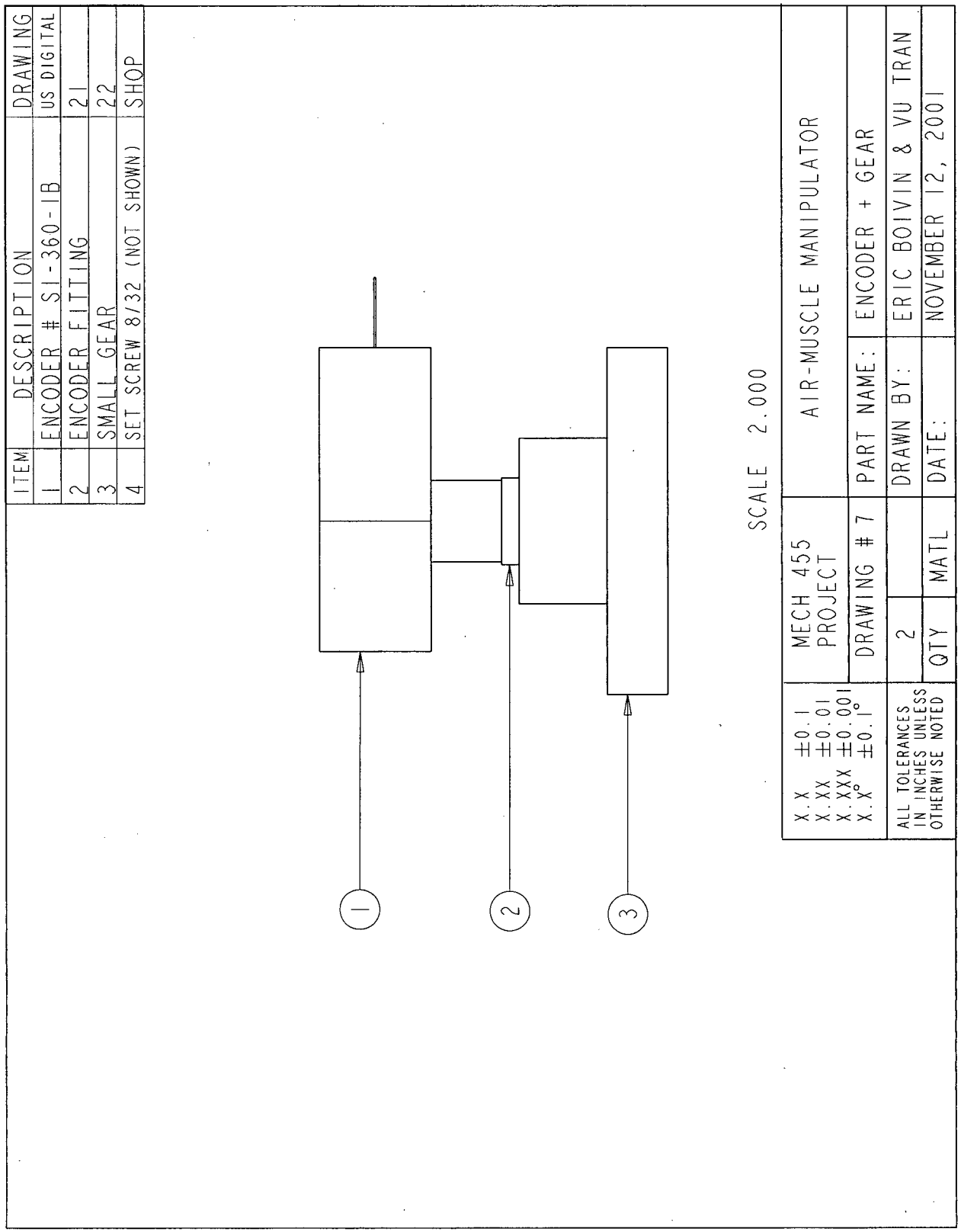

Figure E.7 – Encoder and gear

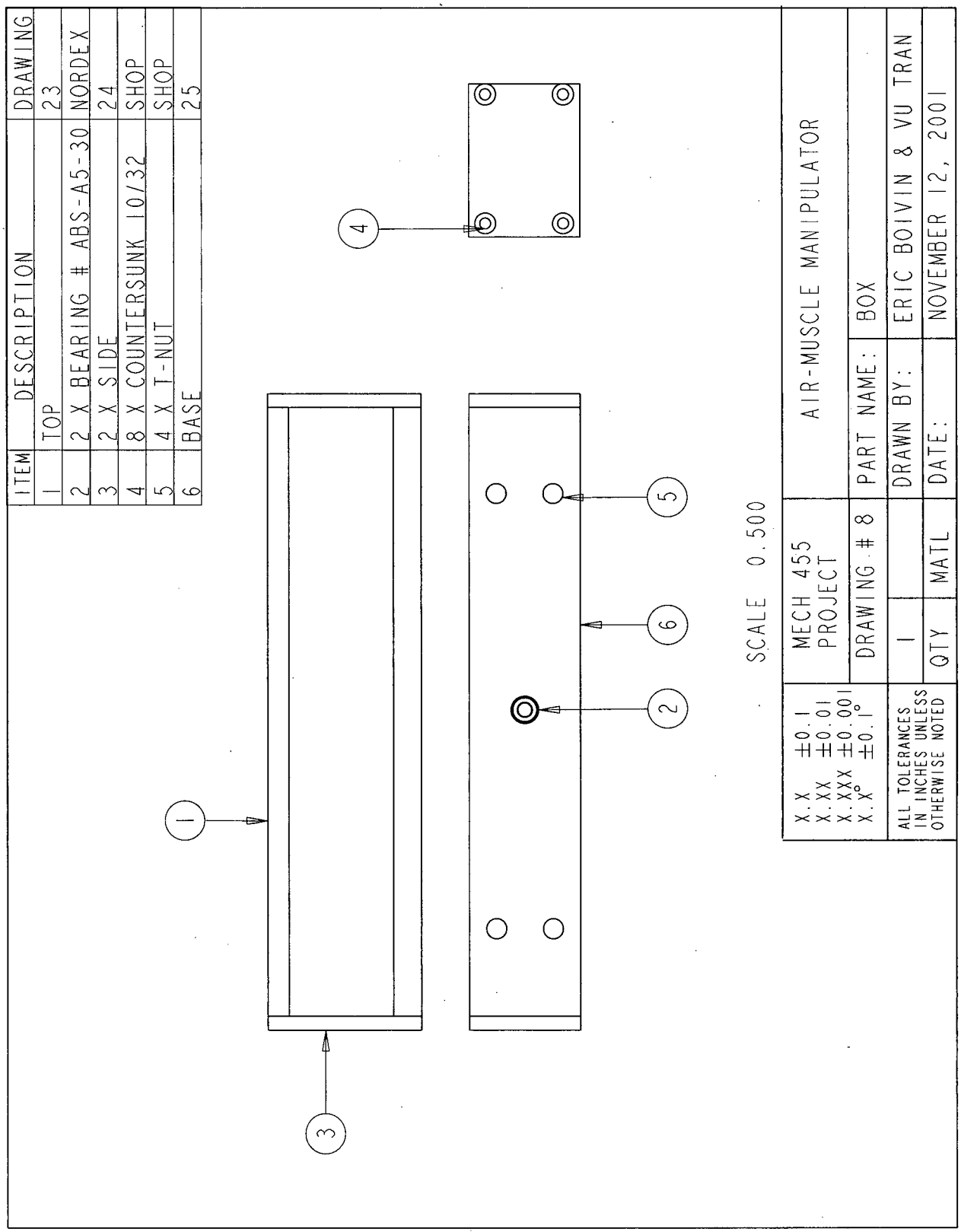

Figure E.8 – Box

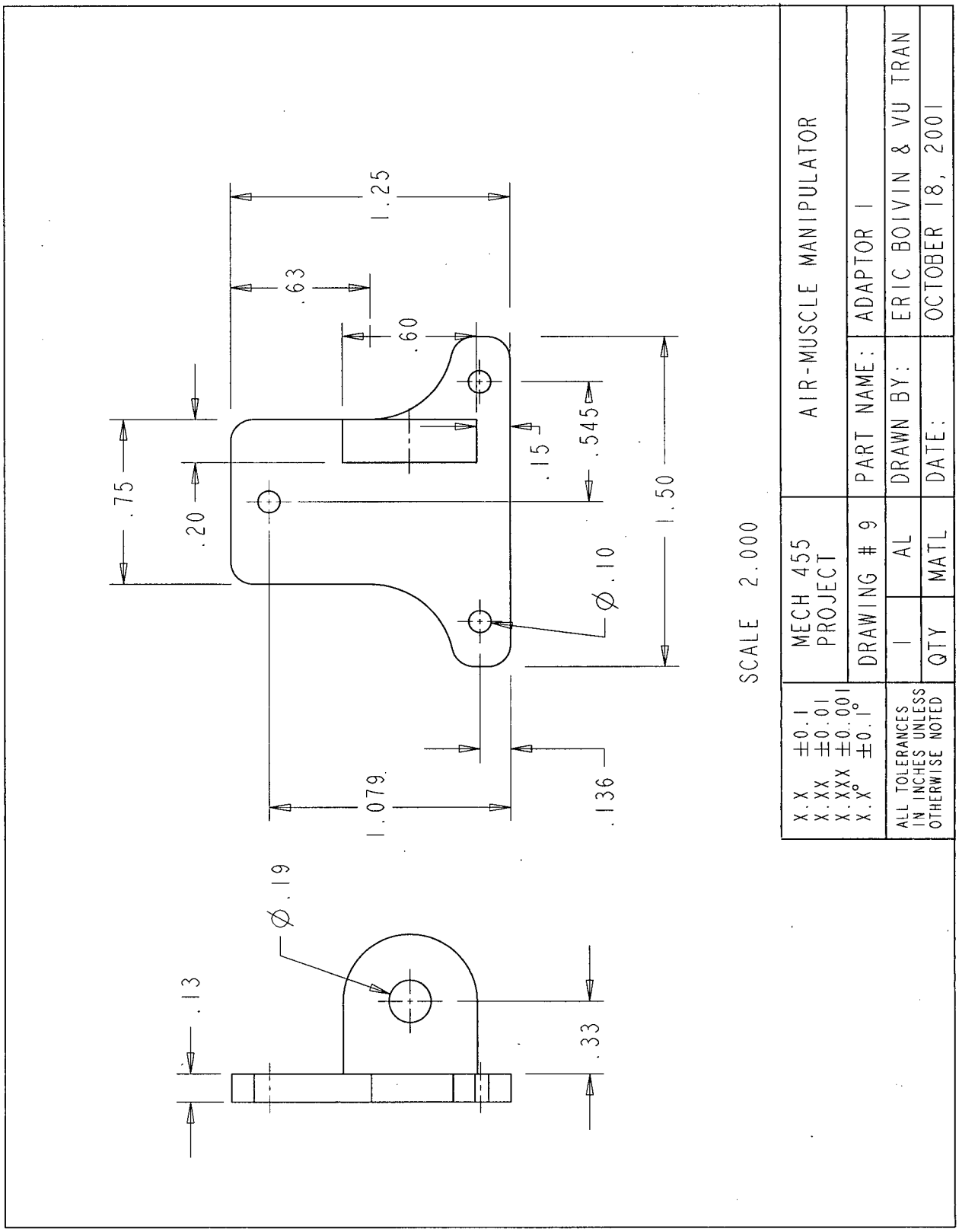

Figure E.9 – Adaptor 1

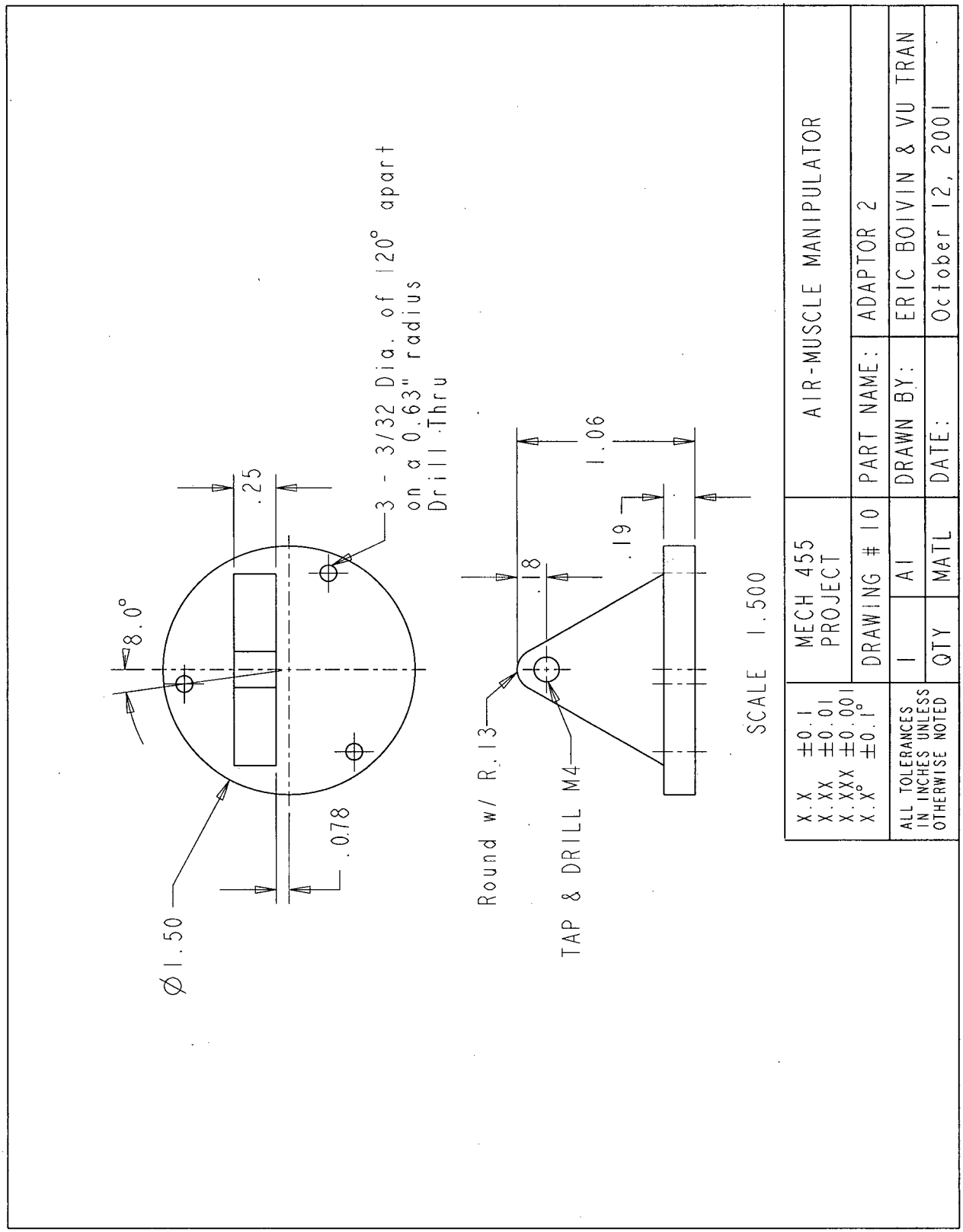

Figure E.10 – Adaptor 2

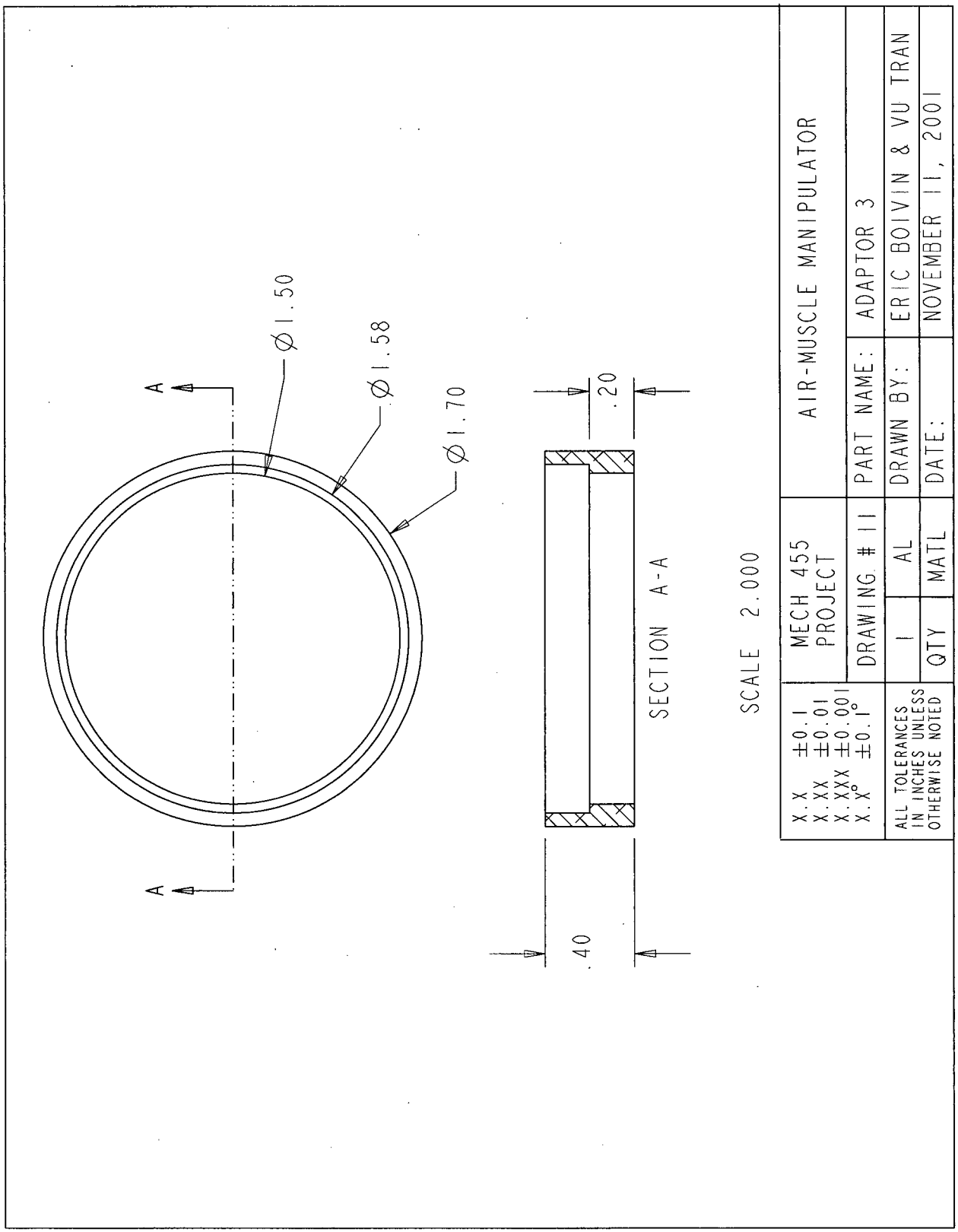

Figure E.11 – Adaptor 3

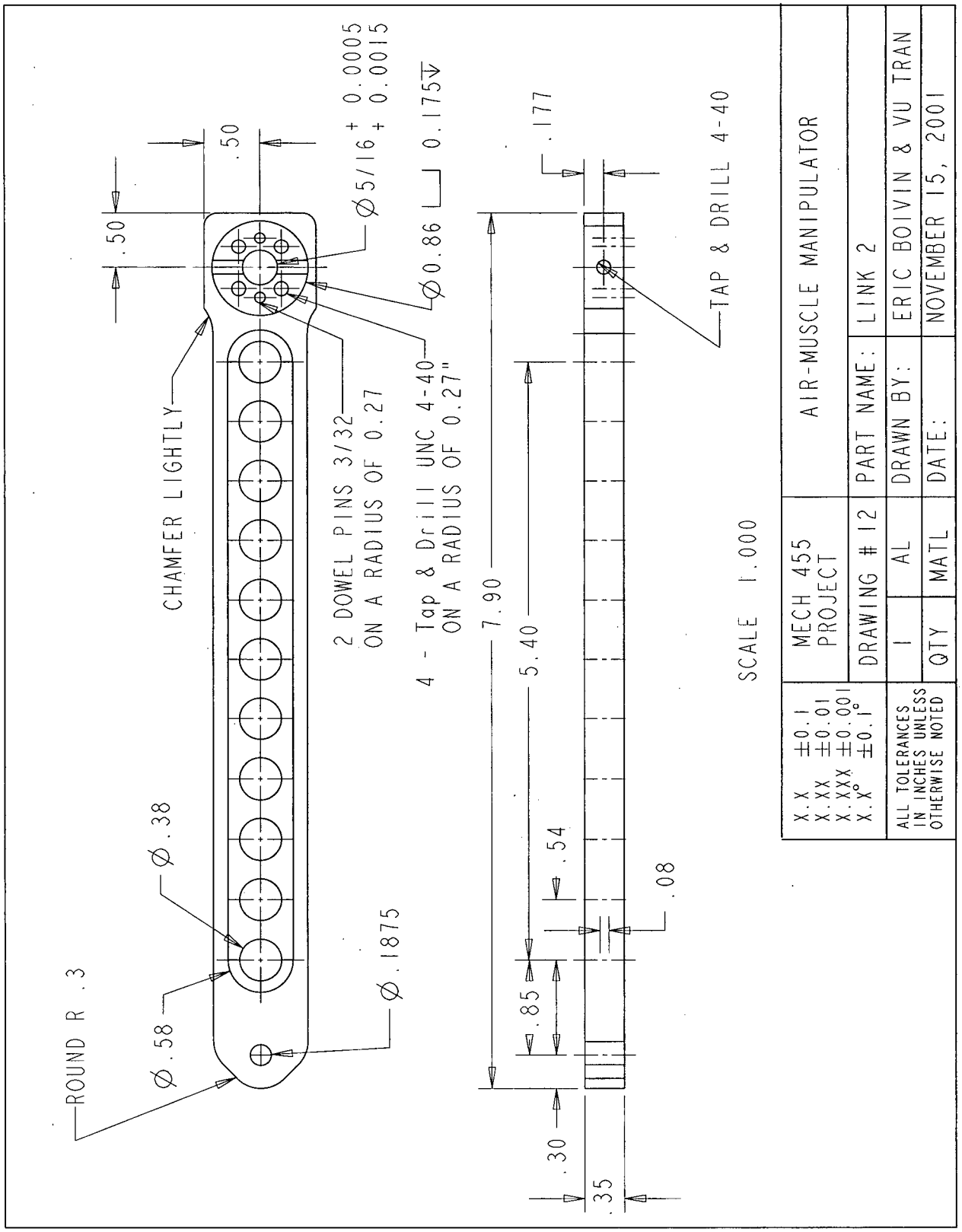

Figure E.12 – Link 2

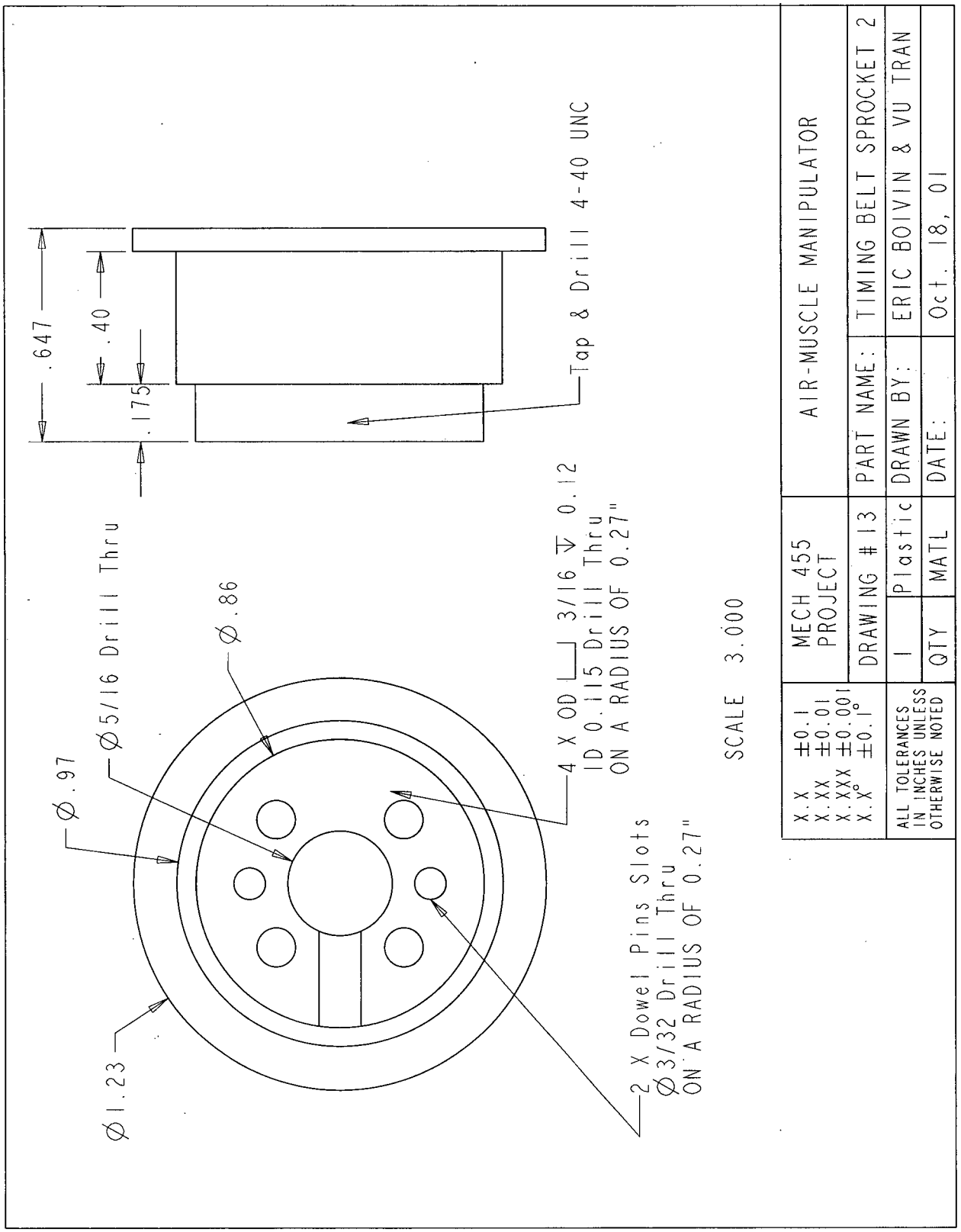

Figure E.13 – Timing belt sprocket 2

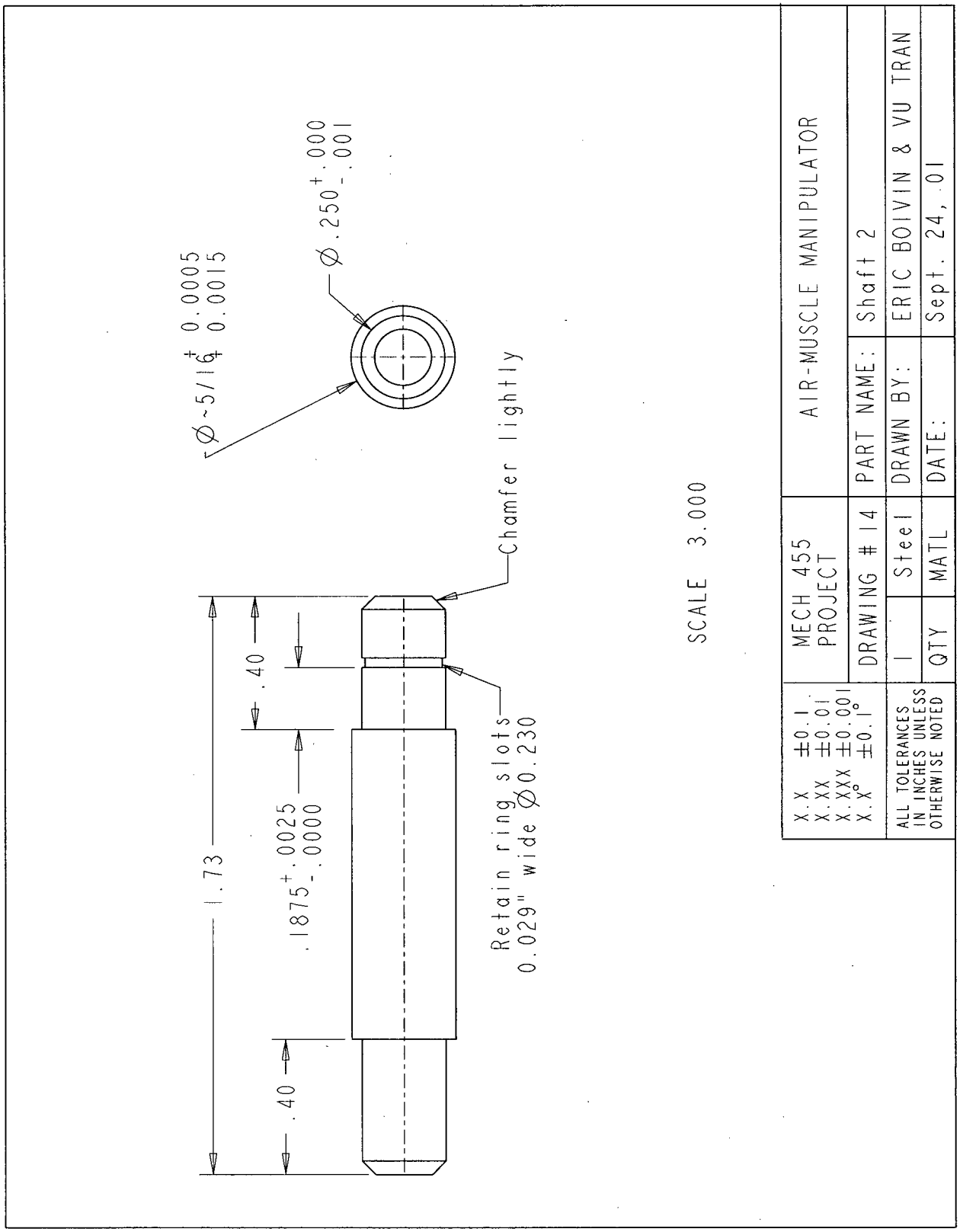

Figure E.14 – Shaft 2

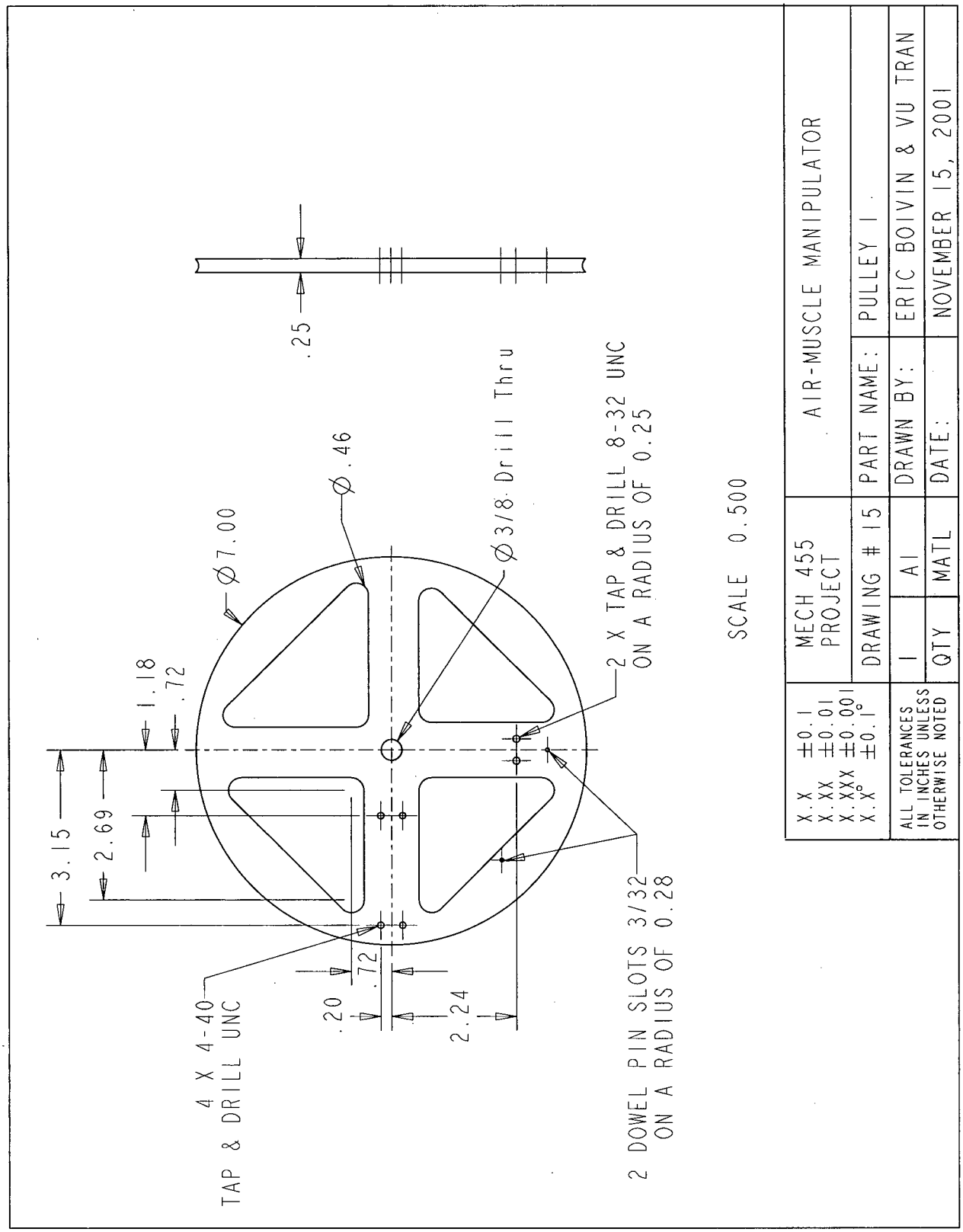

Figure E.15 – Pulley 1

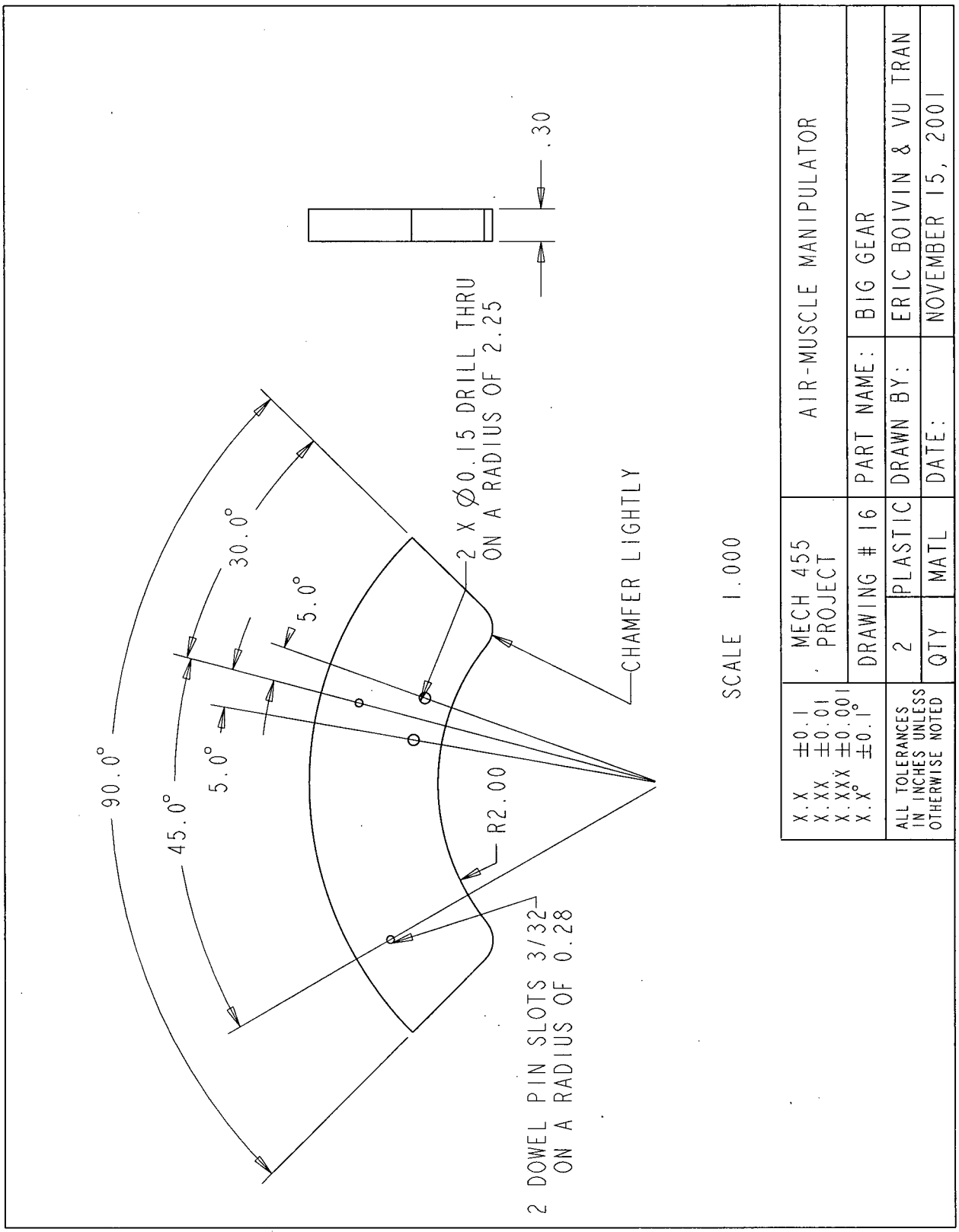

Figure E.16 – Big gear

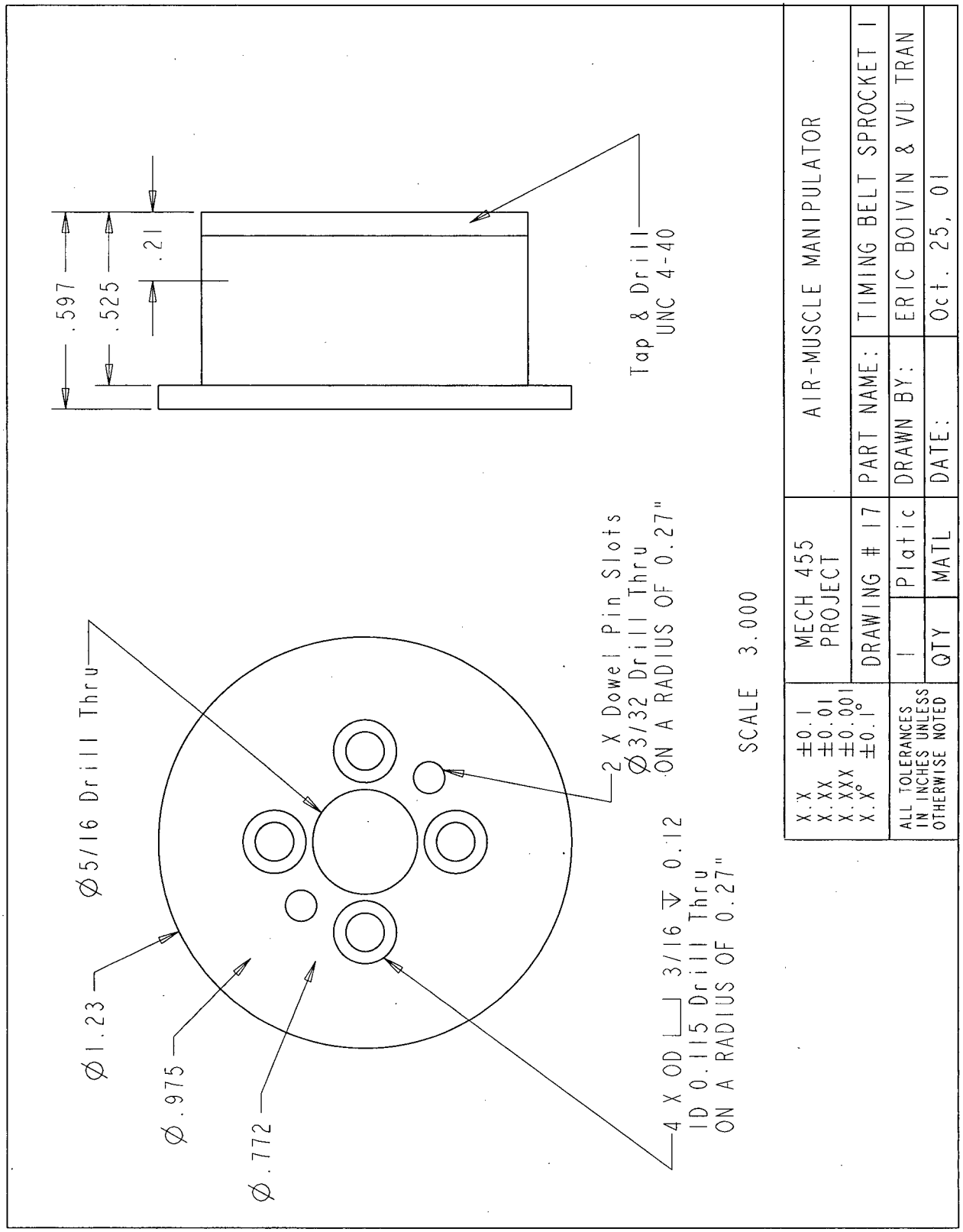

Figure E.17 – Timing belt sprocket 1

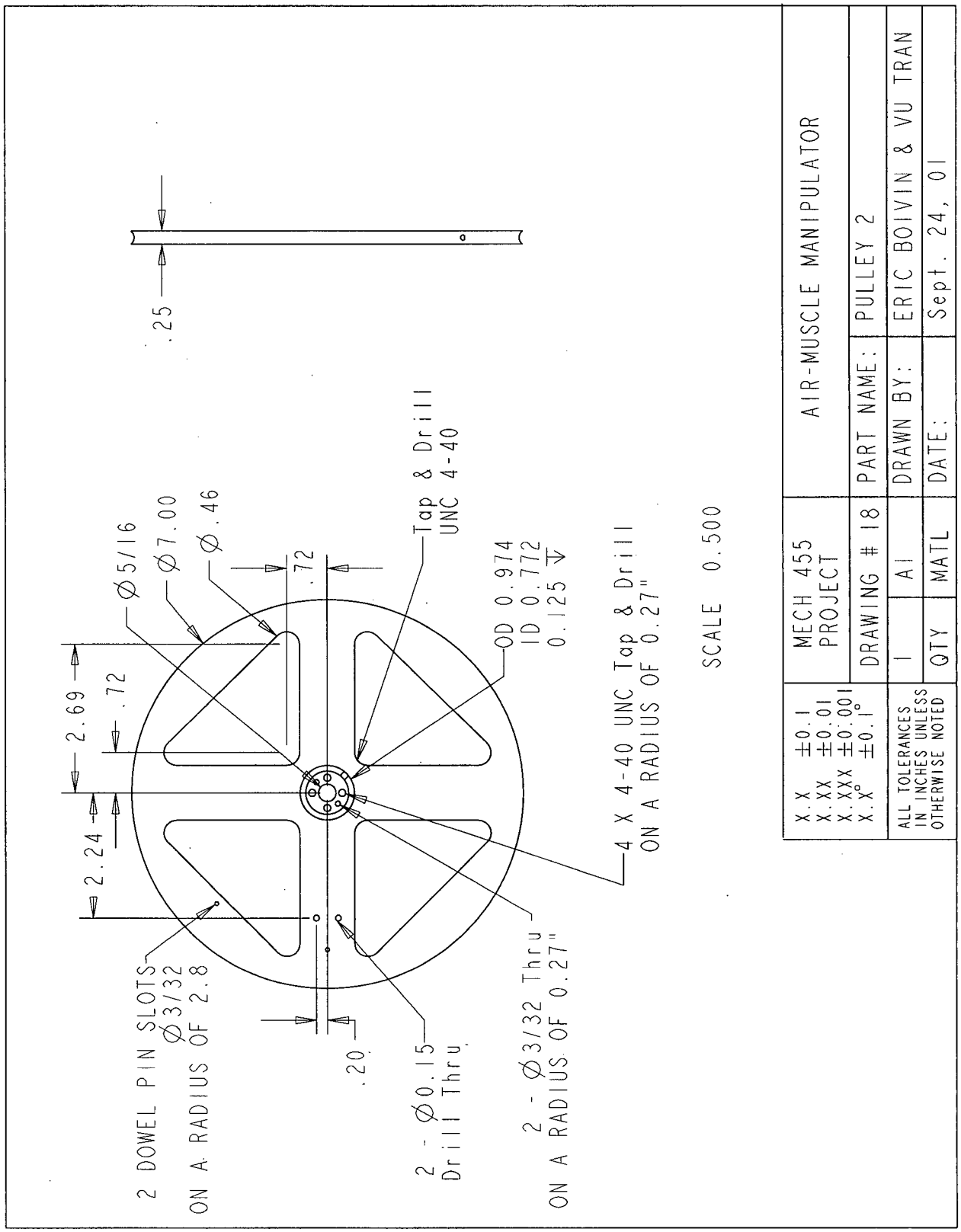

Figure E.18 – Pulley 2

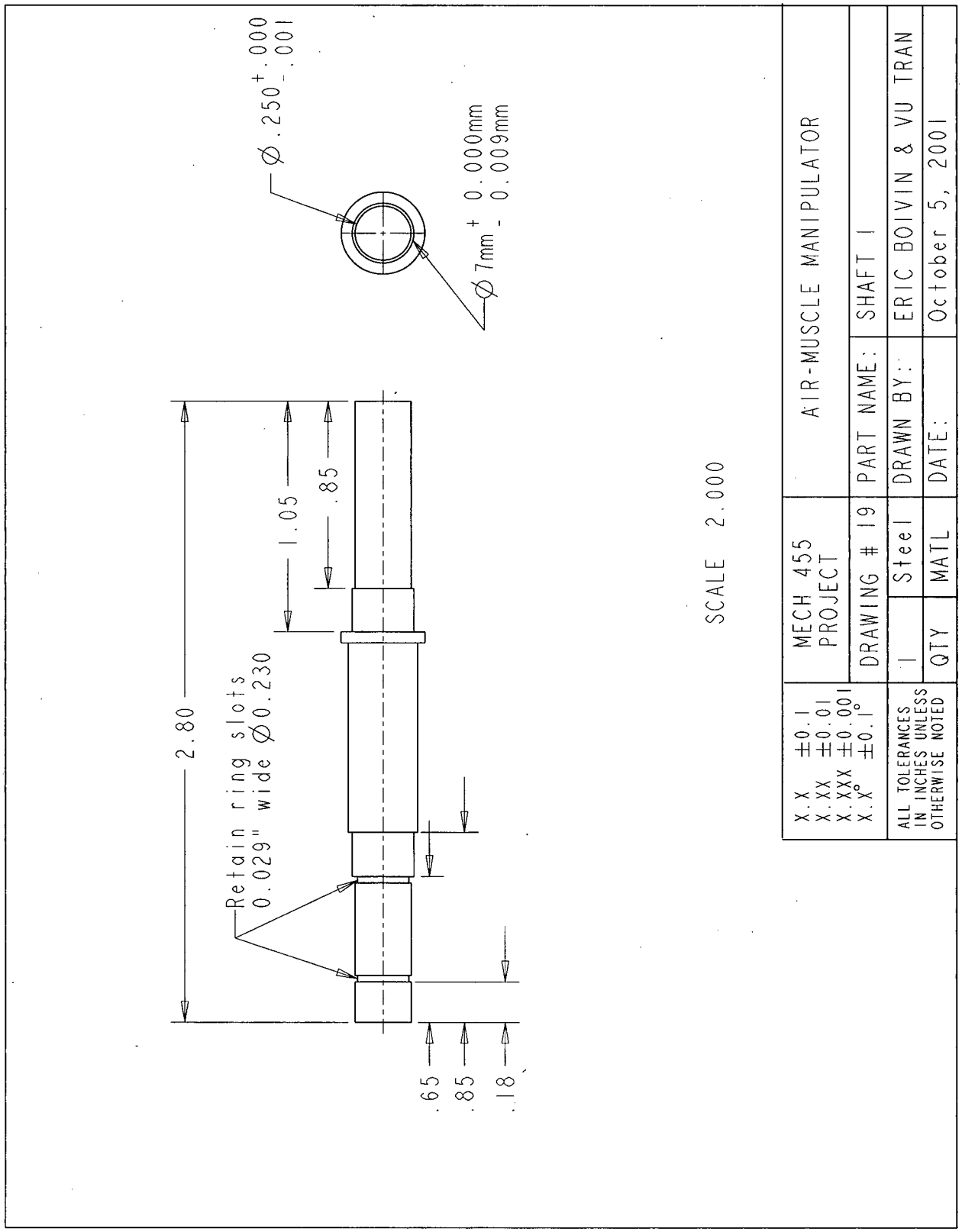

Figure E.19 – Shaft 1

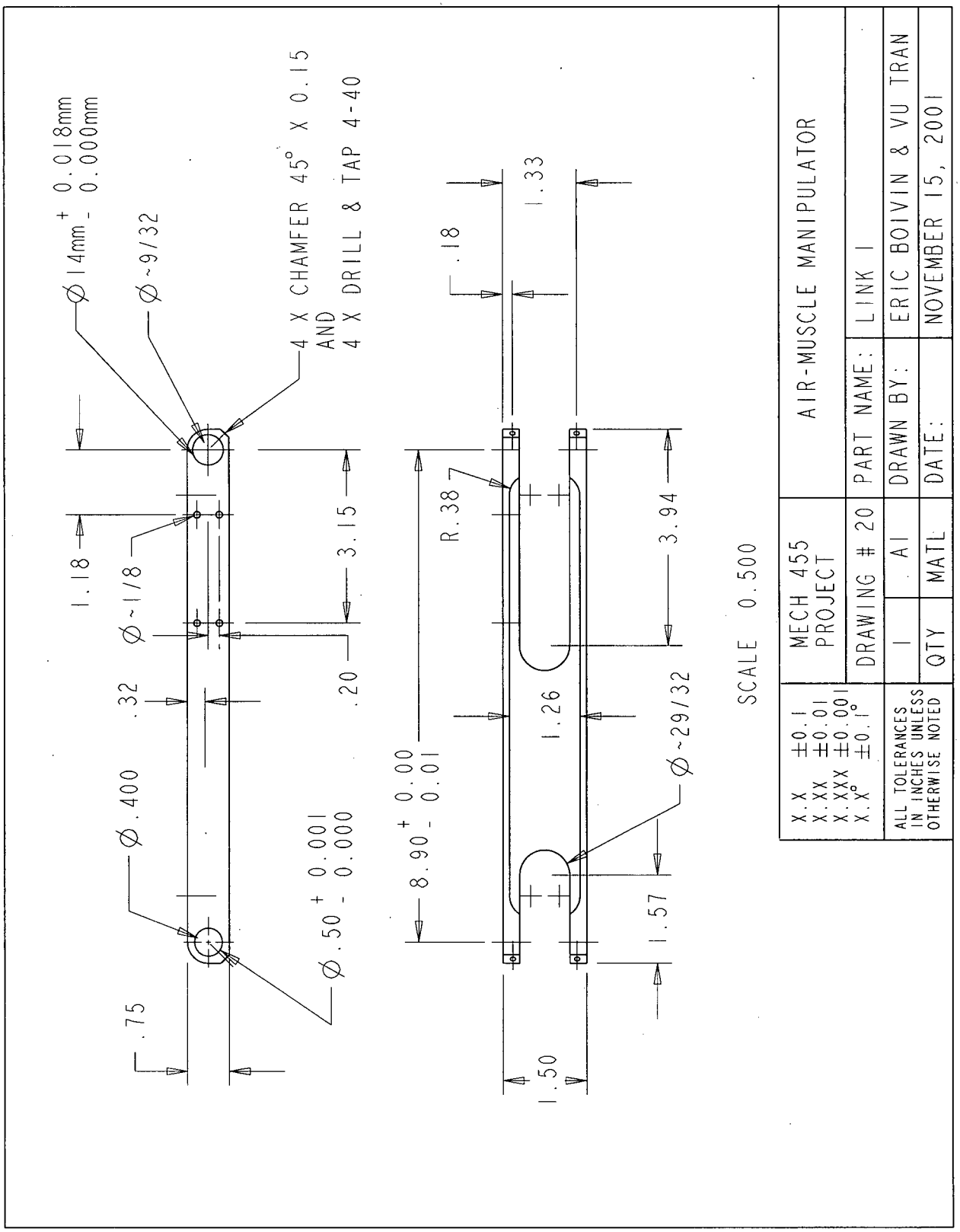

Figure E.20 – Link 1

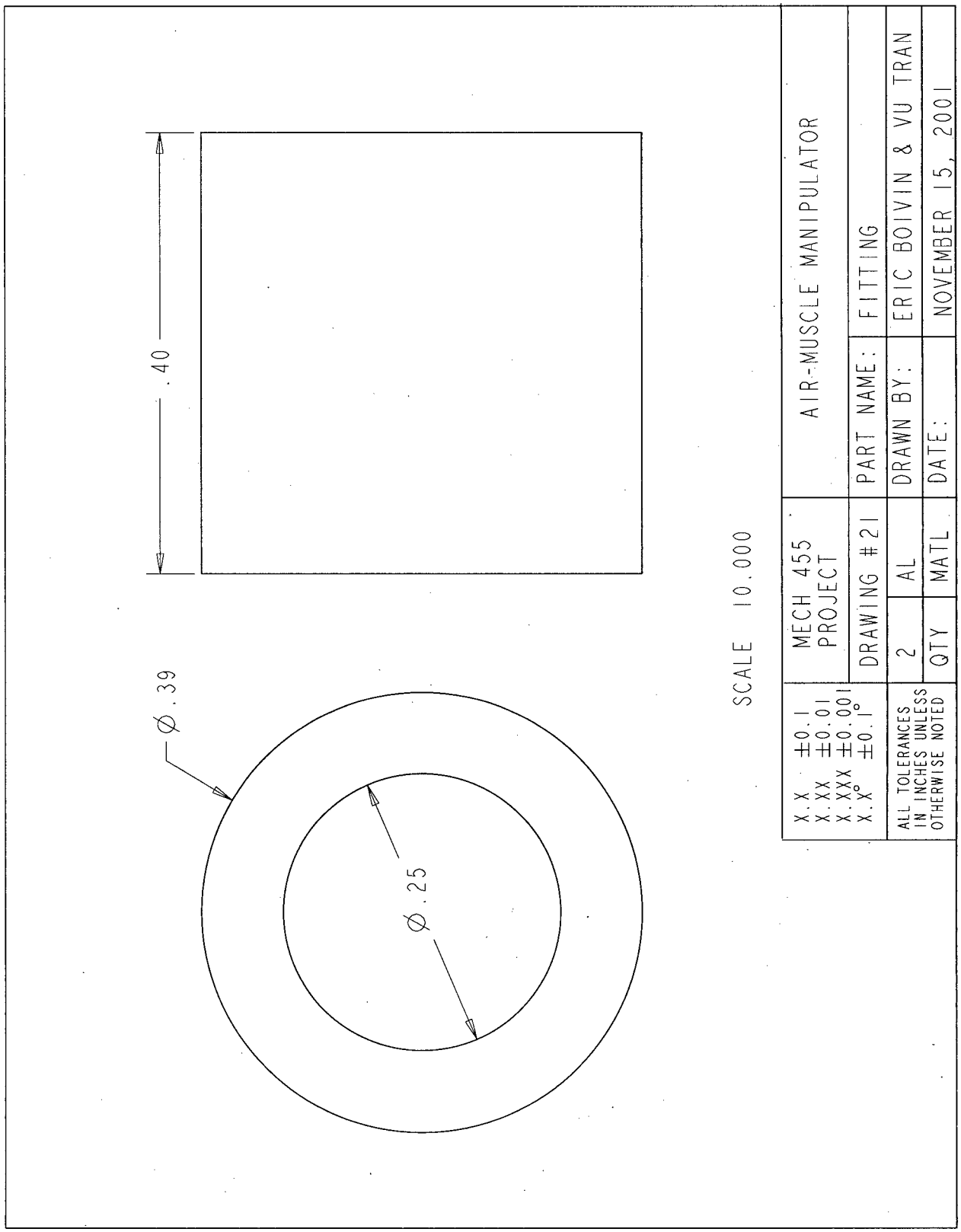

Figure E.21 – Fitting

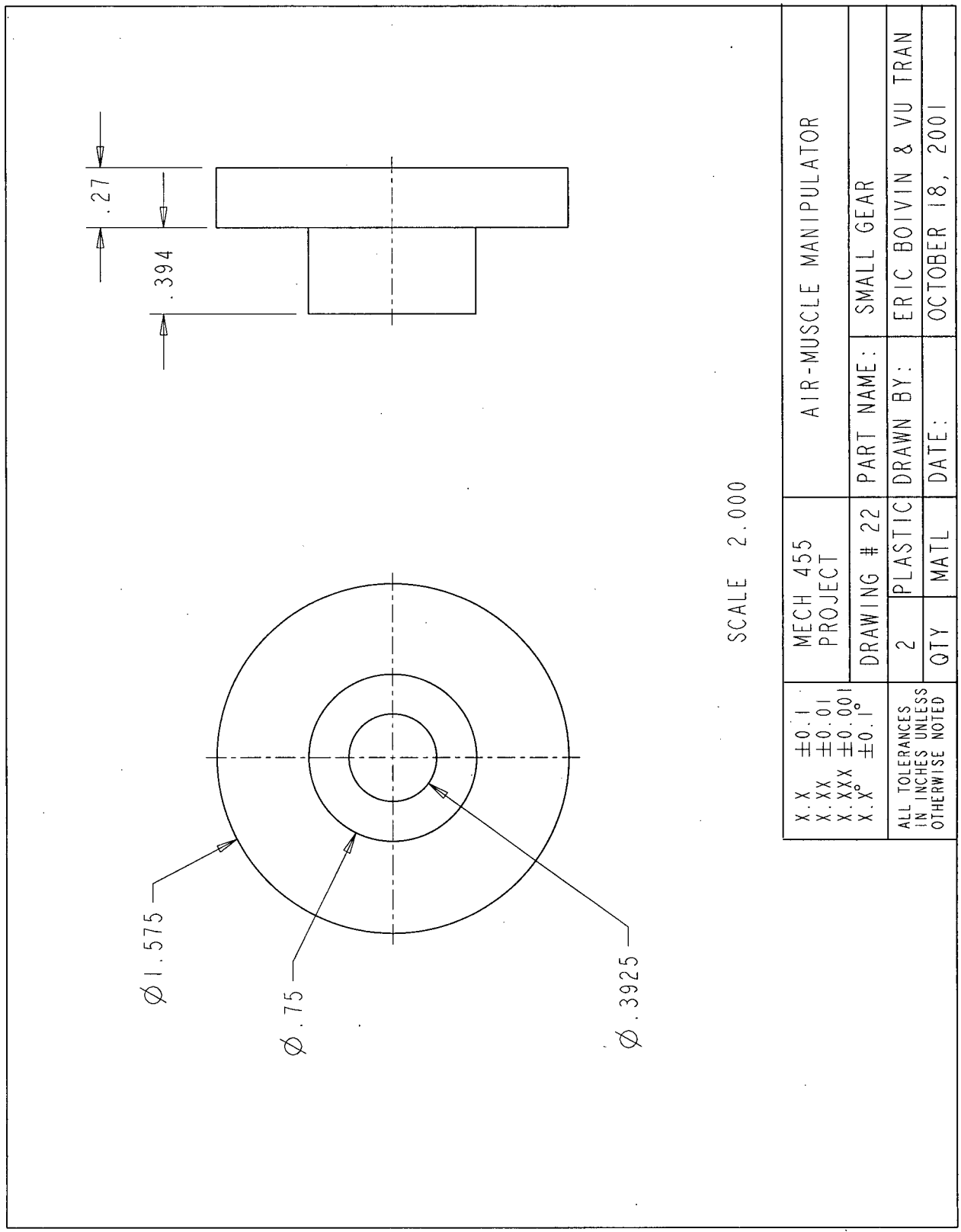

Figure E.22 – Small gear

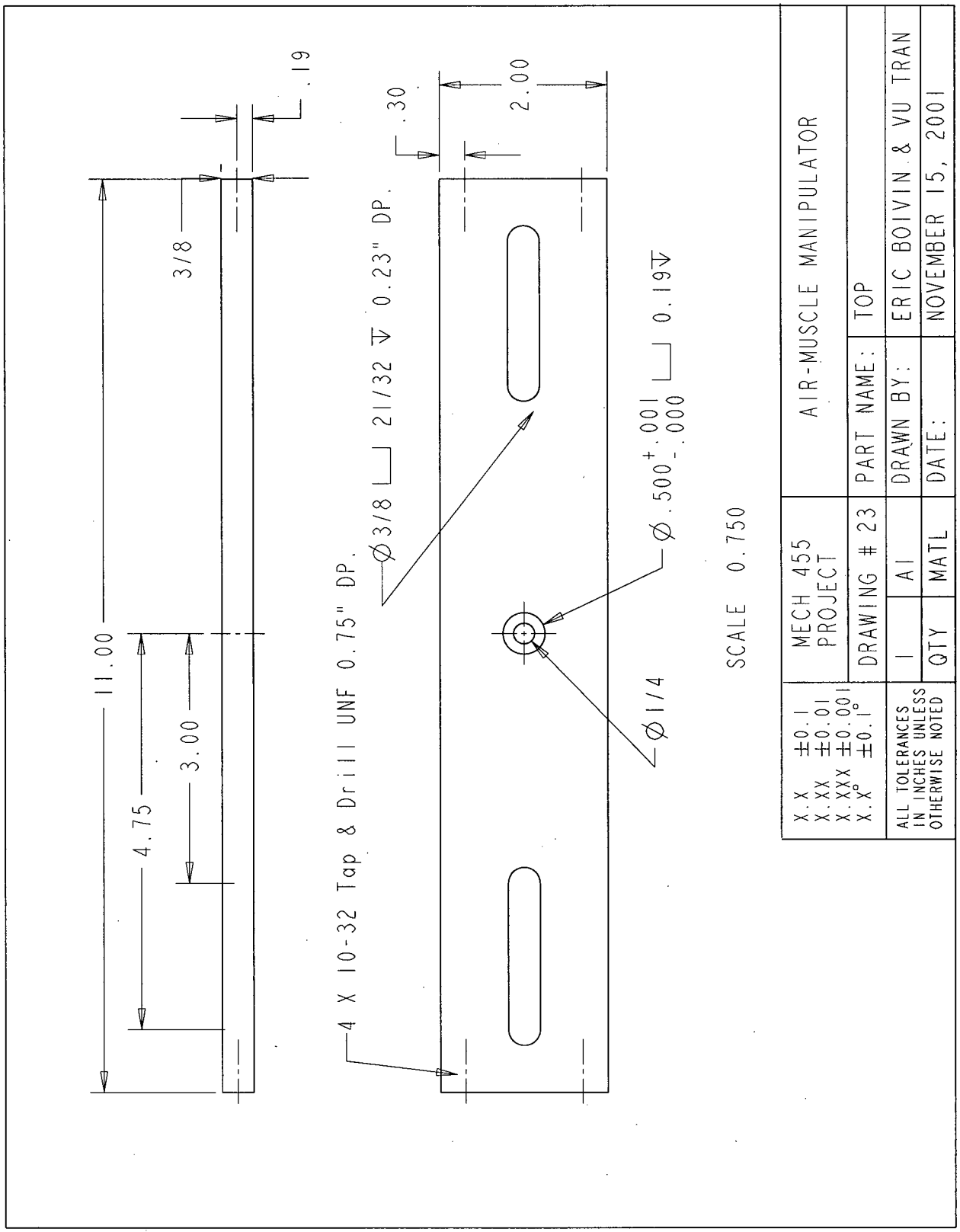

Figure E.23 – Top

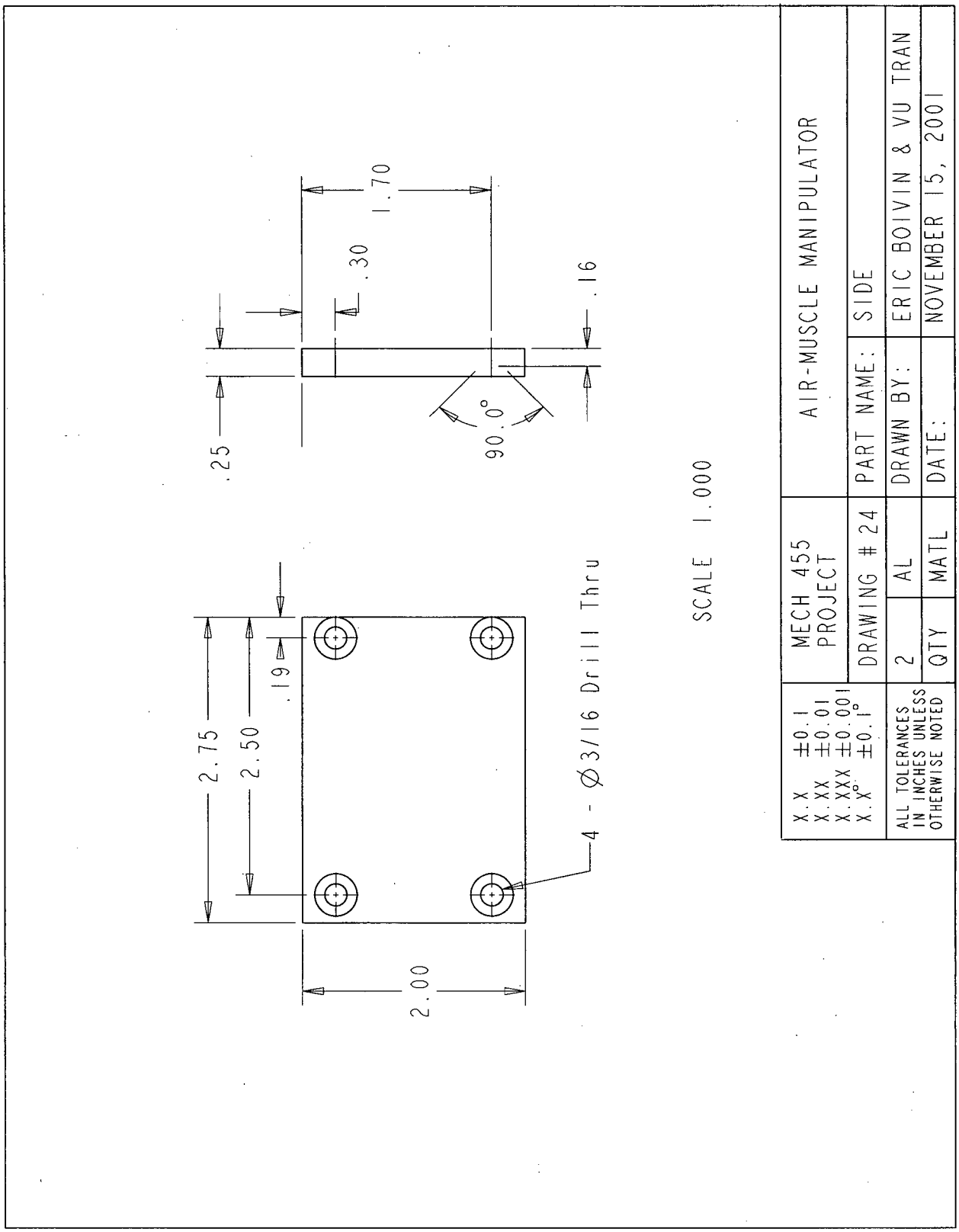

Figure E.24 – Side

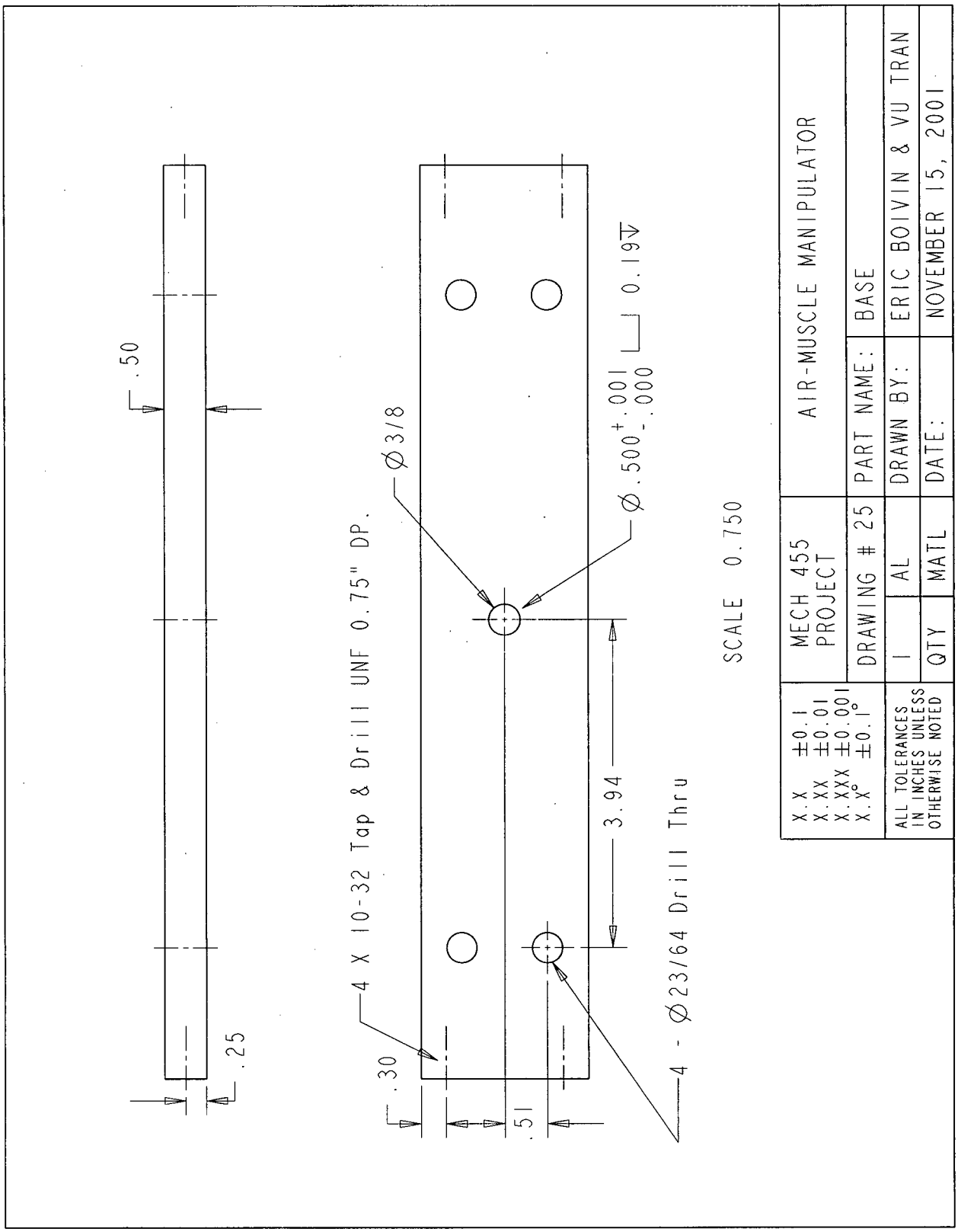

Figure E.25 – Base

Appendix F
Assembly Instructions

Step 1: End Effector (see drawing # 2)

- First attach the back adapter to one side of the force transducer. Use three M3 screws and tight it gently. The adapter can be mounted on any of the two sides and in any of the three different orientations. It would probably be better to use the same configuration every time you want to record data.
- Put the side adapter around the force transducer on the opposite side of the back adapter.
- Insert the front adapter inside the side adapter and fix it with three M3. The back and front adapters must have the same orientation. Once again, tight gently to avoid damaging the expensive force transducer.
- Finally, screw the bearing and its shaft on the front adapter.

Step 2: Link 2 + sprocket (see drawing # 3)

- Insert the timing belt sprocket in link 2. (Note: the hole for shaft 2 is drilled after these two parts are assembled together. Because of that, it is preferable not to take this assembly apart)
- Use four screws and two dowel pins to fasten the link and the sprocket together.
- Don't insert the shaft right now like shown on the drawing.

Step 3: Pulley one + big gear (see drawing # 4)

- First position one of the big gears on pulley 1 using two dowel pins 3/32. Make sure you place it on the right side. If you are not sure which side to choose, you better go trough Step 4 first.
- Fixe the pulley on place with two countersunk screws 8-32.

Step 4: Pulley 2 + sprocket + big gear (see drawing # 5)

- Attach the other big gear on pulley 2 the same way as Step 3.
- Insert the timing belt sprocket in the pulley and fixe it with four 4-40 Allan screws. (Note, you have to make sure that the hole is perpendicular to the pulley)

Step 5: Link 1 drive assembly (see drawing # 6)

Note: before you start this step make sure you have a vice plus a vice-grip. Also make sure all the previous steps are done correctly. Believe me, you don't want to this twice.

- First introduce link 2 in the shorter slot of link 1.
- Insert shaft 2 inside link 2 and the sprocket. The shaft is larger than link 1 and both his tips should be out of the holes. Link 2 and the sprocket are slightly smaller than the slot and should not touch the sides.
- Insert both bearings on shaft 2 inside link 1.
- Put on the belt
- Introduce pulley 2 inside the belt and place it in the larger slot. Both timing belt sprockets should be aligned.
- Orient link 2 correctly according to the big gear on pulley 2. This is to make sure that the gears will not disengage themselves when operating the robot.
- Insert shaft 1 by the upper side. The shoulder of shaft 1 should mate the pulley.
- Insert the metric bearings. This is where you need a vice and some vice-grips. A hammer and your imagination might be useful.
- Finally bolt pulley 1 on link 1, using four Allan screws.
- You can also add 6 set screws: 1 for each bearing and two for link 2.

Step 6: Encoder (see drawing # 7)

- Insert the fitting on the encoder shaft.
- Insert the small gear on the fitting and tight it there with a set screw. If you tight too much you will deform the plastic gear which is not good for the alignment. (Note: this should be done only once the encoder is placed on the top. See step 8)

Step 7: The Box (see drawing # 8)

- First screw the two sides on the base using 4 countersunk screws 10-32. The bearing housing should be on the bottom side.
- Insert shaft 1 (and this includes the two links attached to it) in the base.

- Insert the bearing in its housing.
- Put on the top and screw it with 4 countersunk screws 10-32. The housing should face up.
- Insert the last bearing in the top housing.
- Screw the base on the lab table using 4 T-nuts.

Step 8: Total assembly

- Put the two encoders at their place on the top of the box.
- Put the small gear on (see step 6)
- Bolt the end effector on link 2. It is preferable to use one block washer on each side to avoid slippage. We suggest orienting the end effector with an angle of 20 degrees with link 2.
- Here we do not explain how to mount the air muscles since they might be constructed differently.

Appendix G
Sensors and Calibrations

G.1 Experimental Equipment Specifications

Pneumatic Actuators

Each pneumatic actuator is approximately 33 cm in length. Inside, each consists of rubber surgical tubing (3-mm diameter) and is covered by a tough plastic weave. When the surgical tubing is being inflated, this provides a radial force and the weave contracts, resulting in a decreased length. In addition, the actuators need to be held taut when initially inflated or the tubing inflates non-uniformly against the mesh. These actuators were made in the laboratory with no rigid specifications.

Valves

Solenoid valves: The four Matrix solenoid valves used operate on a pulse width modulation signal. They have a maximum frequency of 200-Hz and their minimum open time is 2-ms. They have three different positions: one to allow for air to be supplied to the actuator, a second to serve as an outlet for air from the actuator to the atmosphere, and a third closed position where no air is exchanged.

Force Transducer

The Precision Transducers force transducer used has a capacity of 50 kg. It has tapped holes on either end, which were used to attach it to a flat plate on which the applied force was impressed, and to the base.

Pressure Transducers

There were two each of two types of pressure transducers. The transducers by Sensotec have a range of 150 psig and came with calibration papers. AutoTran transducers have a minimum range of 100 psi and a 1% accuracy.

Length Encoders

The US Digital length optical encoders measure real-time shaft angle. In the initial set-up they were attached directly to the shaft of the pulley. In the final set-up they were attached to the shafts of toothed gears that meshed with gears on the respective pulleys. Coupled with the gears, they provide ¼ degree of precision on the link position.

Manipulator

The manipulator is a two-link arm that is controlled by two pulleys mounted on a single shaft. The rotation of one pulley translates to the rotation of one link in the same plane of motion. The inner link is directly attached to its pulley and the second link is attached at the end of the first link with freedom to rotate. A high-torque timing belt transmits the force and motion from the second pulley to the second link. By rotating the pulleys, the linkage assembly performs simulated wiping motions. The manipulator was constructed from aluminum. The pulleys are 18 cm in diameter and have a thickness of 0.64 cm. The link directly attached to the pulley is 22.5 cm long and the second link is 18 cm. The links are also 0.64 cm in thickness.

Voltmeter

The Fluke 8010A digital multimeter was used to read out the voltage while doing calibrations.

Digital Scale

Weighing of all of the components used in the calibration of the force transducer was done by a Toledo SM-F digital scale. The accuracy was one tenth of a gram.

G.1.1 Solenoid Valves

Matrix Solenoid Valve Model 821 3/3 NC, Identification code GNK821203C3KK
3 Port, 3 Way High Frequency Valve
www.matrix.to.it/pd009.htm

Description - The Pneumatic Solenoid Valves 820 Series
The research about materials and new technological solutions allowed the realization of a shutter solenoid valve with an extremely simple operation principle and with avant-garde dynamic characteristics. The mass of the moving elements has been reduced to the minimum and every inner friction has been eliminated: in this way, we obtained response times of milliseconds and an operation life over 500 million cycles.

Due to the possibility of controls of speed-up type, their dynamic characteristics are even more improved. Standard solenoid valves with 24 VDC control have a response time lower than 5 ms in opening and 2 ms in closing, with a maximum operation frequency of 200 Hz. On the contrary, solenoid valves with speed-up control have a response time lower than 1 ms, both in opening and in closing, with a maximum operation frequency of 500 Hz.

Besides high-speed characteristics, solenoid valves 820 Series offer flow rate values up to 180 dm3/min (ANR), with feeding pressure from 0 to 8 bar. Controlling the valve through either PWM or PFM techniques, it is possible to vary the passing flow rate and to obtain, in this way, a solenoid valve having a proportional flow rate.

General Characteristics

{PRIVATE "TYPE=PICT;ALT=Pneumatic scheme"}Control Direct - PFM - PWM

Type and function	3/3 NC	
Dimensions (mm)	24.2 x 37 x 48.5	
Fluid	Non-lubricated dry air, neutral gases (-10 +50 °C)	
Filtration rating	Min 40 micron	
Temperature	-10 +50 °C (standard version)	
Response time in opening	24 < 6ms	XX / KK < 3 ms
Response time in closing	24 < 2 ms	XX / KK < 1 ms
Maximum frequency	100 Hz	200 Hz
Weight	130 g	
Product life expectancy	≥ 500 Mls cycles	
Flow rate (at 6 bar)	90 Nl/min - Control tension XX / KK	
No. Outlets	1 Outlet	
No. Electrical controls	2 Controls	
Port connection	Integrated cables IP 62 L = 500mm / 100mm	
Control tension	Speed-up in tension (24VDC) 0.8 W	
Operating pressure	0 - 8 bar	

Materials

Body in PPS, Flanges in Al, Seals in NB

G.1.2 Sensotec Pressure Transducers

Sensotec Model LM 150, serial numbers 70258, 702583
150psig range
www.sensotec.com/pdf/lm.pdf

Sensotec offers the Model LM pressure transducer as a low cost alternative with good performance for high volume applications. Each unit is constructed of welded stainless steel for durability in dry rugged environments. Both gas and liquid pressure overloads of up to 50% over capacity are safely accepted.

Performance	Pressure Range	150psig
	Accuracy (min.)	±0.5% F.S.
Output	1.8mV/V (nom)	
Resolution	infinite	
Environmental	Temperature, Operating	-65°F to 250°F
Temperature, Compensated	60°F to 160°F	
Temperature Effect*		
-Zero (max.)	0.01% F.S./°F	
-Span (max)	0.02% Rdg/°F	
Electrical	Input	10VDC
	Bridge Resistance	350 ohms**
	Electrical Termination (std.)	Cable 3 ft.
Mechanical	Media	Gas, Liquid
	Overload-Safe	50% over capacity
	Pressure Port	¼-18NPT female
	Wetted Parts Material	Stainless steel
	Type	Gage
	Case Material	Stainless steel

* Consult Sensotec on units below 150psi
** 5000 ohm below 150psi

G.1.3 AutoTran Pressure Transducers

Autotran Model 250G, serial numbers 8-B6107213 and 8-B6107156
100psi range
www.autotraninc.com/specs/250g.html

The series 250G is machined from a solid piece of stainless steel and employs a micromachined piezoresistive strain gage fused with high temperature glass to a stainless steel diaphragm. This design provides an exceptionally stable sensor ideal for use in a wide variety of applications. There are no welds, no O-rings, and no silicone oil to leak and cause potential problems. This is a truly tough and compact pressure transducer that comes in a 2-wire, 4-20mA version, or a 3-wire, 1-5V version.

Specifications

{PRIVATE} Pressure Range:	0 to 100 PSI (0 to 7 Bar)
Accuracy:	< 1% of FS
Stability:	+/- 0.25% FS typical
Thermal Effects:	< +/-2% of FS
Compensated Range:	30 to 130 degrees F (0 to 55 degrees C)
Operating Temperature:	-4 to 185 degrees F (-20 to 85 degrees C)
Media Compatibility:	Any media wet or dry compatible with 17-4 PH stainless steel
Input Supply:	10-30 VDC
Supply Current:	10mA maximum (for voltage output)
Load Resistance (Voltage Output):	5K ohm
Load Resistance (Current Output):	1.1K ohm
Output Signal:	1 to 5 VDC, 4 to 20mA two wire
Zero Offset:	+/- 2%
Electrical Connection:	24" 3-wire cable (1-5V), 24" 2-wire cable (4-20mA)
Housing:	Solid one piece 17-4 PH stainless steel
Connections:	¼" NPT
Dimensions:	2.2" L x 7/8" Dia (54.8 mmL x 21.4 mmDia)

G.1.4 Force Transducer

PT (Precision Transducers) Model ST 5, serial number 65266
50kg capacity
www.precisiontransducers.com/pdf/product/ST_SERIES.pdf

Features

- tension and compression universal loading
-compact, lightweight, and easy to handle
-temperature compensation, both zero and span
-compatible with international standard fixings
- tool steel design for high accuracy
- N.S.C. approved models
-electroless nickel plated
- moisture protected
-can be used for multi-point weighing or scale conversion
-full range of mounting accessories (refer over)

Specifications

Nominal capacity	50kg
Nominal output at capacity	2mV/V ± 0.1%
Factory calibration mode	compression
Linearity error	0.017%
Repeatability	0.01%
Zero return, creep (30mins)	0.015%
Temp. effect span/10 deg. C	0.01%
Temp. effect zero/10 deg. C	0.015%
Insulation resistance – brg. to gnd	>5000 M ohms
Insulation resistance – cbl. to gnd	>1000 M ohms
Compensated temp. range	-10 to 50 deg. C
Output resistance	352.2 ohms
Input resistance	410 ohms nominal
Service load	100% of capacity
Safe load	150% of capacity
Mechanical failure	>300% of capacity
Recommended excitation	5V to 15V ac/dc
Maximum excitation	15V dc
Environmental protection	IP65

G.1.5 Length Encoders

US Digital Corp. S1 series Model S1-360-IB
www.usdigital.com/products/s1s2

Features

-2-channel quadrature, TTL square wave outputs
- -40 to +100°C operating temperature
-Tracks from 0 to 100,000 cycles/sec
-Ball bearing option tracks to 10,000 RPM
-Small size
- Low cost
- Single +5V supply
-3rd channel index option

Description

The S1 and S2 series optical shaft encoders are non-contacting rotary to digital converters. Useful for position feedback or manual interface, the encoders convert real-time shaft angle, speed, and direction into TTL-compatible quadrature outputs with or without index. The encoders utilize an unbreakable mylar disk, metal shaft and bushing, LED light source, and monolithic electronics. They may operate from a single +5VDC supply. The S1 and S2 encoders are available with ball bearings for motion control applications or torque-loaded to feel like a potentiometer for front-panel manual interface.

Mechanical Notes

	Ball Bearing:	Sleeve Bushing
{PRIVATE}Acceleration	10,000 rad/sec²	10,000 rad/sec²
Vibration	20 g. 5 to 2KHz	20 g. 5 to 2Khz
Shaft Speed	10,000 RPM max. continuous	100 RPM max. continuous
Shaft Rotation	N/A	Continuous & reversible
Acceleration	50K rad/sec²	N/A
Shaft Torque	0.05 in. oz. max.	0.5 ±0.2 in. oz.
Shaft Loading	1 lb. max.	2 lbs. max. dynamic 20 lbs. max. static
Bearing Life	(40/P) = Life in millions of revs. where P = Radial load in pounds.	N/A
Weight	0.7 oz.	0.7 oz.
Shaft Runout	0.0015 T.I.R. max.	0.0015 T.I.R. max.

Materials & Mounting:

{PRIVATE}Shaft	Brass or stainless
Bushing	Brass
Connector	Gold plated
Hole Diameter	0.375 in. +0.005 - 0
Panel Thickness	0.125 in. max.
Panel Nut Max. Torque	20 in.-lbs.

G.2 Calibration of Equipment

G.2.1 Calibration of Sensotec Pressure Transducers

Sensotec model: LM/2345-03
Serial Number: 702583
Certificate of Calibration
Calibrated at 150 psig
Excited voltage = 10V
Shunt Resistor = 59 ohms
Calibration = 1.7557 mV/V
Shunt Calibration = 1.4851 mV/V
Data taken with Fluke Digital Multimeter (03/13/02): offset = -2.52 V shunt = 4.01 V
current shunt resistance = 87.325 ohms excitation voltage = 8 V
Calculations:
Current shunt calibration = (59 ohms/ 87.325 ohms)*(1.4851 mV/V) =1.003388 mV/V
Current shunt pressure = (1.003388 mV/V/ 1.7557 mV/V)*(150 psig) = 85.725 psig
Calibration Equation: V = offset + P*calibration*8*G/150 psig => G is factor to be determined
4.01 V = - 2.52 + 85.725*1.7557*8*G/150 => G = 0.813498
Therefore inverted calibration curve with gain and offset for ORTS:
Pressure (psig) = 13.12787*Voltage (V) + 33.0822

Sensotec model: LM/2345-03
Serial Number: 702581
Certificate of Calibration
Calibrated at 150 psig
Excited voltage = 10V
Shunt Resistor = 59 ohms
Calibration = 1.6228 mV/V
Shunt Calibration = 1.4843 mV/V
Data taken with Fluke Digital Multimeter (03/19/02): offset = -2.29 V shunt = 4.40 V
current shunt resistance = 87.325 ohms excitation voltage = 8 V
Calculations:
Current shunt calibration = (59 ohms/ 87.325 ohms)*(1.4843 mV/V) =1.002274 mV/V
Current shunt pressure = (1.002274 mV/V/ 1.6228 mV/V)*(150 psig) = 92.643 psig
Calibration Equation: V = offset + P*calibration*8*G/150 psig => G is factor to be determined
4.01 V = - 2.52 + 85.725*1.6228*8*G/150 => G = 0.83435
Therefore inverted calibration curve with gain and offset for ORTS:
Pressure (psig) = 13.84804*Voltage (V) + 31.712

G.2.2 Calibration of Auto Tran Pressure Transducers

Voltage #2: Auto Tran Inc. SN: 8-B6107213
Voltage #3: Auto Tran Inc. SN: 8-B6107156
Voltage #4: Sensotec SN: 702581
Pressure #4: Pressure calculated using the above calibration equation for Sensotec SN: 702581

Pressure	Voltage(#4)	Pressure(#4)	Voltage(#2)	Voltage(#3)
0	-2.29	0	-1.13	-1.1
10	-1.52	10.66905545	-1.58	-1.54
20	-0.84	20.09107844	-2.01	-1.97
30	-0.14	29.79021976	-2.37	-2.35
40	0.56	39.48936107	-2.87	-2.84
50	1.41	51.26688982	-3.4	-3.38
60	2.08	60.55035365	-3.82	-3.8
70	2.94	72.46644155	-4.36	-4.35
80	3.52	80.50287293	-4.71	-4.7
Results: (V, psi)				
Pressure(#2) = -22.314*Voltage(V) - 24.548				
Pressure(#3) = -22.145*Voltage(V) - 23.511				

The resultant calibration equations are linear best fits done automatically in Excel. Note that the pressure is measured in psig.

G.2.3 Calibration of Precision Transducers Force Transducer

The variety of weights used to calibrate in compression:

Part #	Part Mass (g)	Part weight(N)
#1	2709.7	26.582157
#4	3059.5	30.013695
#6	1653.2	16.217892
#11	1198.8	11.760228
#12	525.7	5.157117

		03/19/02	
part #	Weight(N)	voltmeter(V)	w/ horizontal shift (V)
none	0	2.47	2.51
12	5.157117	2.31	2.35
11	11.760228	2.1	2.14
6	16.217892	1.96	2
12+6	21.375009	1.79	1.83
1	26.582157	1.63	1.67
4	30.013695	1.52	1.56
4+12	35.170812	1.35	1.39
4+11	41.773923	1.14	1.18

The orientation of the transducer is horizontal but it was vertical for the measurements of compression under the given weight. Therefore, the right column accounts for a shift in the voltages.
The final calibration equation is: Force (N) = -31.374*Voltage (V) + 78.867

G.2.4 Calibration of US Digital Length Encoders

These are the measured lengths of each actuator at the starting position (end pt.1) and at the end position (end pt. 2)

	length (m)	
muscle	end pt.1(offset)	end pt. 2
M1	0.302	0.388
M2	0.363	0.33
M3	0.366	0.39
M4	0.412	0.326

The offset is the length at the starting position. The gain was determined by comparison with previous calibration data.

Previous calibration data		
	length(m)	
muscle	end pt.1(offset)	slope
M1	0.536254	0.0002638
M2	0.3304	-0.0001
M3	0.374916	0.0001
M4	0.3235	-0.0001

Slope = previous slope * (actual difference in length)/(perceived difference in length)

Sample Calculation:
Slope of M1 = 0.0002638*(0.388-0.302)/(0.536254–0.302) = 9.685E-05

These results are tabulated below:

	length(m)	
muscle	end pt.1(offset)	slope
M1	0.302	9.685E-05
M2	0.363	-1.012E-04
M3	0.366	2.692E-04
M4	0.412	-9.718E-05

M1 & M4 are a paired muscle group. They were attached around the same pulley so they same encoder information. The same goes for M2 & M3. The offset is the measurement of the length of the muscles at the starting position for calibration.

Appendix H

H.1 Free-Space Tests

Each of the below trajectories was followed this the manipulator in free-space. No wall was present for any of the tests.

1_1200 K 1.5cms Jan 30 2004
2_1200 K 1.667cms Jan 30 2004
3_1200 K 1.875cms Jan 30 2004
4_1200 K 2.143cms Jan 30 2004
5_1200 K 2.5cms Jan 30 2004
6_1200 K 3cms Jan 30 2004
7_1200 K 3.75cms Jan 30 2004
8_1200 K 5cms Jan 30 2004
9_1200 K 7.5cms Jan 30 2004
10_1200 K 15cms Jan 30 2004

H.2 Contact Tests

Each of the following points were with and without a bump present on the instrumented contact surface.

1_1.5cms_800K_40.5_comp
2_1.5cms_800K_41.5_comp
3_1.5cms_1400K_40.5_comp
4_1.5cms_1400K_41.5_comp
5_3cms_800K_40.5_comp
6_3cms_800K_41_comp
7_3cms_800K_41_comp
8_3cms_800K_41_comp
9_3cms_800K_41.5_comp
10_3cms_1100K_40.5_comp
11_3cms_1100K_41_comp
12_3cms_1100K_41_comp
13_3cms_1100K_41_comp
14_3cms_1100K_41.5_comp
15_3cms_1400K_40.5_comp
16_3cms_1400K_41_comp
17_3cms_1400K_41_comp
18_3cms_1400K_41_comp
19_3cms_1400K_41.5_comp
20_7.5cms_800K_40.5_comp
21_7.5cms_800K_41.5_comp

22_7.5cms_1400K_40.5_comp
23_7.5cms_1400K_41.5_comp

H.3 Transition Tests

All of these tests were performed once with the wall present.

1_1000K_0.2cm_s_30_deg
2_1000K_0.2cm_s_60_deg
3_1000K_0.2cm_s_90_deg
4_1000K_0.5cm_s_30_deg
5_1000K_0.5cm_s_60_deg
6_1000K_0.5cm_s_90_deg
7_1000K_1cm_s_30_deg
8_1000K_1cm_s_60_deg
9_1000K_1cm_s_90_deg
10_1000K_2cm_s_90_deg
11_1000K_4cm_s_90_deg

Appendix I
Summary of Transition Tests

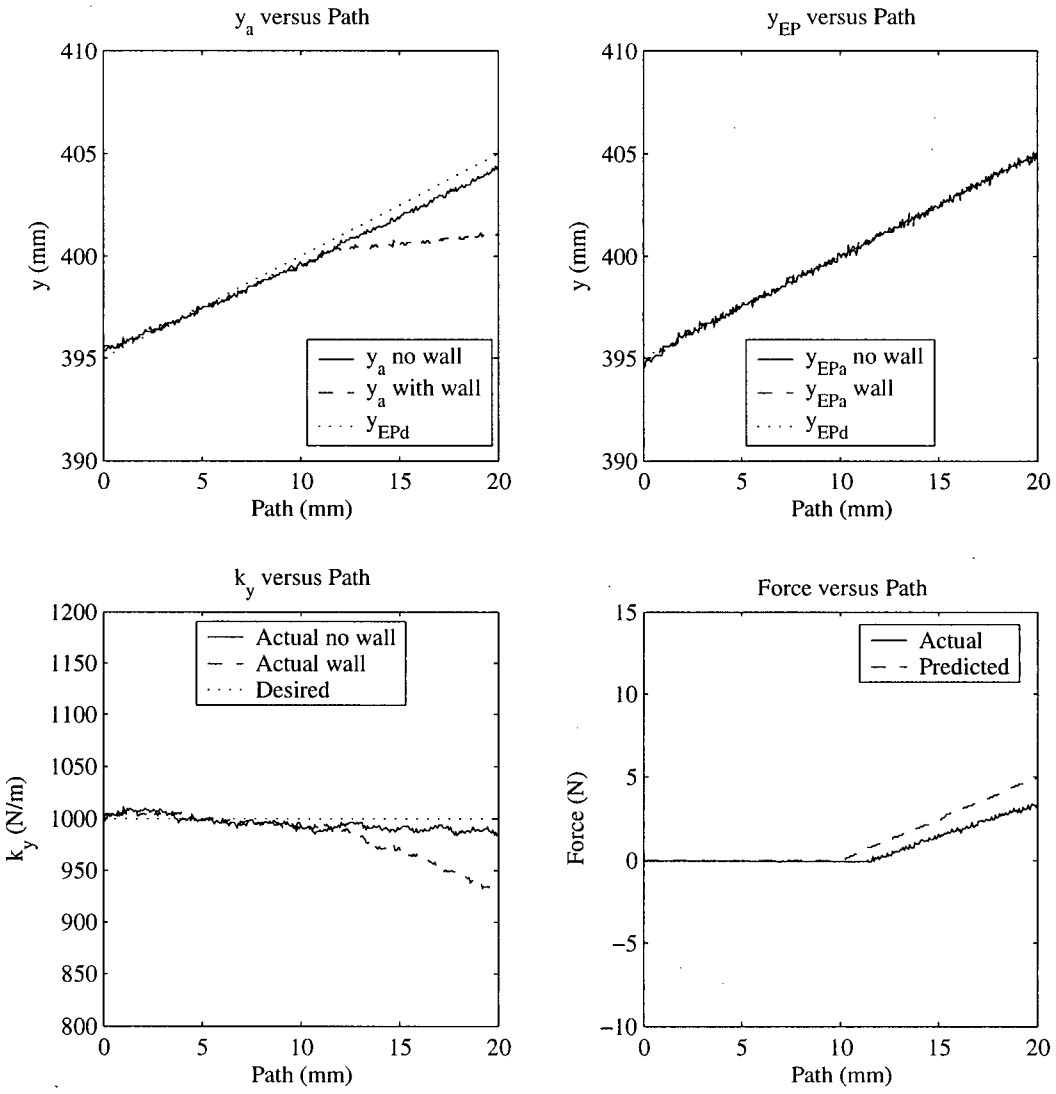

Test #1 – 30 degrees, v=0.2cm/s

Figure I.1 – Transition test #1

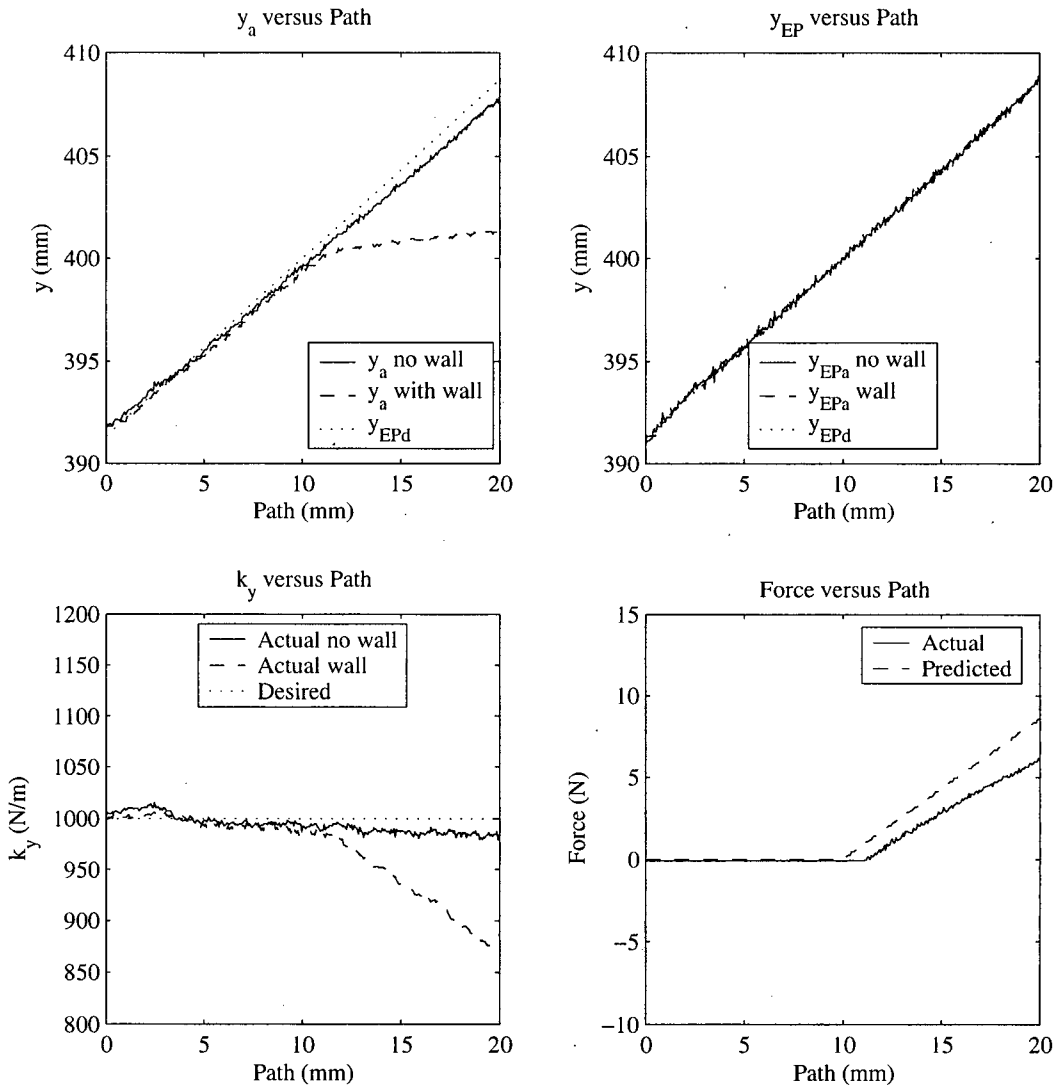

Test #2 – 60 degrees, v=0.2cm/s

Figure I.2 – Transition test #2

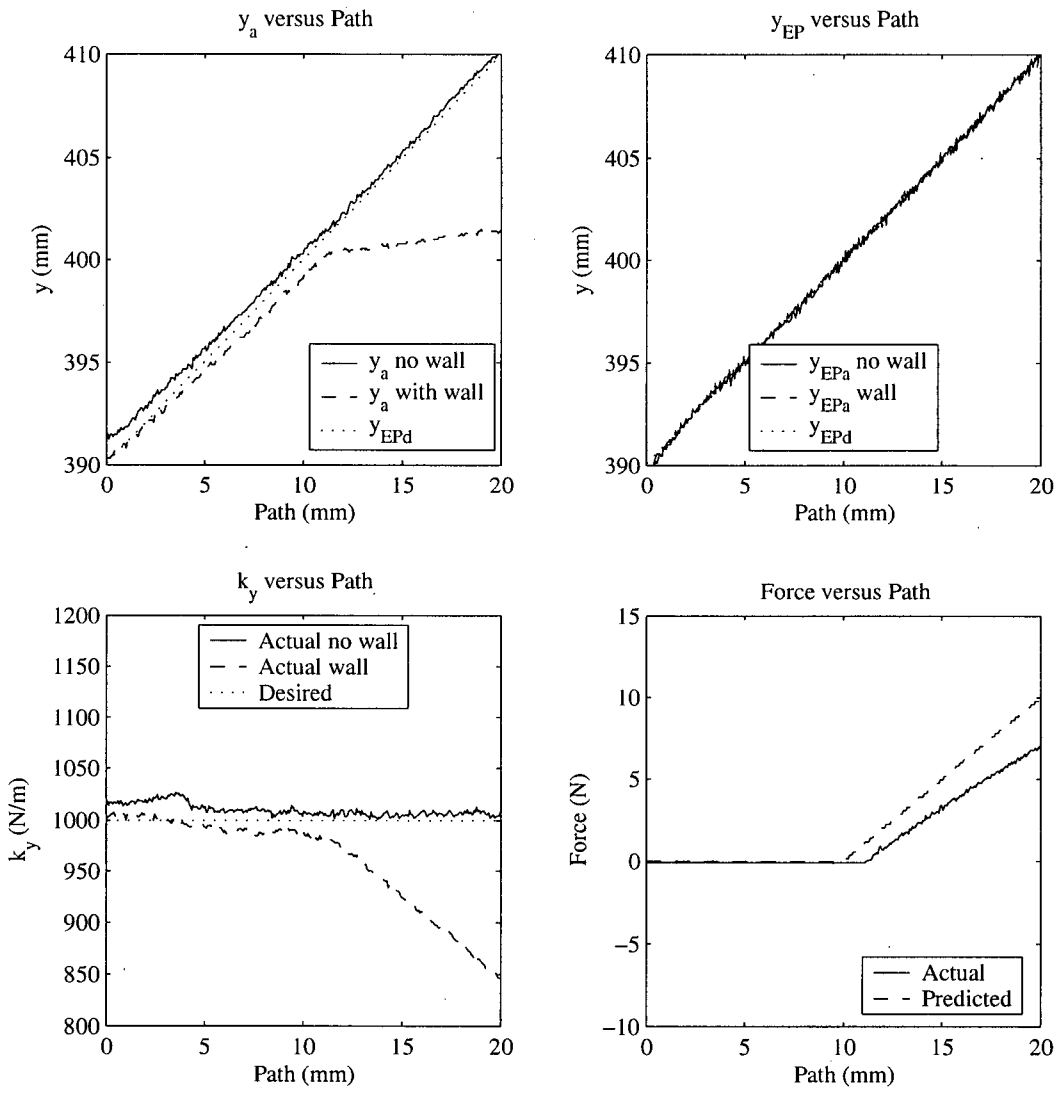

Test #3 – 90 degrees, v=0.2cm/s

Figure I.3 – Transition test #3

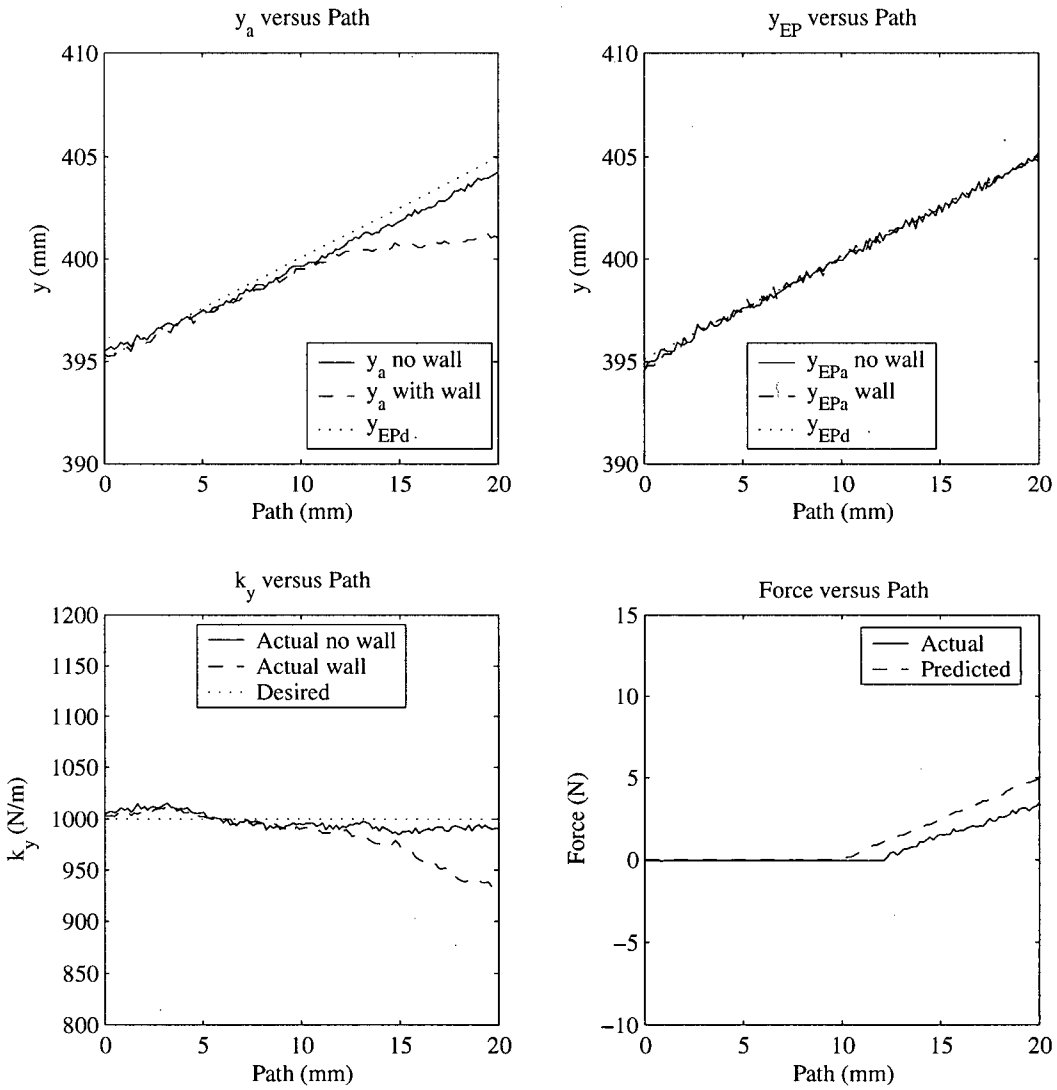

Test #4 – 30 degrees, v=0.5cm/s

Figure I.4 – Transition test #4

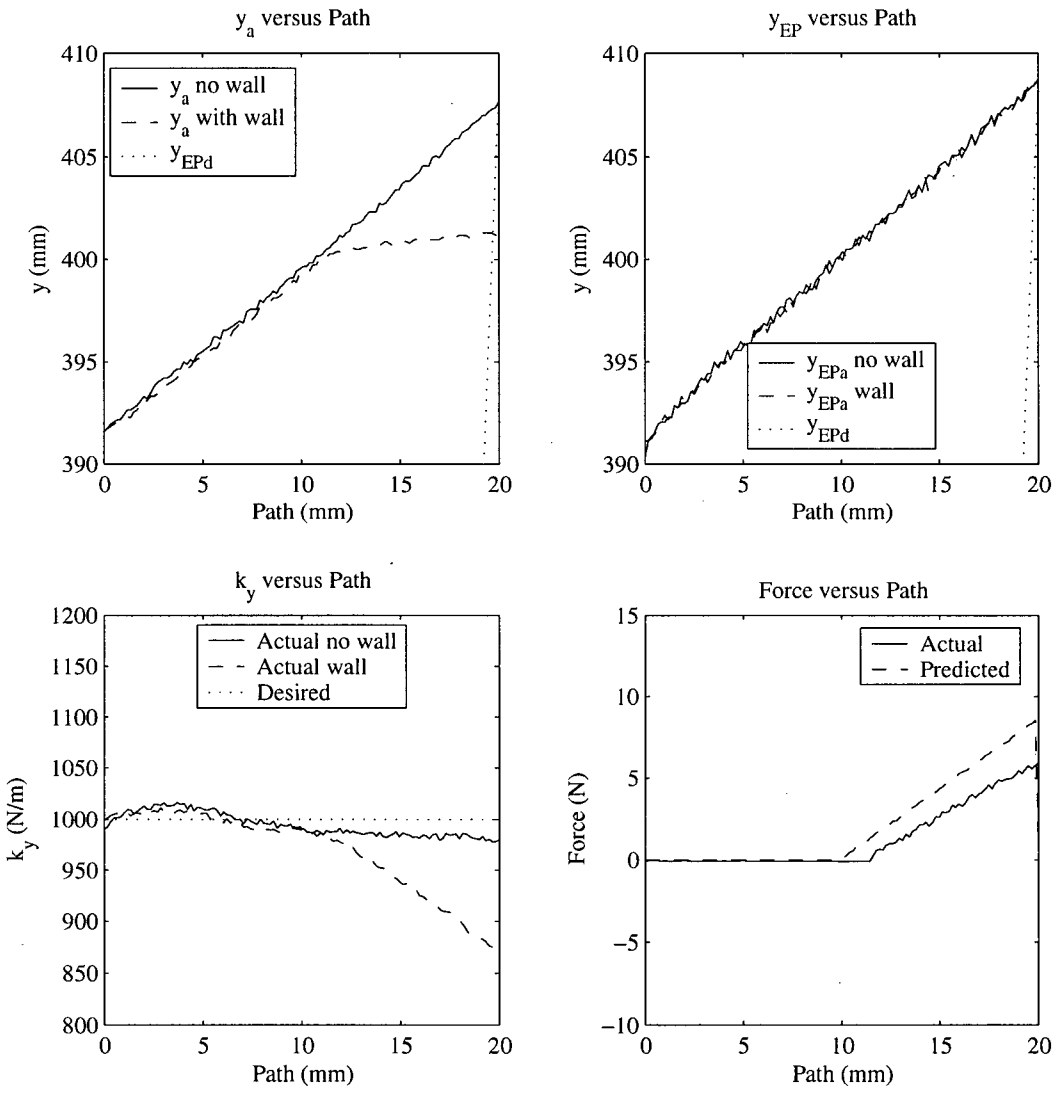

Test #5 – 60 degrees, v=0.5cm/s

Figure I.5 – Transition test #5

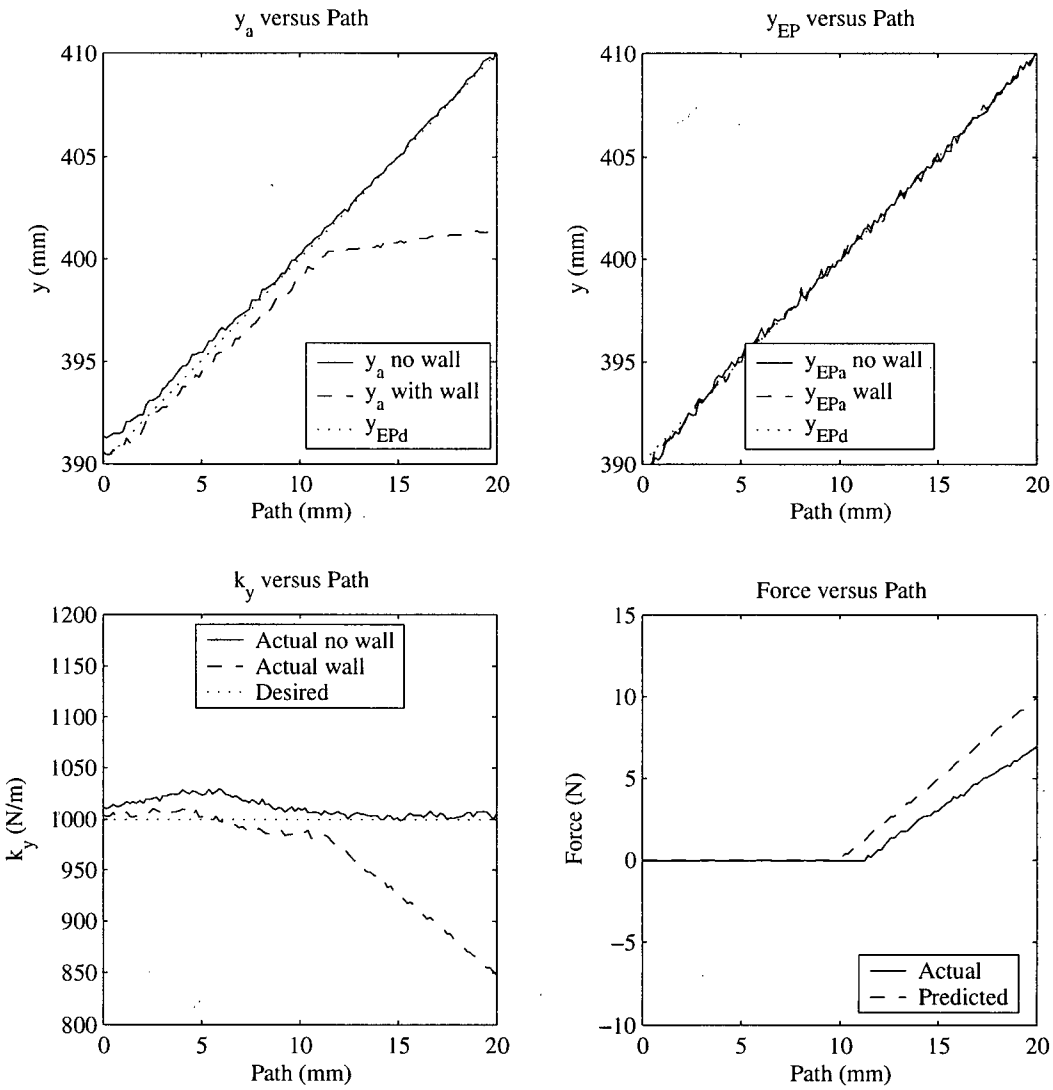

Test #6 – 90 degrees, v=0.5cm/s

Figure I.6 – Transition test #6

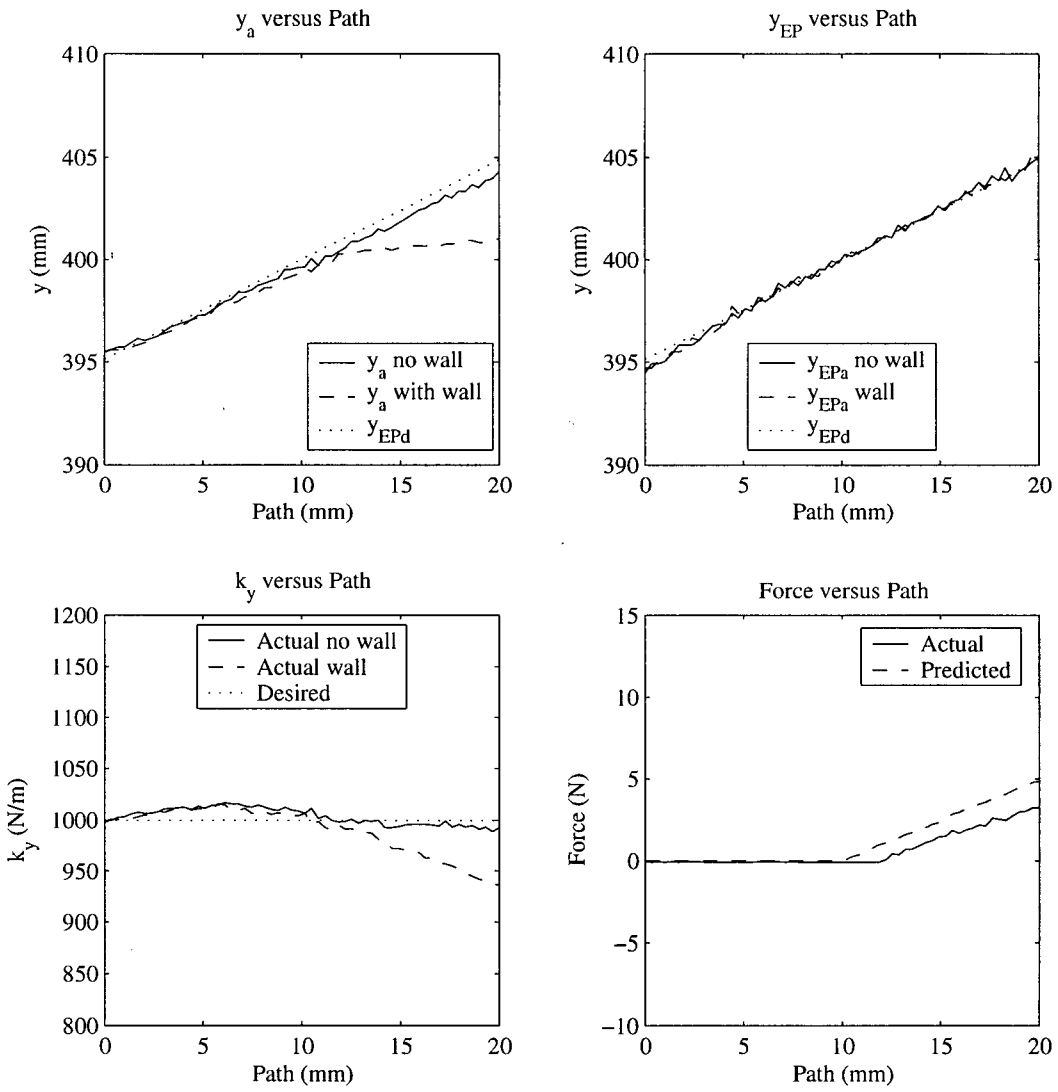

Test #7 – 30 degrees, v=1cm/s

Figure I.7 – Transition test #7

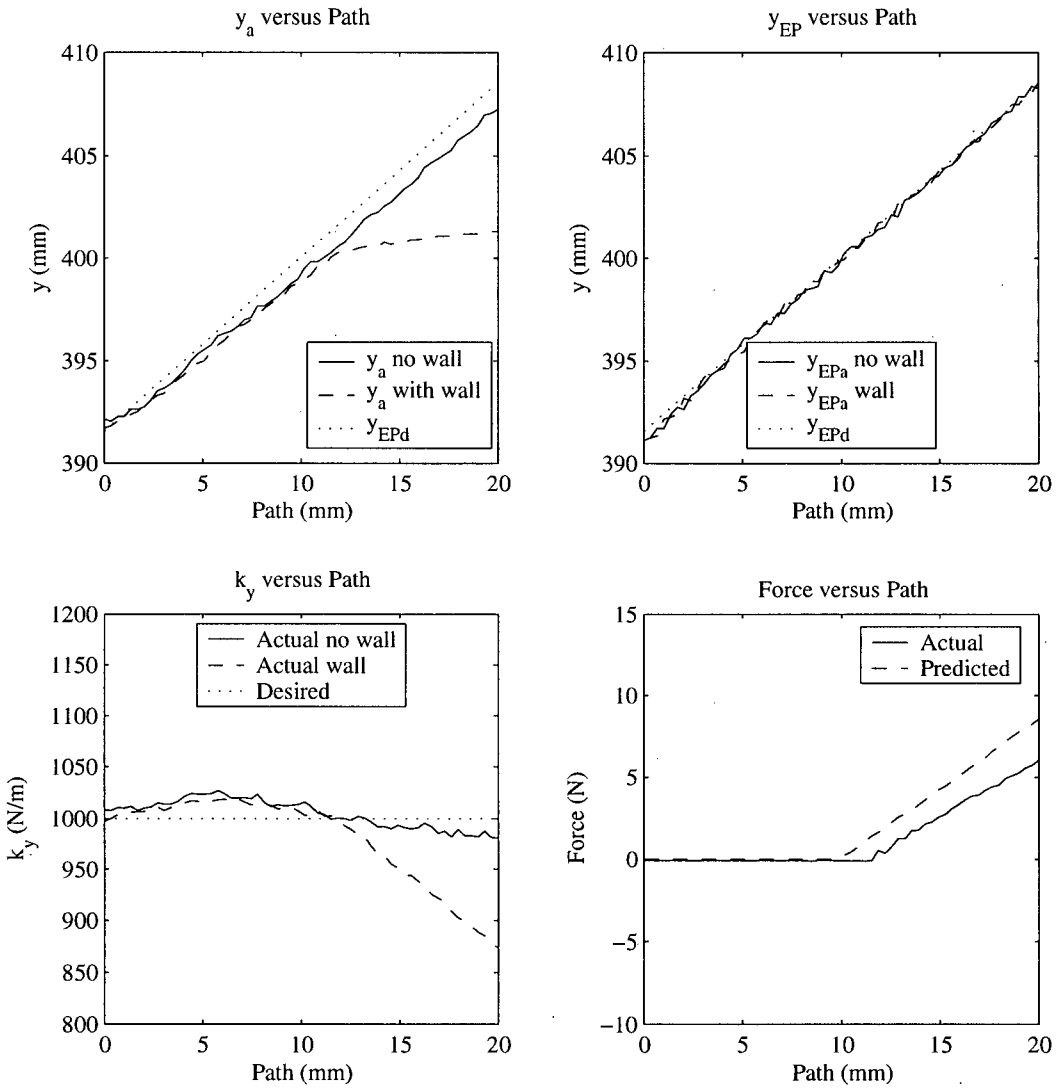

Test #8 – 60 degrees, v=1cm/s

Figure I.8 – Transition test #8

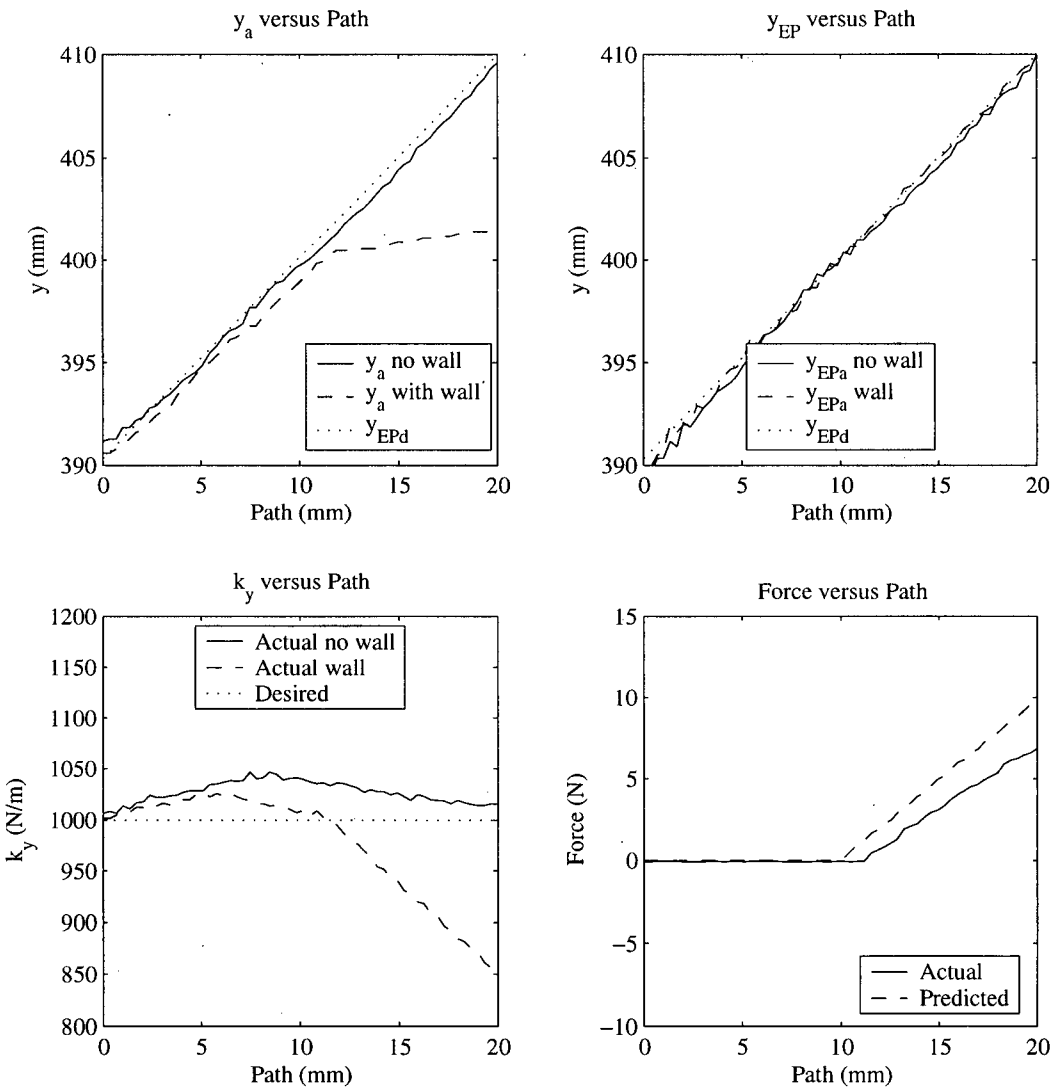

Test #9 – 90 degrees, v=1cm/s

Figure I.9 – Transition test #9

Appendix J
Summary of Contact Tests

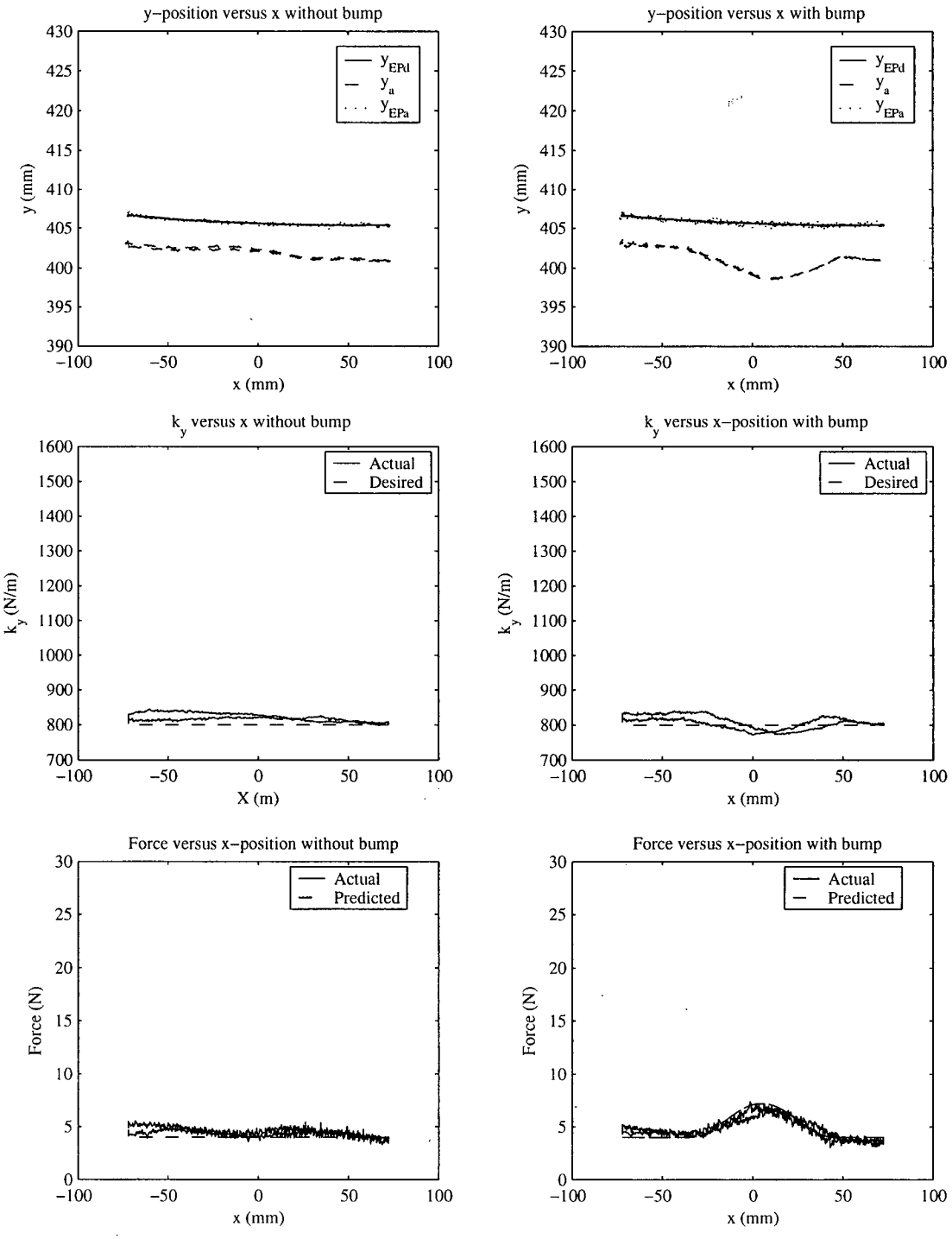

Test #1 – v_x=15mm/s, Y_{ep}=405mm, k_y=800N/m

Figure J.1 – Contact test #1

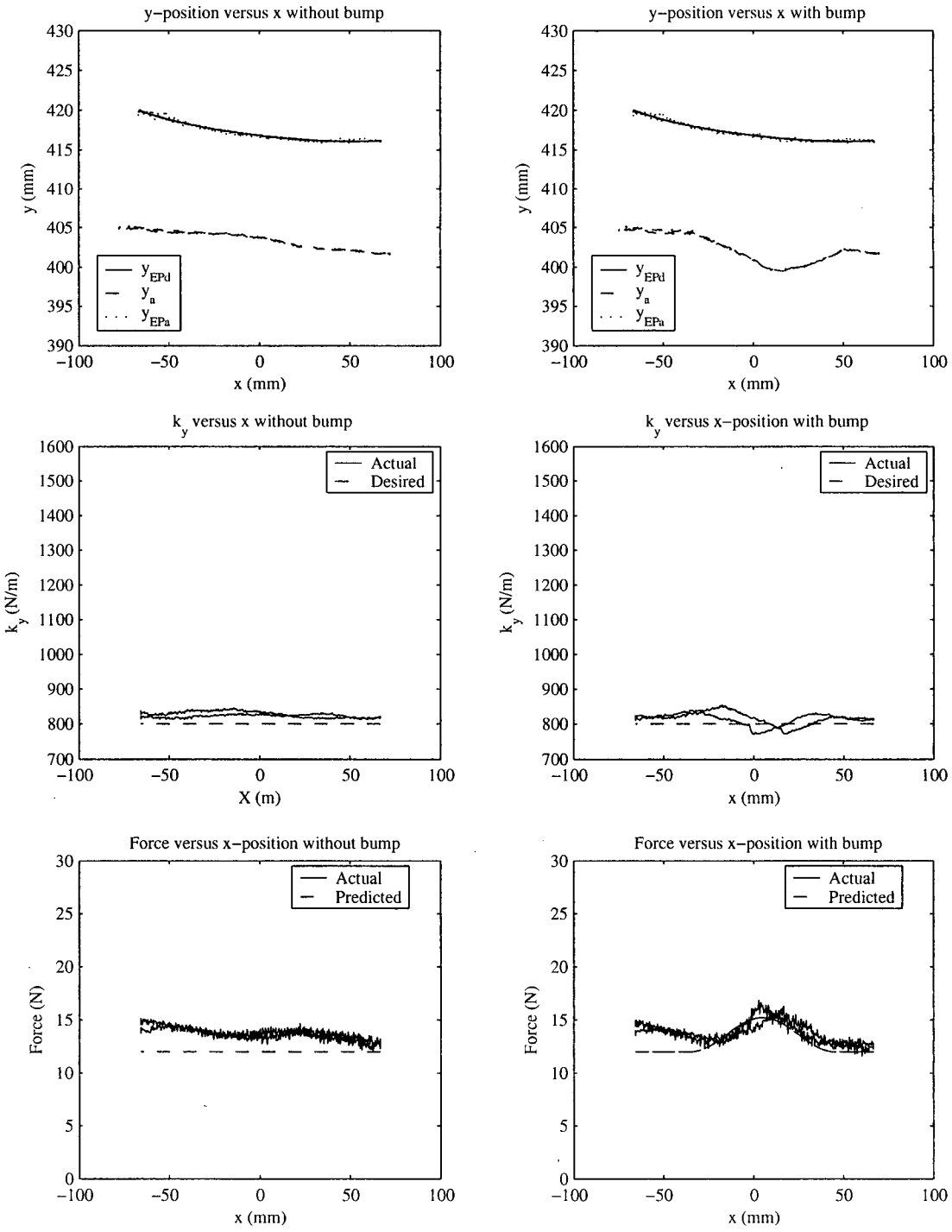

Test #2 – v_x=15mm/s, Y_{ep}=415mm, k_y=800N/m

Figure J.2 – Contact test #2

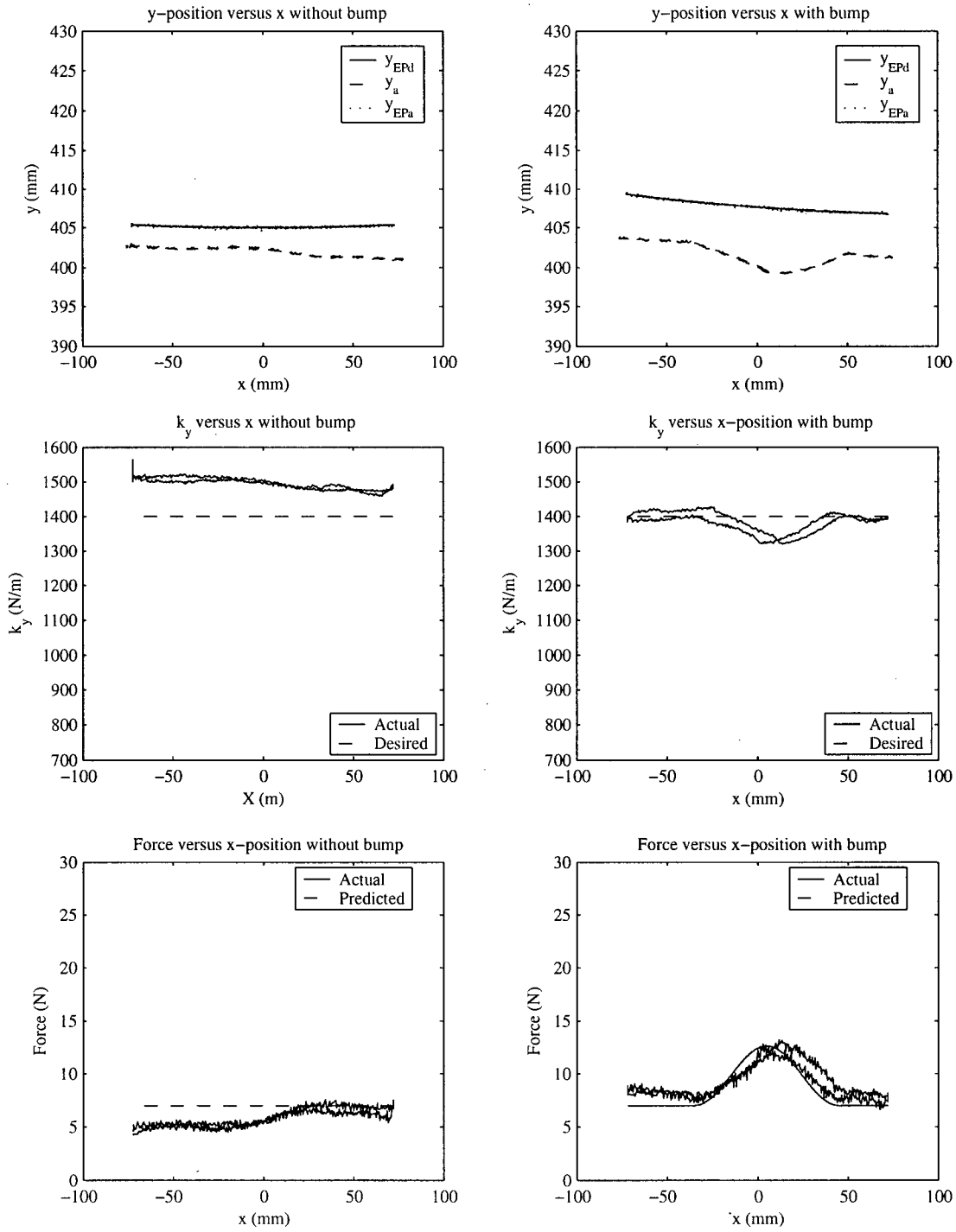

Test #3 – v_x=15mm/s, Y_{ep}=405mm, k_y=1400N/m

Figure J.3 – Contact test #3

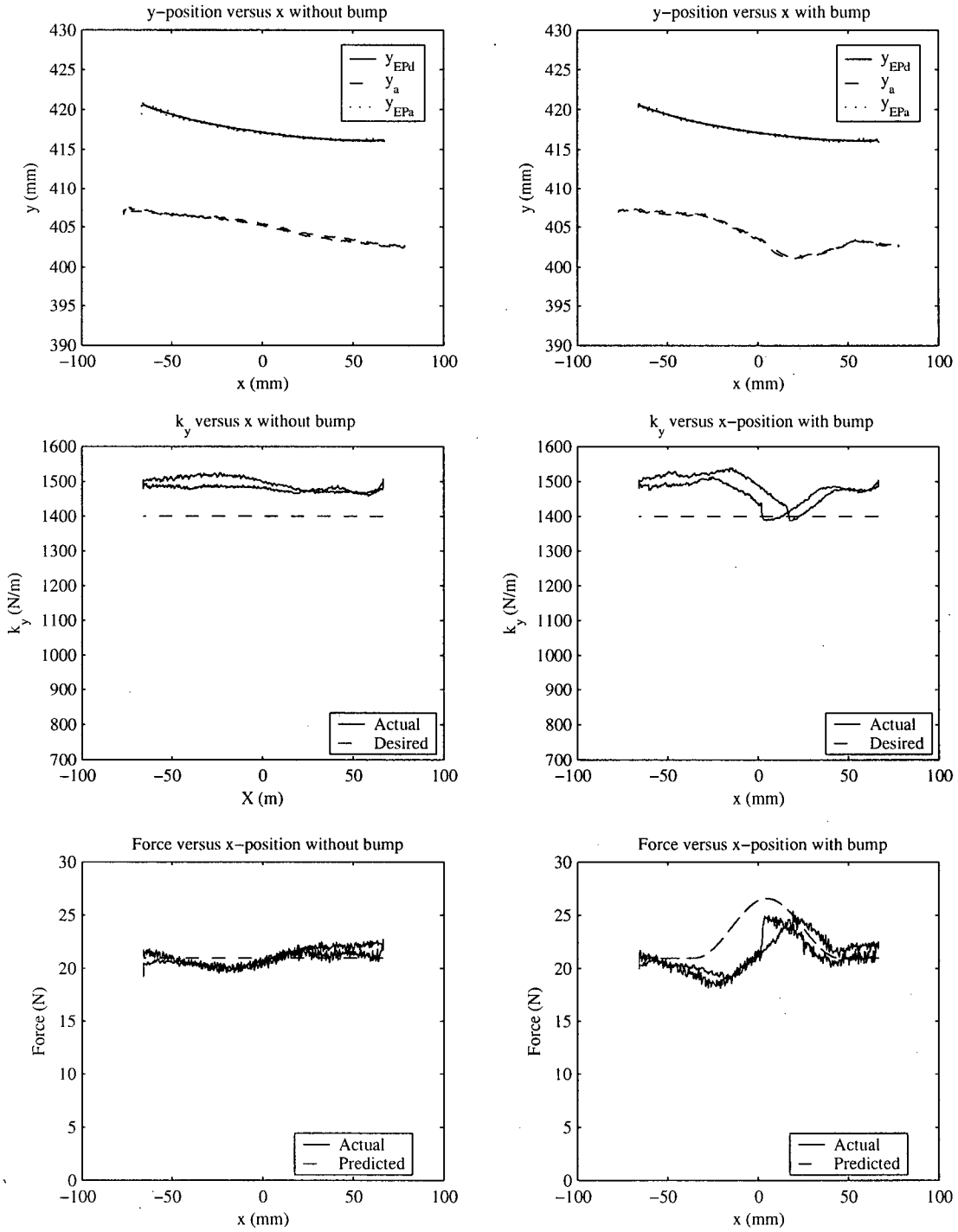

Test #4 – v_x=15mm/s, Y_{ep}=415mm, k_y=1400N/m

Figure J.4 – Contact test #4

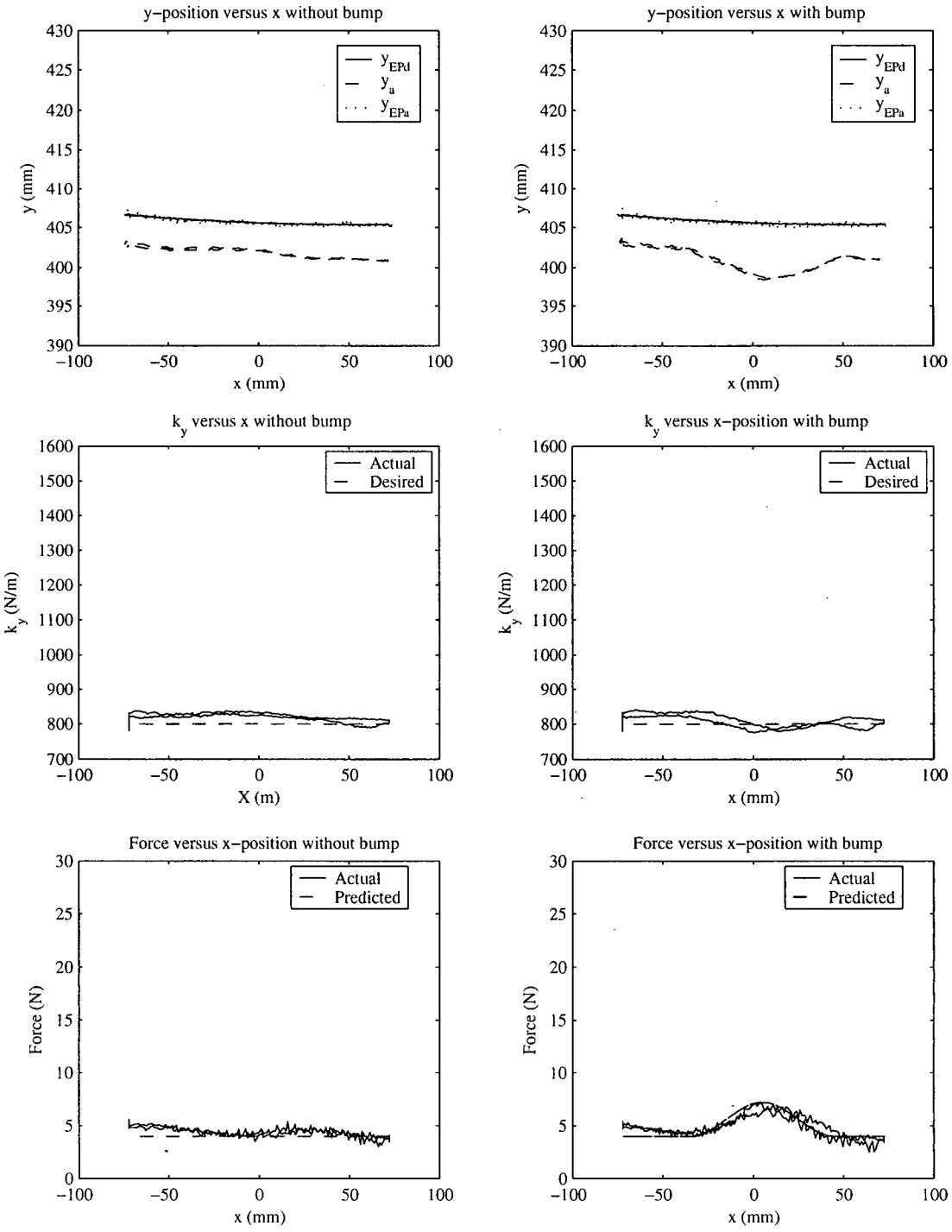

Test #5 – v_x=30mm/s, Y_{ep}=405mm, k_y=800N/m

Figure J.5 – Contact test #5

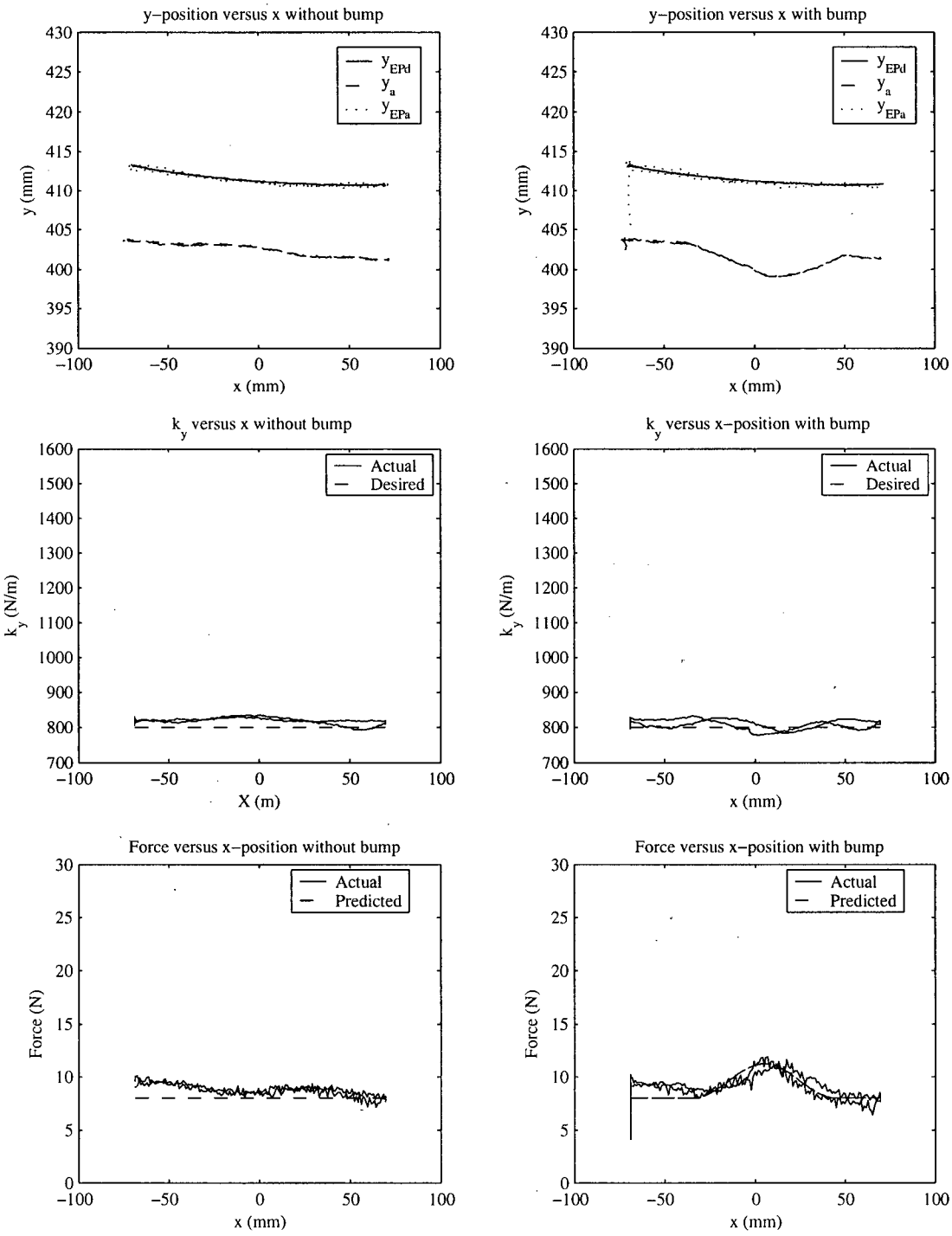

Test #6 – v_x=30mm/s, Y_{ep}=410mm, k_y=800N/m

Figure J.6 – Contact test #6

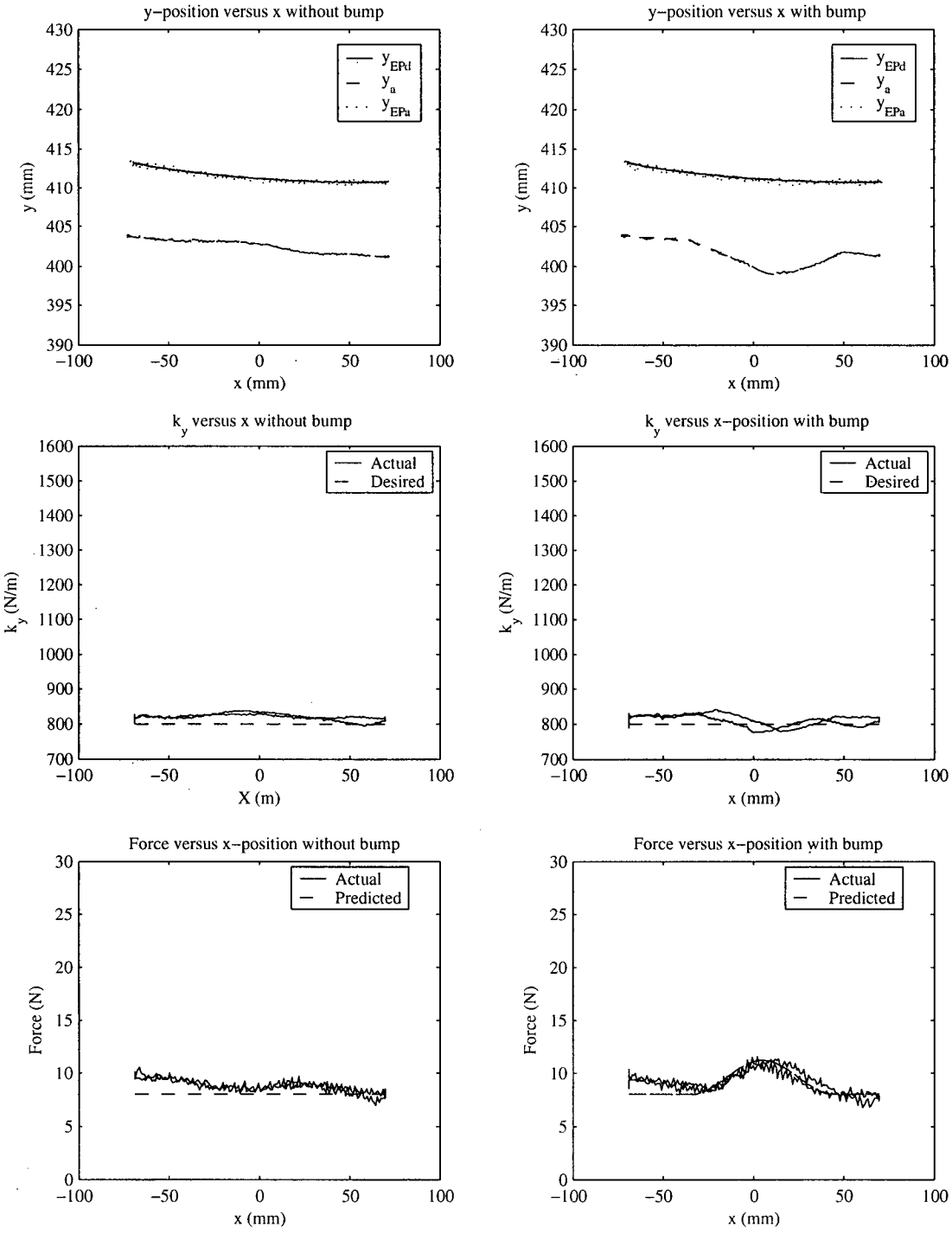

Test #7 – v_x=30mm/s, Y_{ep}=410mm, k_y=800N/m

Figure J.7 – Contact test #7

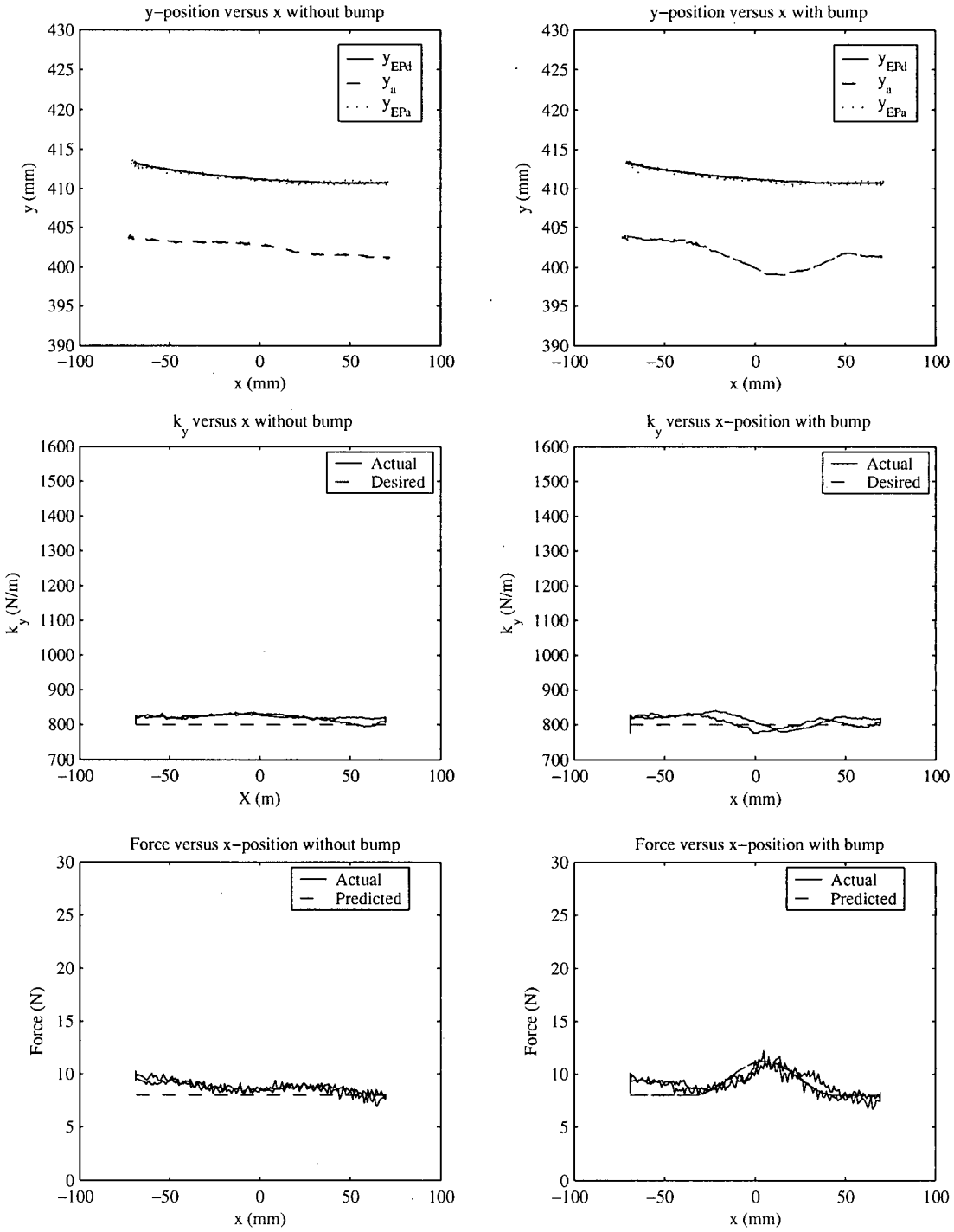

Test #8 – v_x=30mm/s, Y_{ep}=410mm, k_y=800N/m

Figure J.8 – Contact test #8

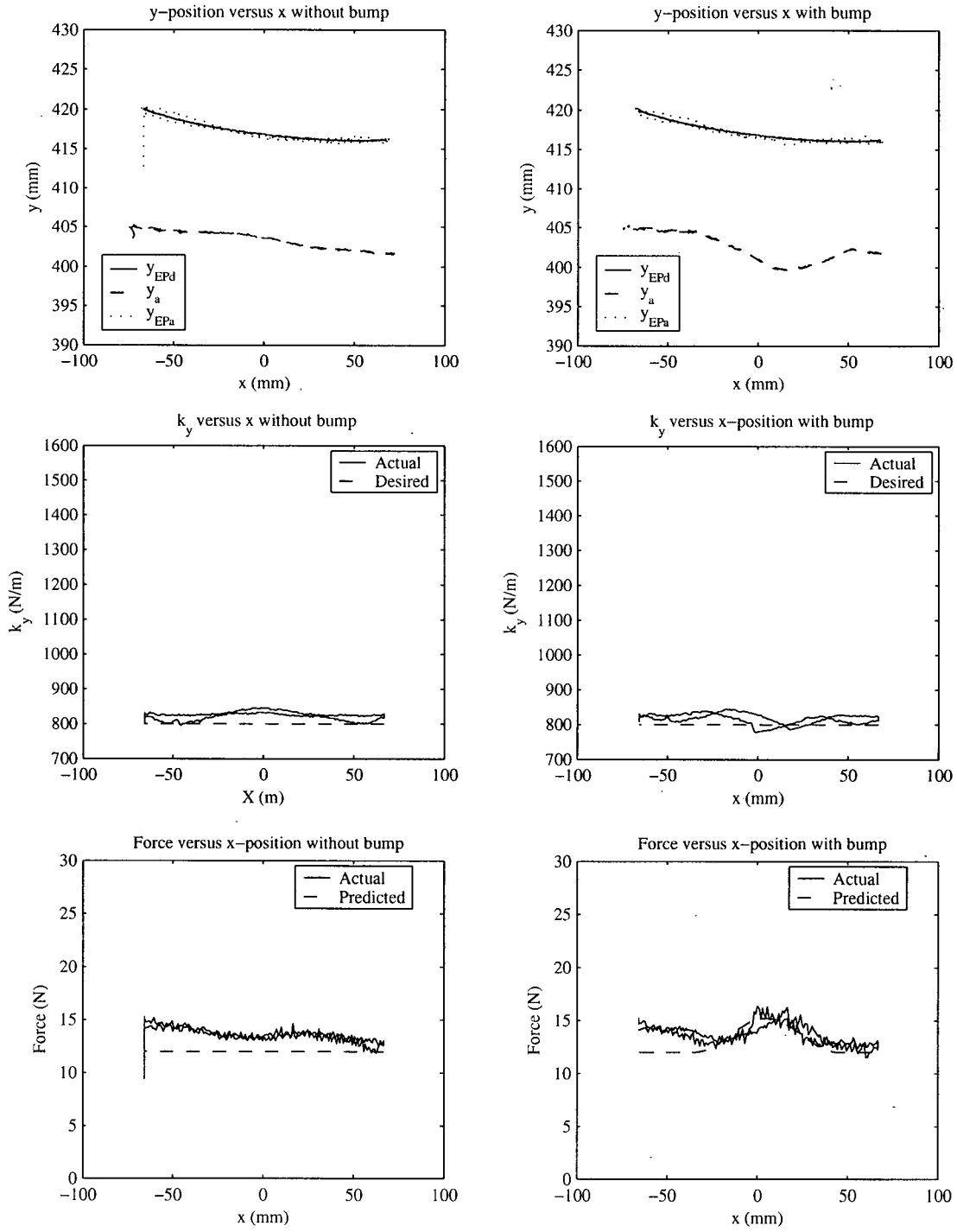

Test #9 – v_x=30mm/s, Y_{ep}=415mm, k_y=800N/m

Figure J.9 – Contact test #9

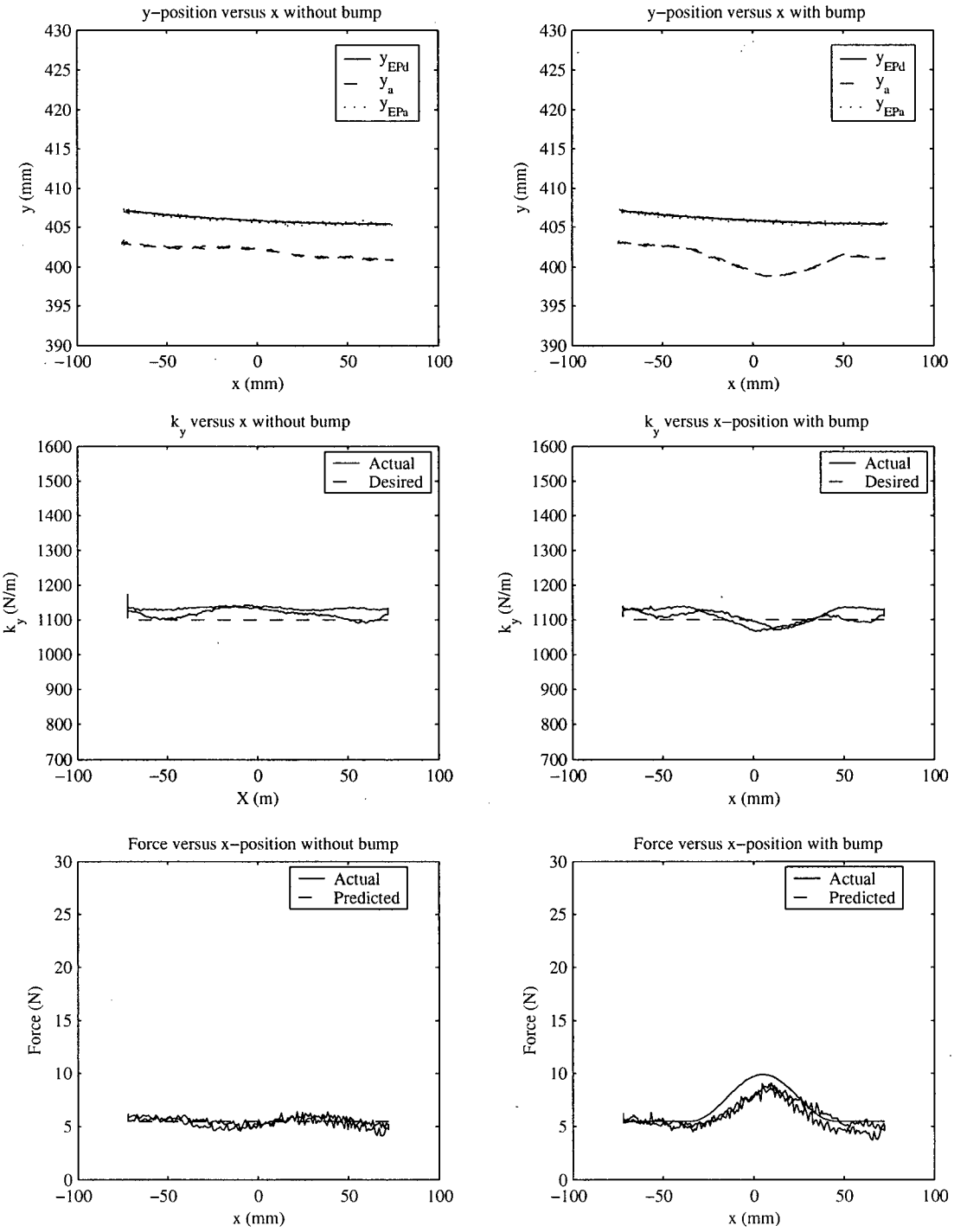

Test #10 – v_x=30mm/s, Y_{ep}=405mm, k_y=1100N/m

Figure J.10 – Contact test #10

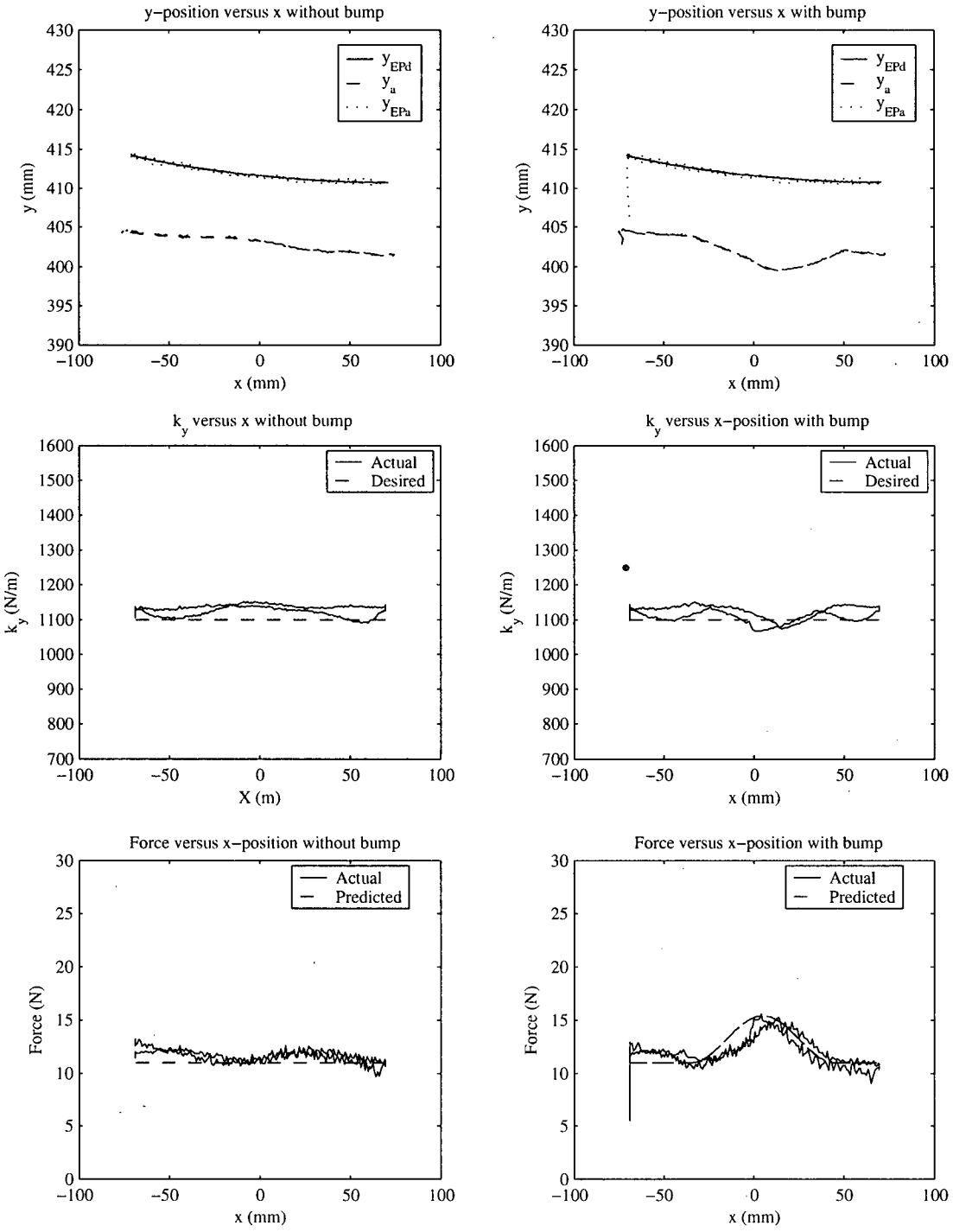

Test #11 – v_x=30mm/s, Y_{ep}=410mm, k_y=1100N/m

Figure J.11 – Contact test #11

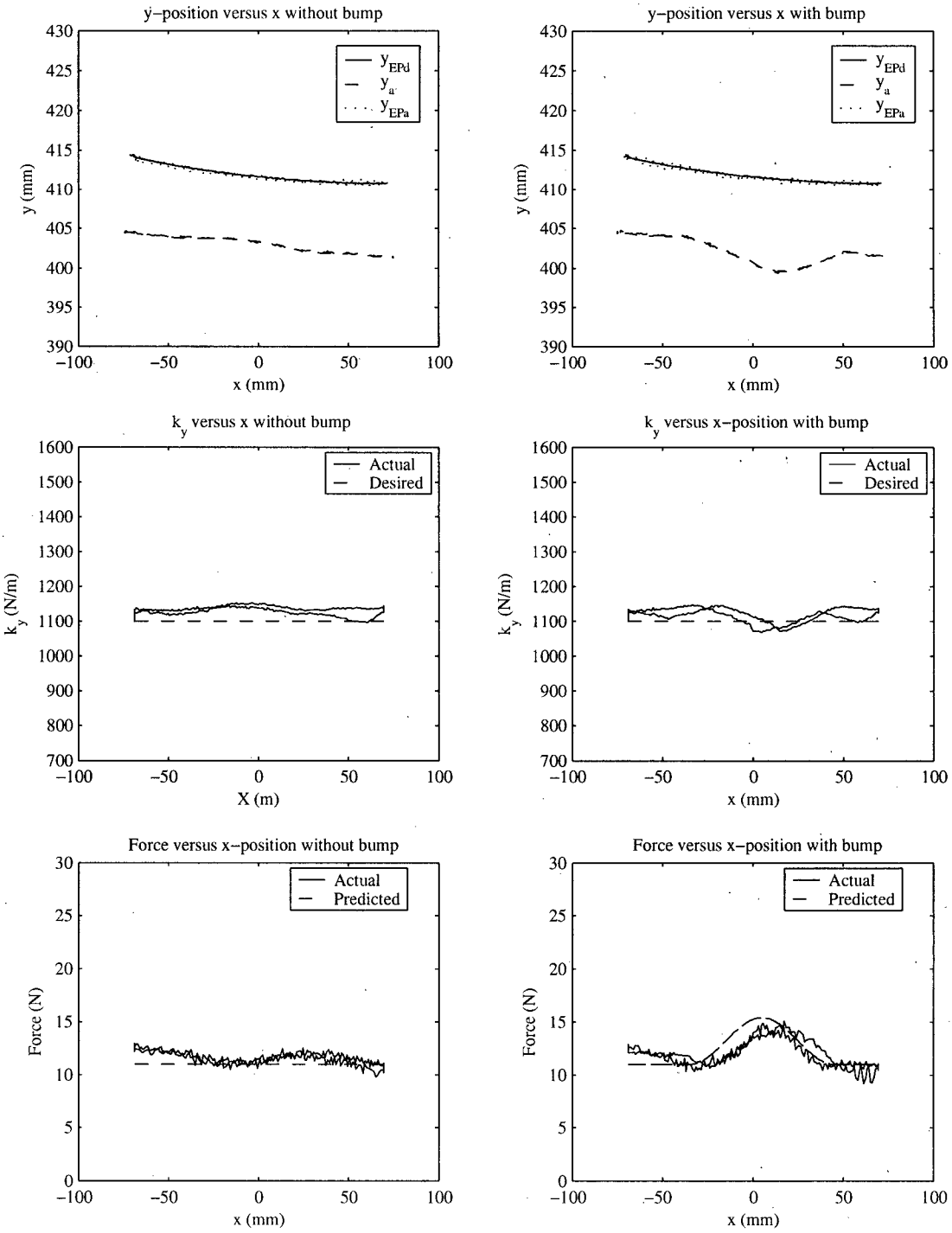

Test #12 – v_x=30mm/s, Y_{ep}=410mm, k_y=1100N/m

Figure J.12 – Contact test #12

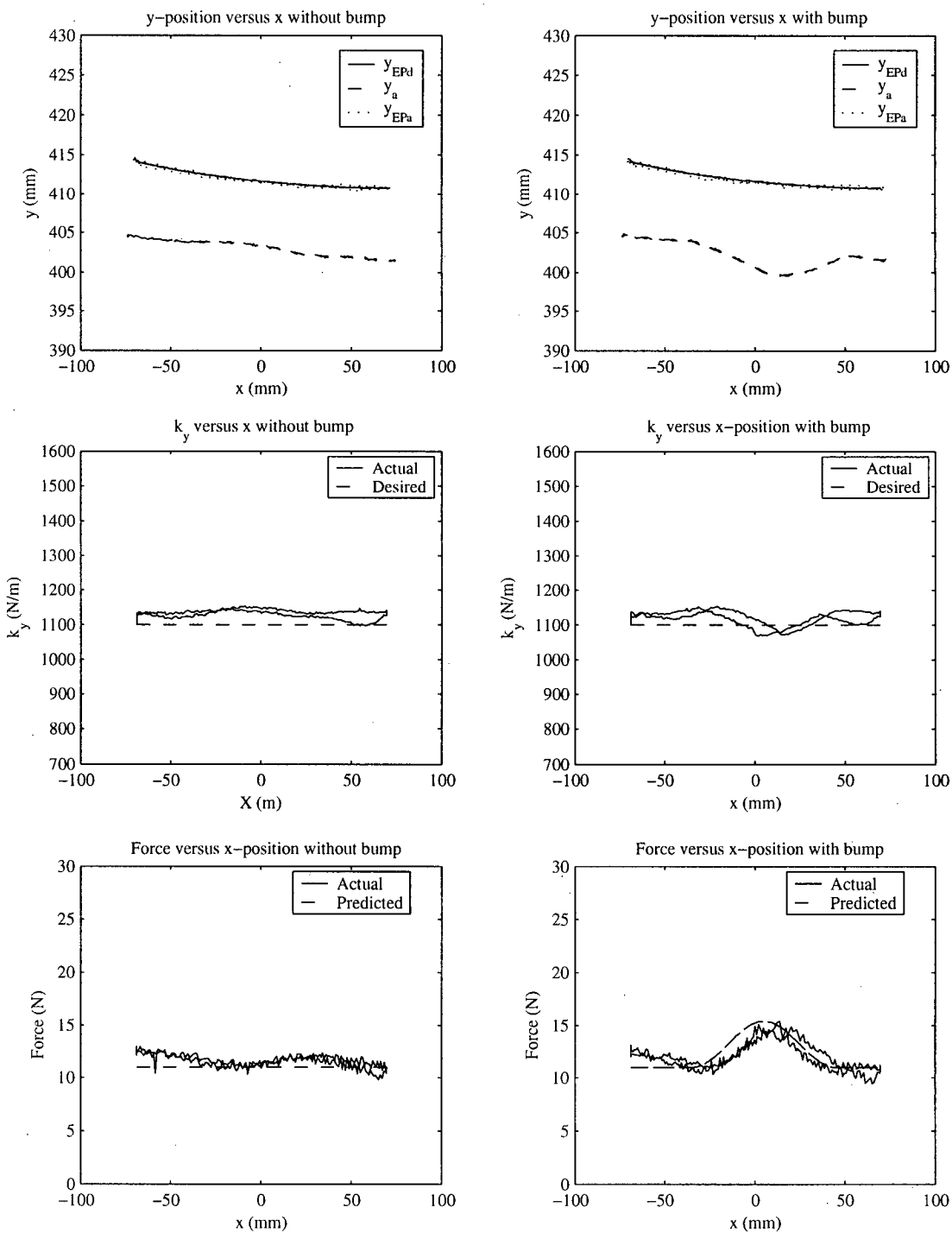

Test #13 – v_x=30mm/s, Y_{ep}=410mm, k_y=1100N/m

Figure J.13 – Contact test #13

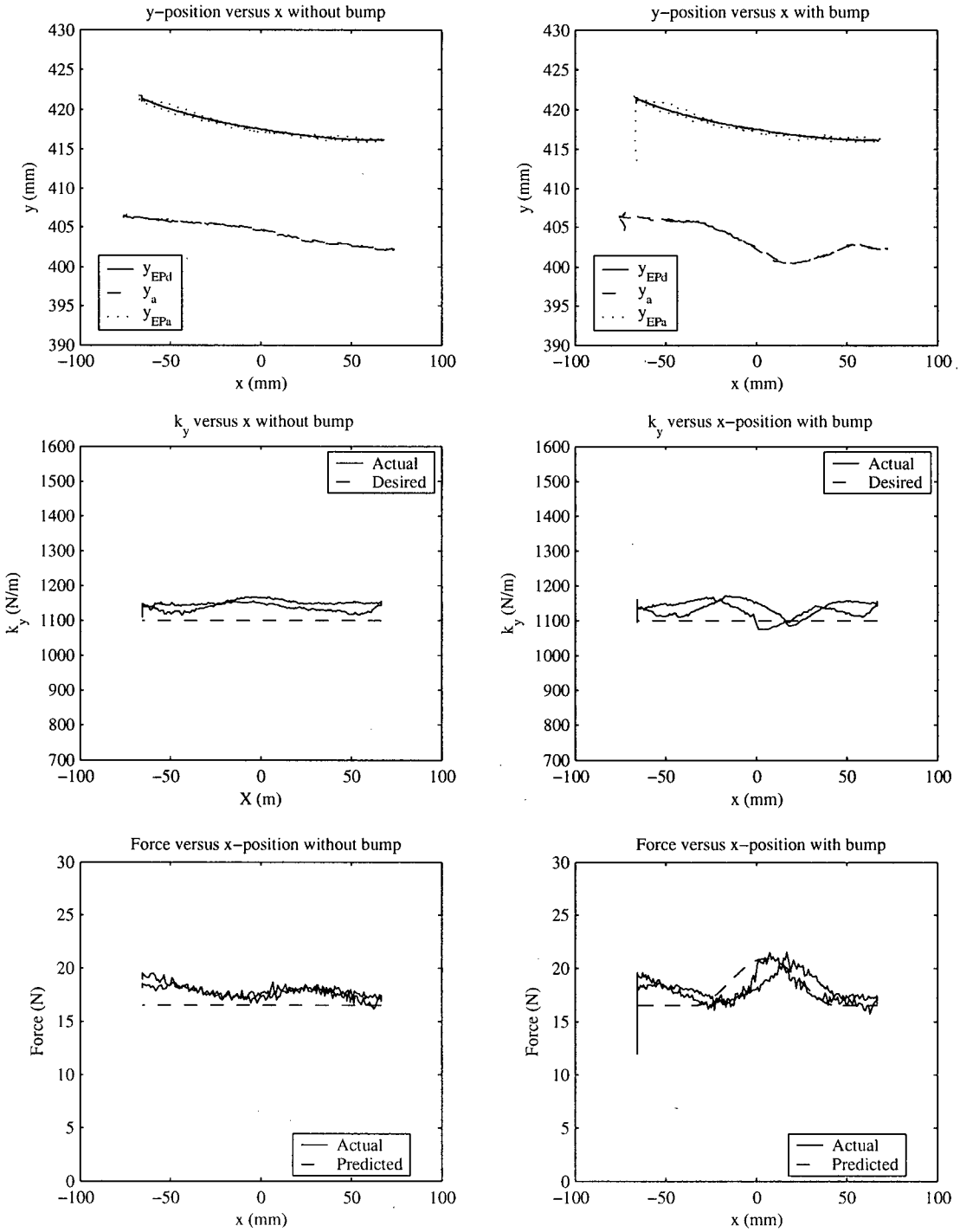

Test #14 – v_x=30mm/s, Y_{ep}=415mm, k_y=1100N/m

Figure J.14 – Contact test #14

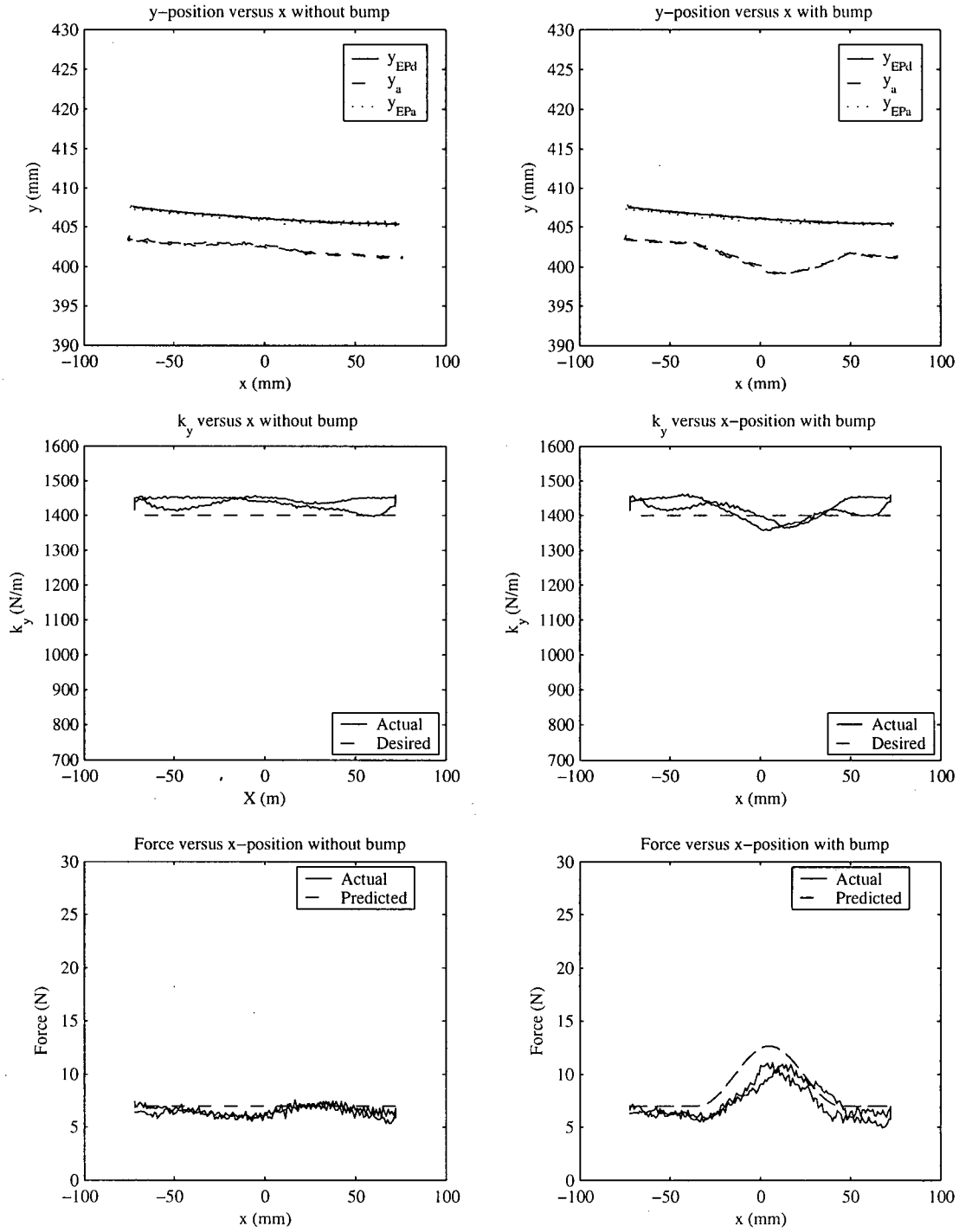

Test #15 – v_x=30mm/s, Y_{ep}=405mm, k_y=1400N/m

Figure J.15 – Contact test #15

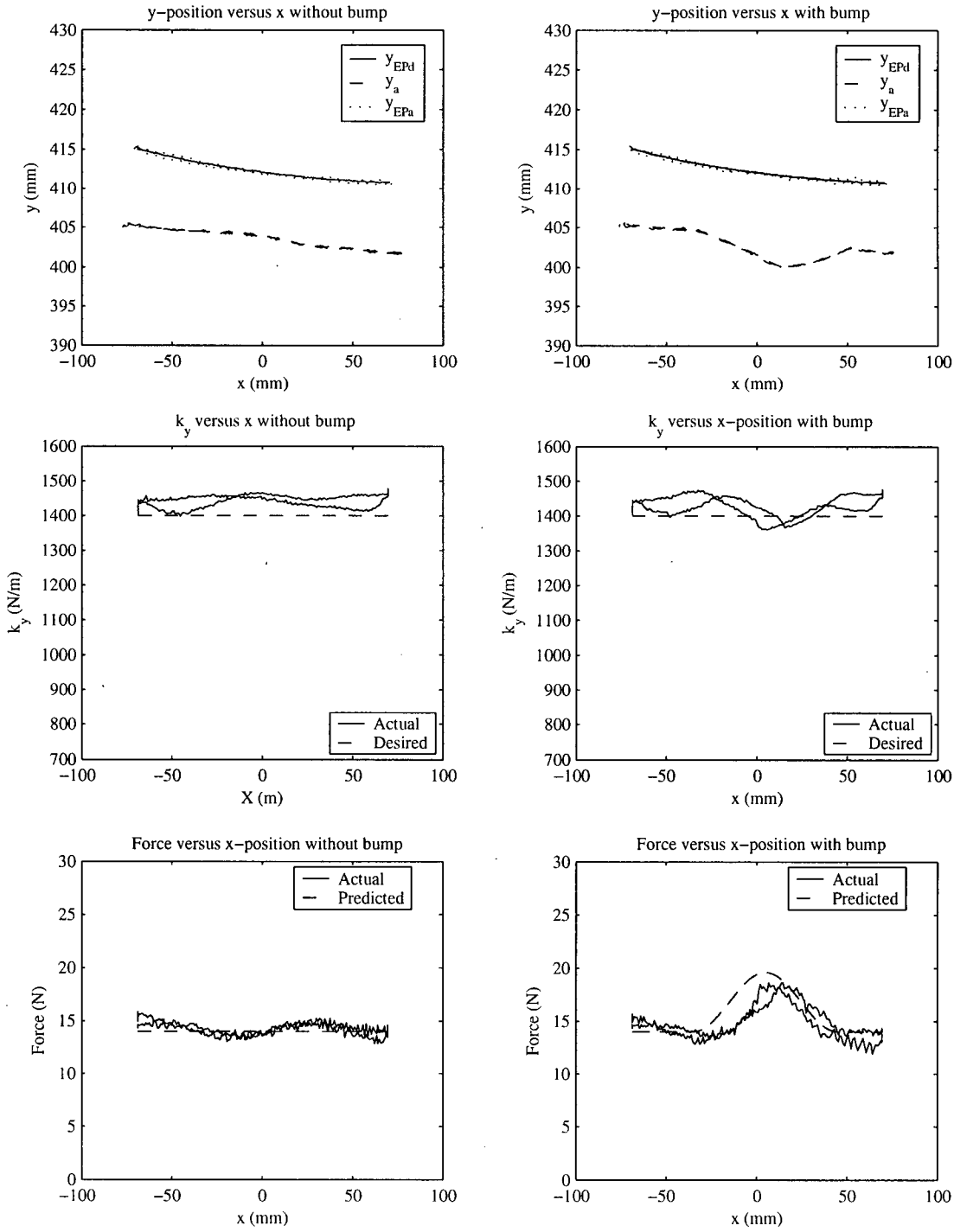

Test #16 – v_x=30mm/s, Y_{ep}=410mm, k_y=1400N/m

Figure J.16 – Contact test #16

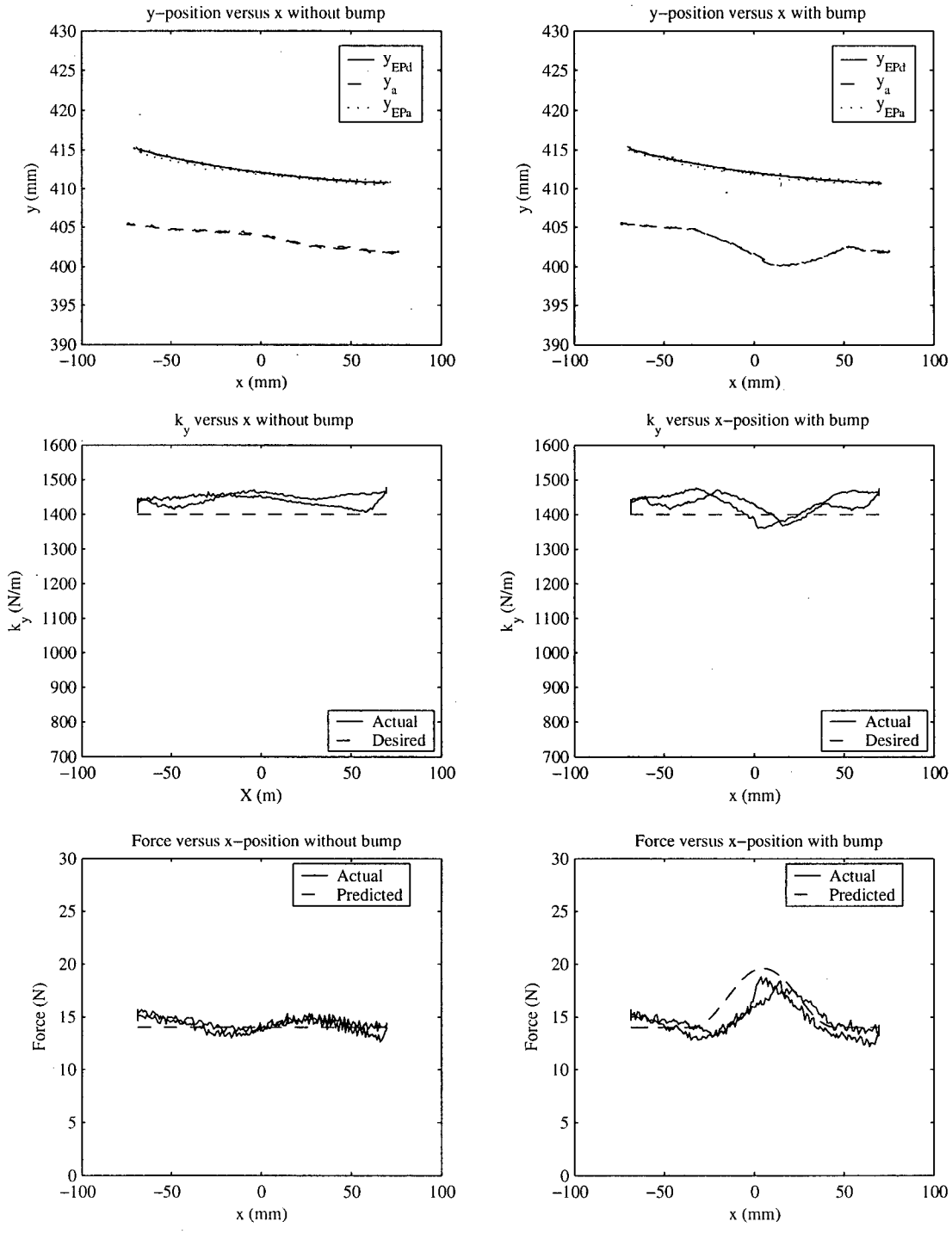

Test #17 – v_x=30mm/s, Y_{ep} =410mm, k_y =1400N/m

Figure J.17 – Contact test #17

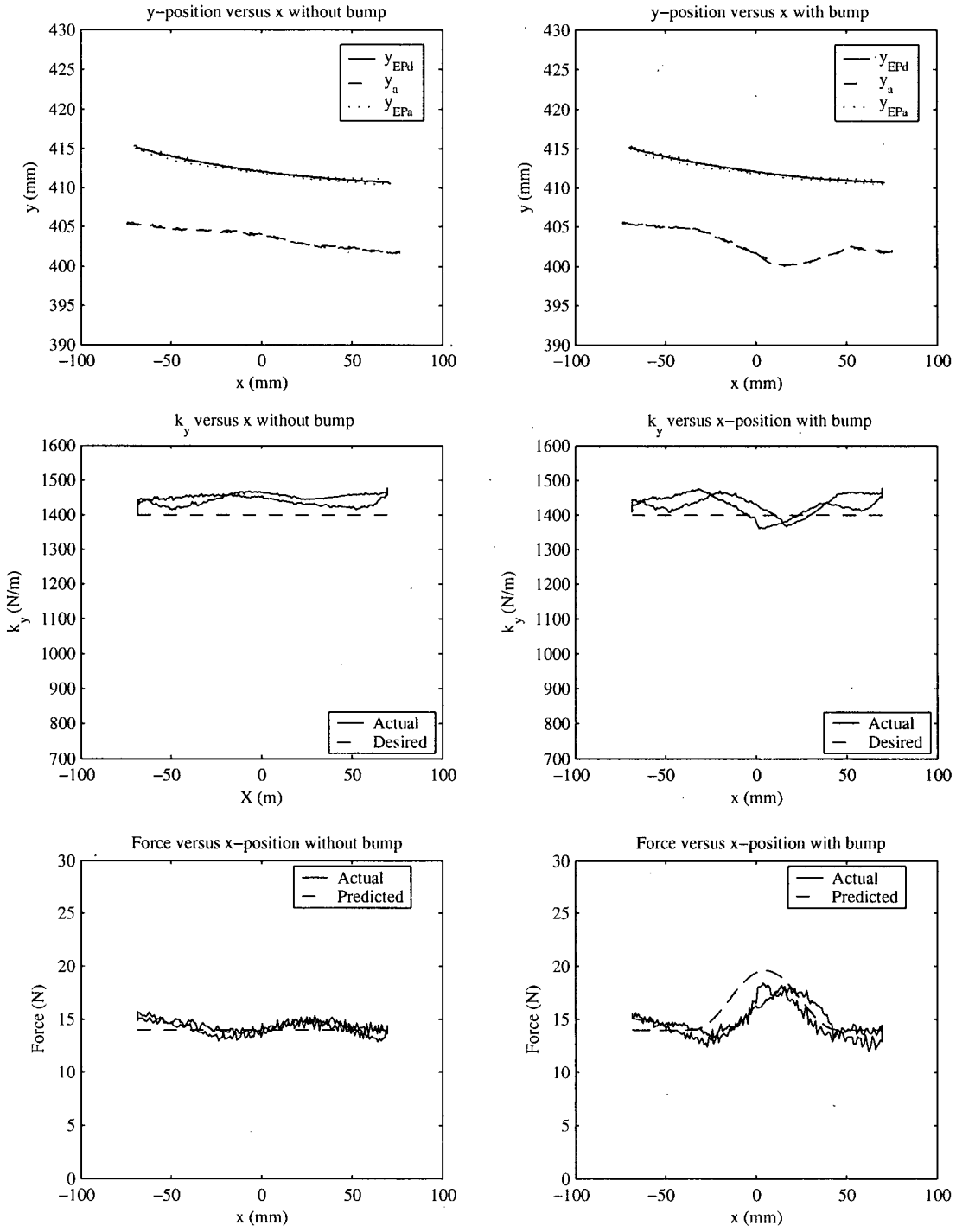

Test #18 – v_x=30mm/s, Y_{ep}=410mm, k_y=1400N/m

Figure J.18 – Contact test #18

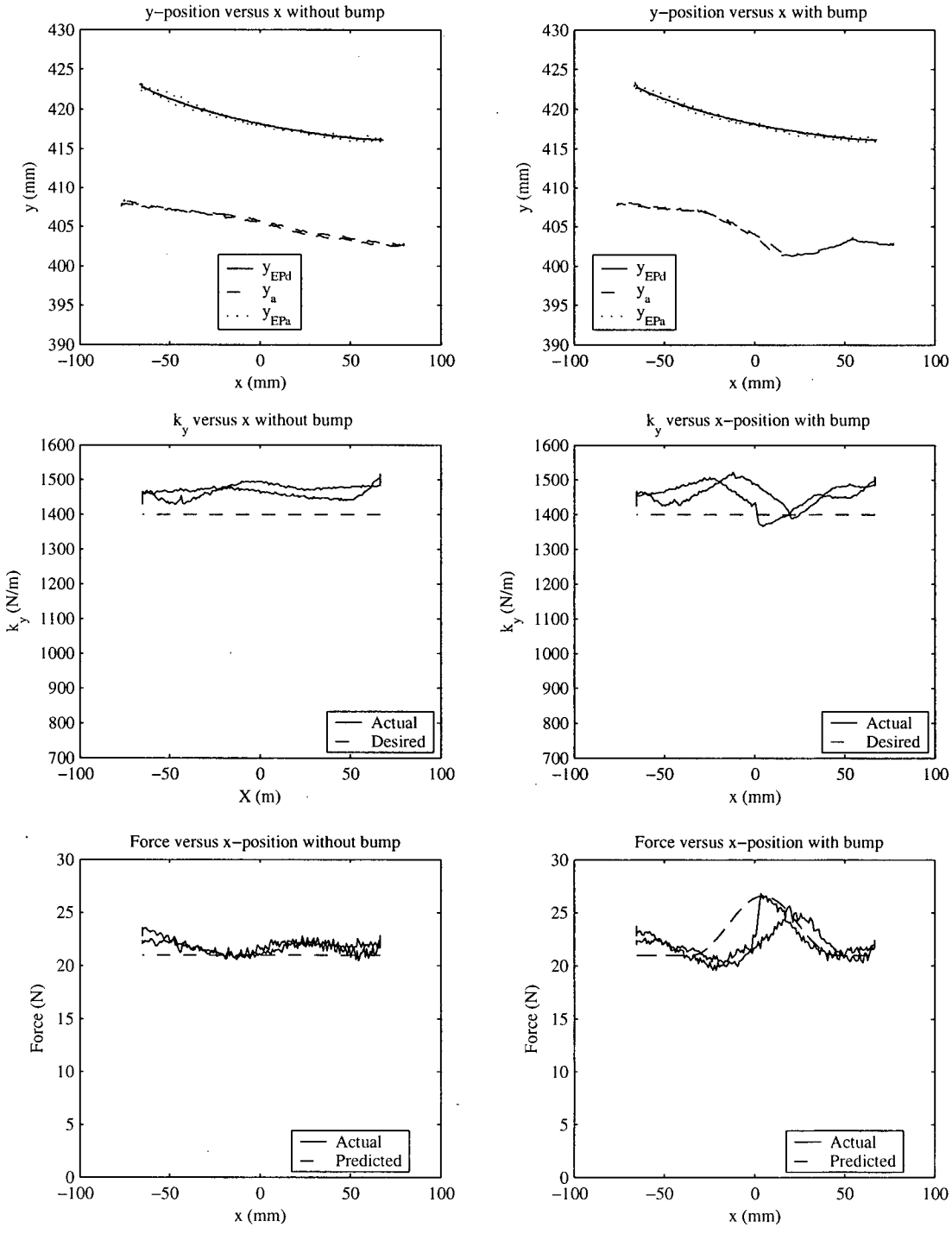

Test #19 – v_x=30mm/s, Y_{ep}=415mm, k_y=1400N/m

Figure J.19 – Contact test #19

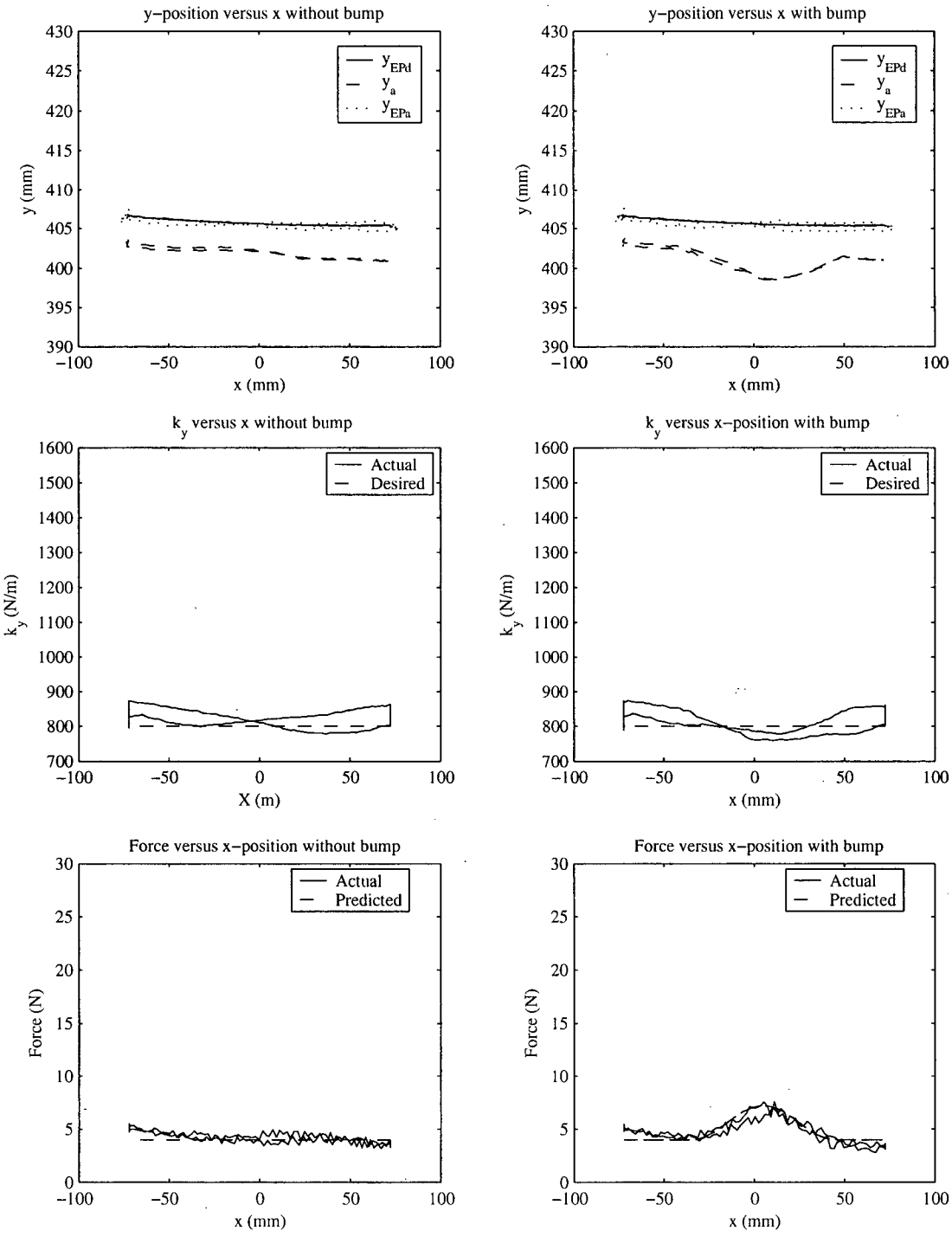

Test #20 – v_x=75mm/s, Y_{ep}=405mm, k_y=800N/m

Figure J.20 – Contact test #20

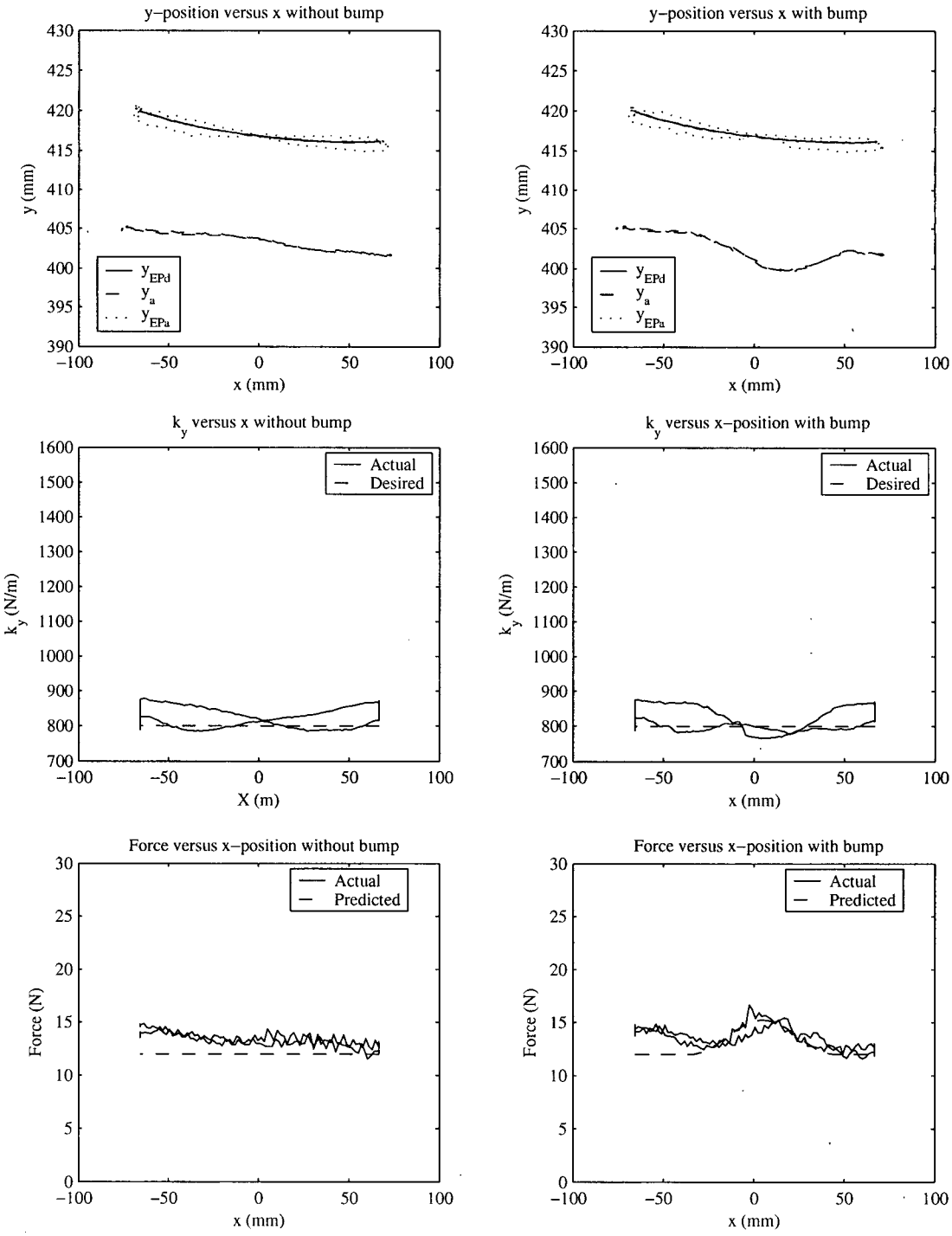

Test #21 – v_x=75mm/s, Y_{ep}=415mm, k_y=800N/m

Figure J.21 – Contact test #21

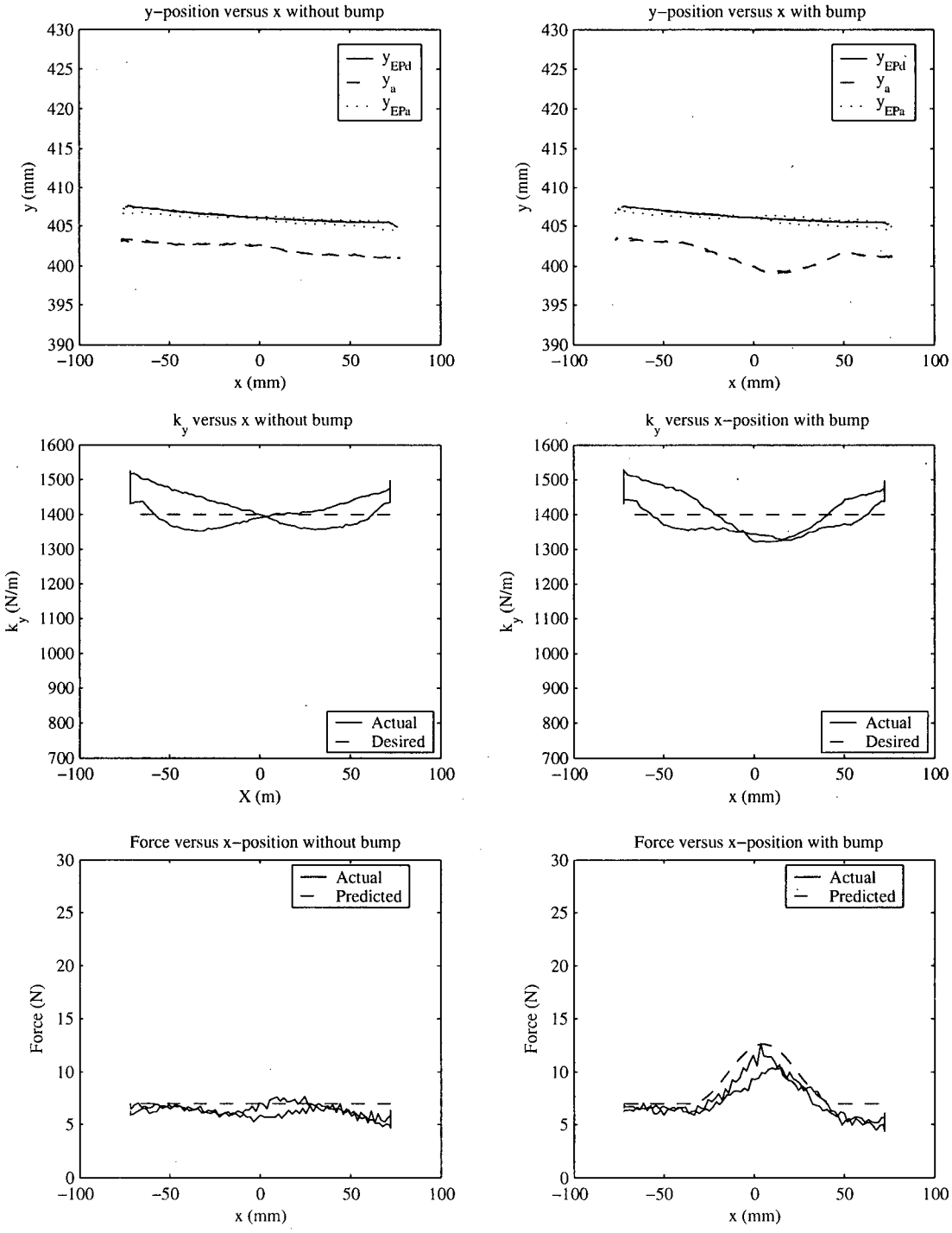

Test #22 – v_x=75mm/s, Y_{ep}=405mm, k_y=1400N/m

Figure J.22 – Contact test #22

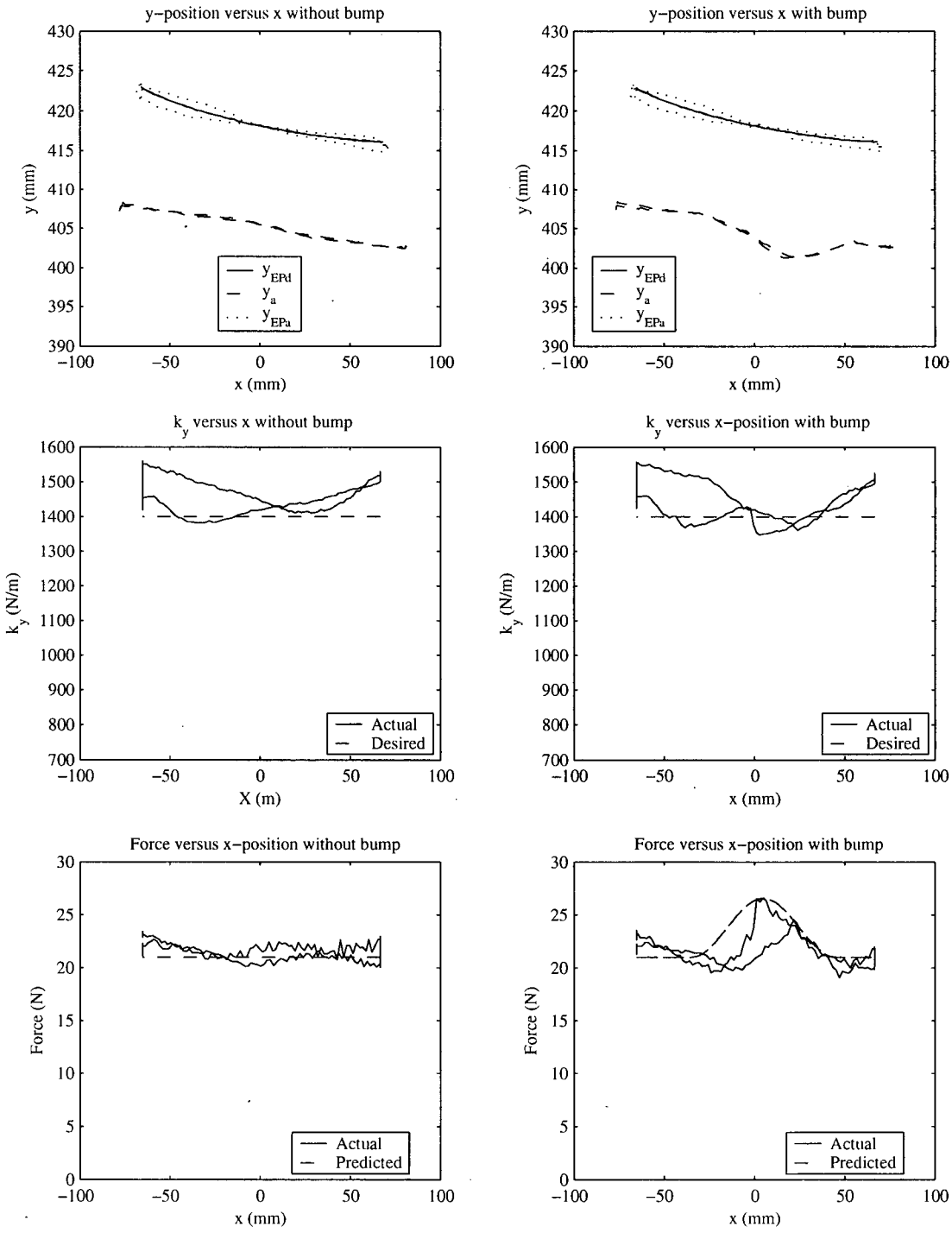

Test #23 – v_x=75mm/s, Y_{ep}=415mm, k_y=1400N/m

Figure J.23 – Contact test #23